IntechOpen

Nanorods and Nanocomposites

*Edited by Morteza Sasani Ghamsari
and Soumen Dhara*

Nanorods and Nanocomposites

*Edited by Morteza Sasani Ghamsari
and Soumen Dhara*

IntechOpen

Supporting open minds since 2005

Notice
Statements and opinions expressed in the chapters are these of the individual contributors and not necessarily those of the editors or publisher. No responsibility is accepted for the accuracy of information contained in the published chapters. The publisher assumes no responsibility for any damage or injury to persons or property arising out of the use of any materials, instructions, methods or ideas contained in the book.

We are IntechOpen,
the world's leading publisher of
Open Access books
Built by scientists, for scientists

4,700+
Open access books available

120,000+
International authors and editors

135M+
Downloads

151
Countries delivered to

Our authors are among the
Top 1%
most cited scientists

12.2%
Contributors from top 500 universities

Interested in publishing with us?
Contact book.department@intechopen.com

Numbers displayed above are based on latest data collected.
For more information visit www.intechopen.com

Meet the editors

Dr. Morteza Sasani Ghamsari is a senior researcher in the Photonics & Quantum Technologies Research School of the Iranian Nuclear Science and Technology Research Institute. His research focuses on photonic materials including metamaterials, quantum dots and plasmonic nanomaterials that can be used in a wide range of applications. His recent interests lie also in nano-bioimaging, 3D printing, nanostructures for tissue engineering (eg, ZnO, TiO 2), and biomaterials including carbon, graphene, and diamond quantum dots. He is a member of the editorial board and is a reviewer for different international journals. He collaborated with local and international academics/researchers on the graduation of post-graduate students and research projects. He edited 3 books and published 3 chapter books and over 95 articles in scientific journals as well as in reviewed conference proceedings.

Dr. Soumen Dhara received his PhD in Physics from the Indian Institute of Technology Guwahati, India. Presently, he is associated with the Faculty of Science, Sri Sri University, India as an Assistant Professor in Physics. Prior to joining the current affiliation, he was a postdoctoral fellow at Kobe University Japan, S. N. Bose National Centre for Basic Sciences, India, Cardiff University, United Kingdom, and Lovely Professional University. He has more than twelve years of research and teaching experience. He was awarded a prestigious JSPS postdoctoral fellowship in 2012 based on his research contribution on semiconducting nanowires. He published more than 30 research articles including 1 review article in high profile international peer-reviewed journals and 3 book chapters. He is also serving as a reviewer in many top-tier international journals on materials science. His research area of interests are semiconductor nanostructures, optoelectronics, solid state lighting and light sensors, spectroscopy of nanomaterials, thinfilm transistors (TFTs) etc.

Contents

Preface

During the past decade, the essential implications of nanotechnology have been proven and it has been established as emerging technology providing new directions of modern research broadly defined as "nanoscale science and technology". With the birth of nanoscience and nanotechnology in the last two decades, the most exciting and fastest growing fields were formed to create the new functional nanoscale dimensions systems and materials. Nanotechnology; research development and commercialization offer high revolutionary instruments and techniques to investigate the material properties at the nanoscale. Such technological advances have inspired new pioneering experiments that have revealed new physical properties and effects of matter at an intermediate level between atomic and bulk. Due to the potential technological applications for nanomaterials, they have become the focus of intense investigations. These materials with different sizes and shapes, such as nanorods and nanocomposites, with identical compositions often possess special properties. The purpose of this book is to provide a perspective on the current status of nanorods and nanocomposites with the contents provided by the scientists and researchers in the related professions. As such, this book is categorized into Part I, with an emphasis on nanorods, and Part II, with the specific importance of nanocomposites.

The book, *NANORODS* and *NANOCOMPOSITES*, provides the reader (students, scientists, and engineers working in the field of materials science and condensed matter physics) with an overview of the advances made on the synthesis of nanorods and nanocomposite materials and their emerging applications for a better lifestyle. The nanorods section covers advanced materials (metals, semiconductors, and organic materials) for nanorods, and growth/synthesis techniques of nanorods. There are six chapters in this section, which covers synthesis, characterizations and applications of gold nanorods, semiconducting oxide nanorods, and some composite nanorods. Emerging applications of the nanorods in various fields ranging from optoelectronic devices, sensors, and electro-optical devices are presented in the chapters. As all the contributing authors of the book are active researchers, they provide an up-to-date summary of their research topics. The readers will be presented with all the recent advances on the topics covered in this book. At the end of each chapter, important outputs of the topic covered and future research directions are provided. The perspective of the research on a special kind of nanostructures, nanorods, is presented in the Prologue.

There is one chapter to introduce the growth process of nanorods and cover the important strategies developed for the growth of various nanorods. Alsultan *et al.* presented the growth strategies of carbon, ZnO, gold, and magnetic nanorods. In addition, there are four chapters that cover the gas sensing application of ZnO written by Wang *et al.;* application of carbon nanorods in EO/IR detectors written by Sood *et al.;* a theoretical study on the structural and melting properties of gold nanorods written by Rida *et al.;* and metallo-dielectric colloidal films by Ana *et al*.

The nanocomposites section covers advanced nanocomposites. There are eight chapters in this section, which covers graphene, graphene like, polymer, and

epoxy nanocomposites. In addition, the mechanical and tribological properties of epoxy nanocomposites have also be considered. Nanocomposite-based sensors are presented in one chapter by Baiju. The kinetic features of epoxy nanocomposites synthesis process is evaluated by Prof. Irzhak Vadim. Also, the classification and application of electrospinning methods are covered. One of the chapters deals with the study of the electrolysis synthesis of copper matrix nanocomposites developed for the fabrication of nano-particulate bulk materials.

The editors hope that this book will contribute to increasing the availability of and access to new developments of nanomaterial synthesis and on nanostructure-property relationships in a specific way, especially in nanorods and nanocomposites.

Morteza Sasani Ghamsari
Solid State Lasers Research Group,
Iran

Soumen Dhara
Faculty of Science,
Sri Sri University,
Odisha, India

Section 1

Nanorods

Prologue: Nanorods – Recent Advances and Future Perspective

Soumen Dhara

1. Introduction

Nanorods (NRs) are a one-dimensional wonder in the nanomaterials science which have shown promising future for its applications in many fields ranging from household appliances [1] to medical technology [2, 3] to space technology [4]. Nanosized materials with an aspect ratio (defined as the ratio of the length to the diameter of the NR) greater than 10 are considered as nanorods. With respect to other nanostructures, they present several advantages, like a larger surface-area-to-volume ratio, a direct carrier conduction path, a large variety of potential novel properties available through the control of size and structure, and high compatibility with standard industrial device fabrication technologies. Such structures are of particular interest to the researchers; we can see from the increasing number of papers, as they exhibit quantum confinement in two dimensions, while the third is relatively unrestricted [5] (**Figure 1**).
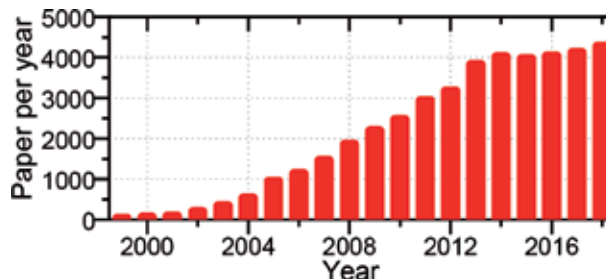
Figure 1.
Increase in the number of publication on the topic on nanorods for the last 20 years (Keywords: "Nanorods"; Source: Scopus).

2. Synthesis methods of nanorods

Nanorods can be grown by using either a *bottom-up* approach or a *top-down* approach. The *bottom-up* approach is the well-explored techniques, and varieties of NRs have been synthesized ranging from elemental metallic, organic, and semiconducting NRs and some complex oxide NRs. The chemical vapor deposition (CVD) is the most used and developed technique to synthesize various metallic, organic, and semiconductor NRs with controllable size and orientation based on a *bottom-up* approach. Control of size (diameter and length) of the NRs and its orientation on the substrate are achieved after extensive research on the growth of NRs by several researchers worldwide. However, it needs precise control of each of the growth parameters, e.g., source of the vapor, vaporization temperature, growth temperature,

vapor partial pressure, catalyst size, etc. to prepare high-quality NRs with preferable size and orientation. There are intense review articles dedicated to the growth of NRs available for further reading. Fortuna et al. [6] presented an in-depth review on the control of growth direction of metal catalyst-assisted synthesis of semiconductor NRs. The key parameters for the radial and axial heterostructures growth and their potential uses in the electronic industry are well summarized by Lu et al. [7].

Another bottom-up approach is chemical synthesis technique to prepare metallic and semiconducting NRs. In this technique, the key component is the cationic surfactant chemical used in the solution mixture which restricts the nucleation in two dimensions. As a result, the nucleation/crystallization process takes place only in one dimension, and hence one-dimensional nanostructures are formed. For example, in the case of ZnO NRs, the most commonly used surfactant is hexamethylenetetramine (HMT). HMT in aqueous solution acts as a bidentate ligand and is capable of bridging zinc(II) ions in solution with another zinc(II) ions available only in the ZnO(002) facet. As a result, ZnO NRs preferentially grow along (002) direction. A comprehensive review of the growth mechanism and the role of HMT with different chemical precursors for the growth of the ZnO NRs are presented by Xu et al. [8]. Several factors influencing the size, morphology, and orientation of the epitaxial ZnO NRs on the solution using the hydrothermal method and tuning of their size and morphology are extensively discussed by Guo et al. [9]. Compared to the CVD technique, the chemical synthesis route is beneficial due to the comparatively low growth temperature, high throughput, and lower production cost. However, the quality of the NRs in terms of crystallinity, presence of defects, and properties, grown in the CVD method, is always much better than in the case of NRs grown by chemical route.

Assembly and integration of highly ordered NR arrays on a large scale are essential for multifunctional devices and systems. Large-scale production of NR array has been achieved by using both the CVD technique and chemical route using a pre-patterned seed layer. Recently, there is a report on the growth of high-yield nanowires/NR arrays by Wei et al. [10]. In this work, they demonstrated an effective approach for controllable wafer-scale fabrication of ZnO NR arrays by combining laser interference lithographic patterning and hydrothermal growth. Laser interference patterning is employed to control the position, size, and orientation of synthesized ZnO NRs, while a hydrothermal chemical method is used to control the morphology and material properties of NRs.

In the top-down approaches, reactive ion etching (RIE) and metal-assisted chemical etching (MACE) are well-developed techniques to grow vertically aligned NRs in a large scale. RIE involves dry etching of Si or SiO_2 by halogen radicals to grow a vertical array of Si NRs with different aspect ratios [11]. Solution-based MACE technique has recently emerged as an effective tool for rapid synthesis of vertically aligned high-yield NRs in a large scale [12]. A noble metal nanoparticle is used as a catalyst to start the growth of the NRs. The shape and size, density, and quality of the NRs are controlled by several parameters: (i) the size and shape of the metal nanoparticles, (ii) intermediate distance between the nanoparticles, (iii) etching parameters (concentration and temperature of the etching solution, and etching time duration), and (iv) crystal quality and orientation of the starting wafer [13]. Both the above-mentioned processes are generally anisotropic, and the use of a protective layer/masking is very important to get uniform NRs.

3. Emerging device applications of nanorods

Based on the several fascinating properties of the NRs which are observed only in the nanoscale regime, researchers successfully fabricated and demonstrated

various prototype devices using NRs. Some of the important recent developments of device applications of NRs are summarized below.

The first step toward the application of any nanomaterials in the electronic industry requires the successful fabrication of transistor with efficient device performance. NRs from different materials ranging from elementary Si to oxide semiconductors to carbon have been successfully exploited in the field effect transistor (FET) devices [1]. So far, the highest mobility of 200 cm^2/V.s has been recently achieved from amorphous zinc oxynitride thin film [14]. Gluschke et al. [15] recently demonstrated a new fabrication method for high-quality gate-all-around TFT structure with independent top and bottom gate lengths. This approach overcomes significant limitations that exist in the wrap-gated NR transistors and the subthreshold swings achieved by this method as low as 38 mV/dec at 77 K for a 150 nm gate length TFT.

NRs have been successfully utilized as a light source by fabricating light-emitting diodes (LEDs) and nanolasers using NRs. There are many reports available where single-color-emitting NR-based LEDs were successfully demonstrated. Recently, core-shell InGaN/GaN NR-based LEDs are investigated for multiband emission. The emission of this LED covers nearly the whole visible region including UV. Emitted wavelengths and intensities are governed by different thicknesses of the InGaN/GaN grown on different crystal facets of the NRs as well as corresponding polarization-induced electric fields. For demonstration of the semiconductor NR laser with high-quality factor, a perfectly vertical orientation and smooth sidewall of the NRs are very important and crucial. From theoretical studies, it is found that the quality factor of the NR laser reduces to one third for a change in the inclination angle of the NRs of one degree (90–89°). Hsu et al. [16] developed an ultraviolet (~365 nm) GaN/Al metal laser that operates at room temperature with a low threshold power density of 5.2 mJ/cm^2. High-quality factor surface plasmon resonance (SPR) modes were achieved by incorporating an additional wet-chemical etching step with potassium hydroxide during the fabrication process. This step created nanorods with very smooth and vertically straight sidewalls that are truly perpendicular to the substrate.

Digital recording of data using light pulse instead of using magnetic field is recently explored by several researchers. The use of metal NRs for the data recording, instead of commonly used magnetic thin films, is realized. Zijlstra et al. [17] succeed to achieve five-dimensional optical recording in gold NRs by spectral and polarization multiplexing in single data bits with metallic nanoparticles for the first time. The gold NRs immersed in the polymer are used in this experiment for their unique SPR effect, and recording was done using a single laser pulse at femtosecond intervals. A DVD-size disk of three layers of gold NRs can hold 1.6 terabytes of information. This recording technology would revolutionize the optical storage industry with further miniaturization of storage devices.

Another important application of NRs is sensing, and varieties of NR-based sensors have been developed to date. In order to improve the sensitivity and time response of the NR-based light sensors, semiconducting NRs, mainly oxides, are exploited by fabricating inorganic-inorganic, inorganic-organic heterostructures, surface roughening, plasma treatment, and doping [18]. The present NR-based light sensors can compete with the existing Si-based thin-film sensors, and few of them are commercially available. A huge amount of work has been done on the NRs for the development of highly sensitive gas sensors for household/industry use and biosensors for the medical applications. So far, various oxide NRs have been utilized for the development of gas sensors which can detect H$_2$, CO, H$_2$S, methanol, acetone, and LPG gases with the sensitivity level down to 0.1 ppm [19]. Yasui et al. [2] developed a sensor composed of ZnO NRs anchored into a

microfluidic substrate and demonstrated a noninvasive early detection of cancer-affected urinary micro-RNA. This technology moves researchers toward the goal of micro-RNA-based noninvasive and simple early cancer diagnoses and timely medical treatment.

NRs also provide an environment-friendly solution to the increasing global demand for energy. NR-based junction solar cells or dye-sensitized solar cells show promising energy conversion efficiency with a long life span. So far, the highest conversion efficiency of 17.8% was reported using InP NRs [20]. ZnO NRs can also be used as a nanogenerator to produce energy by converting mechanical energy to electrical energy (piezoelectricity) due to its nonsymmetrical crystal structure [21]. Furthermore, this technology can be integrated with any nanoelectronic devices/sensors for the development of self-powered wearable electronics.

4. Conclusions and perspectives

Now, NRs can be synthesized in a large scale in *top-down* approach as well as in *bottom-up* approach. For device fabrication, patterning of the substrate is very important, and a low-cost effective pattering technique is yet to develop. So far, many breakthroughs in terms of fascinating properties of the NRs and emerging devices have been achieved after extensive research in the past decade. Now we acquired knowledge of the pros and cons of using NRs for various applications. Many startups are working on commercialization of NR-based devices and successfully brought few such technologies into the market.

In most cases, higher sensitivity and stability were achieved from the devices made with NR heterostructures. The synergistic performance lies in the selection of right materials and the structural quality at the interface of the heterostructures. There is always a scope to improve further by finding a perfectly matched external material and a methodology for an easy formation of the high-quality guest-host interface. There is a huge demand for an environment-friendly technology for the energy-efficient white light source. NRs may fulfill this societal requirement, and to do this, we can realize a core-shell structure with composite oxide NRs or a combination of selective doping and formation of the homojunction.

Further intensive research on designed syntheses and easy nanofabrication of NRs for the large-scale device applications would provide an enormous impact on nanotechnology and open an unprecedented avenue in energy, magnetic, electronic, and spintronic applications. However, the future of NR technology will be dependent on how we can minimize the production cost by maintaining high efficiency and long stability of the devices.

Author details

Soumen Dhara
Faculty of Science, Sri Sri University, Cuttack, Odisha, India

*Address all correspondence to: soumen5484@yahoo.co.in

IntechOpen

References

[1] Li Y, Qian F, Xiang J, Lieber CM. Nanowire electronic and optoelectronic devices. Materials Today. 2006;**9**:18-27

[2] Yasui T et al. Unveiling massive numbers of cancer-related urinary-microRNA candidates via nanowires. Science Advances. 2017;**3**:e1701133

[3] Verdict Media Limited. Stretchable Silver Nanowires Offer Medical Device Breakthrough. 2018. Available from: https://www.medicaldevice-network. com/news/stretchable-silver-nanowires-offer-medical-device-breakthrough/

[4] Chen Y, Zhang W, Yu C, Ni D, Ma K, Ye J. Controllable synthesis of $NiCo_2O_4$/Al core-shell nanowires thermite film with excellent heat release and short ignition time. Materials and Design. 2018;**155**:396-403

[5] Paulowicz I et al. Three-dimensional SnO_2 nanowire networks for multifunctional applications: From high-temperature stretchable ceramics to ultraresponsive sensors. Advanced Electronic Materials. 2015;**1**:1500081

[6] Fortuna SA, Li X. Metal-catalyzed semiconductor nanowires: A review on the control of growth direction. Semiconductor Science and Technology. 2010;**25**:024005

[7] Lu W, Lieber CM. Semiconductor nanowires. Journal of Physics D: Applied Physics. 2006;**39**:R387-R406

[8] Xu S, Wang ZL. One-dimensional ZnO nanostructures: Solution growth and functional properties. Nano Research. 2011;**4**:1013-1098

[9] Guo Z et al. Tuning the growth of ZnO nanowires. Physica B. 2011;**406**:2200-2205

[10] Wei Y, Wu W, Guo W, Yuan RD, Das S, Wang ZL. Wafer-scale high-throughput ordered growth of vertically aligned ZnO nanowire arrays. Nano Letters. 2010;**10**:3414-3419

[11] Fu YQ et al. Deep reactive ion etching as a tool for nanostructure fabrication. The Journal of Vacuum Science and Technology B. 2009;**27**:1520

[12] Huang Z, Geyer N, Werner P, de Boor J, Gosele U. Metal-assisted chemical etching of silicon: A review. Advanced Materials. 2011;**23**:285-308

[13] Ghos R, Giri PK. Silicon nanowire heterostructures for advanced energy and environmental applications: A review. Nanotechnology. 2017;**28**:012001

[14] Yamazaki T et al. Amorphous ZnO_xN_y thin films with high electron Hall mobility exceeding 200 cm^2/V.s. Applied Physics Letters. 2016;**109**:262101

[15] Gluschke JG et al. Achieving short high-quality gate-all-around structures for horizontal nanowire field-effect transistors. Nanotechnology. 2019;**30**:064001

[16] Hsu YC et al. Room temperature ultraviolet GaN metal-coated nanorod laser. Applied Physics Letters. 2013;**103**:191102

[17] Zijlstra P, Chon JWM, Gu M. Five-dimensional optical recording mediated by surface plasmons in gold nanorods. Nature. 2009;**459**:410-413

[18] Dhara S, Giri PK. ZnO nanowire heterostructures: Intriguing photophysics and emerging applications. Reviews in Nanoscience and Nanotechnology. 2013;**2**:147-170

[19] Wei A, Pan L, Huang W. Recent progress in the ZnO

nanostructure-based sensors.
Materials Science and Engineering B.
2011;**176**:1409-1421

[20] Dam DV et al. High-efficiency
nanowire solar cells with
omnidirectionally enhanced absorption
due to self-aligned indium-tin-
oxide Mie scatterers. ACS Nano.
2016;**10**:11414-11419

[21] Wu W, Wang ZL. Piezotronics
and piezo-phototronics for adaptive
electronics and optoelectronics. Nature
Reviews Materials. 2016;**1**:16031

Nanomaterials: An Overview of Nanorods Synthesis and Optimization

Alsultan Abdulkareem Ghassan, Nurul-Asikin Mijan and Yun Hin Taufiq-Yap

Abstract

Nanorods are nanostructures that are the object of fundamental and applied research. They may be prepared from carbon, gold, zinc oxide, and many other materials. They are bigger than individual atoms (measured in angstroms, $1 \text{ Å} = 10^{-10}$ m) and also than small molecules. The turning point for nanomaterials research was the discovery of carbon nanotubes in 1991. Their mechanical, electrical, and optical properties depend upon their size, allowing for multiple applications. Also, nanorods may be functionalized for different applications. In this Chapter, the methods of synthesis and analysis, and the applications of carbon, zinc oxide, gold, and magnetic nanorods are reviewed.

Keywords: nanorods, gold nanorods, ZnO nanorods, carbon nanorods, magnetic nanorods

1. Introduction

Nanomaterials are foundations of nanoscience and nanotechnology. The development of nanomaterial has been attracted great interest in the worldwide in the past few years. The turning point for nanomaterials research was the discovery of carbon nanotubes in 1991 [1]. Nanomaterials are usually defined as having a particle size between 1 and 100 nanometers (nm). They are bigger than individual atoms (measured in angstroms, $1 \text{ Å} = 10^{-10}$ m. One nanometer is millionth of millimeter. It is equal to 100,000 times smaller than the diameter of human hair. After this discovery, there was an explosive increase in the number of research teams working in the field. The properties of nanomaterials deviate from those of "bulk" materials with the same composition, thus allowing for many interesting applications. At nanodimensions, quantum effects, like quantum confinement, permit multiple applications [2–4]. Some of nanotechnology applications include alternative energy [3], electronics [5, 6], catalysis [5], biomedicine [2], batteries [7], water treatment [8], and materials reinforcement [9] (**Figure 1**).

2. Classification of nanomaterial

Classification is based on the number of dimensions, which are not confined to the nanoscale range (<100 nm) (**Figure 2** and **Table 1**):
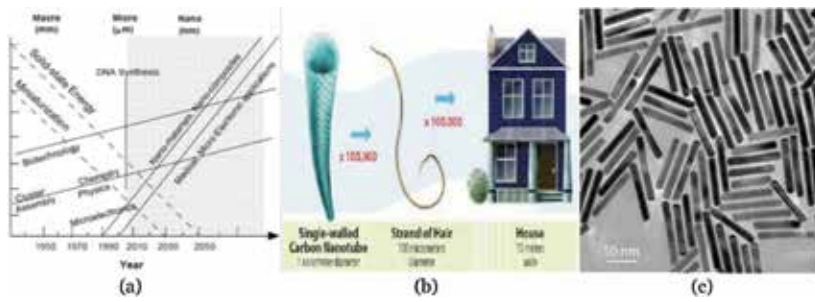
Figure 1.
(a) Evolution of science and technology and the future [10]; (b) an example of nanomaterial comparison; and (c) an example of the nanorod image [11].
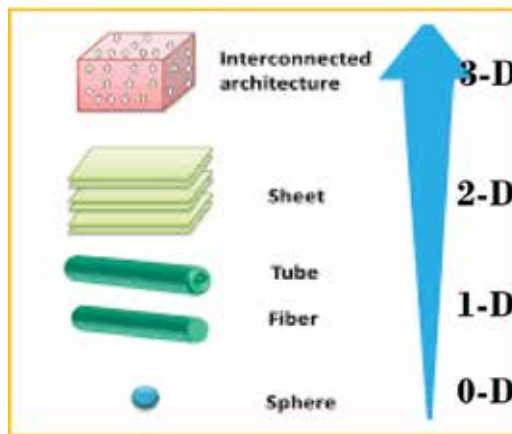
Figure 2.
0-D, 1-D, 2-D and 3-D nanomaterial [12].
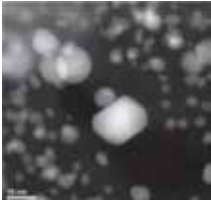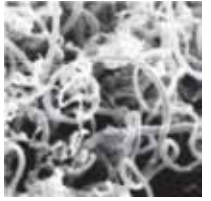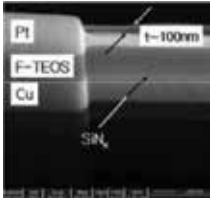
0-D	1-D	2-D	3-D
Material within nanoscale (no dimension or 0-D). It can be amorphous or crystalline (single crystalline or polycrystalline), can composed of single and multi-element, exhibit various shapes and forms, exist individually or incorporated in matrix, exist in the form of metallic, ceramic or polymeric.	One dimension outside the nanoscale. Exhibit needle like-shaped, the material including nanotubes, nanorods, and nanowires. It can be amorphous or crystalline (single crystalline or polycrystalline), Chemically pure or impure, Standalone materials or embedded in within another medium, exist in the form of metallic, ceramic, or polymeric	Two of the dimension not confine to nanoscale, exhibit plate-like shape, the material including nanofilms, nanolayers and nanocoating. It can be amorphous or crystalline, composed of various chemical composition, deposited on a subtracted, exist in the form of metallic, ceramic or polymeric.	Three dimension not confined to the nanoscale, materials possess a nanocrystalline structure, bulk nanomaterials can be composed of a multiple arrangement of nanosize crystals, most typically in different orientations, contain dispersions of nanoparticles, bundles of nanowires, and nanotubes as well as multinanolayers.

Table 1.
Details characteristic of nanomaterial classification.

1. zero-dimensional (0-D);

2. one-dimensional (1-D);

3. two-dimensional (2-D); and

4. three-dimensional (3-D).

3. One-dimensional (1-D): needle-like shape structure

1-D nanostructures as a series of the most important materials owed by it fascinating physical properties. Due distinct structure-dependent properties had lead it application widely especially in solar energy conversion, thermoelectric devices, energy storage technology. 1-D nanostructures mainly show three different morphologies (**Table 2**):

i.   nanorod;

ii. nanowires; and

iii. nanotube.

Among those 1-D nanostructures, nanorods have the advantage as it can be made from most elements (metals and nonmetals) and compounds, and the synthetic requirements for their production are more flexible than for nanotubes and nanowires. Nanorods have typical lengths of 10–120 nm. For example, metallic nanorods, semiconductor nanorods, carbon nanorods, and oxides nanorods, are essential for the development of electronic, optical, magnetic, and micromechanical devices [5, 6].
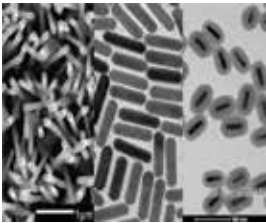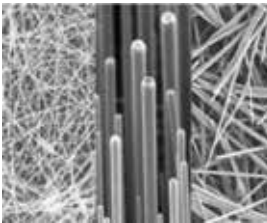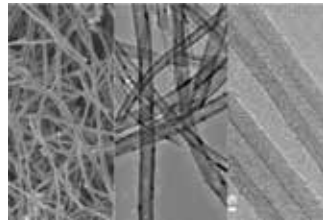
Nanorod	Nanowires	Nanotube [9]
Nanorods similar to nanotube but without internal surface. Less versatile than nanotube but thermally stable	Nanowires have typically diameters of a few tens of nm, but the lengths are not bounded.	Nanotubes are also like nanowires, in terms of diameter, but hollow and with a standard aspect ratio (length divided by width) of 3–5.
Made: carbon, metal oxide, metal	Made: ceramic, metal oxide, metal	Exist as single-or multi-walled.
Application: drug delivery, bioimaging, photothermal therapy nanocapacitors, etc. [5, 6]	Application: magnetic devices, nanowires battery, nanogenerator, semiconductor, etc.	Made: carbon; single-walled carbon nanotubes (SWCNT), multi-walled carbon nanotube (MWCNT) Application: scaffolds or templates for the building [13].

Table 2.
Nanorods, nanowires and nanotube.

4. Advantages of nanorods

Due to their shape anisotropy (physical properties), nanorods are attractive component to be studied and ideal candidates for many application. It was discovered that ability of the nanorods was enhanced as compared spherical particles. This is due to the increase of aspect ratio of the particle lead to the increased of excitation of surface plasmons in the nanoparticles. Particularly, the strength of the dipole moment is within a nanoparticle due to incrementing of surface plasmons. Therefore, an increase of surface plasmons lead to the enhancement of electrical field in nanorods as compared spherical particles. One example of benefit of a rod-like shape demonstrated by Alivisatos and co-workers [14] who observed partially aligned CdSe nanorods provided an effective, directed path for charge carriers to move throughout the photovoltaic device and be collected. Similarly, the incorporation of nanorods within P3HT film could improve the external quantum efficiency by a factor of 3 as the aspect ratio increased from 1 to 10. The accumulation of electrons was improved as the aspect ratio of nanoparticles increased. Furthermore, alignment of nanorods also plays a key role in improving it properties. Work by Winey group [15] studying Ag nanorods for polystyrene composites and discovered that the aspect ratio of anisotropic nanoparticle play role in the electrical conductivity of polymer composites. Particularly, due to the minimal percolation threshold of rod-shape particles as compared to spherical particles. Percolation has been found to be depended on both size and shape of nanoparticles. Larger in both length and diameter of rod-shape particles are expected to share many advantages in the oriental properties of nanorods. Last but not least, nanorods offer more advantages over isotropic (homogeneous and uniform) particles. It can be summarized that the efficiency of nanorods depends strongly on nanorods aspect ratio, volume fraction, polydispersity and orientation.

4.1 Type of nanorods and advanced synthesis method

Various nanorods have been extensively studied such as carbon nanorods, ZnO nanorods, gold nanorods and magnetic nanorods. Recently, various techniques have been proposed for synthesizing the nanorods. It can be classified into either via physical or chemical methods or known as bottom-up or top-down techniques. The method such as thermal hydrolysis, hydrothermal route, sol-gel, vapor condensation, spray pyrolysis, pulse laser decomposition, laser ablation, thermal evaporation, pulse combustion-spray pyrolysis, electro-mechanical, flame spray plasma, microwave plasma, low energy beam deposition, ball-milling, chemical vapor deposition, laser ablation, chemical reduction, co-precipitation, hybrid wet chemical route, physical evaporation, electrophoretic deposition, radio frequency (RF) magnetron sputtering, vapor deposition, metal assisted growth, template assisted routes, metal-assisted growth and seed-based growth, simple chemical etching, etc. Typically, nanorods prepared by controlling the nucleation growth than transverse one.

4.1.1 Carbon nanorods

Carbon nanorods have attracted great interest from past few decades owing to their physical (particle size, shape, large surface area and greater pore size distribution) and chemical properties [16–18]. Nanorods made of carbon also known as "carbon nanorods" and "diamond nanorods." Diamond nanorods have a crystalline structure like diamond with sp^3 carbon hybridization. The yield and purity of

synthesizing the carbon nanorods are strongly dependent on the composition of the inert atmosphere and its pressure. Generally, the carbon nanorods had better physicochemical properties after introducing different functionalities in the carbon nanorods pore surfaces. It will permit many applications, like in catalysis, water treatment, supercapacitors, and others. Carbon nanorods large applied as anodic material in batteries apart from their application like fillers [19] and high performance electrode materials in batteries [20–23]. Till now, various synthesis methods have been proposed and it can be classified as "bottom up" (like synthesis from small molecules or colloidal solutions) or "top down" (like starting with bigger structures). The top-down method for synthesizing carbon nanorods including, simple chemical etching and electrochemical etching. Meanwhile, bottom-up approach including template assisted, metal assisted, hydrothermal route, vapor deposition (CVD), seed based and other synthesis in solution.

A recent finding was discussed on the recent advanced efforts in the preparation of carbon nanorods from metal-organic frameworks (MOFs) [24]. MOFs-a class of porous and crystalline material have attracted a great deal attention due to their fascinating architectures as well as their useful properties [25]. MOFs could be synthesized using both organic and inorganic components. Eventhough MOFs is well-established excellent porous material, yet the thermal transformation of MOFs into carbon materials accompanied by partial or complete collapse of their original morphology. Due to this reasons, the synthesis of nonhollow (solid) 1-D of carbon nanorods with moderate aspect ratio, high surface area and good performance capacitor electrodes is achieved by self-scarified and morphology-preserved thermal transformation of MOF-74 [24] (**Figure 3**).

The reaction of zinc nitrate and 2,5-dihydroxyterephthalic acid in N, N-dimethylformaide (DMF) by traditional hydrothermal method resulted in formation of microcrystalline MOF-74. The room-temperature reaction of those components in the presence of salicylic acid as a modulator led to the formation of rod-shaped MOF-74 (MOF-74-Rod, 30–60 nm wide, 200–500 long) as observed by scanning electron microscopy (SEM) and transmission electron microscopy (TEM).
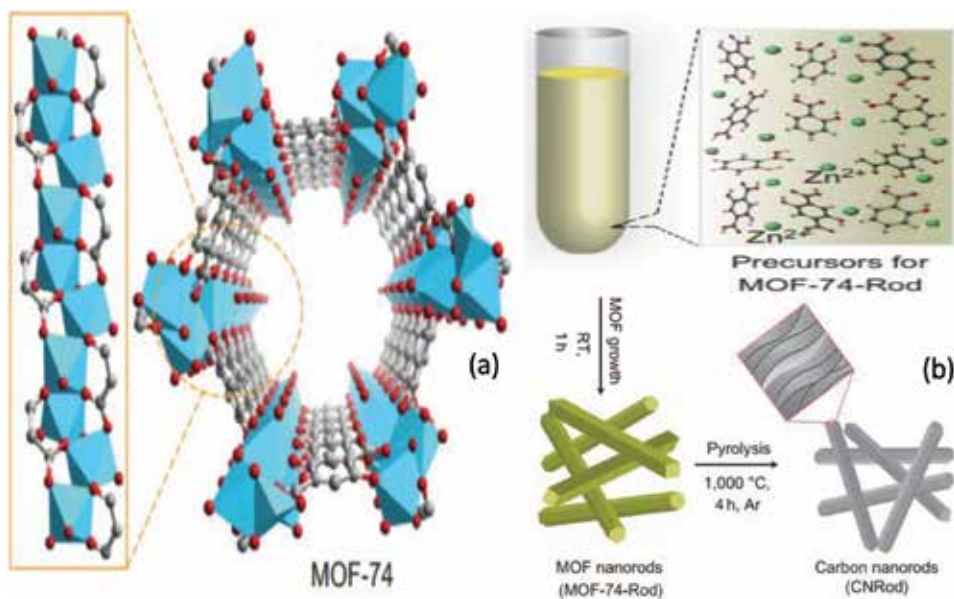

Figure 3.
(a) The secondary building unit and 3-D crystal structure of MOF-74 and (b) scheme of synthesis of MOF-74-rod, carbon nanorods. (b) The secondary building unit and 3-D crystal structure of MOF-74.

The addition of salicylic acid directed MOF growth in a rod-shape morphology by stabilizing the active metal sites on the MOF crystal surface [26]. The thermal transformation of MOF-74-Rod at 1000°C results in the formation of carbon nanorods. In comparison of MOF-74-Rod (377 $m^2 g^{-1}$), higher surface area of MOF-74 (411 $m^2 g^{-1}$) might be attributed to the perfect arrangement of MOF crystallites in the domain structure. The pore size distribution for MOF-74-Rid confirms the formation of micro (∼1.5 nm) and mesopores (∼6.5 nm), whereas MOF-74 shows the presence of microspores (∼1.2 nm) exclusively. The great different in pore size distribution attributed to the formation of voids resulted from lateral attachment of MOF nanorods. The MOF-74-Rod showed excellent capacitor performance with specific capacitance value of 164 F g-1 at sweep rate of 10 mVs^{-1}. Overall from this study, open up new avenues for efficient product of 1-D carbon material with promising applications in electrochemical devices.

4.1.2 ZnO nanorods

ZnO has a wide band-gap (3.37 eV at room temperature). ZnO is known to have wurtzite structure with lattice constant (a) 3.249 Å, (c) 5.207 Å. It has a large excitonic binding energy of 60 MeV, which is greater than the thermal energy at room temperature, makes it a promising candidate for applications in blue-UV light emission and room-temperature UV lasing. ZnO posed an excellent chemical and thermal stability and the electrical properties. Since Zno has lack of center symmetry, make it results in a piezoelectric effect, whereby a mechanical stress/strain could be transformed into electrical voltage and vice versa, due to the relative displacement of the cations and anions in the crystal [27]. Single crystal of ZnO exhibit significantly faster electron transport and greater mobility. The faster electron transport is a result of the high electron diffusion coefficients, which will provide significant advantages to device performance [28]. Since ZnO could emits at the near ultraviolet, has transparent conductivity and piezoelectric properties, thus, ZnO is an interesting material for semiconductor and laser devices, piezoelectric transducers, transparent electronics, surface acoustic wave devices, spin functional devices, and gas sensing. Overall, ZnO is an excellent material for sensor application attributed by its large surface to volume ratio that leads to the enhancement of it sensitivity, bio-safety and bio-compatibility. A recent research has demonstrated that creation of highly oriented and ordered array of ZnO nanostructures has greatly stimulate interest in development of novel devices [29]. The large surface area of nanorods makes ZnO attractive for gas and chemical sensing. High oriented array of ZnO nanorods (and nanowires) can be produced via various chemical, electrochemical and physical deposition techniques such as chemical vapor deposition (CVD) or metal organic CVD (MOCVD), vapor-liquid-solid (VLS) growth, electrochemical deposition (ED) and hydrothermal approaches.

Recently, a great deal of attention has been focused on the study of synthesizing the ZnO nanorods via VLS method. In this case, gold (Au) nanoparticles are used as catalyst in order to promoting the ZnO nanorods formation. Unfortunately, the are some apparent drawbacks in VLS growth technique. Generally, it required high growth temperature > 900°C in order to dissolving the Zn vapor into the Au catalyst simultaneously forming an alloy droplet. After saturated, Zn precipitates out from the droplet and further oxidized as ZnO nanorods grow. The other drawback from VLS growth method is that at the tips of ZnO nanorods there are always impurity particles that might be undesirable for fabrication. Due to this reason, the synthesizing ZnO nanorods via CVD and MOCVD were highlighted. The synthesis temperature used generally mild reaction temperature and high purity of ZnO nanorods could formed.

Apparently, the CVD process took place in a horizontal quartz tube placed in a rapid thermal furnace. **Figure 4(a)** shows a schematic illustration of the CVD furnace including a horizontal quartz tube of 1-in. A high-purity metallic granulated zinc (99.99%) was placed in an alumina boat which was then inserted at the end of quartz ampoule sealed at one end. Au nanoparticles are used as catalyst deposited on Chip B and C. Once the temperature went above the melting point of zinc metal (420°C), zinc would gradually vaporize to fill the quartz vial and then diffuse to Chip B and then to Chip C. The Au catalyst further formed liquid droplet and super saturated with Zn vapor. The nucleation growth of ZnO started with the arrival of oxygen gas. The ZnO will precipitate when the droplet reached a critical radius and continuously growth. Typically, ZnO synthesis was synthesized follow several steps. Initially, the quartz tube evacuated to 10–2 Torr, follow by purged using Ag gas to maintain a 1 atm ambient. The furnace temperature rapidly increased to 700°C under constant Ag flow and maintain within a period of time. Finally, the oxygen gas (O_2 mixed Ag) was then flown through quartz tube forcing a precipitate to form. As shown in **Figure 4(c)**, shows prismatic hexagonal rods of ZnO grown area. The ZnO crystal continuously growth perpendicular from the surface on one single nanowires forming comb
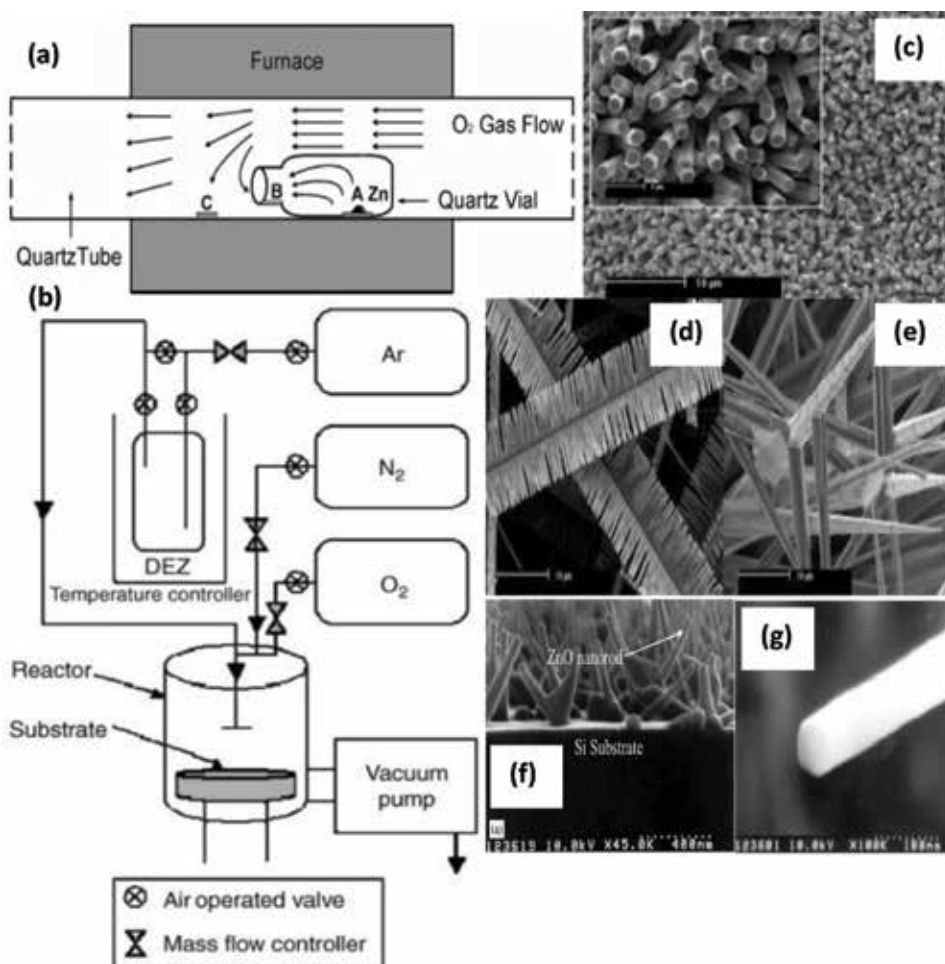
Figure 4.
Schematic illustration of the (a) CVD system with a horizontal quartz tube placed in a furnace. A small quartz vial inside the quartz tube is used to trap zinc vapor during the synthesis process, (b) MOCVD system, (ce) SEM image for ZnO nanorods from CVD system, (f) SEM image for ZnO nanorods from MOCVD system and (g) SEM image of a ZnO nanorod, indicating a diameter of 110 nm.

structure (**Figure 4(d)**). Thick ZnO needle can be found at the outer edge (**Figure 4 (e)**). With sufficient oxygen concentration, wires with larger diameter are grown.

In the case of MOCVD techniques, in MOCVD generally, the use of organic precursor, such as $Zn(C_2H_5)_2$ and O_2 system, are involved. The ZnO films or nanorods were deposited on p-type silicon with (100) orientation. **Figure 4(b)** shows a schematic diagram of the MOCVD system. Mass flow controllers separately controlled the flow of Ar and O_2 gases and the gas flow ratio of Ar to O_2 was in the range of 1–2. The substrate temperature was varied as a process variable ranging from 250 to 500°C [30]. The deposition time was set to 10 min [30]. In this study the SEM image reveals that ZnO nanorods are directly grown on Si substrates (**Figure 4(f)**) and the diameter of ZnO nanorod ranges from 40 to 120 nm (**Figure 4(g)**). In summary, the uniform ZnO nanorods have successfully synthesized in bulk quantities directly on the Si substrate using the MOCVD technique.

Recently, several studies have demonstrates the growth of ZnO nanorods could be achieved molecular beam epitaxy (MBE). In MBE, the growth is performed under clean, low pressure condition and the reactants are very pure Zn metal and atomic O from a plasma generator [31]. In MBE system, the potential contamination is minimized [31]. The ZnO layers typically were grown on p-type silicon wafer Si (100) under conditions: substrate temperature 300–430°C, temperature of the Zn-Knudsen cell 300°C (Zn beads of purity 99.9999 were filled), pressure of the chamber during the growth was $\sim(1-4) \times 10^{-4}$ mbar and oxygen plasma was generated [32]. The ZnO nanorods of reasonable quality could be deposited forming cored nanorod (**Figure 5(a and b)**). This cored nanorods could be produced using Mg-doping during MBE growth. Similarly, Heo et al. [33] report on catalyst-driven MBE of ZnO nanorods. The single ZnO nanorod growth is realized via nucleation on Ag films that are deposited on SiO_2-terminated Si substrate surface (**Figure 5(c)**). Growth occurs at substrate temperatures within range of 300–500°C. The nanorods are uniform cylinders exhibiting diameter of 15–40 nm (**Figure 5(d)**) and lengths in excess of 1 μm. Eventhough CVD, MOCVD and MBE
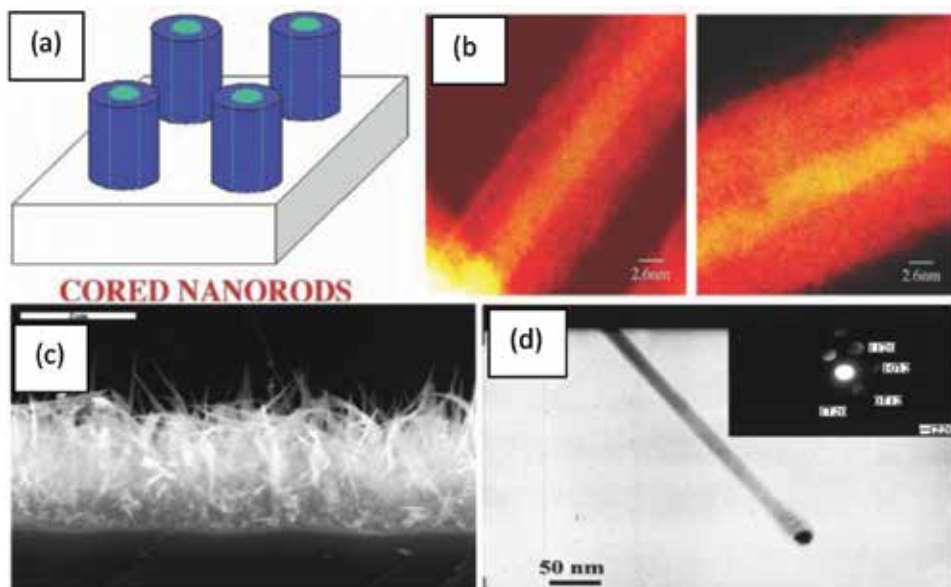
Figure 5.
(a) Schematic of coaxial nanorods having a lateral heterostructure (top), (b) transmission electron micrographs showing cored $(Zn_{1-x}Mg_x)O$ nanorods a having Zn-rich phase surrounded by another $(Zn_{1-x}Mg_x)O$ phase (bottom), (c) SEM image of ZnO nanorods nucleated on Ag-coated Si/SiO$_2$ substrate and (d) TEM and selected area diffraction image of a single crystal ZnO nanorod.

such an attractive technique in developing ZnO nanorods but these growth techniques are complicated and growth temperatures used are high (435°C).

The hydrothermal method [34, 35] has attracted considerable attention due to its unique advantages-it is simple, low temperature (60–100°C), high yield, low cost, uncomplicated process, excellent morphology-well-defined structure and controllable process [36]. Particularly, chemical precursor solution involves in formation of ZnO nanorods via hydrothermal route is Zn salt and hexamethylenetetramine on Si substrates with a seed layer prepared from zinc acetate solution. Polyethyleneimine was added to the solution to increase the nanorod aspect ratio [37]. The growth temperature and the growth time were constantly kept at lower temperature < 100°C and under certain period of time. Recently, ZnO nanorods with hexagonal structure were synthesized via hydrothermal route by Polsongkram and co-workers using zinc nitrate $[Zn(NO_3)_2 \, 6H_2O]$ that was mixed with hexamethylenetetramine (HMT) $(C_6H_{12}N_4)$ solution and treated under temperature 60–95°C. It is evident that the at 95°C, the sample mainly consists of ZnO nanorods and most of them assembly into branched and urchin-like morphologies (**Figure 6(a)**). It was discovered that the hexagonal ZnO nanorods formed about 2 mm in length 100–150 nm in diameter. The nanorods grown larger (thick branched rods) when the temperature reduce to 75 and 60°C [35] (**Figure 6(c** and **d)**). This study also found that controlled growth of nanorods ranging from a thinner to a larger diameter can be realized by appropriate choice of the initial precursor concentration and deposition time. The hexagonal ZnO nanorods formation via hydrothermal method also in agreement with Phromyothin findings (**Figure 6(d** and **e)**) [38]. Similarly, this study also discovered that as the precursor concentration increased, the average diameter of ZnO nanorods will enlarge. It can be suggested that the precursor concentration provides the crucial role on the physical morphology and crystal growth direction of ZnO nanorods.

Last but not least, the ZnO nanorods also could be synthesized via ED method. ED method has many advantages including a low growth temperature, simple and low cost process without the need for vacuum systems for preparing ZnO nanorods with high crystallinity, being suited for scale-up and good electrical contact between the structures and the substrate [39]. However, in ED method when the ZnO nanorods were growth using electrochemical on transparent conducting oxides (TCOs, i.e. ITO and FTO), electrodes and a previously deposited ZnO seed layer are necessary to precisely control the morphology and aspect ratio of the as-grown ZnO nanostructures. In ED method the ZnO nanorods were electrodeposited from the zinc nitride aqueous solution in an electrode system. Typically, electrodepositions were conducted in a water bath at 80°C. **Figure 6(f)** presents the electrodeposited ZnO results, the result showed the SEM images of ZnO nanorods on predeposited PAN film [40]. The ZnO nanorods exhibited good vertical alignment, and with significant hexagonal cross section and a relatively uniform size with an average diameter of 180 nm.

4.1.3 Gold nanorods

Much attention has been given recently to gold nanorods (Au nanorods), mainly due to their applications in biomedicine. Gold nanorods show two absorption bands, known as surface plasmon resonance (SPR) bands, called the TSPR (transverse) in the visible and LSPR (longitudinal) in the near infrared (NIR) region [41]. This last one is useful for medical applications because NIR radiation is the one that penetrates the most in living tissues. The absorbed radiation is converted into heat, thus showing promise for cancer treatment. Also, these nanorods have localized surface plasmon resonances (LSPRs) that allow for unique scientific and technical applications [42]. In particular, the synthesis of well-defined size and shapes
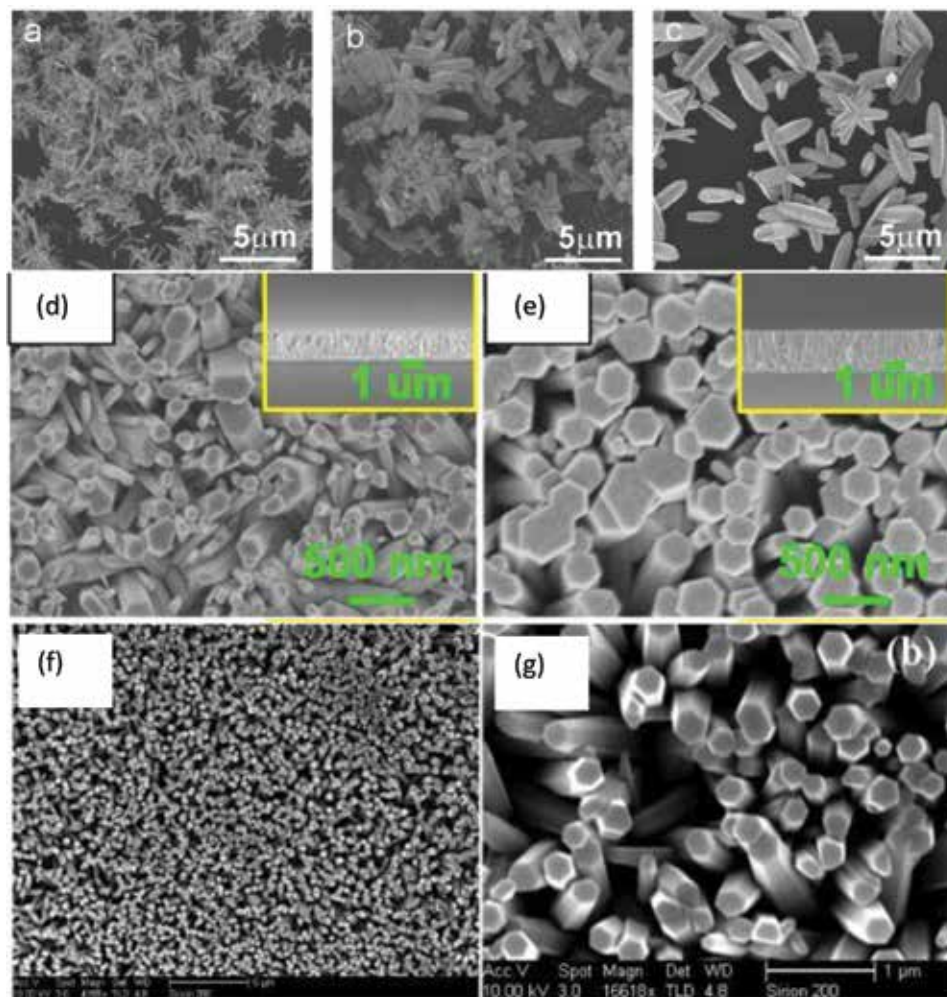
Figure 6.
Scanning electron microscopy (SEM) images of the ZnO nanorods grown from ZnNO$_3$-0.040 M: HMT-0.025 M aqueous solution in 30 min at different temperatures: (a) 95°C, (b) 75°C and (c) 60°C [35], (d and e) FESEM images of ZnO nanorods synthesized via hydrothermal method [38] and (f and g) SEM images of ZnO nanorods via ED method.

of Au nanorods has attracted much attention due to its importance in electronic and optical properties of these nanomaterials. The longitudinal bands of Au nanorods can be tuned by changing their aspect ratio, simultaneously make it possible to gain absorption bands at the desired wavelength in the NIR. Small change in aspect ratio will result in drastic change in the NIR absorption wavelength. The Au nanorods could be synthesized via two general growth approaches, which are bottom-up and top-down methods. For bottom-up methods, Au nanorods are generated through nucleation in aqueous solutions and subsequent overgrowth, where Au salts are usually used to provide the Au source through reduction. Particularly, bottom-up method including wet-chemical, electrochemical, sonochemical, solvothermal, microwave-assisted and photochemical reduction technique. All of these method involving the use of reduced aqueous solvated Au salts by various reducing agents, such as sodium borohydride, ascorbic acid, and small Au clusters, under different external stimuli (triggering the reduction of Au salt). The length of Au nanorods could be elongated with the use of template, it serves to confine the growth along one direction during the reduction.

The electrochemical method was the first technique for developing the Au nanorods. Briefly, the Au and Pt were used as the anode and cathode, respectively. These electrodes will be immersed in an electrolytic solution containing the cationic surfactant such as hexadecyltrimethylammonium bromide (CTAB) and co-surfactant. The CTAB works as supporting electrolyte and stabilizer (preventing aggregation of the nanorods), and CTAB induces the formation of rods. The length of the nanorods is determined by the presence of a silver plate in the solution. The silver metals react with the Au ions generated by the dissolution of the anode. The researchers found that the amount of dissolved silver and the concentration of Ag^+ ions determined the length of the nanorods [25]. The larger the area of silver plate, the higher the amount of Ag+ ion species formed and the higher the speed of silver will be released and thus, the longer the Au nanorods formed [43].

Based on previous literature for Au nanorods formation via bottom-up method, seed mediated growth has been by far the most efficient and popular approach [44]. This method utilizes "soft templates" for growing Au (**Figure 7**), which was developed by Murphy and El-Sayed studies [42]. Highly yield monodis-perse Au nanorods with greater uniformity could be developed via this method. Typically, small Au nanoparticles seed of ~1.5 nm is initially prepared by reducing chloroauric acid with borohydride in an aqueous CTAB solution [42]. The seed solution will be mixed with growth solution containing metal salt (weak reducing agent) such as ascorbic acid and a surfactant-directing agent CTAB. The CTAB will absorbed onto Au nanorods forming a bilayer. It is suggested that aspect ratio of Au nanorods can be controlled by ratio metal see/metal salt in growth solution. According to former study, the CTAB will bind to the crystallographic faces of Au existing along the sides of pentahedrally twinned rods, as compared to the faces at the tip. The seed-mediated growth technique is the presence of CTAB is one of the most widely used and the yields of the nanorods from the seed-mediated growth method can be as high as 99%. It have been reported that the size and shape of Au
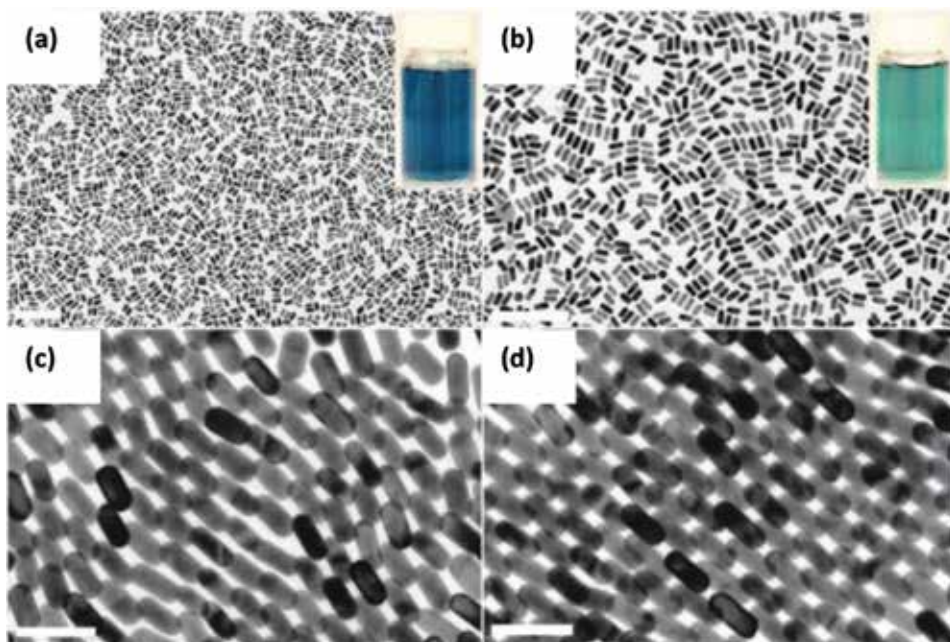
Figure 7.
(a–d) TEM images for Au nanorods synthesized via seed-mediated growth with the addition of aromatic additive [45].

nanorods could be tailored by adjusting the growth condition such as the pH of growth solution, composition of surfactant, amount of the reagent, growth temperature and structure of the seed in the seed-mediated growth process. Interestingly, recent study demonstrated high yield and greater uniformity of Au nanorods could be obtained via seed-mediated growth through the use of aromatic additive to CTAB [45]. **Figure 7(a** and **c)** showed TEM images of Au nanorods synthesized with 0.0126 M sodium 3-methylsalicylate (additive) present in the growth solution. The nanorods obtained have an average diameter of 14.0 (1.0 nm and a length of 33.0 ± 2.5 nm. On the other hand, slightly longer nanorods are made when 0.010 M sodium salicylate is used as the additive (**Figure 7(b** and **d)**).

Eventhough the bottom-up method results in excellent monodisperse Au nanorods with small diameter and high uniformity, yet them suffer some drawback where typically, selective placement of Au nanorods at desired locations on substrates by the bottom-up methods has been very difficult owing to the random nature of the reduction of Au ions and the deposition of Au atoms in reaction solutions. Moreover, the shape and size of Au nanorods also varied from different synthesis batches. This will affect their optical and catalytic properties and applications. Last but not least, bottom-up method suffers in placing Au nanorods into large-area, ordered arrays. Due to these reasons, top-down approaches gained interest.

It is well-established that top-down method could promote high production homogeneous Au nanorods with controlled particle geometries and regular inter-particle arrangements, which is valuable for quantitative characterization as well as device applications. In top-down methods, Au nanorods are obtained through a combination of different physical lithography processes and Au deposition [42]. Particularly, there are two technique used for top-down method in synthesizing the Au nanorods. First method is through the removal of Au from predeposited Au films using ion beam or etching techniques. Second method is by employing the lithography techniques to create mask. Au layer then deposited on the substrate which is covered by the mask via physical method: thermal, electron-beam evaporation or sputtering. The synthesized Au nanorods further obtained from lift-off process. Generally, the size of Au nanorods obtained via top-down method is limited by the resolution of lithography method. Interestingly, recent study by Koh and co-worker reported that state-of-the-art electron beam lithography system able to produce the size of Au nanorods within diameter ranging from ~10 to >100 nm [46]. The Au nanorods were fabricated on 30-nm-thick silicon-nitride (SiN) membranes (**Figure 8(a)**). High-resolution TEM images of individual nanostructures of Au nanorods in **Figure 8(b)** reveal that the Au nanostructures
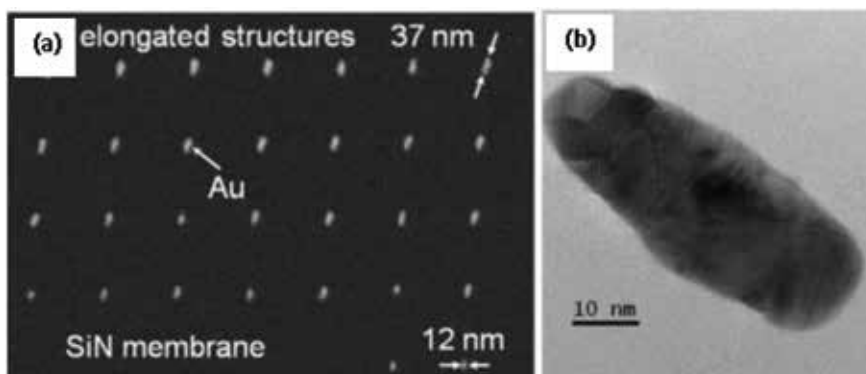
Figure 8.
(a) SEM images of an array of Au nanostructures with elongated and (b) TEM image of individual Au nanorods [46].

were polycrystalline in nature. The polycrystallinity of the metal structures could potentially be a drawback of lithographically defined metal structures, as chemically synthesized metal nanoparticles can be a single crystal when synthesized in certain conditions. Eventhough, Au nanorods successfully synthesized via top-down method yet this method is time consuming and costly makes them impractical for fabrication of Au nanorods in bigger scales. Furthermore, Au nanorods obtained from vacuum deposition techniques also can degrade their plasmonic properties due to the electron scattering at the grain boundaries. Due to these reason had limit their usage in device application and simultaneously make the top-down method to be unattractive in fundamental research.

4.1.4 Magnetic nanorods

Nanostructured iron oxide magnetite (Fe_3O_4) behaves supermagnetic and widely used in the biomedical field as well as device application. Generally, the magnetic nanoparticle could be utilized as nanoadsorbents, cancer diagnostic and treatment, contrast agent in magnetic resonance imaging (MRI), etc. Meanwhile for 1-D magnetite extremely important in building block for nanodevices. It has been found that size and shape of magnetite nanoparticles play key role in controlling the corresponding properties [47]. The magnetite nanoparticles could be synthesis via aqueous co-precipitation, magnetic field induction, CVD, template mediated, etc. [48–50]. The aqueous co-precipitation of Fe^{2+} and Fe^{3+} by a base, usually sodium hydroxide or aqueous ammonia, is the well-known method which is usually carried out for synthesizing the magnetite nanoparticle [51]. This method is the most scalable chemical synthesis routes which results in iron oxide nanospherical crystal. However, there is a study also found that innovative modification in co-precipitation technique through incorporation of special aqueous solution will lead to the formation of nanocubes or nanorods iron oxide particle's. This was in agreement with Khalil finding's [52].

Recently, considerable attention has been drawn to production of 1-D magnetite nanorods due to their high surface to volume ration and superior properties. Due to the high aspect ratio, magnetic nanorods have the high values of coercivity and produce a lot of heat in high frequency magnetic field, which offer longer blood circulation times, stronger interaction with tumors, enhanced retention at tumor sites and improved targeting efficiency [47, 53]. All of these reasons stimulate their making in excellent candidates as targeting pharmaceutical carrier or MRI contrast agents. For instance, iron oxide nanocubes including nanorods structure with a length larger than 100 nm could be achieved via thermal decomposition, wet chemical, hydrothermal, template mediated, solvothermal, hydrolysis and sol-gel.

Thermal decomposition method involved chemical decomposition at high temperature, lead to the breaking of the chemical bonds. The thermal decomposition method for synthesis iron oxide nanorods involve metal-organic compound. The obtained nanorods generally with diameter and length within range of 50–100 nm. This method typically led large nanorods structure due to the annealing by high reaction temperature. It is in agreement with Chen et al. finding reported that with the increasing reaction temperature, the aspect ratio of the products decreases to some extent, thus no any rod-like particles produced when high temperatures synthesis method is used [54]. Meanwhile, eventhough the co-precipitation method is a conventional method for synthesizing iron oxide nanorods, yet this method often uses trioctylphosphine (TOP), tributylphosphine (TBP), trioctylphosphine oxide (TOPO) or oleylamine (OA) and other long chain amines as solvents and capping agents in order to prevent the uncontrolled precipitation. Since this nanoparticle used for biomedical application, hence the nanoparticles of iron oxides

should be a nontoxic. The usage of nontoxic capping agent and stabilizer eliminates the use of toxic and expensive chemical such as TOP, TBP or amines.

In the past years, the wet chemical synthesis of iron oxide nanorods via one step wet chemical method have been reported by several groups [54, 55]. Chen's group reported in the one-step synthesis method and a surfactant, polyethylene glycol (PEG) was used as template and ferrous ammonia sulfate was use as precursor [54]. This study agreed that a formation of iron oxide nanorods can be achieved at longer retention synthesis time and adjusting the diffusion of ammonia by implementation a suitable ratio between the rates of deposition and oxidation of ferrous ions. These were in agreement with TEM image the iron oxide synthesize at from 2 to 10 h and it is reveals that the iron oxide nanorods could be obtained upon extended reaction time. By adjusting pressure of ammonia, i.e., adjusting the concentration of aqueous ammonia in the right flask also results in formation of pure magnetite phase. Further study on synthesizing iron oxide nanorods via wet chemical method were also reported by Ahmed and co-worker [56]. The obtained nanoparticles were rod shaped and consisted mainly of maghemite (Υ-Fe_2O_3) phase. The nanoparticles also appear superparamagnetic behavior under room temperature.

Solvothermal method is an effective method for producing iron oxide nanorods. Si et al. present a method for obtaining the iron oxide nanorods via solvothermal method, and product showed formation of iron oxide nanorods with diameter size within range of 58–250 nm and width from 8 to 64 nm (**Figure 9(a** and **b)**) [57]. The iron oxide nanorods obtained exhibit uniform size and greater dispersion in
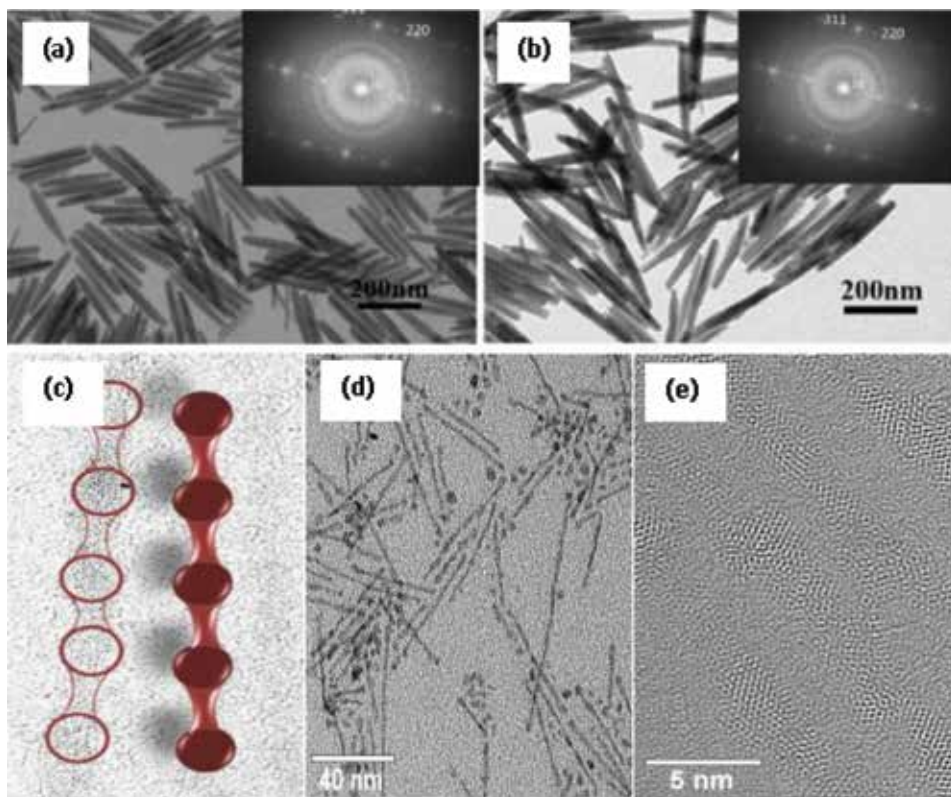

Figure 9.
TEM image of iron oxide nanorods in (a) cyclohexane and (b) water prepared via solvothermal method [57], (c) iron oxide nanorods mechanism via template mediated approach, (d) TEM image of the iron oxide nanorods, and (e) high resolution TEM image of iron oxide nanorods synthesized via template mediated approach [59].

nonpolar solvent (cyclohexane). It also revealed the single crystalline nature of nanorods is successfully produced upon synthesis process. The effectiveness of solvothermal method in producing iron oxide nanorods was in agreement Sun and co-worker finding, which reported that Fe_3O_4 single crystal nanorods with a uniform length between 64 and 140 nm can be prepared using $Fe(CO)_5$ in the presence of oleic acid through a solvothermal process [58].

Recent by Kloust et al. also discovered that the iron oxide nanorods can be produced directly from template mediated approach [59]. The iron oxide nanorods synthesis directly from iron oleate in one-step procedure. The iron oleate is used as a precursor. In this method, the iron oxide nanodot string together in a row to form rods-structure (**Figure 9(c)**). Based on the TEM image the formed iron nanorods exhibit a mean length of approximately 24 nm and mean diameter 2.5 nm with an associated aspect ratio of 10 (**Figure 9(d)**). The iron oxide nanorods produced particularly small and thin nanorods. The nanodot string combination mechanism have been confirmed in TEM micrograph, which shows the alignment of single dot characteristic. The high resolution TEM image of iron oxide nanorods (**Figure 9(e)**) confirms this characteristic and show twisted crystal-orientations of single nano-crystal. Further magnetic characterization reveals that the iron oxide nanorods synthesized via template mediated approach posed super-paramagnetic behavior. In the blocked state the nanorods exhibit a magnetic easy axis parallel to the long axis of nanorods due to the enhancement shape anisotropy. Kloust et al. [59] also presented a method for preparation of iron oxide nanorods with a template approach, where iron oxide nanodots string together. The procedure uses iron oleate as a precursor and is a one-step synthesis. A precise tuning of the width of the nanorods between 1 and 6 nm was realized.

Hydrothermal method might flexible method for synthesizing iron oxide nanorods. Thus, several procedures have been developed [48–50]. Hydrothermal methods rely on the ability of water at elevated pressures and temperatures to hydrolyze and dehydrate metal salts, and the very low solubility of the resulting iron oxide in water at these conditions to generate supersaturation [60]. Extremely high supersaturation could be achieved in the reaction process attributed by the lower solubility of metal hydroxides and oxides, thus very fine crystals will form. Similar case with thermal decomposition methods, the hydrothermal system also involves high temperature synthesis condition. Thus, the size of the nanoparticles had a larger particle (if the hydrothermal method proceed under supercritical temperature (<350°C)). This was due to the promotion of crystal growth that results from the dissolution and precipitation process in sub-critical water. The particle size also increased with the increase in reaction pressure in supercritical water [61]. Liang and co-workers report the variation of crystallite and particles size of iron oxide at temperature 250 and 350°C; the crystallite size of iron oxide increased significantly as the temperature was raised from 250 to 350°C. This phenomenon is due to the nucleation process which occurred as the monomer concentration reached the saturation point [62]. Interestingly, the size of particles will reduce and become smaller if the hydrothermal method proceeded under temperature > 380°C (above critical temperature). This is probably due to a rather low solvent power of supercritical water and an extremely high hydrolysis rate of iron salt in supercritical water. Therefore, very high super-saturation is achieved in which results in fine iron oxide crystals nucleating in situ immediately. It is in agreement with Arai et al. study [61]. Eventhough hydrothermal method considered effective in synthesizing iron oxide nanoparticles, yet the particles shape difficult to control in order to form pure rod-like structure.

Other method that effective in synthesizing the iron oxide nanorods is sol-gel method. Piao et al. reported on wrap-bake-peel process for nanostructural

transformation from β-FeOOH nanorods to biocompatible iron oxide nanocapsules [63]. This process involves silica coating, heat treatment and lastly the removal of silica layer, in order to transform the phases and structures of nanostructured materials while preserving their nanostructural characteristic. Water dispersible hollow iron oxide nanocapsules were obtained by applying the wrap-bake-peel process to β-FeOOH nanoparticles. The synthesized magnetite nanocapsules could be successfully used not only as a drug-delivery vehicle, but also as a T2 MRI contrast agent.

5. Optimization of nanorods material production

Although the process of synthesis of metallic nanoparticles provides a number of benefits, it is still difficult to achieve formation of nanoparticles of various shapes and sizes, which is significant as shape and size dictate possible nanoparticle activity. Therefore, regulation of nanoparticle shape and size has received a great deal of attention. When marine microbes were employed to synthesize metallic nanoparticles, consideration was given to a range of factors related to metallic nanoparticle nucleation and formation. More specifically, to achieve metallic nanoparticles of uniform size and shape, the factors of pH, reaction temperature, time and reactant concentrations were taken into account.

5.1 pH

The development of metallic nanoparticles depends significantly on the pH of the reaction medium [64]. Gold nanoparticles mediated by Rhodopseudomonas capsulate occurred at pH ranging between 4 and 7, while extracellular formation of gold nanoparticles of round shape and 10–20 nm in size occurred at pH 7 and a number of nanoplates occurred at a pH value of 4. Comparable results were obtained when Shewanella algae were used to synthesize gold nanoparticles intracellularly under conditions without oxygen and with H_2 gas serving as electron donor at a temperature of 25°C [65]. Thus, gold nanoparticles of 10–20 and 15–200 nm in size respectively occurred in periplasmic space with pH 7 and on bacterial surface with pH 2.8. Hence, it can be concluded that pH has great significance for morphological modulation and detection of nanoparticle development site.

5.2 Temperature

The dependence of microorganism-based synthesis of metallic nanoparticles as well as nanoparticle morphology and yield on the temperature of reaction is well established. In a recently conducted study, silver nanoparticles were synthesized extracellularly by *Phoma glomerate* supernatant under conditions of bright sunlight [66]. The maximum yield of silver nanoparticles was achieved at 25°C, while the temperatures of 90, 65, 37 and 4°C were associated with gradually diminishing yield. Furthermore, alkaline pH enabled synthesis optimization. A different study introduced silver nitrate solution in cell-free filtrate of fungus *Trichoderma viride* and silver nanoparticles were synthesized under conditions without light and at different temperatures for a period of 1 day. Thus, round-shaped silver nanoparticles of 2–4 nm in size formed at 40°C, round- and rod-shaped nanoparticles of 10–40 nm in size were observed at 27°C, and nanoplates of 80–100 nm in size formed at 10°C [67].

5.3 Time

Metallic nanoparticle size and shape also depend on the synthesis reaction time. One study employed *Vibrio alginolyticus* supernatant to synthesize silver nanoparticles extracellularly and observed that the greater the reaction time the higher the yield was, while the UV-vis peak was maintained more or less unchanged; on the other hand, the UV-vis peak shifted toward higher wavelength in the context of intracellular synthesis [68]. The conclusion derived was that extracellular synthesis of silver nanoparticles had time-dependent yield but size was unaffected. However, intracellular synthesis was associated with size enlargement as the reaction time was increased. Comparable results were obtained by a different study that undertook extracellular synthesis of silver and gold nanoparticles by employing single-cell protein (Spirulina platensis) [69]. Nanoparticles expanded in size as the reaction time was increased, whilst also showing greater aggregation and greater instability [70]. Another study synthesized various metallic nanoparticles with a range of microorganism species and observed that yield increased in direct proportion with reaction time increase [71].

5.4 Concentration of reactants

The development of metallic nanoparticles is subject to the influence of reactant concentration as well. One study reported that the size and shape of gold nanoparticles were considerably impacted by the use of different gold salt concentration alongside *Penicillium brevicompactum* supernatant in reaction medium [72]. Gold salt concentrations of 1 and 2 mM respectively resulted in round gold nanoparticles of 10–50 and 10–70 nm nanoparticles. Furthermore, hexagonal and triangular particles developed when round nanoparticles were added. Nanoparticles of 50–120 nm with particles of different shapes (round, triangular, diamond-like) developed at gold salt concentration of 3 mM. A different study also found that lower and higher metal salt concentrations respectively led to the development of round nanoparticles and triangular and hexagonal nanoplates [73]. Moreover, there is evidentiary support that increase in yeast extract concentration leads to the development of nanoparticles of reduced size [74], while increase in fungal filtrate concentration intensifies development of nanoparticles [66]. In addition, a study highlighted that manipulation of parameters of environment and nutrition enabled synthesizing nanoparticles with control of size and shape [71]. Thus, the above evidence confirms that regulation of metallic nanoparticle size and shape is significantly dependent on reactant concentration.

6. Conclusion

In summary, uniform 1-D magnetite nanorods showed fascinating physical properties this due to the distinct structure-dependent properties of nanorods structures. Larger in both length and diameter of rod-shape particles are expected to share many advantages in the oriental properties of nanorods. Last but not least, nanorods offer more advantages over isotropic (homogeneous and uniform) particles. It can be summarized that the efficiency of nanorods depends strongly on nanorods aspect ratio, volume fraction, polydispersity and orientation. There are many methods for synthesizing carbon nanorods, ZnO nanorods, Au nanorods and iron oxide nanorods. Overall, bottom-up was very effective method for synthesizing nanorods particles. Yet, bottom-up method still suffer with some drawbacks; placing metal into large area, ordered array and purity problem. Due to these

reasons, top-down approaches gained interest, but top-down method is time consuming and costly for industrial practical.

Acknowledgements

Author details

Alsultan Abdulkareem Ghassan*, Nurul-Asikin Mijan and Yun Hin Taufiq-Yap
Faculty of Science, Catalysis Science and Technology Research Centre (PutraCat), Universiti Putra Malaysia, UPM Serdang, Selangor, Malaysia

*Address all correspondence to: kreem.alsultan@yahoo.com

IntechOpen

References

[1] McDonnell T, Korsmeyer S. Helical microtubules of graphitic carbon. Nature. 1991;**354**:56-58

[2] Marangoni VS, Cancino-Bernardi J, Zucolotto V. Synthesis, physico-chemical properties, and biomedical applications of gold nanorods—A review. Journal of Biomedical Nanotechnology. 2016;**12**:1136-1158. DOI: 10.1166/jbn.2016.2218

[3] Kislyuk VV, Dimitriev OP. Nanorods and nanotubes for solar cells. Journal of Nanoscience and Nanotechnology. 2008;**8**:131-148. DOI: 10.1166/jnn.2008.N16

[4] Terrones M, Hsu WK, Kroto HW, Walton DRM. Nanotubes: A revolution in materials science and electronics. Topics in Current Chemistry. 1999;**199**:189-234. DOI: 10.1007/3-540-68117-5_6

[5] Li Y, Yang XY, Feng Y, Yuan ZY, Su BL. One-dimensional metal oxide nanotubes, nanowires, nanoribbons, and nanorods: Synthesis, characterizations, properties and applications. Critical Reviews in Solid State and Materials Sciences. 2012;**37**:1-74. DOI: 10.1080/10408436.2011.606512

[6] Patzke GR, Krumeich F, Nesper R. Oxidic nanotubes and nanorods—Anisotropic modules for a future nanotechnology. Angewandte Chemie International Edition. 2002;**41**:2446-2461. DOI: 10.1002/1521-3773 (20020715)41:14<2446::AID-ANIE2446>3.0.CO;2-K

[7] Ruska M, Kiviluoma J. Renewable electricity in Europe: Current state, drivers, and scenarios for. VTT Tied—Valt Tek Tutkimusk. 2011;**2020**:1-72. DOI: 10.1039/c1ee01598b

[8] Chong MN, Jin B, Chow CWK, Saint C. Recent developments in photocatalytic water treatment technology: A review. Water Research. 2010;**44**:2997-3027. DOI: 10.1016/j.watres.2010.02.039

[9] Esawi AMK, Farag MM. Carbon nanotube reinforced composites: Potential and current challenges. Materials and Design. 2007;**28**:2394-2401. DOI: 10.1016/j.matdes.2006.09.022

[10] Bhat MA, Nayak BK, Nanda A, Lone IH. Nanotechnology, metal nanoparticles, and biomedical applications of nanotechnology. In Oncology: Breakthroughs in Research and Practice. IGI Global; 2017. pp. 311-341

[11] González-Rubio G, Díaz-Núñez P, Rivera A, Prada A, Tardajos G, González-Izquierdo J, et al. Femtosecond laser reshaping yields gold nanorods with ultranarrow surface plasmon resonances. Science (80-). 2017;**358**:640-644. DOI: 10.1126/science.aan8478

[12] Sajanlal PR, Sreeprasad TS, Samal AK, Pradeep T. Anisotropic nanomaterials: Structure, growth, assembly, and functions. Nano Reviews. 2011;**2**:5883. DOI: 10.3402/nano.v2i0.5883

[13] Genck W. Science and technology of the twenty-first century: Synthesis, properties, and applications of carbon nanotubes. Chemical Engineering Progress. 2008;**104**:22-24. DOI: 10.1146/annurev.matsci.33.012802.100255

[14] Mutiso RM, Sherrott MC, Rathmell AR, Wiley BJ, Winey KI. Integrating Simulations and Experiments to Predict Sheet Resistance and Optical Transmittance in Nanowire Films for Transparent Conductors. ACS nano; 2013;**7**(9):7654-7663

[15] Hore MJ, Composto RJ. Functional Polymer Nanocomposites Enhanced by

Nanorods. Macromolecules. 2013;**47**(3): 875-887

[16] Rao MV, Amareshwari VV, Mahender C, Himabindu V, Anjaneyulu Y. Flame synthesis of carbon nanorods with/without catalyst. International Journal of Innovation and Applied Studies. 2013;**3**:1-5

[17] Abdulkareem-Alsultan G, Asikin-Mijan N, Lee HV, Taufiq-Yap YH. A new route for the synthesis of La-Ca oxide supported on nano activated carbon via vacuum impregnation method for one pot esterification-transesterification reaction. Chemical Engineering Journal. 2016;**304**:61-71

[18] Abdulkareem-Alsultan G, Asikin-Mijan N, Lee HVV, Albazzaz AS, Taufiq-Yap YH. Deoxygenation of waste cooking to renewable diesel over walnut shell-derived nanorode activated carbon supported CaO-La$_2$O$_3$ catalyst. Energy Conversion and Management. 2017;**151**: 311-323. DOI: 10.1016/j.enconman.2017.09.001

[19] Herrera-Ramirez JM, Perez-Bustamante R, Aguilar-Elguezabal A. An overview of the synthesis, characterization, and applications of carbon nanotubes. Carbon-Based Nanofillers and Their Rubber Nanocomposites. 2019:47-75. DOI: 10.1016/B978-0-12-813248-7.00002-X

[20] Yuan Z, Dong L, Gao Q, Huang Z, Wang L, Wang G, et al. SnSb alloy nanoparticles embedded in N-doped porous carbon nanofibers as a high-capacity anode material for lithium-ion batteries. Journal of Alloys and Compounds. 2019;**777**:775-783. DOI: 10.1016/j.jallcom.2018.10.295

[21] Abdulkreem-Alsultan G, Islam A, Janaun J, Mastuli MSS, Taufiq-Yap Y-H, et al. Synthesis of structured carbon nanorods for efficient hydrogen storage. Materials Letters. 2016;**179**:57-60. DOI: 10.1016/j.matlet.2016.05.030

[22] Abdulkareem-Alsultan G, Asikin-Mijan N, Mansir N, Lee HV, Zainal Z, Islam A, et al. Pyro-lytic de-oxygenation of waste cooking oil for green diesel production over Ag$_2$O$_3$-La$_2$O$_3$/AC nano-catalyst. Journal of Analytical and Applied Pyrolysis. 2018;**137**:171-184. DOI: 10.1016/j.jaap.2018.11.023

[23] Alsultan A, Mijan A, Taufiq-Yap YH. Preparation of activated carbon from walnut shell doped La and Ca catalyst for biodiesel production from waste cooking oil. Materials Science Forum. Trans Tech Publications; 2016; **840**:348-352

[24] Pachfule P, Shinde D, Majumder M, Xu Q. Fabrication of carbon nanorods and graphene nanoribbons from a metal-organic framework. Nature Chemistry. 2016;**8**:718-724. DOI: 10.1038/nchem.2515

[25] Pérez-Juste J, Pastoriza-Santos I, Liz-Marzán LM, Mulvaney P. Gold nanorods: Synthesis, characterization and applications. Coordination Chemistry Reviews. 2005;**249**: 1870-1901. DOI: 10.1016/j.ccr.2005.01.030

[26] Yu D, Yazaydin AO, Lane JR, Dietzel PDC, Snurr RQ. A combined experimental and quantum chemical study of CO$_2$ adsorption in the metal-organic framework CPO-27 with different metals. Chemical Science. 2013;**4**:3544-3556. DOI: 10.1039/c3sc51319j

[27] Wahab HA, Salama AA, El-Saeid AA, Nur O, Willander M, Battisha IK. Optical, structural and morphological studies of (ZnO) nano-rod thin films for biosensor applications using sol gel technique. Results in Physics. 2013;**3**: 46-51. DOI: 10.1016/j.rinp.2013.01.005

[28] Dharmanto SH, Sebayang D. The simple fabrication of nanorods mass production for the dye-sensitized solar

cell. In: MATEC Web Conf. 2017. p. 101. DOI: 10.1051/matecconf/201710103006

[29] Li Q, Kumar V, Li Y, Zhang H, Marks TJ, Chang RPH. Fabrication of ZnO nanorods and nanotubes in aqueous solutions. Chemistry of Materials. 2005;**17**:1001-1006. DOI: 10.1021/cm048144q

[30] Kim KS, Kim HW. Synthesis of ZnO nanorod on bare Si substrate using metal organic chemical vapor deposition. Physica B: Condensed Matter. 2003;**328**: 368-371. DOI: 10.1016/S0921-4526(02) 01954-3

[31] Norton DP, Heo YW, Ivill MP, Ip K, Pearton SJ, Chisholm MF, Steiner T. ZnO: Growth, doping and processing. Materials today; 2004;**7**(6):34-40

[32] Asghar M, Mahmood K, Raja MY, Hasan MA. Synthesis and characterization of ZnO nanorods using molecular beam epitaxy. Advances in Materials Research. 2012;**622–623**: 919-924. DOI: 10.4028/www.scientific. net/AMR.622-623.919

[33] Heo YW, Varadarajan V, Kaufman M, Kim K, Norton DP, Ren F, et al. Site-specific growth of Zno nanorods using catalysis-driven molecular-beam epitaxy. Applied Physics Letters. 2002;**81**:3046-3048. DOI: 10.1063/ 1.1512829

[34] Song J, Baek S, Lim S. Effect of hydrothermal reaction conditions on the optical properties of ZnO nanorods. Physica B: Condensed Matter. 2008;**403**: 1960-1963. DOI: 10.1016/j.physb.2007. 10.337

[35] Polsongkram D, Chamninok P, Pukird S, Chow L, Lupan O, Chai G, et al. Effect of synthesis conditions on the growth of ZnO nanorods via hydrothermal method. Physica B: Condensed Matter. 2008;**403**:3713-3717. DOI: 10.1016/j.physb.2008.06.020

[36] Julkapli NM, Bagheri S. Graphene supported heterogeneous catalysts: An overview. International Journal of Hydrogen Energy. 2014;**40**:948-979. DOI: 10.1016/j.ijhydene.2014.10.129

[37] Yu F, Wang R. Deep oxidative desulfurization of dibenzothiophene in simulated oil and real diesel using heteropolyanion-substituted hydrotalcite-like compounds as catalysts. Molecules. 2013;**18**: 13691-13704. DOI: 10.3390/ molecules181113691

[38] Phromyothin D, Phatban P, Jessadaluk S, Khemasiri N, Kowong R, Vuttivong S, et al. Growth of ZnO nanorods via low temperature hydrothermal method and their application for hydrogen production. Materials Today: Proceedings. 2017;**4**: 6326-6330. DOI: 10.1016/j. matpr.2017.06.134

[39] Romero M, Henríquez R, Dalchiele EA. Electrochemical deposition of ZnO nanorod arrays onto a ZnO seed layer: Nucleation and growth mechanism. International Journal of Electrochemical Science. 2016;**11**:8588-8598. DOI: 10.20964/2016.10.61

[40] Chang M, Cao X, Zeng H. Electrodeposition growth of vertical ZnO nanorod/polyaniline heterostructured films and their optical properties. Journal of Physical Chemistry C. 2009;**113**:15544-15547. DOI: 10.1021/jp903881d

[41] Vigderman L, Khanal BP, Zubarev ER. Functional gold nanorods: Synthesis, self-assembly, and sensing applications. Advanced Materials. 2012; **24**:4811-4841. DOI: 10.1002/ adma.201201690

[42] Chen H, Shao L, Li Q, Wang J. Gold nanorods and their plasmonic properties. Chemical Society Reviews. 2013;**42**:2679-2724. DOI: 10.1039/ c2cs35367a

[43] Tian Y, Liu H, Zhao G, Tatsuma T. Shape-controlled electrodeposition of gold nanostructures. The Journal of Physical Chemistry. B. 2006;**110**: 23478-23481. DOI: 10.1021/jp065292q

[44] Grzelczak M, Pérez-Juste J, Mulvaney P, Liz-Marzán LM. Shape control in gold nanoparticle synthesis. Chemical Society Reviews. 2008;**37**:1783-1791. DOI: 10.1039/ b711490g

[45] Ye X, Jin L, Caglayan H, Chen J, Xing G, Zheng C, et al. Improved Size-Tunable Synthesis of Monodisperse Gold Nanorods through the Use of Aromatic Additives. ACS nano; 2012;**6** (3):2804-2817

[46] Koh AL, McComb DW, Maier SA, Low HY, Yang JKW. Sub-10 nm patterning of gold nanostructures on silicon-nitride membranes for plasmon mapping with electron energy-loss spectroscopy. Journal of Vacuum Science & Technology B: Microelectronics and Nanometer Structures Processing, Measurement, and Phenomena. 2010;**28**: C6O45-C6O49. DOI: 10.1116/1.3501351

[47] Geng Y, Dalhaimer P, Cai S, Tsai R, Tewari M, Minko T, et al. Shape effects of filaments versus spherical particles in flow and drug delivery. Nature Nanotechnology. 2007;**2**:249-255. DOI: 10.1038/nnano.2007.70

[48] Ramzannezhad A, Gill P, Bahari A. Fabrication of magnetic nanorods and their applications in medicine. BioNanoMaterials. 2017;**18**:1-31. DOI: 10.1515/bnm-2017-0008

[49] Lu AH, Salabas EL, Schüth F. Magnetic nanoparticles: Synthesis, protection, functionalization, and application. Angewandte Chemie International Edition. 2007;**46**: 1222-1244. DOI: 10.1002/anie. 200602866

[50] Laurent S, Forge D, Port M, Roch A, Robic C, Vander Elst L, et al. Magnetic iron oxide nanoparticles: Synthesis, stabilization, vectorization, physicochemical characterizations, and biological applications. Chemical Reviews. 2008;**108**:2064-2110. DOI: 10.1021/cr068445e

[51] Han C, Ma J, Wu H, Wei Y, Hu K. A low-cost and high-yield production of magnetite nanorods with high saturation magnetization. Journal of the Chilean Chemical Society. 2015;**60**: 2799-2802. DOI: 10.4067/ S0717-97072015000100005

[52] Khalil MI. Co-precipitation in aqueous solution synthesis of magnetite nanoparticles using iron(III) salts as precursors. Arabian Journal of Chemistry. 2015;**8**:279-284. DOI: 10.1016/j.arabjc.2015.02.008

[53] Nikitin A, Khramtsov M, Garanina A, Mogilnikov P, Sviridenkova N, Shchetinin I, et al. Synthesis of iron oxide nanorods for enhanced magnetic hyperthermia. Journal of Magnetism and Magnetic Materials. 2019;**469**: 443-449. DOI: 10.1016/j.jmmm.2018. 09.014

[54] Chen S, Feng J, Guo X, Hong J, Ding W. One-step wet chemistry for preparation of magnetite nanorods. Materials Letters. 2005;**59**:985-988. DOI: 10.1016/j.matlet.2004.11.043

[55] Satuła D, Kalska-Szostko B, Szymański K, Dobrzyński L, Kozubowski J. Microstructure and magnetic properties of iron oxide nanoparticles prepared by wet chemical method. Acta Physica Polonica A. 2008;**114**:1615-1621. DOI: 10.12693/ APhysPolA.114.1615

[56] Ahmad M, Ahmad N, Aslam M. Synthesis of iron oxide nanorods. Advanced Science Focus. 2013;**1**: 150-155. DOI: 10.1166/asfo.2013.1014

[57] Si JC, Xing Y, Peng ML, Zhang C, Buske N, Chen C, et al. Solvothermal synthesis of tunable iron oxide nanorods and their transfer from organic phase to water phase. CrystEngComm. 2014;**16**: 512-516. DOI: 10.1039/c3ce41544a

[58] Sun H, Chen B, Jiao X, Jiang Z, Qin Z, Chen D. Solvothermal synthesis of tunable electroactive magnetite nanorods by controlling the side reaction. Journal of Physical Chemistry C. 2012;**116**:5476-5481. DOI: 10.1021/jp211986a

[59] Kloust H, Zierold R, Merkl J-P, Schmidtke C, Feld A, Pöselt E, et al. Synthesis of iron oxide nanorods using a template mediated approach. Chemistry of Materials. 2015;**27**:4914-4917. DOI: 10.1021/acs.chemmater.5b00513

[60] Teja AS, Koh PY. Synthesis, properties, and applications of magnetic iron oxide nanoparticles. Progress in Crystal Growth and Characterization of Materials. 2009;**55**:22-45. DOI: 10.1016/j.pcrysgrow.2008.08.003

[61] Hakuta Y, Ura H, Hayashi H, Arai K. Effects of hydrothermal synthetic conditions on the particle size of γ-AlO (OH) in sub and supercritical water using a flow reaction system. Materials Chemistry and Physics. 2005;**93**: 466-472. DOI: 10.1016/j.matchemphys.2005.03.047

[62] Liang MT, Wang SH, Chang YL, Hsiang HI, Huang HJ, Tsai MH, et al. Iron oxide synthesis using a continuous hydrothermal and solvothermal system. Ceramics International. 2010;**36**: 1131-1135. DOI: 10.1016/j.ceramint.2009.09.044

[63] Piao Y, Kim J, Bin Na H, Kim D, Baek JS, Ko MK, et al. Wrap-bake-peel process for nanostructural transformation from B-FeOOH nanorods to biocompatible iron oxide nanocapsules. Nature Materials. 2008;**7**: 242-247. DOI: 10.1038/nmat2118

[64] He S, Guo Z, Zhang Y, Zhang S, Wang J, Gu N. Biosynthesis of gold nanoparticles using the bacteria Rhodopseudomonas capsulata. Materials Letters. 2007;**61**:3984-3987. DOI: 10.1016/j.matlet.2007.01.018

[65] Konishi Y, Tsukiyama T, Tachimi T, Saitoh N, Nomura T, Nagamine S. Microbial deposition of gold nanoparticles by the metal-reducing bacterium Shewanella algae. Electrochimica Acta. 2007;**53**:186-192. DOI: 10.1016/j.electacta.2007.02.073

[66] Gade A, Gaikwad S, Duran N, Rai M. Green synthesis of silver nanoparticles by Phoma glomerata. Micron. 2014;**59**:52-59. DOI: 10.1016/j.micron.2013.12.005

[67] Mohammed Fayaz A, Balaji K, Kalaichelvan PT, Venkatesan R. Fungal based synthesis of silver nanoparticles-An effect of temperature on the size of particles. Colloids Surfaces B Biointerfaces. 2009;**74**: 123-126. DOI: 10.1016/j.colsurfb.2009.07.002

[68] Rajeshkumar S, Malarkodi C, Paulkumar K, Vanaja M, Gnanajobitha G, Annadurai G. Intracellular and extracellular biosynthesis of silver nanoparticles by using marine bacteria vibrio Alginolyticus. International Journal of Nanoscience and Nanotechnology. 2013;**3**:21-25

[69] Wong CC, Casado IT, Álvarez YC, Legón ZM. Caracterización clínico-epidemiológica de la miopía en la población infantil de un municipio de Venezuela. Revista Cubana de Pediatría. 2011;**83**:149-157. DOI: 10.1007/s10853-008-2745-4

[70] Strategies OM, Author B, Hedenstr A, Society A, Url MS, Linked UTCR. Microalga *Scenedesmus* sp.: A potential low-cost green machine for silver

nanoparticle synthesis. 2015;**90**: 1298-1309

[71] Husseiny SM, Salah TA, Anter HA. Biosynthesis of size controlled silver nanoparticles by Fusarium oxysporum, their antibacterial and antitumor activities. Beni-Suef Univ J Basic Appl Sci. 2015;**4**:225-231. DOI: 10.1016/j. bjbas.2015.07.004

[72] Mishra A, Tripathy SK, Wahab R, Jeong SH, Hwang I, Yang YB, et al. Microbial synthesis of gold nanoparticles using the fungus Penicillium brevicompactum and their cytotoxic effects against mouse mayo blast cancer C2C12cells. Applied Microbiology and Biotechnology. 2011;**92**:617-630. DOI: 10.1007/s00253-011-3556-0

[73] Pimprikar PS, Joshi SS, Kumar AR, Zinjarde SS, Kulkarni SK. Influence of biomass and gold salt concentration on nanoparticle synthesis by the tropical marine yeast Yarrowia lipolytica NCIM 3589. Colloids Surfaces B Biointerfaces. 2009;**74**:309-316. DOI: 10.1016/j. colsurfb.2009.07.040

[74] Chauhan A, Zubair S, Tufail S, Sherwani A, Sajid M, Raman SC, et al. Fungus-mediated biological synthesis of gold nanoparticles: Potential in detection of liver cancer. International Journal of Nanomedicine. 2011;**6**: 2305-2319. DOI: 10.2147/IJN.S23195

Chapter 3

ZnO Nanorods for Gas Sensors

Yanmin Wang

Abstract

ZnO nanorods have been widely used to detect low-concentration gases due to its range of conductance variability, response toward both oxidative and reductive gases, and highly sensitive and selective properties. In this chapter, the fabrication methods of ZnO nanorods, their controllable growth, their different configurations, their modification for improving sensing property, and their composites for gas sensors are thoroughly introduced. The synthesis methods to fabricate ZnO nanorods consist of hydrothermal method, microemulsion synthesis, microwave-assisted hydrolysis preparation, gas-solution-solid method, spray pyrolysis, sono-chemical route, simple solution route, and so on. The controllable fabrication of ZnO nanorods can be realized by control growth, selective growth, and diameter regulation. Different structures formed by ZnO nanorods include cross-linked configuration, flowerlike structure, and multishelled hollow spheres and hollow microsemispheres, as influence their sensing properties. ZnO nanorods can be modified by doping, functionalization, decoration, and sensitization for enhancing the sensing property. ZnO can be combined with graphene, carbon nanotubes, SnO_2, In_2O_3, and Fe_2O_3 to form core-shell composites for gas sensor.

Keywords: ZnO nanorods, fabrication, modification, composites, gas sensor

1. Introduction

With the development of economy and society, the increasingly serious environmental problems have become the world topics of concern to people. Gas sensors have been widely used in medicine industry and ecology to protect people from harmful gases [1]. Generally, gas-sensing mechanism is founded on the electron transport between adsorbed oxygen species and test gas molecules [2]. The response of sensor is not only determined by the amount of adsorbed oxygen species but also by the specific surface area, structure, active sites, and electron properties of sensing materials.

Metal oxide semiconductor sensors have attracted great attention for a long time because they have advantages such as low cost, online operation, low power consumption, high sensitivity under ambient conditions, and high compatibility with microelectronic processing [3]. Metal oxide gas sensors function through controlling the electrical conductivity upon exposure to gases. A number of metal oxides, such as TiO_2, ZnO, SnO_2, Fe_2O_3, WO_3, etc., have been employed for gas sensors [4].

Among them, ZnO has been widely used to detect low-concentration gases, such as ethanol, benzene, nitrogen oxide, liquid petroleum gas, and other species due to a wide band gap, low-cost environmentally benign components, nontoxicity [5], good thermal and chemical stability, high-electron mobility, large exciton binding energy, and its range of conductance variability and response toward

both oxidative and reductive gases [6, 7]. Since ZnO thin film was used to detect gaseous components at about 400°C for the first time in 1966 [8], ZnO has been widely investigated due to its good and stable gas-sensing properties. Various ZnO morphologies provide different sensing performances [9]. For instance, ZnO nanopetals have a sensitivity of 119–20 ppm NO_2 gas at room temperature [10]. Monodisperse ZnO hollow six-sided pyramids have a sensitivity of about 15 to dimethylformamide (DMF) and 187 to ethanol [11]. The flowerlike ZnO nanostructures showed the highest response of 144.38 and excellent selectivity to ethanol 500 ppm at 360°C [12].

Gas sensors based on one-dimensional ZnO nanostructures have recently attracted much attention due to its high sensitivity and low power consumption [13, 14]. Especially ZnO nanorods have been widely used for detecting low-concentration gases due to its range of conductance variability, response toward both oxidative and reductive gases, and highly sensitive and selective properties. In this chapter, the fabrication methods of ZnO nanorods, their controllable growth, their different configurations, their modification for improving sensing property, and their composites for gas sensors are thoroughly introduced.

2. Fabrication methods of ZnO nanorods

2.1 Hydrothermal method

A two-step low-temperature hydrothermal method was adopted to synthesize ZnO nanorods (NR) selectively grown on-chip as shown in **Figure 1**. The electrodes of Pt on Cr were fabricated by sputter deposition and lift-off technique on a glass substrate (**Figure 1(A)**). On a glass substrate, small zinc islands were sputter deposited as nucleation sites for the ZnO nanorod growth (**Figure 1(B)**). In the next two steps, an equimolar solution of Zn $(NO_3)_2 \cdot 6H_2O$ and $(CH_2)_6N_4$ was used. The solution was used for growth nucleation of short ZnO nanorods in the first step (**Figure 1(C)**), whereas it was used for the nanorods elongation in the second step (**Figure 1(D)**). Nanorod junctions were formed by the connection of long porous nanorods from neighboring islands.
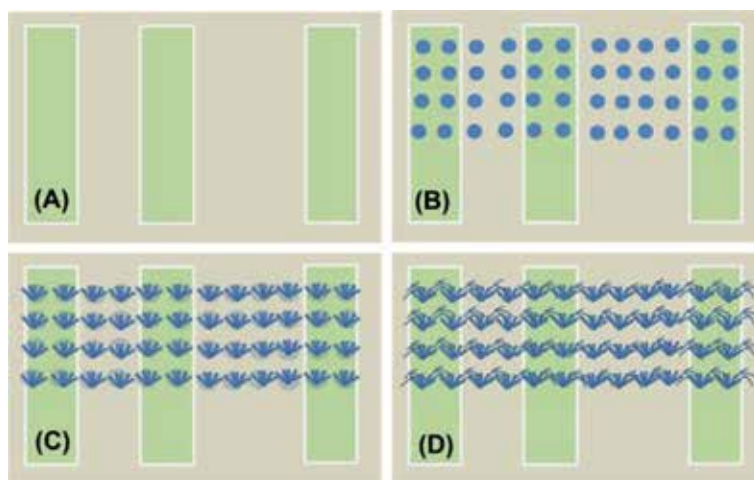
Figure 1.
Formation of ZnO NRs junctions by two-step hydrothermal growth: (A) deposition of Pt electrodes, (B) deposition of Zn seed islands, (C) growth of dense ZnO nanorods (first step), and (D) growth of long porous ZnO nanorods (second step).

Figure 2(A) shows the SEM images of the sensing part of the ZnO NR sensor. As shown in **Figure 2(A)** and **(B)**, the isolated islands were designed as nucleation sites for creating NR junctions within the conducting path from one electrode to the other of the sensor. ZnO NRs in **Figure 2(C)** is a porous material formed from nanocrystals, and its surface is very rough. The measurement of the nanorod gas sensor toward NO_2, ethanol, hydrogen, and ammonia indicated that the sensitivity to NO_2 was the highest [15].

2.2 Microemulsion synthesis

Zinc oxide nanorods were prepared by surfactant-assisted microemulsion method. The microemulsion for the synthesis of ZnO nanorod consists of surfactant such as ethyl benzene acid sodium salt (EBS), dodecyl benzene sulfonic acid sodium salt (DBS), and zinc acetate dihydrate ($ZnAc_2 \cdot 2H_2O$) in xylene. Then the mixture solution of hydrazine monohydrate and ethanol was added drop-wisely to the microemulsion at room temperature by simultaneous agitation. After refluxing the resulting precursor-containing mixture and centrifuging the milky white suspension, the precipitate was rinsed and dried [16].

The aspect ratio of ZnO nanorods was affected by the alkyl chain length of surfactant. ZnO nanorods synthesized by EBS with short alkyl chain length show higher aspect ratio than those by DBS. The response of ZnO nanorods to CO in air was strongly affected by the surface area, defects, and oxygen vacancies. Therefore, ZnO nanorods synthesized by the microemulsion synthesis have large aspect ratio and enhanced gas-sensing properties.

2.3 Microwave-assisted hydrolysis preparation

Highly oriented (002) plane-bounded ZnO nanorods ended with a surface defect hexagonal plane were prepared through microwave-assisted hydrolysis and used as a CO gas detector [17]. In the growth process, growth solution was prepared by dissolving zinc nitratehexahydrate ($ZnNO_3 \cdot 6H_2O$) and hexamethylenetetramine
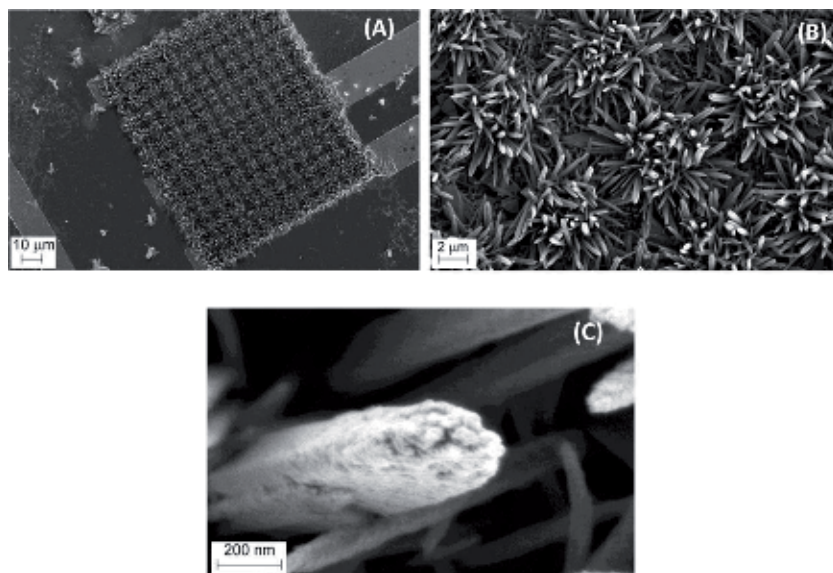
Figure 2.
(A) SEM image of ZnONRs synthesized with hydrothermal method at 85°C within Pt electrodes. (B) Higher magnification of ZnO NRs grown from different islands making NR junctions. (C) Image of a single ZnO NR.

(HMT) in deionized water. Subsequently, a seeded-FTO substrate immersed in the growth solution was processed in the microwave oven. The sensor with these ZnO nanorods presented a remarkable response at 81.1% toward 100 ppm CO gas exposure and recovery time of approximately 2.5 min. The microwave-assisted hydrolysis is an excellent approach to fabricate ZnO nanorods used for low-concentration CO gas detection system at room temperature.

2.4 Gas-solution-solid method

ZnO nanorod arrays on Zn substrate were prepared by the so-called gas-solution-solid method [18]. The aligned ZnO nanorods on substrates were obtained by putting Zn foils above an ammonia solution. The growth mechanism is studied and proposed as shown in **Figure 3**. The Zn foil is first put above the ammonia solution (**Figure 3**-1). The evaporation and condensation of ammonia solution formed a thin layer on the surface of Zn foil (**Figure 3**-2). At the beginning of ZnO nanorod growth, Zn on the surface of substrate is oxidized by O_2 to produce ZnO, as then reacts with $NH_4 \cdot OH$ to form $Zn(OH)_2$ in the thin layer of ammonium solution. The putative reactions relevant to the synthesis of the aligned upright ZnO nanorods are as follows:

$$2Zn + O_2 \longrightarrow 2ZnO \tag{1}$$

$$Zn O + NH_4 \cdot OH \longrightarrow Zn(OH)_2 + NH_3 \tag{2}$$
$$\longrightarrow Zn^{2+} + 2OH^- + NH_3$$

$$Zn^{2+} + 4NH_3 \longrightarrow [Zn(NH_3)_4]^{2+} \tag{3}$$

$$[Zn(NH_3)_4]^{2+} + 4OH^- \longrightarrow [ZnO_2]^{2-} + 4NH_3 + 2H_2O \tag{4}$$

$$[ZnO_2]^{2-} + H_2O \longrightarrow ZnO + 2OH^- \tag{5}$$
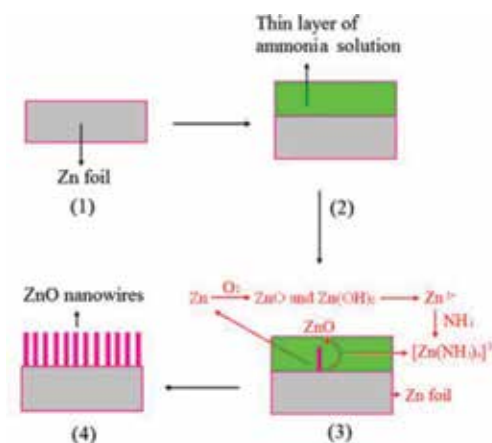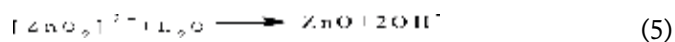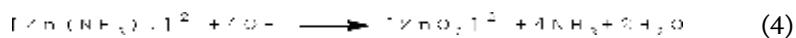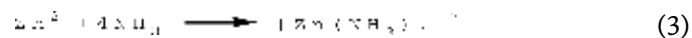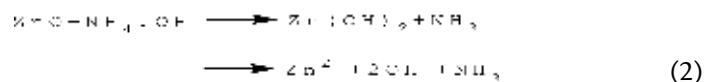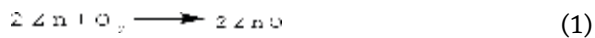
Figure 3.
Schematic diagram showing the ZnO nanorod arrays growth.

According to the Bravais-Donnay-Harker law, once nucleate, crystal planes with smaller dhkl values grow faster, and the ZnO growth along [0001] is much faster than that along other directions. Ammonia in the solution acts as a transporter of Zn^{2+} ions (**Figure 3**-3). Finally, ZnO nanorod arrays are formed on Zn substrates (**Figure 3**-4). The sizes of ZnO nanorod arrays could be controlled by tuning the reaction time and the concentration of the ammonia aqueous solution. ZnO nano-array sensor has both high sensitivity to ammonia and reversibility at room temperature (25°C). And the response could be kept at least 5 days when the current intensity reduced to 50% of maximum.

2.5 Spray pyrolysis

ZnO nanorods with different sizes of hexagonal pillar shape have been successfully synthesized by spray pyrolysis technique (SPT). Zinc acetate solution was obtained by dissolving zinc acetate dihydrate in the mixture of methanol and double distilled water. During spray pyrolysis process, the precursor solution droplets close to the preheated substrates thermally decomposed and formed the highly adherent zinc oxide film. During the pyrolytic process, the following reaction takes place.

$$Zn(CH_3COO)_2 \rightarrow CH_3COOH + H_2 \uparrow + CO_2 \uparrow \tag{6}$$
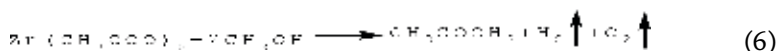
Highly uniform crystalline films were obtained upon the post deposition annealing at 500°C for 1 h in air. The spray pyrolysis setup used is schematically illustrated in **Figure 4**. The thin films comprise well-shaped hexagonal ZnO nanorods with a diameter of 90–120 nm and length of up to 200 nm. The gas-sensing properties of these films toward gases such as ethanol, CO_2, NH_3, CO, and H_2S exposure have been investigated at operating temperature from 30 (room temperature) to 450°C. The ZnO nanorods thin films showed much better sensitivity and stability to H_2S gas (100 ppm) at 50°C than the conventional ZnO materials without nanostructures [19].

2.6 Sonochemical route

A sonochemical route provides an effective way to grow vertically aligned ZnO nanorod arrays on a Pt-electrode patterned alumina substrate under ambient conditions [20]. **Figure 5(a)** shows the sensor substrate with the interdigitated
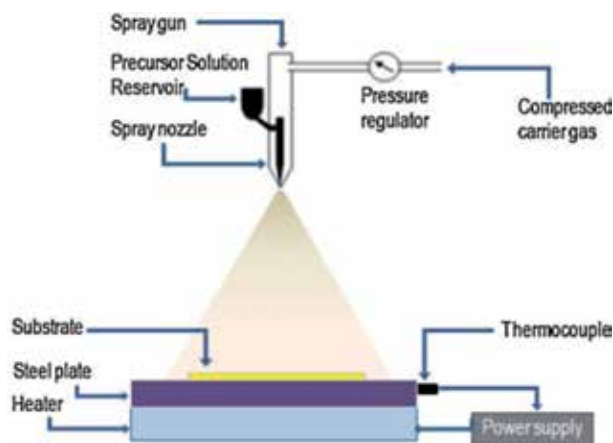
Figure 4.
The scheme of the spray pyrolysis setup.
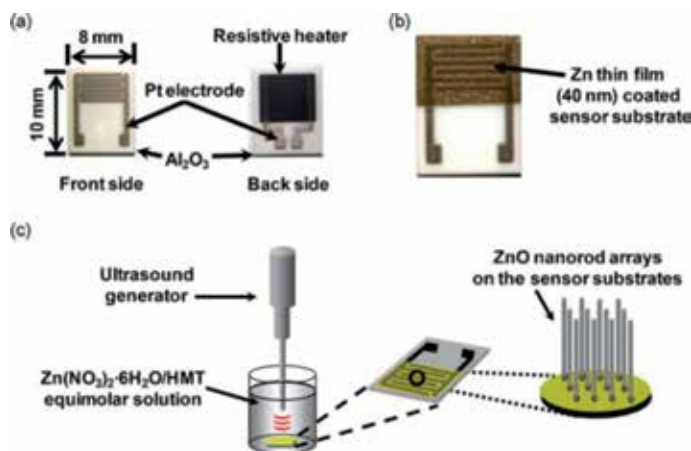
Figure 5.
(a) Photograph of sensor substrate including interdigitated comblike Pt electrodes and a resistive heater. (b) Zn thin-film sputtered sensor substrate. (c) A schematic illustration for the sonochemical growth of vertically aligned ZnO nanorod arrays on a sensor substrate.

comblike Pt electrodes on the front side and a resistive heater on the back. Upon the deposition of Zn thin film (40 nm) on the interdigitated Pt electrodes using RF sputtering technique as shown in **Figure 5(b)**, the sensor substrate was immersed in a mixed aqueous solution of $Zn(NO_3)_2 \cdot 6H_2O$ and $(CH_2)_6N_4$. Ultrasonic waves at an intensity of 39.5 W/cm^2 were introduced in the solution for 1 h. **Figure 5(c)** shows the scheme of the sonochemical growth of vertically aligned ZnO nanorod arrays on the substrate. The ZnO nanorods have the average diameter of 50 nm and length of 500 nm. The gas sensor based on sonochemically grown ZnO nanorod has high sensitivity to NO_2 gas with a very low detection limit of 10 ppb at 250°C and short response and recovery time.

2.7 Simple solution route

Dodecyl benzene sulfonic acid sodium salt (DBS) was used as a modifying agent in a simple solution route to fabricate well-crystallized ZnO nanorods [21]. Zinc acetate dihydrate $[Zn(AC)_2 \cdot 2H_2O]$ and DBS with a ratio of 1:8.5 were dissolved in a mixed solvent of ethylene glycol and xylene. Then a hydrazine monohydrate ethanol solution was drop-wisely introduced into the solution. After the reaction completed, the mixture was subsequently heated to boiling point (140°C) and refluxed. The resulting products were cooled down naturally, washed, and finally dried in the vacuum at 70°C. The ZnO nanorods sensors are highly sensitive and selective to TEA at low concentration of 0.001–1000 ppm among the gases of toluene, ethanol, benzene, and acetone. The prepared ZnO sensors to TEA exhibit high selectivity and superior sensitivity with the response of 6–0.001 ppm TEA at 150°C.

3. Controllable fabrication of ZnO nanorods

3.1 Growth control

The growth characteristics of the ZnO nanorod arrays (ZNAs) deposited using a wet chemical route were affected by several parameters, such as zinc seed layer morphology, zinc ion concentration, solution pH, deposition time, and growth temperature [7]. The surface and the cross-sectional FESEM images of the ZnO

nanorod films prepared with different growth times were shown in **Figure 6**. The length/diameter aspect ratio of the ZNAs also increased as the reaction time is extended [**Figure 6(a)** and **(c)**]. With the prolonged deposition time, upright and wider nanorods can be produced, but the nanorods easily merge with each other as they grow longer. The alignment of the nanorods in **Figure 6(a3)**, **(b3)**, and **(c3)** changes as the growth time is prolonged.

The length and inter-rod space have important influence on the gas-sensing performance of the devices. The ZnO:6 nanorods sample has small length and quite large spacing between them. However, both the length and the inter-rod spacing of the ZnO:9 nanorods samples are adequate and beneficial for the sensing performance. Nevertheless, for the ZnO:12 sample, the interspaces between nanorods are smallest due to the overlap between the nanorods. The gas sensors with ZnO:9 nanorod samples exhibits a high sensitivity of 3100% toward 100 ppm NO_2 at 175°C.

3.2 Selective growth

Selective growth of ZnO nanorod arrays with well-defined areas was developed to fabricate the NO_2 gas sensor. The seed layer was created by ink-jetting the seed solution on the interdigitated electrodes. Then, vertically aligned ZnO nanorods were grown by the hydrothermal approach on the patterned seed layer. The effects of the seed solution properties and the ink-jet printing parameters on the printing performance and the morphology of the nanorods were investigated [22].

FESEM images in **Figure 7** show the morphology of patterned ZnO nanorod films. ZnO nanorods are selectively grown on a round grown area with a diameter of 650 μm as shown in **Figure 7(a)**. **Figure 7(b)** and **(c)** present the enlarged edge images of the grown area. In **Figure 7(c)** the ZnO nanorod were selectively grown in a direction perpendicular to the substrate to produce vertically aligned arrays
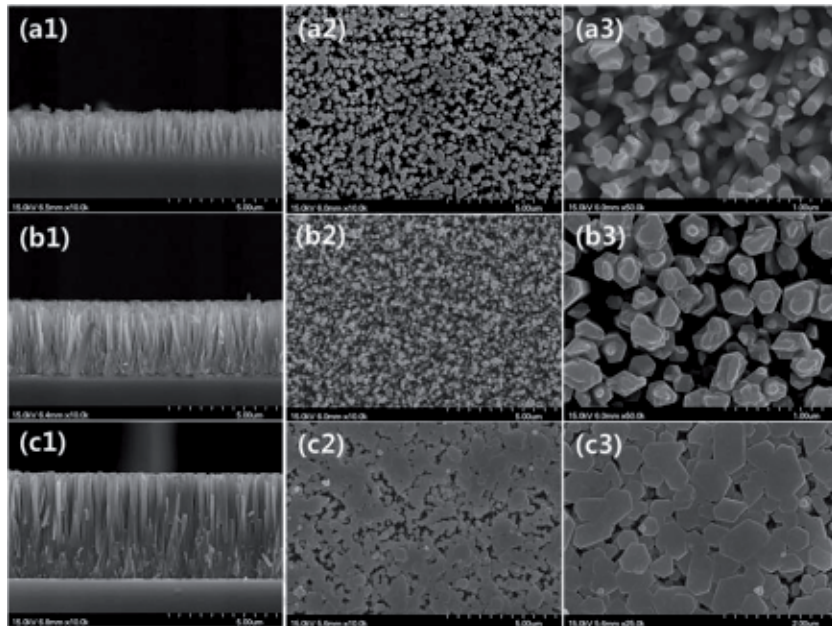
Figure 6.
FESEM images of ZnO thin-film sample ZnO:6 to ZnO:12 (a1, a2, and a3) show cross-sectional view of ZnO:6, ZnO:9, and ZnO:12, respectively. a2, a3, b2, b3, c2, and c3 reveal low- and high-magnification FESEM images of ZnO thin-film sample ZnO:6 to ZnO:12.
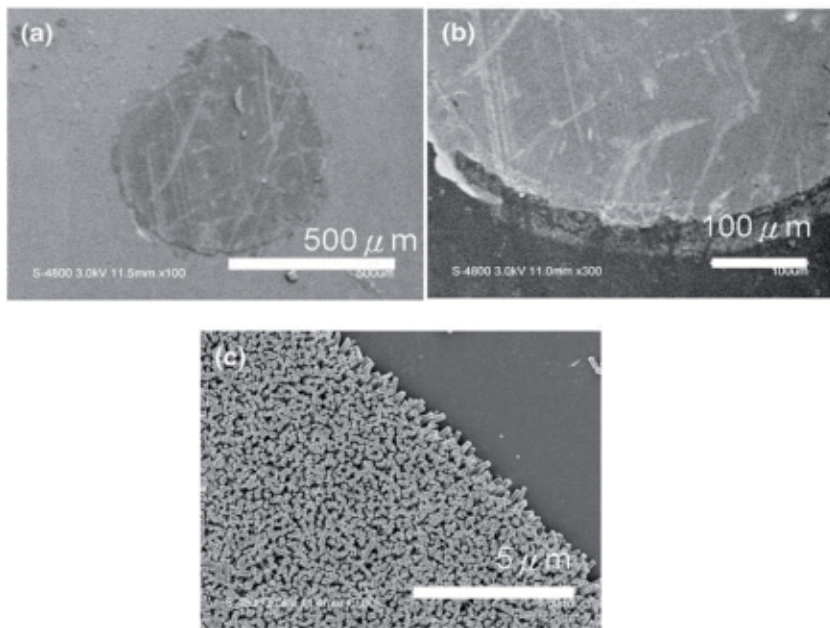
Figure 7.
FESEM images of the selective grown ZnO nanorods micropattern: (a) entire pattern, (b) edges of the grown area, and (c) enlarged images of the nanorods.

of ZnO nanorods on the patterned area. Such a nanorod-array structure with high surface-to-volume ratio favors the adsorption and desorption of NO_2 gas on the sensor.

The influence of different rod growth times on the morphology of ZnO nanorod films was investigated by FESEM with cross-sectional images illustrated in **Figure 8**. The ZnO nanorods become longer but the diameters of the nanorods nearly keep constant with the extension of the growth time. For example, the lengths of the ZnO nanorods grown for 2 and 4 h are 500 and 1300 nm, respectively, but their diameters are nearly the same in the range of 50–80 nm for both cases. Nanorod morphology has strong influence on the response performance of the sensor. The increasing nanorod aspect ratio increases the nanorod surface area and thus allows more gas adsorption interface. Larger fraction of the nanorod is depleted upon adsorption of NO_2. Longer growth time of the ZnO nanorod sensor results in longer nanorod so that the corresponding sensor has higher sensitivity than that with shorter growth time.
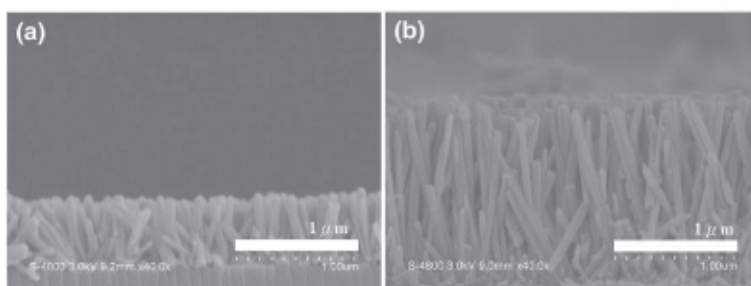
Figure 8.
FESEM images of the cross section of ZnO nanorods prepared with different rod growth time (a) 2 h and (b) 4 h.

3.3 Diameter regulation

The size (diameter or length) of ZnO nanorods grown via hydrothermal method is affected by several factors such as concentration of precursors, growth temperature, and time. The average diameter of ZnO nanorods can be regulated by changing growth time. The average diameter is about 35 nm with the growth time of 0.5 h. Upon the growth time over 1 h, the average diameter rapidly increases up to 100 nm when the growth time is 2.5 h. But then the average diameter keeps nearly constant as the growth time is elongated [23]. ZnO nanorod arrays were successfully synthesized on Si substrates using two-step route including spin-coating seed on substrates and chemical bath deposition (CBD) growth. The diameter of ZnO nanorods can be controlled by changing seed density on substrates or NaOH concentration in solution. Increasing spin-coating times leads to better seed density so that the diameter of ZnO nanorods decreases from 150 to 70 nm as the spin-coating times increase from 1 to 50. And the diameter of ZnO nanorods obviously increases with NaOH concentration increasing [24].

Solvent polarity has a special effect on final dimension of the ZnO nanorods synthesized using a one-step solvothermal method. The diameter of ZnO nanorods decreased with the moderated polarity by introducing less polar ethanol solvent. The diameter of the ZnO nanorods can be regulated by adjusting ethanol content in the solvent in that the diameter of the ZnO nanorods decreases as ethanol content in the solution increases. **Figure 9** shows SEM images of samples a0, a10, a20, a30, a40, and a50 prepared by introducing 0, 10, 20, 30, 40, and 50 vol% ethanol solvent, respectively. **Figure 9(a)** shows ZnO nanorod surface full of flocs when
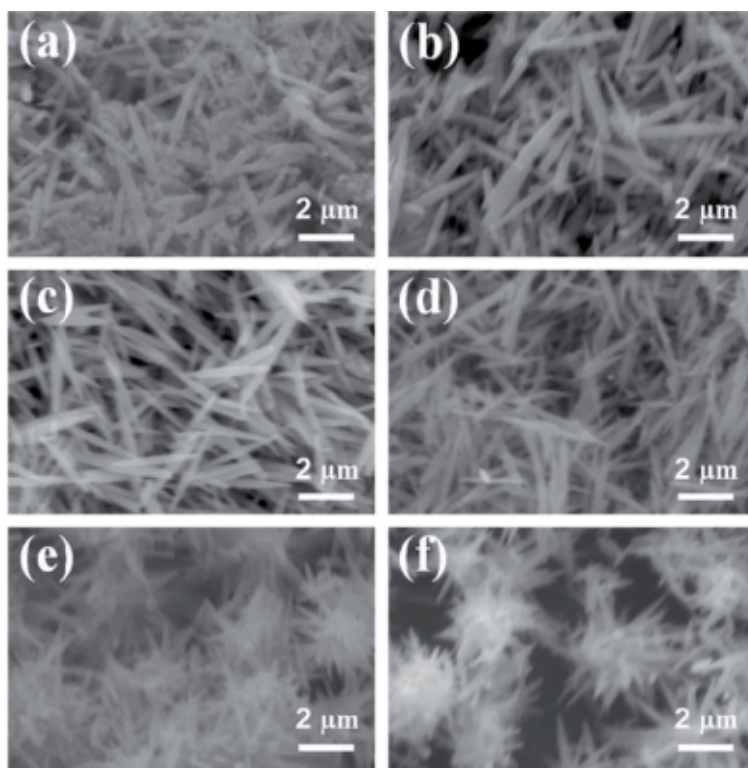
Figure 9.
SEM images of ZnO nanorod samples (a) a0, (b) a10, (c) a20, (d) a30, (e) a40, and (f) a50 prepared with 0, 10, 20, 30, 40, and 50 vol% ethanol solvent.
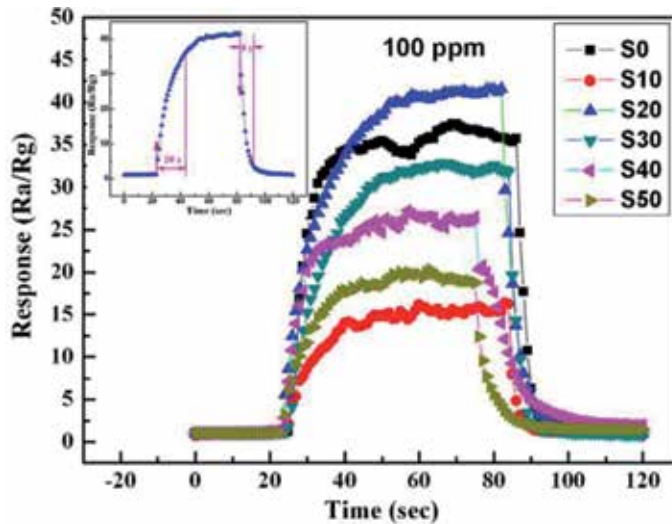
Figure 10.
Response and recovery curves toward 100 ppm ethanol at the optimum working temperature of 370°C.

prepared in pure water solvent. The flocs disappeared upon the addition of 10 vol% ethanol, as shown in **Figure 9(b)**. When ethanol was increased to 20 vol% (**Figure 9(c)**) and 30 vol% (**Figure 9(d)**), ZnO nanorods show uniform, well-defined, and well-dispersed morphologies. The average nanorod diameter decreased from 360 to 220 nm when ethanol percentage in solvent increased from 10 to 50%.

Figure 10 shows transient response and recovery curves of the ZnO nanorod sensors toward 100 ppm alcohol vapor at the optimum working temperature of 370°C. Here the sensors fabricated using samples a0, a10, a20, a30, a40, and a50 are labeled as S0, S10, S20, S30, S40, and S50, respectively. It is apparent that S20 is much superior to others. The inset with a single response and recovery curve of S20 measured at the same condition indicates that its sensor has the response of 42 and very sharp response and recovery time of 20 and 8 s, respectively [25].

4. Different structures formed by ZnO nanorods

4.1 Cross-linked configuration

Ammonia sensors based on ZnO nanorods (NRs) with a cross-linked configuration has excellent sensing performance by shrinking the interdigitated electrode spacing d. The electrode spacing d, working temperature, and gas concentration strongly influence the steady- and dynamic-responses and the related repeatability and different gaseous response performance [26]. Reducing the electrode spacing d increased the ammonia sensor response S because the configuration of ZnO NRs is transformed. The studied sensor with an electrode spacing d of 2 μm at 573 K shows a highest ammonia sensor response S of 81.6 toward 1000 ppm NH_3/air gas and could detect NH_3/air with a lower ammonia concentration of 10 ppm. Moreover, the response S of the ammonia sensor is temperature dependent, as is mainly attributed to reactions of oxygen species. The adsorption-time (τ_a) and desorption-time (τ_b) constants of the studied sensor (d = 2 μm) at 573 K are less than 3 min. The improvement of ammonia-sensing ability could result from the formation of more cross-linked configurations. Finally, the studied sensor with a cross-linked configurations shows good ammonia gas-sensing response and repeatability.

4.2 Flowerlike structures

Rather vertically aligned ZnO rods with flowerlike structures synthesized via carbothermal reduction vapor phase transport (CTR-VPT) method exhibited good crystallinity with preferential c-axis orientation and considerable quantity of oxygen vacancy [27]. **Figure 11** shows the ZnO nanorods have diameter in the range of 300–500 nm and length in the range of 7–9.5 µm. In this configuration, a porous network formed by nanorods consists of directional channels for gas diffusion in and out. The interconnected nanorods provide a continuous electrical path for carrier transport between the two gold electrodes. The flowerlike bundle of rods increases the effective surface area and thus enhances gas sensitivity. The H_2S sensor with the ZnO nanorods of the flowerlike structure exhibits a high response (e.g., S = 296 at 1 ppm and 581 at 5 ppm) and good selectivity at room temperature and 250°C. However, the response and recovery times decreased with the increasing temperature.

4.3 Multishelled hollow spheres

ZnO with multishelled hollow spheres of 5 mm in diameter were prepared by a facile solvothermal process in a ternary solvent system. The anisotropic single-crystalline nanorod building blocks with uniform diameter of about 40 nm are highly directional in the as-synthesized products. The evolution process of hollow ZnO core-shell structures consists of a two-step self-assembly process and symmetric Ostwald ripening starting from the inner core and at the interface of the core and shell. The hollow spheres and core-shell structures could be obtained by simply adjusting the composition of the mixed solvents, as is critical to the packing design [28]. In comparison of the hollow structures and nanorods at all working temperatures, the double-wall hollow structures exhibited the highest sensitivity to formaldehyde gas due to the high donor-related (DL) and the low acceptor-related
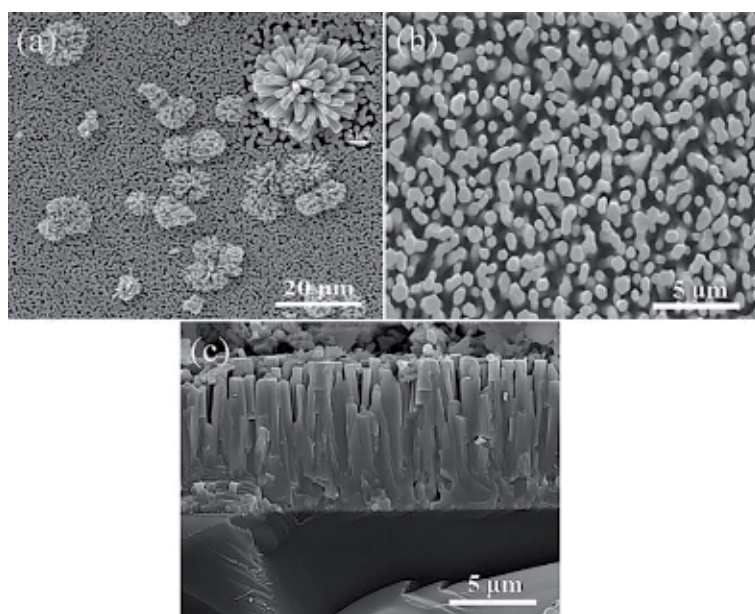
Figure 11.
(a and b) Typical top view and (c) cross-sectional SEM images of the vertically aligned ZnO rods with flowerlike structures. Inset of **Figure 10(a)** *shows magnified image of one of the flowers.*

(AL) intrinsic defects. ZnO semiconductor with high response and selectivity to H_2S as well as good stability was obtained by controlling the shape-defined building units and their assembly structure.

4.4 Hollow microhemispheres

Self-assembling ZnO nanorods into 3D ZnO hollow microhemispheres is simply done by solvothermal reaction of zinc and alkali source in the presence of ethylene glycol. The 3D ZnO hollow microhemispheres were synthesized by the primary formation of glycolate precursors and subsequent transformation into ZnO. Glycol such as EG and the solvothermal process play the critical role in the synthesis. Numerous orderly and radical nanorods in the 3D ZnO hollow microhemispheres have the diameter of about 50 nm and length of several hundred nanometers. Furthermore, high sensitivity for ethanol and ammonia as well as quick response and recovery time at room temperature were obtained for the 3D ZnO hollow microhemisphere-based gas sensor due to the high surface-to-volume ratio [29].

5. Modification of ZnO nanorods

5.1 Doping

The ZnO-sensing performance can be effectively improved by doping with transition metal elements. Vertically aligned yttrium-doped ZnO nanorod (YZO NR) arrays were synthesized by a one-pot hydrothermal method [30]. The Y doping concentration strongly influences the surface morphology of the NRs. With the dopant concentration increasing, longer and sharper NRs with high aspect ratio formed, and the aspect ratio of the YZO NRs was increased from 11 to 25. The Y doping reduced the ZnO NR resistivity to its minimum by a factor of 115 for the $Y_{0.10}ZnO$. And the corresponding sensor gave the highest sensitivity toward all the tested gas species with the lowest breakdown voltage. The sensitivity of the sensor based on Y-doped ZnO nanorod arrays was enhanced up to sixfold, and the breakdown voltage from the highly conductive YZO NRs significantly reduced. The Cr-doped ZnO sensor presents the response of 104 to 100 ppm acetone at 300°C, as is four times higher than that of ZnO sensor. The increase of electron concentration optimized by Cr doping improved the sensing response and selectivity [31].

5.2 Functionalization

The sensitivity and responding kinetics of metal oxide semiconductors (MOS) can be improved by the surface functionalization with noble metal NPs (e.g., Pd, Au, and Pt) because it provides the preferred adsorption and activation sites for the target analyte to react with the ionosorbed oxygen. CuO with a low band gap of 1.2–2.0 eV is a p-type semiconductor and can form p-n junctions with n-type metal oxides to extend the space-charge region, as locally narrows the conducting channel for the charge carriers in the ZnO. The p-n junction is thus more sensitive to gas molecule-induced charge transfer, and the gas-sensing selectivity and sensitivity is improved. CuO-functionalized ZnO nanorods were synthesized by a chemical bath deposition method. And their sensor showed enhanced gas response compared with bare ZnO NRs. According to both a collective- and a local-site approach, the deposition of CuO altered the overall band structure and surface properties of the ZnO [32].

5.3 Decoration

Pd-decorated ZnO nanorod structures were fabricated by sputter depositing Pd on the hydrothermally grown ZnO nanorods and the subsequent oxidation for detecting H_2S gas at room temperature. The dissociation of H_2S gas molecules on Pd accelerated, as facilitated the room temperature-sensing capability [33]. Therefore, the Pd decoration enhanced the sensing response to H_2S at the examined operation temperatures. **Figure 12(a)** shows higher response level of ZnO:Pd nanorod structure than the ZnO nanorod structure at 300°C. **Figure 12(b)** shows a more dramatic effect of Pd at room temperature because the response of the ZnO:Pd sensor to 500 ppm H_2S is approximately ~16% compared with the pure ZnO nanorod of no H_2S-sensing response at RT. The Pd-decorated ZnO nanorods showed a stable performance as well as good stability and repeatability. The response time was approximately 12 min, but the recovery time was much longer, approximately 10 h. Moreover, the CaO-decorated n-ZnO nanorods showed stronger response to NO_2 than the pristine ZnO nanorods [34].

5.4 Sensitization

The sensitivity and the selectivity of the sensor can be improved by different strategies such as incorporating dopants, applying ultraviolet (UV) irradiation, and sensitizing the sensing layer with noble metals (Au, Pt, Pd) and metal oxides (CuO, SnO_2). It is known that sensitizing the sensing layer by noble metals is most
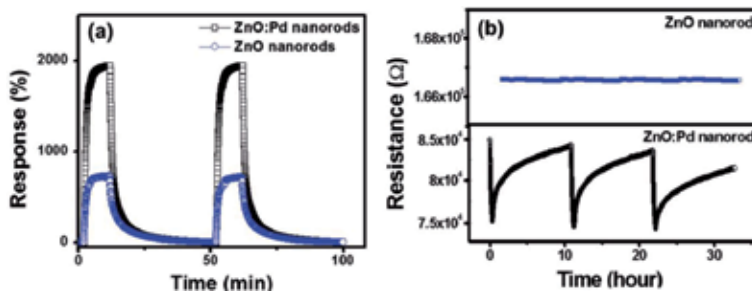
Figure 12.
Comparison of H_2S sensing between ZnO and ZnO:Pd nanorod structures at (a) 300°C and (b) room temperature.
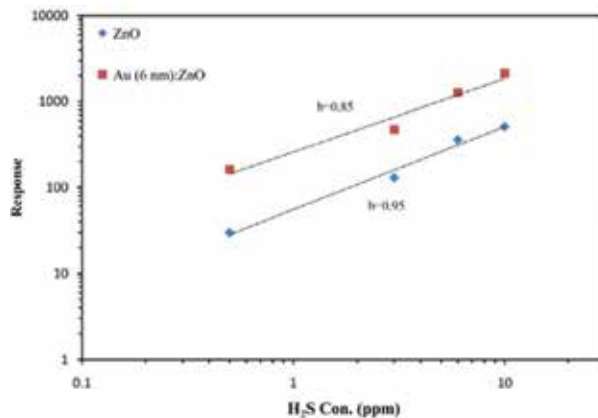
Figure 13.
Response of sensors based on pure and Au-modified ZnO samples versus different concentrations of H_2S gas.

effective. The sputter deposition of Au layer with different nominal thicknesses on ZnO nanorods enhanced the sensing response to H_2S at room temperature (25°C). When Au layer with 6 nm nominal thickness is deposited, higher response and selectivity to H_2S than those reported in the literature are obtained. The sensing response at room temperature was enhanced because Au islands formed Schottky barriers at Au-ZnO interface, introduced surface active sites, and increased effective surface area through surface coarsening. The response of both pure and Au-sensitized rods increases with the gas concentration as shown in **Figure 13**. The fabricated sensor based on the Au-sensitized ZnO nanorods is able to detect H_2S gas of ppb level [1].

6. ZnO nanorod-based composites

6.1 ZnO@ZIF-8 core-shell nanorod film

Figure 14 shows ZnO@ZIF-8 (zeolitic imidazolate framework-8) core-shell nanorod film was designed and synthesized through a facile solution deposition method for H_2 gas sensor. The ZnO@ZIF-8 core-shell nanorod film with a thin, fine-grain, porous ZIF-8 shell realized the selective response for H_2 over CO and enhances the H_2 sensitivity [35]. The 2-methylimidazolate (HmIM) concentration plays a crucial role in forming the core-shell structure and controlling the ZIF-8 grain size. The H_2O/DMF volume ratio influenced the integrity of the core-shell structure, and the reaction time affects its continuity. The introduction of more oxygen vacancies to the ZnO@ZIF-8 core-shell nanorod film enhanced H_2 sensitivity in comparison with the raw ZnO nanorod film. The ZnO@ZIF-8 core-shell nanorod film has highly porous microstructure owing to the contribution of the ZIF-8 shell. The strengthened molecular sieving effect of the ZIF-8 shell because of its fine-grain (<140 nm) structure resulted in no response for CO for the ZnO@ZIF-8 core-shell nanorod film. The selective response of H_2 over CO was realized by the integration of ZnO with ZIF-8 and the control of their microstructures.

6.2 ZnO/MWNTs hierarchical nanostructure

ZnO/multiwall carbon nanotubes (MWNTs) composite with a hierarchical nanostructure was fabricated using layer-by-layer self-assembly technique. The
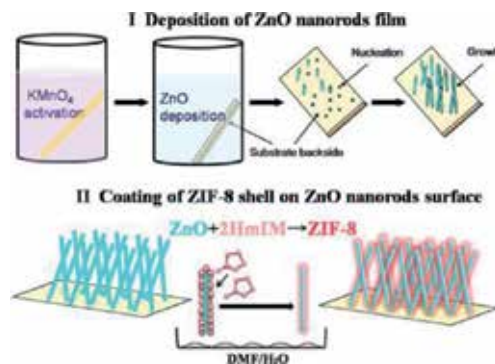
Figure 14.
Formation process of ZnO@ZIF-8 core-shell nanorod films: (I) ZnO nanorod films were deposited on the KMnO4-activated substrates; (II) ZnO@-ZIF-8 core-shell nanorod films were fabricated by immersing the ZnO nanorod films into the 2-methylimidazolate (HmIM) solution [the solvent contained H_2O and N,N-dimethylformamide (DMF)].

as-prepared ZnO was nanorod-shaped crystal in **Figure 15(a)**. **Figure 15(b)** indicates the interdigitated or interweaved MWNTs with a random network structure. **Figure 15(c)** shows that the ZnO/MWNTs film comprised ZnO nanorods and MWNTs wrapped closely together. **Figure 15(d)** shows the XRD spectra of ZnO, MWNTs, and ZnO/MWNTs film. A peak at 2 h angle of 25.18 occurred in the XRD pattern of MWNTs and major peaks at 2 h angle of 24.72, and 31.78 were observed in the XRD patterns of ZnO/MWNTs nanocomposite.

Figure 16 compared the gas-sensing properties of pure ZnO sensor, ZnO/PSS and ZnO/MWNTs sensors tested under the same experimental environment toward 5–500 ppm ethanol gas concentration. The sensing properties of the ZnO/MWNTs nanocomposite sensor were significantly superior to those of pure ZnO sensor and ZnO/PSS nanocomposite sensor. For instance, pure ZnO, ZnO/PSS, and ZnO/MWNTs sensors have the normalized response values of 2.6, 3, and 4.5% to 50 ppm ethanol gas, respectively.

Furthermore, **Figure 17** compares the response and recovery characteristics for the three sensors exposed to 50 ppm ethanol gas. ZnO, ZnO/PSS, and ZnO/MWNTs sensor exhibits the response time of 13, 11, and 7 s and the recovery time of 17, 19, and 11 s for, respectively. The response and recovery time of ZnO/MWNTs sensor is much shorter than those of the other two sensors. Therefore, the ZnO/MWNTs film sensor exhibited more outstanding sensitivity, prompter response recovery time and better repeatability than the other two sensors [36].

6.3 Fe_2O_3/ZnO core-shell nanorods

Fe_2O_3/ZnO core-shell nanorods prepared by hydrolysis method [37] have higher surface area than bulk ZnO sensor materials. High response, good stability, and short response/recovery time were obtained for the resultant Fe_2O_3/ZnO gas sensor to detect low concentrations of various combustible gases. The ZnO shell of about 2–3 nm was coated on the surface of Fe_2O_3 nanorods and much thinner than the conventional ZnO-based sensor devices. The response/recovery time was less
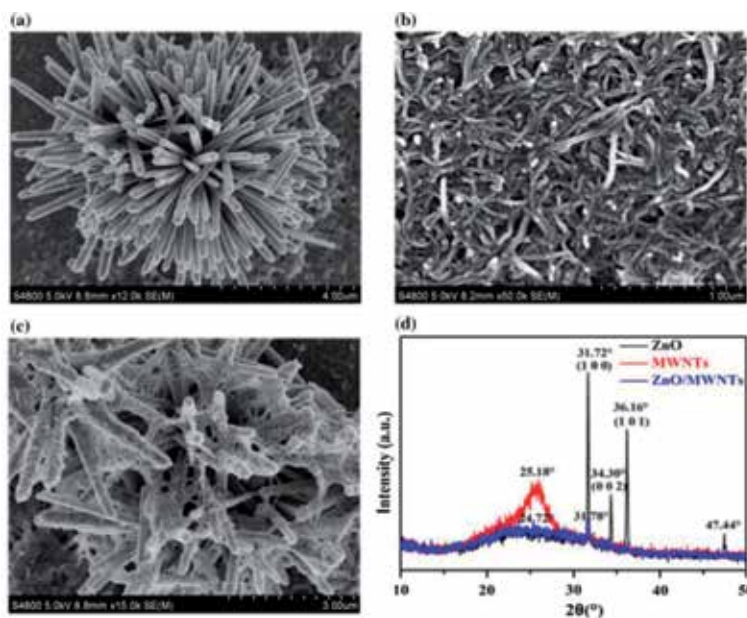
Figure 15.
SEM images of ZnO film (a), MWNTs film (b), and ZnO/MWNTs film (c) and XRD observation of ZnO, MWNTs, and ZnO/MWNTs films (d).
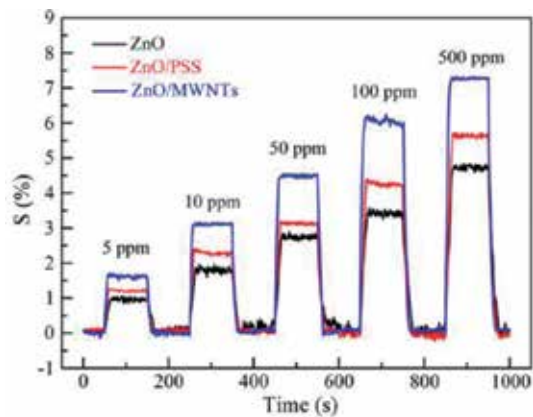
Figure 16.
Normalized response of ZnO, ZnO/PSS, and ZnO/MWNTs film sensors to various ethanol concentrations.
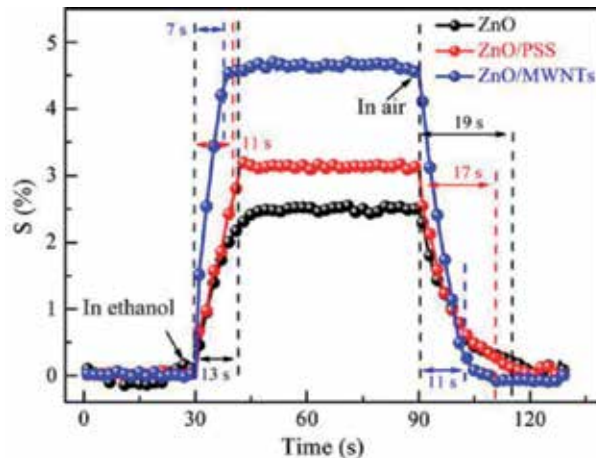
Figure 17.
The response and recovery characteristics of ZnO, ZnO/PSS, and ZnO/MWNTs film sensors exposed to 50 ppm ethanol gas at room temperature.

than 20 s, and the response slightly decreased after 4 months. The present Fe_2O_3/ZnO core-shell nanorods with these favorable gas-sensing features are particularly attractive as a promising practical sensor.

6.4 Ga_2O_3-core/ZnO-shell nanorods

Ga_2O_3-core/ZnO-shell nanorods were fabricated by the thermal evaporation of GaN powders and subsequent atomic layer deposition of ZnO [38]. The diameter of the nanorods ranges from a few tens to a few hundreds of nanometers, and their length is up to a few hundreds of micrometers. The cores of the nanorods were single crystal monoclinic Ga_2O_3, and their shells were single crystal ZnO. The sensors based on multiple networked Ga_2O_3-core/ZnO-shell nanorods showed responses of 7247, 21,352, 32,778, and 27,347% (181, 474, 692, and 355 times larger than those of bare-Ga_2O_3 nanorod sensors) at NO_2 concentrations of 10, 50, 100, and 200 ppm, respectively, at 300°C. The core-shell nanorods have much better response to NO_2 gas than the other material nanosensors reported previously. Ga_2O_3 nanorods encapsulated by ZnO exhibits substantial improvement in the response to NO_2 gas,

as can be explained by the space-charge model. The Ga_2O_3-ZnO heterojunction facilitates or restrains electron transfer as a lever and enhances the sensing properties of the core-shell nanorod sensor. Moreover, the recovery time of the core-shell nanorods was almost 1/3 that of the bare-Ga_2O_3 nanorods at a NO_2 concentration of 10 ppm and almost a half at other NO_2 concentrations, even if the response time of the former is longer than that of the latter.

6.5 In_2O_3-core/ZnO-shell nanorods

The two-step fabrication process of In_2O_3-core/ZnO-shell nanorods comprises the thermal evaporation of a 1:1 mixture of In_2O_3 and graphite powders and the atomic layer deposition of ZnO [39]. The core-shell nanorods have the diameter in the range of 100–200 nm and the length up to a few hundreds of micrometers. The thickness of the ZnO-shell layer in the core-shell nanorod ranged from 5 to 10 nm. The nanorods consist of bcc-structured polycrystalline In_2O_3 as cores and simple hexagonal-structured polycrystalline ZnO as shells. The responses of the multiple networked In_2O_3-core/ZnO-shell nanorod sensors at H_2S concentrations of 10, 25, 50, and 100 ppm were 34.11, 34.55, 35.77, and 28.86%, respectively, at 300°C and 4.2, 4.0, 4.0, and 3.5 times larger than those of bare-In_2O_3 nanorod sensors, respectively. Based on the space-charge model, the In_2O_3-ZnO heterojunction acts as a lever to facilitate or restrain the electron transfer and thus enhances the sensing properties of the core-shell nanorod sensor. In addition, the In_2O_3-core/ZnO-shell nanorods sensor exhibits shorter response and recovery times than the bare-In_2O_3 nanorods for any H_2S concentration.

6.6 ZnO NRs-Gr/M hybrid architectures

The ZnO nanorods (NRs) and graphene (Gr) (ZnO NRs-Gr/M) hybrid architectures fabricated in **Figure 18** [40] accommodated the flexural deformation without mechanical or electrical failure for bending radius below 0.8 cm under the repeated bending and releasing up to 100 times. Furthermore, the gas sensors can detect ethanol gas vapor at the ppm level with the sensitivity (resistance in air/resistance in target gas) as high as ~9 for 10 ppm ethanol. The combination of 1D nanocrystals
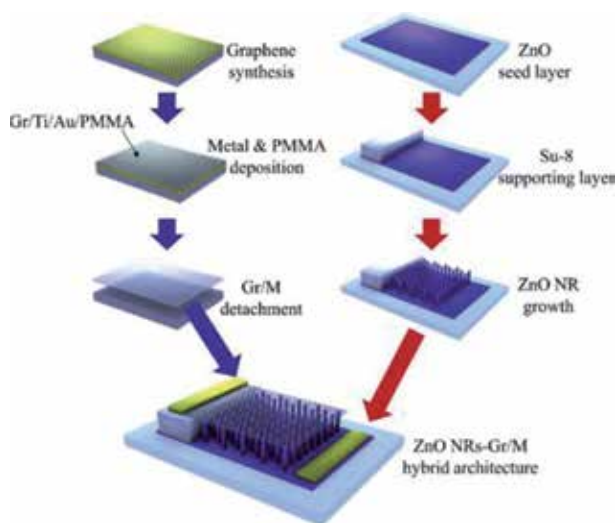
Figure 18.
Schematic illustration of the key steps for fabricating the ZnO NRsG-r/M hybrid architectures.

and 2D Gr improves the performances of the sensors and also imposes additional mechanical functions to the devices.

7. Conclusions and future outlooks

In this chapter, ZnO nanorods for gas sensors were reviewed. ZnO nanorods with various kinds of morphology were synthesized by different fabrication methods. Their synthesis processes including some reaction formula were introduced, and the sensing properties such as fast response, high responsibility, and good stability were described. Furthermore, the growth of ZnO nanorods can be controlled by tuning the reaction parameters. ZnO nanorods were selectively grown on the seed layer, and their morphology was influenced by the rod growth time. The diameter of ZnO nanorods can be regulated by the solution concentration, the growth time, and the seed density. The ZnO nanorods can form different special structures, and their improvement of the sensing properties was explained from a microscopic point of view. For instance, the flowerlike structure of ZnO nanorods increases the effective surface area and thus enhances gas sensitivity. The sensing performance can be effectively improved by doping with transition metal elements, surface functionalization with noble metals, and decoration with Pd or CaO. Finally, the core-shell nanorods composite based on ZnO, hierarchical nanostructure ZnO/MWCNTs composite, and ZnO nanorods-Gr/M hybrid architectures combine the advantages of both components and improve the performance of the sensors. In the future, novel fabrication methods, further modification, and more composites with different materials are perspectives for the sensors based on ZnO nanorods. The sensing properties such as responsibility and stability need to be improved for the practical application. Moreover, the sensing mechanism of the ZnO nanorods sensors is unclear and necessary to be declared. In summary, great progress have been made on the research of ZnO nanorods for gas sensors; however, improvement area still exists for the further study.

Author details

Yanmin Wang
College of Materials Science and Engineering, Shandong University of Science and Technology, Qingdao, Shandong, P. R. China

*Address all correspondence to: yanmin_w@163.com

IntechOpen

References

[1] Hosseini ZS, Mortezaali A, Zad AI, Fardindoost S. Sensitive and selective room temperature H_2s gas sensor based on Au sensitized vertical Zno nanorods with flower-like structures. Journal of Alloys and Compounds. 2015;**628**:222-229. DOI: 10.1016/j.jallcom.2014.12.163

[2] Yu L, Liu S, Yang B, Wei J, Lei M, Fan X. Sn-Ga Co-doped ZnO nanobelts fabricated by thermal evaporation and application to ethanol gas sensors. Materials Letters. 2015;**141**:79-82. DOI: 10.1016/j.matlet.2014.11.049

[3] Hoefer U, Frank J, Fleischer M. High temperature Ga_2O_3-gas sensors and SnO_2-gas sensors: a comparison. Sensors and Actuators B. 2001;**78**(1):6-11. DOI: 10.1016/s0925-4005(01)00784-5

[4] Miller DR, Akbar SA, Morris PA. Nanoscale metal oxide-based heterojunctions for gas sensing: A review. Sensors and Actuators B: Chemical. 2014;**204**:250-272. DOI: 10.1016/j.snb.2014.07.074

[5] Datta N, Ramgir N, Kaur M, Ganapathi SK, Debnath AK, Aswal DK, et al. Selective H_2S sensing characteristics of hydrothermally grown ZnO-nanowires network tailored by ultrathin CuO layers. Sensors and Actuators B. 2012;**166-167**(6):394-401. DOI: 10.1016/j.snb.2012.02.079

[6] Lv Y, Lin G, Xu H, Chu X. Gas-sensing properties of well-crystalline ZnO nanorods grown by a simple route. Physica E: Low-dimensional Systems and Nanostructures. 2007;**36**(1):102-105. DOI: 10.1016/j.physe.2006.09.014

[7] Vanalakar SA, Patil VL, Harale NS, Vhanalakar SA, Gang MG, Jin YK, et al. Controlled growth of ZnO nanorod arrays via wet chemical route for NO_2 gas sensor applications. Sensors and Actuators B: Chemical.

2015;**221**:1195-1201. DOI: 10.1016/j.snb.2015.07.084

[8] Seiyama T, Kato A, Fujiishi K, Nagatani M. A new detector for gaseous components using semiconductive thin films. Analytical Chemistry. 1966;**38**(8):1502-1503. DOI: 10.1021/ac60240a031

[9] Li XB, Ma SY, Li FM, Chen Y, Zhang QQ, Yang XH, et al. Porous spheres-like ZnO nanostructure as sensitive gas sensors for acetone detection. Materials Letters. 2013;**100**(6):119-123. DOI: 10.1016/j.matlet.2013.02.117

[10] Sonker RK, Sabhajeet SR, Singh S, Yadav BC. Synthesis of ZnO nanopetals and its application as NO_2 gas sensor. Materials Letters. 2015;**152**:189-191. DOI: 10.1016/j.matlet.2015.03.112

[11] Jin WX, Ma SY, Tie ZZ, Xu XL, Jiang XH, Li WQ, et al. Synthesis of monodisperse ZnO hollow six-sided pyramids and their high gas-sensing properties. Materials Letters. 2015;**159**:102-105. DOI: 10.1016/j.matlet.2015.06.085

[12] Luo J, Ma SY, Sun AM, Cheng L, Yang GJ, Wang T, et al. Ethanol sensing enhancement by optimizing ZnO nanostructure: From 1D nanorods to 3D nanoflower. Materials Letters. 2014;**137**:17-20. DOI: 10.1016/j.matlet.2014.08.108

[13] Gurav KV, Deshmukh PR, Lokhande CD. LPG sensing properties of Pd-sensitized vertically aligned ZnO nanorods. Sensors and Actuators B: Chemical. 2011;**151**(2):365-369. DOI: 10.1016/j.snb.2010.08.012

[14] Pawar RC, Shaikh JS, Suryavanshi SS, Patil PS. Growth of ZnO nanodisk, nanospindles and nanoflowers for gas sensor: Ph dependency. Current Applied Physics. 2012;**12**(3):778-783. DOI: 10.1016/j.cap.2011.11.005

[15] Jiao M, Chien NV, Duy NV, Hoa ND, Hieu NV, Hjort K, et al. On-chip hydrothermal growth of ZnO nanorods at low temperature for highly selective NO_2 gas sensor. Materials Letters. 2016;**169**:231-235. DOI: 10.1016/j.matlet.2016.01.123

[16] Lim SK, Hwang S-H, Kim S, Park H. Preparation of ZnO nanorods by microemulsion synthesis and their application as a CO gas sensor. Sensors and Actuators B: Chemical. 2011;**160**(1):94-98. DOI: 10.1016/j.snb.2011.07.018

[17] Tan ST, Tan CH, Wu YC, Chi CY, Umar AA, Ginting RT, et al. Microwave-assisted hydrolysis preparation of highly crystalline ZnO nanorod array for room temperature photoluminescence-based CO gas sensor. Sensors and Actuators B: Chemical. 2016;**227**:S0925400515307851. DOI: 10.1016/j.snb.2015.12.058

[18] Qiu Y, Yang M, Fan H, Xu Y, Shao Y, Yang X, et al. Synthesis of ZnO nanorod arrays on Zn substrates by a gas-solution-solid method and their application as an ammonia sensor. Journal of Materials Science. 2014;**49**(1):347-352. DOI: 10.1007/s10853-013-7711-0

[19] Shinde SD, Patil GE, Kajale DD, Gaikwad VB, Jain GH. Synthesis of ZnO nanorods by spray pyrolysis for H_2S gas sensor. Journal of Alloys and Compounds. 2012;**528**:109-114. DOI: 10.1016/j.jallcom.2012.03.020

[20] Oh E, Choi H-Y, Jung S-H, Cho S, Kim JC, Lee K-H, et al. High-performance NO_2 gas sensor based on ZnO nanorod grown by ultrasonic irradiation. Sensors and Actuators B: Chemical. 2009;**141**(1):239-243. DOI: 10.1016/j.snb.2009.06.031

[21] Lv YZ, Li CR, Guo L, Wang FC, Xu Y, Chu XF. Triethylamine gas sensor based on ZnO nanorods prepared by a simple solution route. Sensors and Actuators B: Chemical. 2009;**141**(1):85-88. DOI: 10.1016/j.snb.2009.06.033

[22] Chang C-J, Hung S-T, Lin C-K, Chen C-Y, Kuo E-H. Selective growth of ZnO nanorods for gas sensors using ink-jet printing and hydrothermal processes. Thin Solid Films. 2010;**519**(5):1693-1698. DOI: 10.1016/j.tsf.2010.08.153

[23] Yuan Z, Yu J, Wang N, Jiang Y. Well-aligned ZnO nanorod arrays from diameter-controlled growth and their application in inverted polymer solar cell. Journal of Materials Science: Materials in Electronics. 2011;**22**:1730-1735. DOI: 10.1007/s10854-011-0353-6

[24] Li X, Wang J, Yang J, Lang J, Cao J, Liu F, et al. Size-controlled fabrication of ZnO micro/nanorod arrays and their photocatalytic performance. Materials Chemistry and Physics. 2013;**141**:929-935. DOI: 10.1016/j.matchemphys.2013.06.028

[25] Yin M, Liu M, Liu S. Diameter regulated ZnO nanorod synthesis and its application in gas sensor optimization. Journal of Alloys and Compounds. 2014;**586**:436-440. DOI: 10.1016/j.jallcom.2013.10.081

[26] Chen T-Y, Chen H-I, Hsu C-S, Huang C-C, Wu J-S, Chou P-C, et al. Characteristics of ZnO nanorods-based ammonia gas sensors with a cross-linked configuration. Sensors and Actuators B: Chemical. 2015;**221**:491-498. DOI: 10.1016/j.snb.2015.06.122

[27] Hosseini ZS, Zad AI, Mortezaali A. Room temperature H_2S gas sensor based on rather aligned ZnO nanorods with flower-like structures. Sensors and Actuators B: Chemical. 2015;**207**:865-871. DOI: 10.1016/j.snb.2014.10.085

[28] Hu P, Han N, Zhang X, Yao M, Cao Y, Zuo A, et al. Fabrication of ZnO nanorod-assembled multishelled hollow spheres and enhanced performance

in gas sensor. Journal of Materials Chemistry. 2011;**21**(37):14277. DOI: 10.1039/c1jm11919b

[29] Zhang H, Wu J, Zhai C, Du N, Ma X, Yang D. From ZnO nanorods to 3D hollow microhemispheres: Solvothermal synthesis, photoluminescence and gas sensor properties. Nanotechnology. 2007;**18**(45):455604. DOI: 10.1088/0957-4484/18/45/455604

[30] Lee WC, Fang Y, Turner JFC, Bedi JS, Perry CC, He H, et al. An enhanced gas ionization sensor from Y-doped vertically aligned conductive ZnO nanorods. Sensors and Actuators B: Chemical. 2016;**237**:724-732. DOI: 10.1016/j.snb.2016.06.146

[31] Zhang GH, Deng XY, Wang PY, Wang XL, Chen Y, Ma HL, et al. Morphology controlled syntheses of Cr doped ZnO single-crystal nanorods for acetone gas sensor. Materials Letters. 2016;**165**:83-86. DOI: 10.1016/j.matlet.2015.11.112

[32] Rai P, Jeon SH, Lee CH, Lee JH, Yu YT. Functionalization of ZnO nanorods by CuO nanospikes for gas sensor applications. RSC Advances. 2014;**4**(45):23604-23609. DOI: 10.1039/c4ra00078a

[33] Hieu NM, Kim H, Kim C, Hong S-K, Kim D. A hydrogen sulfide gas sensor based on Pd-decorated ZnO nanorods. Journal of Nanoscience and Nanotechnology. 2016;**16**(10):10351-10355. DOI: 10.1166/jnn.2016.13158

[34] Sun GJ, Lee JK, Choi S, Lee WI, Kim HW, Lee C. Selective oxidizing gas sensing and dominant sensing mechanism of N-CaO-decorated N-ZnO nanorod sensors. ACS Applied Materials and Interfaces. 2017;**9**(11):9975-9985. DOI: 10.1021/acsami.6b15995

[35] Wu X, Xiong S, Mao Z, Hu S, Long X. A designed ZnO@Zif-8 core-shell nanorod film as a gas sensor with excellent selectivity for H_2 over CO. Chemistry-A European Journal. 2017;**23**(33):7969-7975. DOI: 10.1002/chem.201700320

[36] Zhang D, Sun Y, Zhang Y. Fabrication and characterization of layer-by-layer nano self-assembled ZnO nanorods/carbon nanotube film sensor for ethanol gas sensing application at room temperature. Journal of Materials Science: Materials in Electronics. 2015;**26**(10):7445-7451. DOI: 10.1007/s10854-015-3378-4

[37] Si S, Li C, Wang X, Peng Q, Li Y. Fe_2O_3/ZnO core-shell nanorods for gas sensors. Sensors and Actuators B: Chemical. 2006;**119**(1):52-56. DOI: 10.1016/j.snb.2005.11.050

[38] Jin C, Park S, Kim H, Lee C. Ultrasensitive multiple networked Ga_2O_3-core/ZnO-shell nanorod gas sensors. Sensors and Actuators B: Chemical. 2012;**161**(1):223-228. DOI: 10.1016/j.snb.2011.10.023

[39] Park S, Kim H, Jin C, Lee C. Enhanced gas sensing properties of multiple networked In_2O_3-core/ZnO-shell nanorod sensors. Journal of Nanoscience and Nanotechnology. 2013;**13**(5):3427-3432. DOI: 10.1166/jnn.2013.7231

[40] Yi J, Lee JM, Park WI. Vertically aligned ZnO nanorods and graphene hybrid architectures for high-sensitive flexible gas sensors. Sensors and Actuators B: Chemical. 2011;**155**(1):264-269. DOI: 10.1016/j.snb.2010.12.033

Study of Structural and Melting Properties of Gold Nanorods

Rida Essajai

Abstract

MD simulations combined with the embedded-atom method have been applied to study the structural and melting properties of gold nanorods (AuNRs) of different sizes. The simulation results for the actual structure of AuNRs obtained after energy minimization processes revealed that the AuNRs with largest cohesive energies tend to be structurally more stable than those with smallest ones. Then, it was found that each actual structure of AuNR is classified as an irregular structure composed of a crystalline gold core covered by an amorphous gold shell. In addition, the results showed that the melting of the AuNR surface is an inhomogeneous, gradually occurring process. Besides, it was established that the premelting ratio is inversely correlated with the AuNR size, indicating that the premelting phenomenon is more pronounced in large NP sizes than in small ones.

Keywords: gold nanorods, size effect, thermodynamic properties, melting temperature, premelting temperature, MD simulations

1. Introduction

Gold-based nanorods have attracted and continue to attract the attention of a vast amount of scientists from all over the world thanks to their fundamental and pragmatic significance. Due to their exciting properties that are found to be absent in corresponding bulk counterpart, the gold nanorods (AuNRs) are useful nanoobjects in many applications [1–14]. Especially, considerable attention has been paid over the past decades to AuNRs, because of their great importance in fabricating the new generation of nanomolecular and molecular electronics as mentioned in Ref. [15]. Besides, AuNRs can be added to base fluids in order to better improve the effective thermal properties of the nanofluids [16]. It is worth noting here that the technological properties of molecular electronic devices and the thermal property enhancement of nanofluids strongly depend on both the state of AuNR surface and temperature at which their structures change. Nonetheless, the temperature-dependent surface structure of single metal nanoparticles was ignored by several authors, where they did not take into account the surface premelting stage during the analysis of the melting process in the nanoparticles [17–19]. Therefore, it is necessary to understand the AuNR melting properties before fabricating new nanodevices based on them or suspending them in an energetic system (fluid). However, to our knowledge, the investigation on the melting properties of these nanoobjects is still lacking in the theoretical and experimental reports and, thus, needs intensive studies. To this end, the MD simulations combined with the

embedded-atom method (EAM) will be applied to study the melting behaviors of AuNRs. For this purpose, a series of results will be presented in the present work that is organized as follows: In Section 2, there is a short description of the computational method and the calculation procedure. Section 3 deals with the simulation results of AuNRs. Finally, the main conclusions arising from this work are summarized in Section 4.

2. Computational methodology

All MD simulations were performed with the LAMMPS package [20], and the atomistic visualizations were carried out by Ovito [21]. First of all, eight different model systems of rod-shaped nanoparticles were constructed using LAMMPS, where the ratio between their diameters to their lengths is more than 1:10. (Example of structure can be seen in **Figure 1.**) The detailed parameters of all rod-shaped nanoparticles are listed in **Table 1**. Furthermore, embedded-atom method (EAM) potential was adopted to describe the interatomic interaction that has been developed from the density functional theory (DFT) by Daw and Baskes [22]. Moreover, this potential has been successfully used by our group in a variety of computational disciplines [23–26]. The EAM potential used here was parameterized by Grochola et al. [27] to describe the gold–gold interactions by adjusting its parameters with experiments and ab initio calculations.

The total energy given by the EAM is written as a sum of an embedding function $F_i(\overline{\rho_i})$ and pair potential $\phi_{i,j}(r_{ij})$ as

$$E = \sum_i F_i(\overline{\rho_i}) + \frac{1}{2}\sum_{i,j}\phi_{i,j}(r_{ij}) \tag{1}$$

Figure 1.
Structure of rod-shaped Au nanoparticle generated by lamps (D = 6.3 nm, Lz = 61.86 nm, D:lz = 0.1, and 111147 atoms). The atomic structures are visualized by Ovito.

Nanoparticles	NP1	NP2	NP3	NP4	NP5	NP6	NP7	NP8
D (nm)	2.03	3.84	4.64	5.07	6.3	7.32	8.42	9.44
Lz (nm)	19.43	30.43	41.25	50.55	61.86	72.43	83.34	93.04
N (atoms)	8907	13,907	42,375	74,164	111,147	149,133	194,139	243,880

Table 1.
Diameter D, length lz, and total number atoms (N) for the AuNRs.

where the factor $\frac{1}{2}$ is included in order to avoid double computation of the atom couples, $r_{ij} = \left| \vec{r_j} - \vec{r_i} \right|$ is the scalar distance, and $\overline{\rho_i}$ is the host electron density induced by all encirclement atoms j at the position of atom i. The host electron density is given by

$$\overline{\rho_i} = \sum_{i \neq j} \rho_i(r_{ij}) \tag{2}$$

In order to investigate the melting properties of AuNRs of different sizes, a series of MD simulations were carried out. First, all models considered in this work are equilibrated over 500,000 time steps in the NVT ensemble at zero temperature using the velocity Verlet method with a fixed time step of 1 fs and neglecting the periodic boundary conditions (PBCs) in three dimensions. Then after energy minimization process, the actual model systems at 0 K were obtained and characterized using two structural techniques, namely, the coordination number (CN) analysis and the common neighbor analysis (CNA) method. The final point of the simulations is that all the simulated equilibrium samples are heated by increasing the temperature from 0 to 2300 K using NVT.

In order to predict the melting temperatures of AuNRs, the variation of thermodynamic properties (including the potential energy per atom (U) and the heat capacity (C)) with respect to temperature was analyzed. The heat capacity is obtained from the ensemble averages of U and its square, as [28]

$$\frac{C}{K_B} = \frac{1}{N K_B^2 T^2} \left(\langle U^2 \rangle - \langle U \rangle^2 \right) + \frac{3}{2} \tag{3}$$

where T is the temperature, N is the number of atoms, and K_B is the Boltzmann constant.

Besides the thermodynamic properties, the melting temperature of NPs is also explored by analyzing the variation in other physical quantities in terms of the temperature [29]. In this context, the Lindemann index is regarded as one of the most important of these quantities. Additionally, this index is a tool to examine the NP in the layer form in order to determine from where the NP melting begins. The Lindemann index of each layer, $\delta_{L(i)},$ is represented as [30]

$$\delta_{L(i)} = \frac{2}{N_{L(i)} (N_{L(i)} - 1)} \sum_{j < k} \frac{\sqrt{\langle r_{jk}^2 \rangle - \langle r_{jk} \rangle^2}}{\langle r_{jk} \rangle} \tag{4}$$

where $L(i)$ is the *ith* layer, r_{jk} is the distance between atoms k and j, $N_{L(i)}$ is number of atoms of the *ith* layer, and the bracket $\langle \rangle$ represents the ensemble average.

3. Results and discussions

Although the initial structures of gold nanorods can be generated by using LAMMPS, these original structures are not the nanorods with equilibrium states (i.e., metastables). Therefore, it is necessarily to get the actual model systems (i.e., the real calculation models) before studying the structural analysis.

Using the MD simulation, the temporal evolution of each nanostructure passes through several states until it reaches a more stable one, corresponding to minimum

total energy, but remains metastable, resulting from its surface atoms always wanting to aggregate to reduce surface energy as was indicated in Ref. [5]. After this pretreatment stage, the structure stability of AuNRs was investigated by the size-dependent cohesive energy (the absolute value of total energy) of the AuNR, and the results were plotted in **Figure 2**.

As expected, it is found that the calculated cohesive energies of the particles are lower than that of the bulk Au which was obtained previously [23, 31]. It was also established that the cohesive energy of AuNR is very sensitive to the size. The cohesive energy value increases with increasing AuNR size. This behavior seems to indicate that the AuNRs of higher energies tend to be structurally more stable and it can be explained in terms of reducing the influence of surface free energy (i.e., energy of all of the dangling bonds in the surface) resulting from the decrease in the dangling bonds to total bonds ratio when increasing the size.

Within the framework of the local structural characterization of AuNRs, the common neighbor analysis (CNA) technique was adopted. For more details on this method, see Refs. [23, 32, 33]. Once AuNRs in their equilibrium states were obtained (see **Figure 3a** which displays the section of [100]-oriented equilibrium AuNR at different sizes), the two categories of Au atoms in each NR were calculated by the CNA technique; then their percentage were illustrated in **Figure 3b**. It was found from **Figure 3b** that for the smallest AuNR (D = 1.622 and Lz = 15.26 nm), there is a significant percentage of unidentified structures (47.5%), while proportion of *fcc* structures is identified by 52.5%. It was moreover observed that for all AuNR sizes, the fraction of Au atoms having *fcc* structures is higher than those possessing unidentified structures. Also, it was found that when the AuNR size increases, the fraction of both the *fcc* structure and unidentified one are, respectively, an increasing and decreasing function until they reach percentages of 82.5 and 17.5% at size correspondent to D = 8.704 nm and Lz = 86.12 nm (NP8).

In order to describe in more details the local atomic-level structures in different size of AuNRs, the coordination number (CN) about each individual atom was calculated; then the results are presented in **Figure 4**. It was shown that each actual structure of the AuNR obtained after energy minimization process reveals the core-shell structure composed by a crystalline gold core (full-coordinated atoms with the CN = 12) covered by an amorphous gold shell. This last part is divided into two
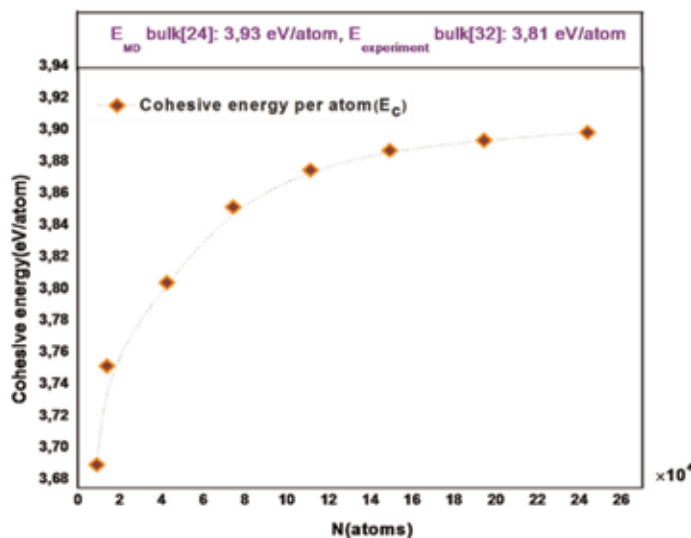
Figure 2.
The cohesive energy per atom as a function of the AuNR size (N) after energy minimization.
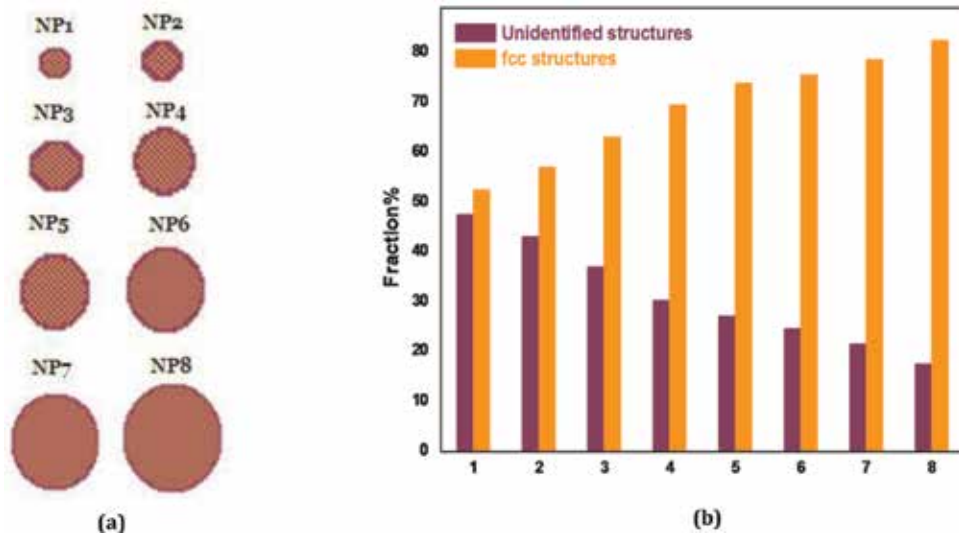
Figure 3.
(a) Sections of [100]-oriented AuNRs after energy minimization. (b) The atomic structures are visualized by Ovito. The percentage of each category of atoms in AuNRs is counted by using the CNA method, yellow for fcc structures and purple for unidentified structures.

layers: the first contains atoms located on the subsurface layer (CN = 11 and 10), the second consists of atoms located on the free-surface layer, corresponding to both low-index facets [i.e., {110} and {100} facets with the CN = 7 and CN = 8 and their perimeter (edge and corner with the CN < 7)]. Apparently, the shell part of the NP is inherently different from the core one, where its atoms possess structure intermediate between the bulk liquid structure and the bulk solid one. It is worth mentioning that the classification of AuNRs in core-shell constructions obtained here supports the previous experimental and simulated studies carried out on single metal nanoparticles [23–26, 34, 35]. Furthermore, it was seen from **Figure 4** that for all simulated AuNRs, the fraction of liquid-like atoms located in the shell part is smaller than that of solid-like atoms located in the core part. It was also found that for all actual structures of AuNRs, the liquid-like atoms located in the area of low-index facets (7 and 8 coordinated atoms) exhibit the highest fraction in the shell part. In addition, when the AuNR size increases, the fraction of atoms' core part increases from 51 to 83%, while the total fraction of shell atoms decreases from 49 to 17%. These findings are consistent with those previously reported by the CNA analysis. The results of the current study indicates that the ratio of low-coordinated atoms to full-coordinated atoms is inversely correlated with the AuNR size.

Figure 5 shows the typical trend of potential energy (U) and heat capacity (C) of different AuNR sizes as a function of temperature T during the heating process from 0 to 2300 k. For each AuNR, it was established that the U curve presents a jump at the same temperature that the C curve has a sharp peak corresponding to the complete melting point (T_{pm}) of the AuNR (observed at 1270.17 K for NP1, 1306.43 for NP2, 1330.34 for NP3, 1349.18 for NP4, 1361.85 for NP5, 1367.07 for NP6, 1372.52 for NP7, and 1377.65 K for NP8). As predicted, the results observed here reveal that the complete melting points of AuNRs are lower than that of bulk Au obtained previously [23, 36]. It was also found that, as the AuNR size increases, the simulated value of T_{pm} increases. This behavior is in agreement with previous results [37, 38]. Notably, the increase of T_{pm} could be attributed to the decrease in the ratio of low-coordinated atoms to full-coordinated ones (i.e., the total number
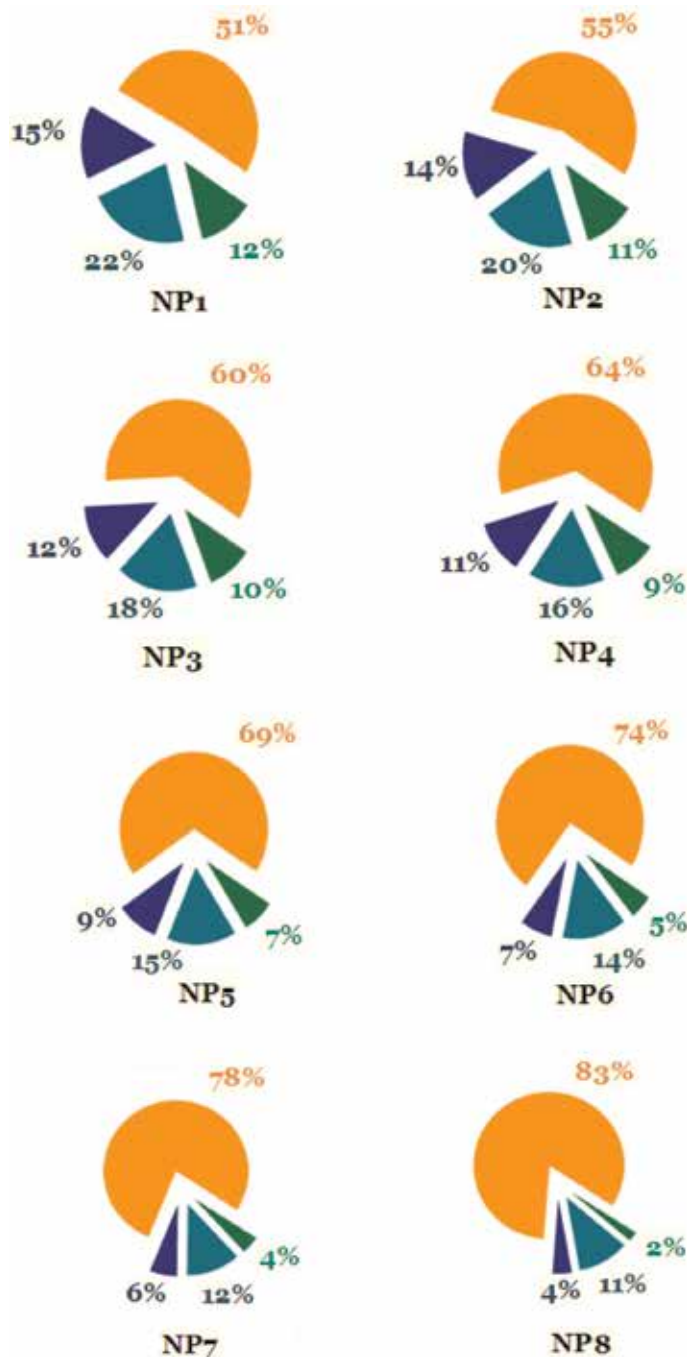
Figure 4.
The distribution of the coordination numbers of AuNR for different sizes, orange for fcc *structures, royal for second layer (CN = 11, 10), olive for Perimeter atoms (CN < 7), and dark cyan for facet atoms (CN = 7, 8).*

of bonds in the NP increases); hence, AuNRs with large sizes require more temperature to completely melt than those with small sizes.

Now we will turn to **Figure 6**, which shows the temperature-dependent Lindemann index value of free-surface atoms (δ_L) for different AuNR sizes. It is easy to see that in the beginning of the heating process, the δ_L increases slowly and linearly, thus suggesting that all surface atoms merely vibrate around their original
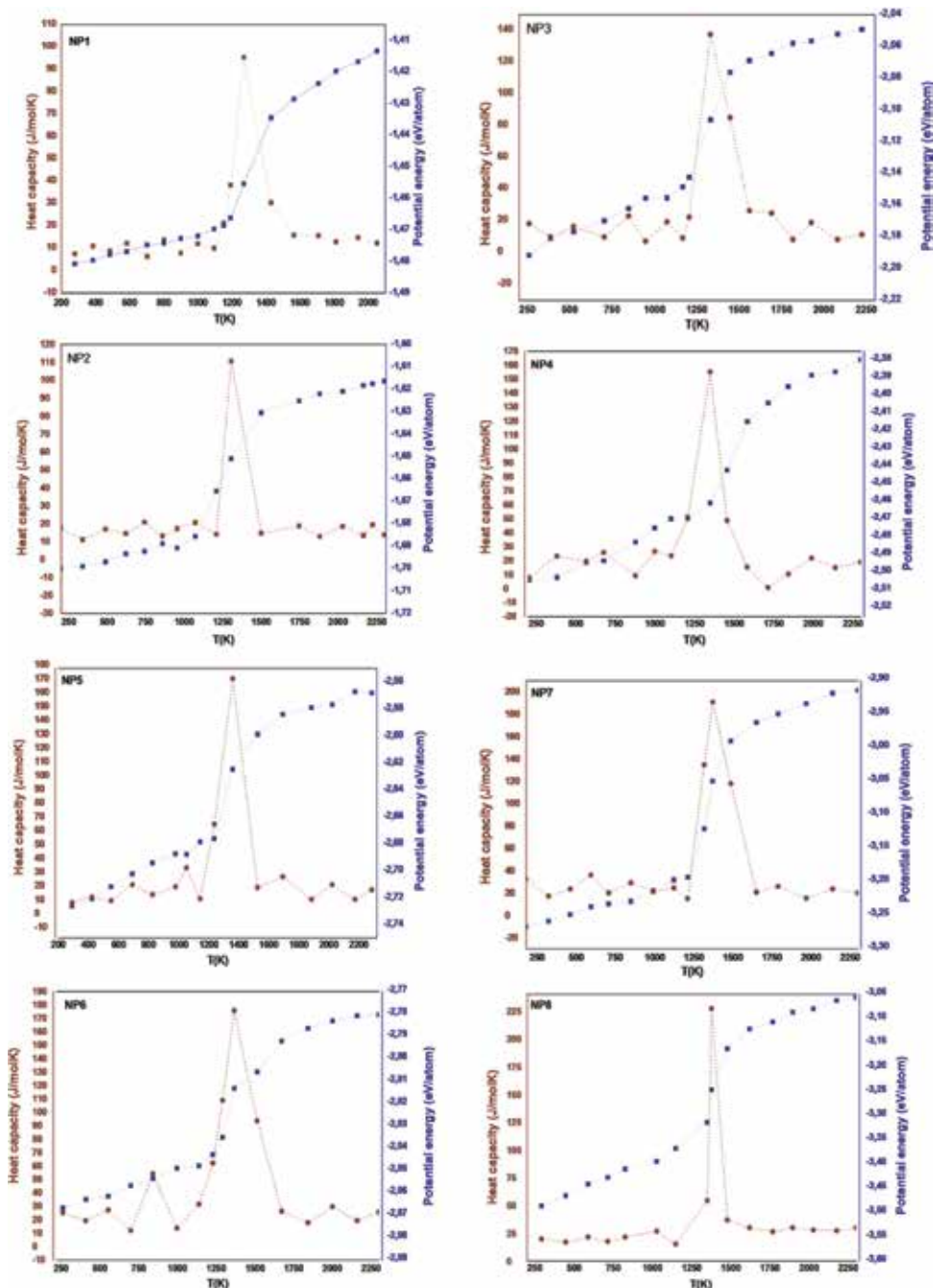
Figure 5.
Variation of the heat capacity and potential energy per atom of AuNR for different sizes, during the heating process.

lattice positions. Then, δ_L abruptly jumped, and its factor is many times greater than before, from which the premelting phenomenon occurs at the temperature before that of complete melting; hence some liquid-like atoms start to appear. It is evident that after the sharp rise, δ_L increased with fluctuations at several temperatures. This latter can be ascribed to the nonhomogeneous nature of the melting of free-surface atoms originating from the coexistence between two types of atoms: those who are moving and those who are remaining strongly constrained in their solid ordering
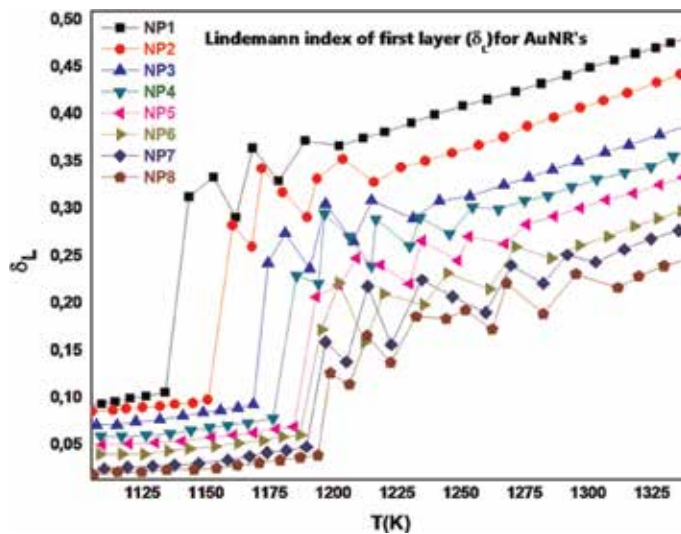
Figure 6.
Temperature-dependent Lindemann index of first layer for AuNRs.

against premelting phenomenon. Besides, it was observed that the fluctuations presenting in δ_L curve are attenuated progressively with the increase in temperature until completely damped. This may be due to the increased amount of liquid-like atoms until they form a continuous liquid layer. It can be clearly shown from **Figure 6** that the higher temperature region where δ_L increases monotonically is in the liquid-like range of the first layer for AuNR different sizes. This liquid region of δ_L curve may correspond with the fact that all surface atoms moved cooperatively.

Once again according to **Figure 6**, the onset of premelting temperature (T_{sm}) of each actual structure of the AuNR is determined from the temperature where δ_L curve shows a sharp increase. The results showed that T_{sm} decreased from 1198.82 K for NP8 to 1142.87 K for NP1, and considering the T_{pm} already determined from U and C curves (**Figure 5**), its value is above the T_{sm} one. It was also found that the T_{sm} value decreased by 177.51 for NP8, 174.17 for NP7, 170.57 for NP6, 165.40 for NP5, 159.25 for NP4, 151.98 for NP3, 139.18 for NP2, and 127.3 for NP1, compared with the T_{pm} one. On the basis of the above, it was concluded that all AuNRs in the present study are passing through the surface premelting stage during heating process.

Our attention will now be drawn to identifying how the ratio between T_{sm} and T_{pm} of AuNR also called the premelting ratio varies in terms of size. One of the main objectives of this investigation is to provide insights into the AuNR size-dependent premelting phenomenon. Hence, this study aims to fill this void in the existing literature. **Figure 7** is given to show the behavior of the premelting ratio of AuNR as a function of the size (N). It was found that the premelting ratio value decreases when the NP size increases, thus indicating that the premelting phenomenon is less pronounced in small NP sizes than in large ones.

4. Conclusions

In summary, the structural and melting properties of AuNRs have been investigated by means of MD simulations combined with the embedded-atom method (EAM) potential. The simulation results for the actual structure of AuNRs revealed
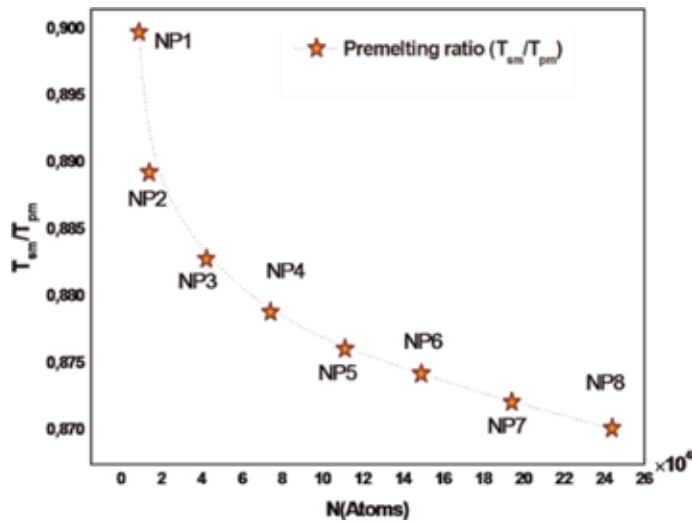
Figure 7.
Premelting ratio as a function of the particle size (N).

that AuNRs of smaller cohesive energies tend to be structurally less stable than those larger ones. Then, the local structure characterization of the actual structure of AuNRs carried out by using the CN and CNA techniques showed that each AuNR is classified as an irregular structure which is composed of a crystalline gold core that is covered by an amorphous gold shell. Further, it was shown that melting temperatures of the actual structure of AuNRs are below that in bulk state. In addition, it was found that the surface melting in the actual structure of AuNRs is an inhomogeneous, gradually occurring process. Besides, the result of the size-dependent premelting ratio proved that the premelting phenomenon is less pronounced in small AuNRs than in large ones.

Author details

Rida Essajai
Group of Semiconductors and Environmental Sensor Technologies- Energy
Research Center, Faculty of Science, Mohammed V University, Rabat, Morocco

*Address all correspondence to: rida.essajai@gmail.com

IntechOpen

References

[1] Yu-Ying Y, Chang S-S, Lee C-L, Chris Wang CR. Glod nanorods: Electrochemical synthesis and optical properties. The Journal of Physical Chemistry. B. 1997;**101**(34):6661-6664

[2] Hu H, Reven L, Rey A. First-principles density functional theory (DFT) study of glod nanorod and its interaction with alkanethiol ligands. The Journal of Physical Chemistry. B. 2013; **117**:12625-12631

[3] Huang X, Neretina S, El-Sayed MA. Glod nanorods: From synthesis and properties to biological and biomedical applications. Advanced Materials. 2009; **21**:4880-4910

[4] Murphy CJ, Gole AM, Stone JW, Sisco PN, Alkilany AM, Goldsmith EC, et al. Gold nanoparticles in biology: Beyond toxicity to cellular imaging. Accounts of Chemical Research. 2008; **41**:1721-1730

[5] Qiu Y, Liu Y, Wang L, Xu L, Bai R, Ji Y, et al. Surface chemistry and aspect ratio mediated cellular uptake of Au nanorods. Biomaterials. 2010;**31**: 7606-7619

[6] Huang X, El-Sayed IH, Qian W, El-Sayed MA. Cancer cells assemble and align glod nanorods conjugated to antibodies to produce highly enhanced, sharp, and polarized surface Raman spectra: A potential cancer diagnostic marker. Nano Letters. 2007;**7**:1591-1597

[7] Durr NJ, Larson T, Smith DK, Korgel BA, Sokolov K, Ben-Yakar A. Two-photon luminescence imaging of cancer cells using molecularly targeted glod nanorods. Nano Letters. 2007;**7**: 941-945

[8] Huff TB, Tong L, Zhao Y, Hansen MN, Cheng JX, Wei A. Hyperthermic TEMPeffects of gold nanorods on tumor cells. Nanomedicine. 2007;**2**:125-132

[9] Milette J, Toader V, Reven L, Lennox RB. Tuning the miscibility of gold nanoparticlesdispersed in liquid crystals *via* the thiol-for-DMAPreaction. Journal of Materials Chemistry. 2011;**21**: 9043-9050

[10] Liao Q, Mu C, Xu DS, Ai XC, Yao JN, Zhang JP. Glod nanorod arrays with good reproducibility for high-performance surface-enhanced Raman scattering. Langmuir. 2009;**25**: 4708-4714

[11] Singh AK, Senapati D, Wang S, Griffin J, Neely A, Candice P, et al. Gold nanorod based selective identification of *Escherichia coli* bacteria using two-photon Rayleigh scattering spectroscopy. ACS Nano. 2009;**3**: 1906-1912

[12] Nappa J, Revillod G, Abid JP, Russier-Antoine I, Jonin C, Benichou E, et al. Hyper-Rayleigh scattering of gold nanorods and their relationship with linear assemblies of gold nanospheres. Faraday Discussions. 2004;**269**:935-939

[13] Durr NJ, Ericson MB, Ben-Yakar A. Multiphoton luminescence from gold nanoparticles as a potential diagnostic tool for early cancer detection. In: Herold KE, Rasooly A, editors. Biosensors and Molecular Technologies for Cancer Diagnostics. Oxford: Taylor & Francis; 2012. pp. 307-322. DOI: 10.1080/00107514.2013.766641.ch17

[14] Oldenburg L, Hansen MN, Zweifel DA, Wei A, Boppart SA. Plasmon-resonant gold nanorods as low backscattering albedo contrast agents. Optics Express. 2006;**14**:6724-6738

[15] Service RF. Breakthrough of the year. Molecules get wired. Science. 2001;**294**:2442

[16] Jeon J, Park S, Lee BJ. Optical property of blended plasmonic

nanofluid based on glod nanorods. Optics Express. 2014;**22**:1101-1111

[17] Fang K-C, Weng C-I, Ju S-P. An investigation into the structural features and thermal conductivity of silicon na noparticles using molecular dynamics simulations. Nanotechnology. 2006;**17**: 3909-3914

[18] Nanda KK, Sahu SN, Behera SN. Liquid-drop model for the size-dependent melting of low-dimensional systems. Physical Review A. 2002;**66**: 013208

[19] Shi FG. Size dependent thermal vibrations and melting in nanocrystals. Journal of Materials Research. 1994;**9**: 1307-1313

[20] LAMMPS Users Manual 30. Sandia National Laboratories; 2 Oct 2014

[21] Stukowski A. Visualization and analysis of atomistic simulation data with OVITO–the open visualization tool. Modelling and Simulation in Materials Science and Engineering. 2010;**18**:015012

[22] Daw MS, Baskes MI. Embedded-atom method: Derivation and application to impurities, surfaces, and other defects in metals. Physical Review B. 1984;**29**:6443

[23] Essajai R, Hassanain N. Molecular dynamics study of melting properties of gold nanorods. Journal of Molecular Liquids. 2018;**261**:402-410

[24] Essajai R, Rachadi A, Feddi E, Hassanain N. MD simulation-based study on the thermodynamic, structural and liquid properties of gold nanostructures. Materials Chemistry and Physics. 2018;**218**:116-112

[25] Erko S. Physica E. 2000;**8**:210-218

[26] Qi W. Nanoscopic thermodynamics. Accounts of Chemical Research. 2016; **49**(9):1587-1595

[27] Grochola G, Russo SP, Snook IK. On fitting a gold embedded atom method potential using the force matching method. The Journal of Chemical Physics. 2005;**123**:204719

[28] Bagrets A, Werner R, Evers F, Schneider G, Schooss D, Wölfle P. Lowering of surface melting temperature in atomic clusters wif a nearly closed shell structure. Physical Review B. 2010;**81**:075435

[29] Kart HH, Yildirim H, Ozdemir KS, Cagin T. Physical properties of Cu nanoparticles: A molecular dynamics study. Materials Chemistry and Physics. 2014;**15**:204-212

[30] Yang Z, Yang X, Xu Z. Molecular dynamics simulation of the melting behavior of Pt−Au nanoparticles with core−shell structure. Journal of Physical Chemistry C. 2008;**112**:4937-4947

[31] Kittel C. Introduction to Solid State Physics. 5th ed. New York: Wiley; 1976

[32] Wu L, Zhang Y, Wen Y-H, Zhu Z-Z, Sun S-G. Molecular dynamics investigation of structural evolution of fcc Fe nanoparticles under heating process. Chemical Physics Letters. 2011; **502**:207-210

[33] Stukowski A. Structure identification methods for atomistic simulations of crystalline materials. Modelling and Simulation in Materials Science and Engineering. 2012;**20**:45021

[34] Huang WJ, Sun R, Tao J, Menard LD, Nuzzo RG, Zuo JM. Coordination-dependent surface atomic contraction in nanocrystals revealed by coherent diffraction. Nature Materials. 2008;**7**:308

[35] Qi W, Huang B, Wang M. Structure of unsupported small palladium nanoparticles. Nanoscale Research Letters. **4**(3):269-273

[36] Shim J-H, Lee B-J, Cho YW. Thermal stability of unsupported glod nanoparticle: a molecular dynamics study. Surface Science. 2002;**512**: 262-268

[37] Qi WH. Size TEMPeffect on melting temperature of nanosolids. Physica B. 2005;**368**:46-50

[38] Buffat Ph, Borel J-P. Size effect on the melting temperature of gold particles. Physical Review A. 1976;**13**: 2287

Nanostructure Technology for EO/IR Detector Applications

Ashok K. Sood, John W. Zeller, Gopal G. Pethuraja,
Roger E. Welser, Nibir K. Dhar
and Priyalal S. Wijewarnasuriya

Abstract

This chapter covers recent advances in the development of nanostructure-based material technologies to benefit next-generation electro-optical (EO) and infrared (IR) sensor and imager applications. Nanostructured materials can now be integrated into a variety of technological platforms, offering novel optoelectrical properties that greatly enhance device performance in many practical applications. Use of novel carbon nanotube (CNT) based materials has enabled new approaches for applying nanostructure design methodologies that can offer enhanced performance for low-cost bolometers for IR detection and imaging applications. We will discuss the development of carbon nanostructure based infrared detectors and arrays, including concepts that will provide high performance, high frame rate, and uncooled microbolometers for mid-wave infrared (MWIR) and long-wave infrared (LWIR) band detection. In addition, nanostructured antireflection (AR) coatings are being developed that significantly enhance transmission over a broad spectrum, providing substantial improvements in device performance compared to conventional thin film AR coatings. These nanostructured AR coatings have been demonstrated over visible to LWIR spectral bands on various substrates. In this chapter, we discuss both theoretical and measured results of these diverse nanostructure technologies to advance sensing performance over a wide range of spectral bands for defense, space, and commercial applications.

Keywords: sensors, detectors, infrared, electro-optical, carbon nanotubes nanostructures, antireflection coatings

1. Introduction

Nanostructures come in many different physical forms having varied and diverse optoelectronic properties that enable them to benefit many different applications, of which electro-optic/infrared (EO/IR) detectors and systems may be considered in the forefront. Rapid advances in these technologies that have recently taken place are enabling the development of more capable sensing and imaging systems and subsystems with notable improvements in performance. Such nanostructure-based devices and systems operating from the visible to long-wave infrared (LWIR) portions of the electromagnetic spectrum have been and continue to be developed for use in a variety of defense and commercial applications [1, 2].

Detectors and imaging arrays operating over the visible spectrum (~400–700 nm) are mostly Si-based, consisting of charge-coupled device (CCD) imagers and complementary metal oxide semiconductor (CMOS) technologies. For detection of infrared (IR) wavelengths invisible to the human eye, which span the range of approximately 1.0 μm in the near-infrared (NIR) to beyond 30 μm, other materials and technologies are required [3].

The IR spectrum is categorized based primarily on the spectral locations of atmospheric transmission windows (**Figure 1**). IR radiation falling within these bands can generally be transmitted and/or received with relatively low attenuation. The NIR and short-wave infrared (SWIR) bands (~0.8–2.5 μm) like the visible mostly involve reflected light, for which materials including InGaAs, InP, and Ge are used for detection and imaging. For the mid-wave infrared (MWIR: 3–5 μm) and LWIR (8–14 μm) wavebands, which conversely involve detection of objects emitting thermal radiation, HgCdTe and InSb based focal plane arrays (FPAs), strained-layer superlattice (SLS) structures, and microbolometers (e.g., Si-MEMS devices) have been and are being utilized [4].

Uncooled microbolometers used as detectors in thermal cameras have traditionally been based on silicon as well as vanadium oxide material deposited on silicon. However, the use of novel carbon nanotube-based detector elements in IR microbolometer pixels is attractive due to the potential for high electron mobilities and high temperature sensitivity [5]. Carbon nanotubes (CNTs) basically comprise hexagonal sheets of graphene, a material with enhanced electrical capabilities, rolled into cylinders that exhibit exceptional conductivity and strength [6].

In following sections of this chapter, we discuss integration of CNTs in detector elements for next-generation high performance, high frame rate, and uncooled bolometer arrays that can provide enhanced sensitivity for MWIR and LWIR band detection and imaging [7, 8].

Sensors and detector arrays generally comprise semiconductor materials characterized by high refractive indexes, which results in significant optical reflection from the top surface that reduces light throughput into and thus light absorbed by the detector. To address this, nanostructured antireflection (AR) coatings have been developed to reduce unwanted reflections and increase the transmission of light from visible to LWIR wavelengths, thereby improving detector performance [9, 10].
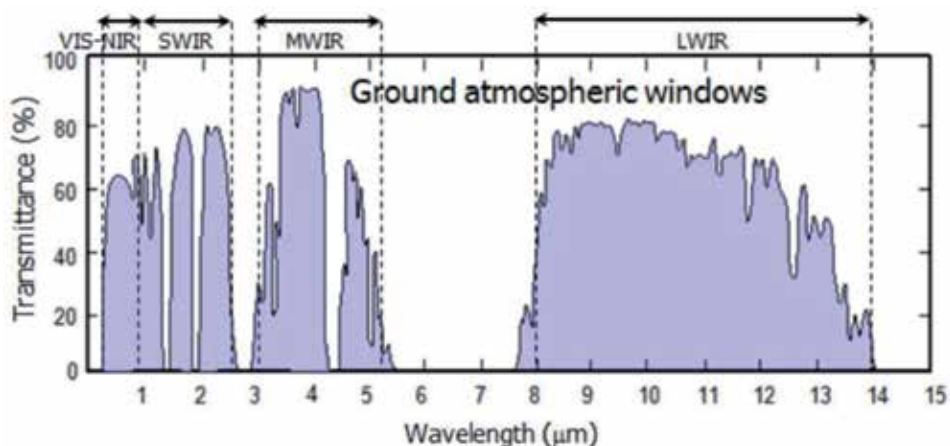
Figure 1.
IR spectral band atmospheric windows [3].

We likewise discuss in this chapter the growth processes, performance, and device applications of these advanced nanostructured AR coatings capable of minimizing reflection losses over a wide range of wavelengths and incident angles.

2. Carbon nanotube-based microbolometers for IR imaging

2.1 Properties and applications of carbon nanotubes

Graphene is a two-dimensional analogue of carbon-based graphite material that has exceptional electrical characteristics, e.g., mobilities up to 15,000–200,000 cm^2/Vs, derived from the bonding characteristics of the carbon sheets [5].

There are multiple pathways for creating graphene sheets, which include: exfoliation, unzipping through etching, growth from sublimation, and epitaxial growth from a catalyst layer [11]. The absence of a band gap in graphene limits voltage and power gains that may be achieved through operation of a device in the saturation regime. To overcome this, several doping strategies as shown in **Figure 2** have been proposed and tested, including: electrostatic doping, chemical doping, and stress or geometry restricted doping by breaking the graphene periodicity [5, 11]. Since it can be doped electrostatically, graphene provides a useful solution for certain electronic applications such the channels in field effect transistors (FETs) [12].

Carbon nanotubes (CNTs), which like graphene are allotropes of carbon, may be considered formed of hexagonal sheets of graphene rolled into cylinders (**Figure 3**). CNTs exhibit bandgaps in the range of zero to ~2 eV, and demonstrate metallic or semiconducting behavior depending mainly on their diameter and orientation of the hexagonal graphene structure along the axis of the tube (armchair, zigzag, or
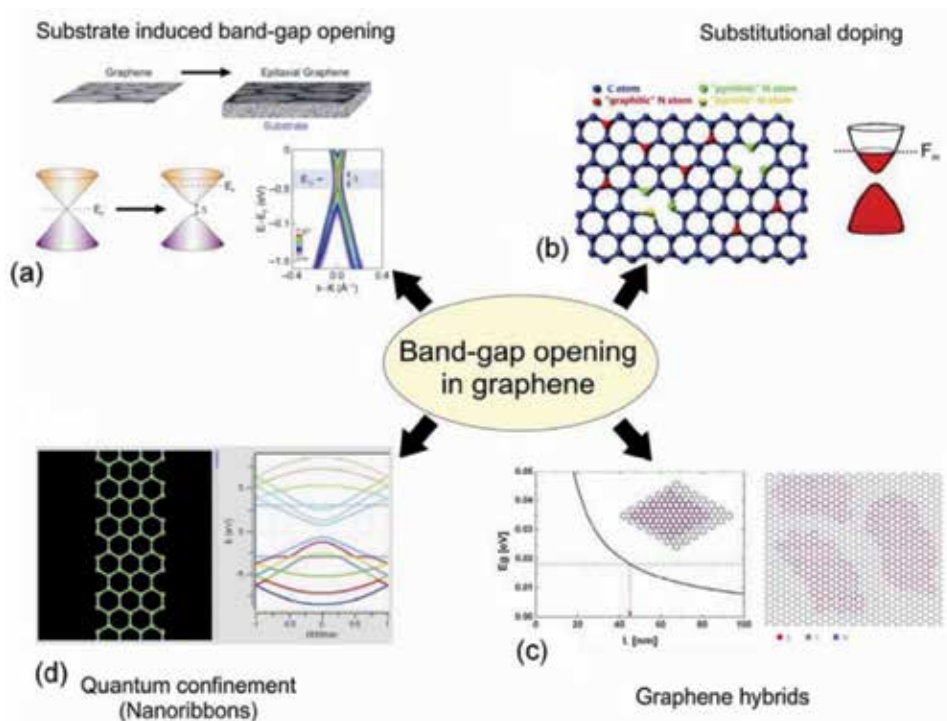
Figure 2.
Diagram showing multiple mechanisms for inducing a band gap in graphene [5, 11].
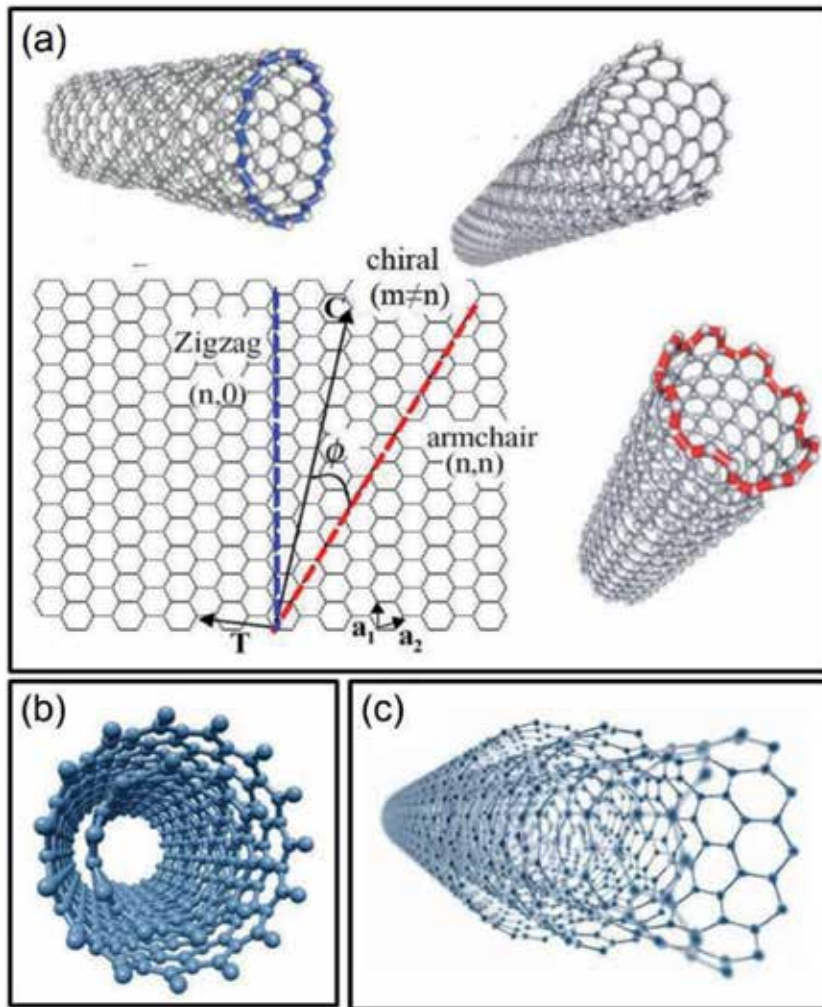
Figure 3.
Structural models of carbon nanotubes categorized based on the number of walls. (a) SWCNTs structures based on their chirality (zigzag, armchair, and chiral). (b) Structure of MWCNTs made up of two concentric shells. (c) MWCNTs composed of many overlapping shells [13].

chiral) as illustrated in **Figure 3(a)** [13]. CNTs can exhibit exceptional conductivity, and as a result have found application in nanoscale FETs that have enabled novel devices including intermolecular logic gates [5].

CNTs fall under two main categories: single-walled carbon nanotubes (SWCNTs), like those shown in **Figure 3(a)**, and multiwalled carbon nanotubes (MWCNTs), depicted in **Figure 3(b)** and **(c)** [14]. As their names suggest, SWCNTs comprise single sheets of graphene for the outer walls, while MWCNTs are composed of multiple overlapping sheets of graphene rolled up in cylindrical forms. The lengths of SWCNTs are usually in the 50–300 nm range (though up to centimeter lengths are possible) with typical diameters of 1–2 nm, while diameters of MWCNTs can exceed 100 nm [13].

2.2 Designing optimal microbolometer elements with CNTs

The novel application we are considering involves using CNT materials in the design of bolometer elements for MWIR and LWIR band detection and imaging.

These pixel elements are fabricated above the CMOS readout circuit unit cells. The focus will be on the development of relatively small (5–10 μm) bolometer unit cells with enhanced temperature coefficients of resistance (TCRs) and frequency response in the 1–10 kHz range. The feasibility of such arrays makes possible a significant number of defense and commercial applications involving uncooled IR detection and imaging.

2.2.1 Photon- vs. thermal-based detectors

Detectors of IR radiation can be generally separated into two distinct categories: photon-based and thermal-based detectors [15, 16]. Photon-based detectors involve the absorption of incident photons as governed by the bandgap of the detector material, where the absorbed photons create electron-hole pairs that produce a photocurrent. Photon detectors may be further classified as p-n junction detectors, avalanche photodiodes, photoconductors, and Schottky diodes. Photon-based IR absorbers have a fast absorption response, but typically require cooling due to thermal effects.

Thermal-based IR detectors, though normally characterized by a much slower absorption response, commonly operate at room temperature and typically have higher responsivities at longer (e.g., IR band) wavelengths [15]. In such devices, the absorption of incident IR radiation raises the temperature of the material. In pyrometers, this is achieved through changes in electrical polarization, while in bolometers by changes in the resistance of the absorbing material. Through incorporating CNT absorbing material into bolometer pixel elements these temperature-based resistance changes may be further enhanced, thereby enabling improved detection and imaging capabilities.

2.2.2 Temperature coefficient of resistance

The temperature that a bolometer pixel reaches after exposure to IR radiation can be determined by measuring its electrical resistance. This in turn may be achieved by comparing this resistance to a lookup table, or by using knowledge of the temperature coefficient of resistance (TCR). A large TCR, which corresponds to a higher thermal resistance that results in a larger rise in temperature, is desirable for achieving greater temperature resolution.

The TCR of a material is defined as the change in electrical resistance per degree Kelvin divided by the absolute electrical resistance measured at the quiescent point:

$$TCR = \frac{1}{R_e}\frac{dR_e}{dT} \tag{1}$$

The electrical resistance of a pixel after it reaches a temperature ΔT above its ambient becomes:

$$R_e(T) = R_e(T_0)(1 + TCR) \tag{2}$$

From this relationship, the pixel temperature may be calculated.

2.2.3 CNTs as bolometric elements

Microbolometers are specific types of bolometers used as detectors in thermal cameras that have traditionally been based on vanadium oxide (VOx) or amorphous

silicon material on silicon. Using carbon-based CNT detector elements in IR microbolometer pixels is attractive due to their high mobility, large thermal resistance, and intrinsically high TCR values [4]. The high thermal conductivity, high strength, and other optical and electrical properties of CNTs that can be varied over a wide spectral range likewise contribute towards their usefulness in this application.

The low electrical resistance and corresponding high conductivity of CNTs are mainly attributed to electrons tunneling between adjacent nanotubes and corresponding unimpeded flow of electrical current. The tunnel barrier height between the CNTs directly impacts the amount of heating that takes place for a given electric field. Assuming that electrons can transport across it, this barrier is governed by Fowler-Nordheim-type tunneling or thermionic emission. The expected associated TCR values can be calculated using the following expression:

$$I = q \int_0^\infty T_t(E)v(E)DOS(E)f(E,T)dE \qquad (3)$$

where T_t, v, DOS, and f are the transmission coefficient, thermal velocity, density of states, and distribution function, respectively, for electrons in the CNT. We have performed this calculation of TCR and current as a function of barrier height and electric field, and these results are shown in **Figure 4** [16].

The theoretical TCR values for a CNT film are plotted in **Figure 4(a)** as a function of the electric field between the nanotubes and the barrier height. The calculations predict a comparatively very large TCR, which can be attributed to the relatively large barrier height between adjacent SWCNTs. If a relatively low barrier height on the order of 0.06 eV is assumed, then a TCR of approximately 2.5% is obtained. It is noted that a TCR of this magnitude is associated with very low output currents. **Figure 4(b)** shows the plotted bolometer current density as a function of barrier height and electric field.

Research on this CNT absorber material has provided proof-of-principle demonstrations of extraordinary TCRs in devices [7]. Within the temperature region where the composite material undergoes a volume phase transition, considerable changes in resistance are observed. Negative TCRs of magnitude larger than −10%/°C were determined, and other composite structures with thinner suspended
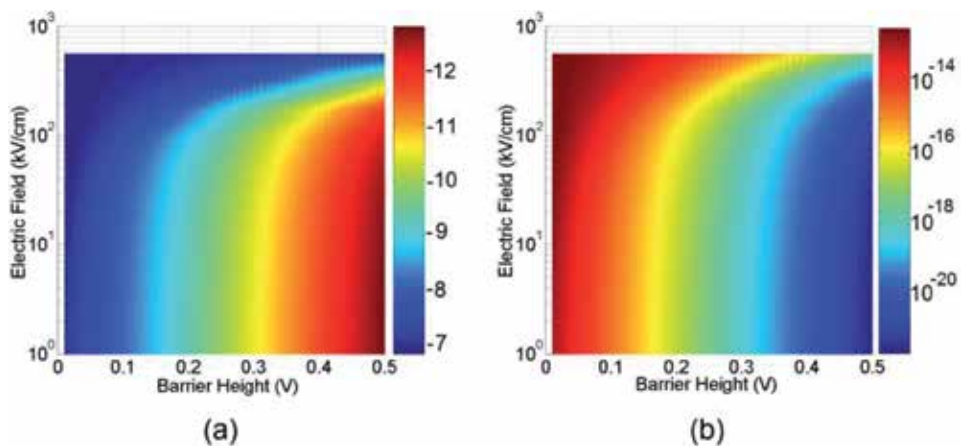
Figure 4.
(a) Contour plot of TCR vs. electric field and barrier height between SWCNTs of the film (color bar scale in units of %TCR); (b) bolometer current as a function of electric field and barrier height (color bars scale in units of amperes) [16].

films achieved TCRs in excess of −50%/°C. Such high TCR values enable up to a threefold enhancement in detector responsivity.

2.3 Model for CNT-based IR bolometers

This section includes an assessment of the design of bolometer elements using carbon nanotubes as both the IR absorbing material and electrical response material [14]. The aim is to first determine the thermal response of the bolometer absorber, and then establish how the electrical characteristics of the CNT material are altered by changes in temperature following IR absorption. Here the focus is on an absorbing material composed of a CNT film comprising randomly situated CNTs each of 2 nm thickness.

2.3.1 Heat flow equation

To determine the temperature of the material in the presence of IR radiation, we start with the heat flow equation. This partial differential equation relates the time rate of change in temperature to the position and the rate of net heat that is absorbed by the material as a function of time and position:

$$C_v \frac{\partial T}{\partial t} = \kappa \nabla^2 T + H_{net} \qquad (4)$$

where C_v is the thermal capacitance (J/K cm^3), κ is the thermal diffusion coefficient (W/K cm), and H_{net} is the net power absorbed by the material (W/cm^3). To solve this equation for the CNT bolometer, we must first determine C_v and κ for the CNT and CNT film.

2.3.2 Thermal capacitance of CNT absorber

To determine the heat capacity of a carbon nanotube, we first determine the internal vibrational energy of the CNT, and then take the derivative with respect to temperature. The internal energy is found by calculating the energy of each vibrational mode, multiplying by the probability that the mode is populated using Bose-Einstein statistics, and then summing over all the allowed modes.

Since the number of allowed modes is dependent on the diameter and wrapping angle of the CNTs, we must take a statistical sample. After multiplying the heat capacity of the individual CNTs by the number of CNTs in the film to provide a reasonable value for the heat capacity of the film, and inserting numerical values for physical constants, we arrive at the following average numerical value for the thermal capacity of a CNT:

$$C_{vt} \approx 1.4 \times 10^{-18} L d \qquad (5)$$

where L is the CNT length in microns and d is the CNT diameter in nanometers.

2.3.3 CNT thermal diffusion coefficient

In addition to the thermal capacitance, we need to determine the thermal diffusion coefficient and then the thermal resistance of a single CNT. Experiments on isolated CNTs have involved fitting the coefficient of thermal diffusion to data, obtaining the following expression [16]:

$$\kappa(L, T) = \left[3.7 \times 10^{-7} T + 9.7 \times 10^{-10} T^2 + \frac{9.3}{T^2}\left(1 + \frac{0.5}{L}\right)\right]^{-1} \tag{6}$$

From κ we can obtain the thermal resistance R_T of a single CNT using the following definition:

$$R_T = \frac{4L}{\kappa \pi d^2} \tag{7}$$

Using typical values for a CNT gives the following numerical value for its thermal resistance:

$$R_T \approx 5 \times 10^8 (L/d^2) \tag{8}$$

where R_T is in units of K/W. Thus, a CNT that is 1 μm long and 1 nm in diameter will have a thermal resistance of ~5 × 10^8 K/W.

2.3.4 Net IR radiation power absorbed

Now that the thermal diffusion and capacitance are known, to begin solving the above heat flow equation in order to determine the bolometer temperature we first need to determine the net IR power absorbed by the bolometer, H_{net}. This parameter can be established using the Stefan-Boltzmann law for blackbody radiation, which relates the net power absorbed to the temperatures of the subject and of the bolometer using the following expression:

$$H_{net} = \sigma A \varepsilon \left(T_{obj}^4 - T_b^4\right) \tag{9}$$

where σ, A, ε, T_{obj} and T_b are the Stefan-Boltzmann constant, cross-sectional area, emissivity, object of interest temperature, and bolometer absorber temperature, respectively. **Figure 5** shows the net IR power absorbed by the absorber material as a function of bolometer temperature for objects radiating at 20.0°C and
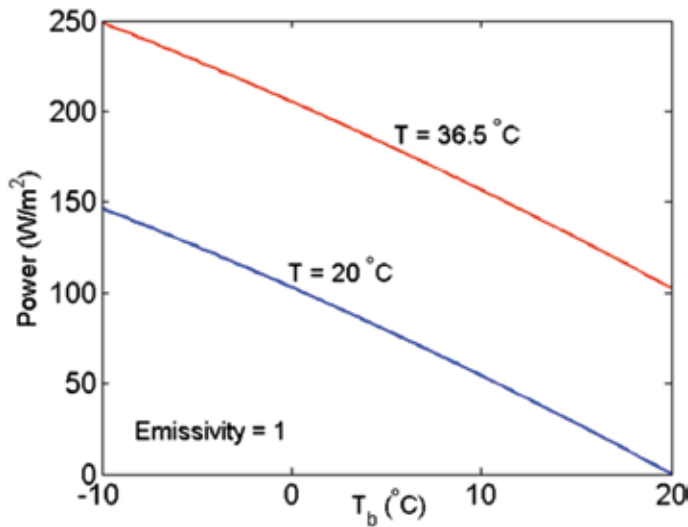
Figure 5.
Net power received by bolometer as a function of bolometer temperature [16].

36.5°C [16]. Cooling the bolometer down to 30°C below room temperature enables significantly more power to be absorbed, which can lead to a much stronger signal.

2.3.5 Calculating the bolometer temperature distribution

Using the above expressions for C_{vt}, κ, and H_{net}, we can convert the heat flow equation above into a thermal network like that illustrated in **Figure 6** [14]. Each resistor in the figure represents the thermal resistance of the CNTs in series with the thermal resistance between adjacent CNTs. The capacitors represent the thermal capacity of the individual CNTs, while the current sources represent the net IR radiation absorbed by each CNT.

This thermal network contains thousands of nodes, where there is a specific equation relating the thermal resistance, capacitance, and net power for each node. This system of equations can be solved to determine the temperature as a function of position and time throughout the bolometer absorber.

The output data from these calculations are shown plotted in **Figure 7** for different CNT network types [16]. Here, we assume the pixel tightly packed with CNTs and H_{net} of 1 nW. Two different thermal resistance values were modeled for the nanotubes: 5×10^8 K/W and 1×10^9 K/W, shown in **Figure 7(a)** and **(b)**, respectively.

As expected, a higher thermal resistance results in a greater temperature difference from the ambient. We note that in general the thermal resistance also rises with increasing temperature, resulting in further heating of hot spots. The color-mapped temperature gradients of the contact legs that connect the film to the readout integrated circuit (ROIC) can be clearly seen in **Figure 7**.

2.4 CNT-based microbolometer pixels

Networks of SWCNTs are considered as potential replacements for VOx and amorphous silicon in uncooled microbolometer-based infrared focal plane arrays
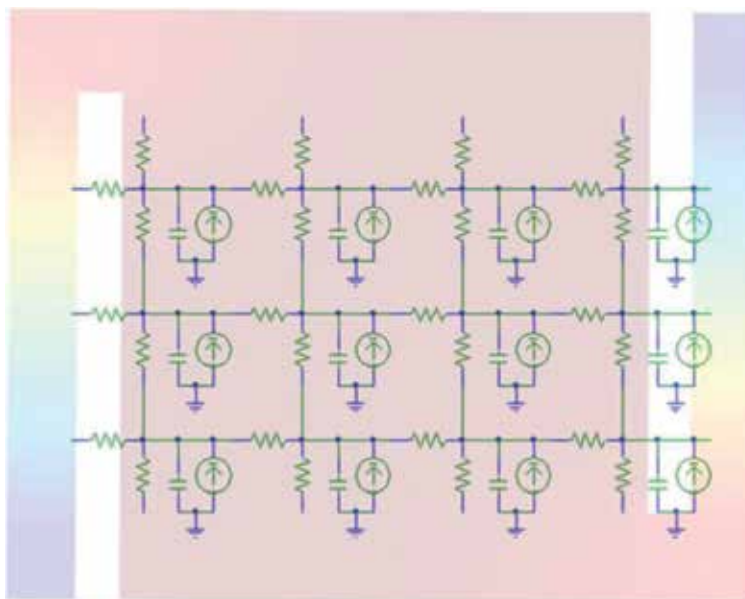
Figure 6.
Schematic of superimposed thermal network for calculating temperature map of CNT-based bolometer absorber [14].
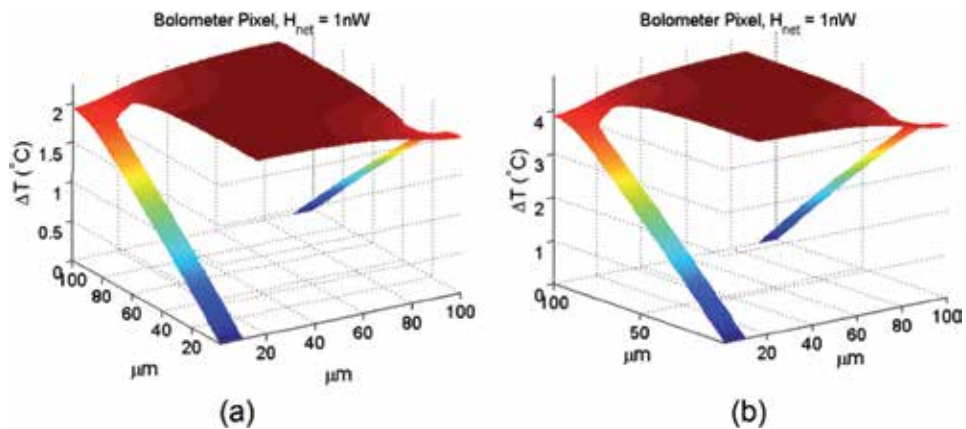
Figure 7.
Temperature map of bolometer pixel when net absorbed power H_{net} is 1 nW, and CNT thermal resistance is (a) 5×10^8 K/W and (b) 1×10^9 K/W. The pixel is assumed to be tightly packed with CNTs [16].
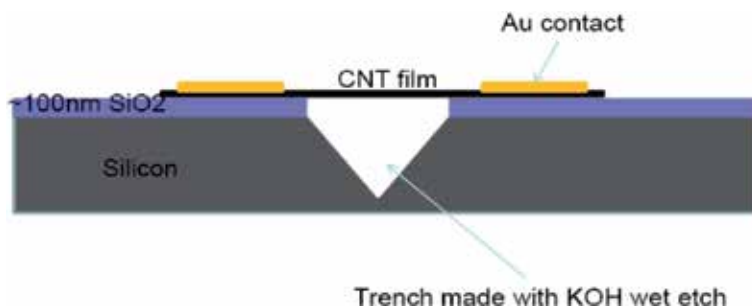
Figure 8.
CNT bolometer test fixture to evaluate CNT film quality [14].

(IRFPAs). These SWCNT-based microbolometer pixels can be fabricated on top of the CMOS readout circuit unit cell. Several potential benefits of SWCNTs over existing state-of-the-art films include low thermal mass, high absorption coefficients in the IR, and TCRs greater than 4%/K.

Another benefit of utilizing SWCNTs involves their compatibility with CMOS wafer processes, which can enable cost-effective manufacturing for uncooled IRFPAs. SWCNTs suspended in either aqueous solutions or other solvents may be applied uniformly to a silicon wafer using standard wafer fabrication equipment. Once this process is optimized, the back end of line (BEOL) standard CMOS process can be modified to continue processing SWCNT microbolometers.

The adaption of SWCNTs to CMOS process technologies has demonstrated the potential for very small pixel sizes with sufficient yields [13]. In addition, there is evidence that unlike devices using VOx and amorphous Si, SWCNT-based microbolometers are not limited in performance due to the $1/f$ noise floor [14].

Optimization of the growth of SWCNTs and MWCNTs has been performed. Grown CNTs have been shown to be easily separable from the growth substrate. Good length/diameter uniformity has also been demonstrated. **Figure 8** shows the fixture used to evaluate the CNT films for bolometric applications [14]. This fixture was employed for evaluation of the optoelectronic characteristics of the CNT samples.

In addition, preliminary TCR measurements have been carried out with CNT materials, examples of which are shown in **Figure 9**. **Figure 9(a)** shows a scanning

electron microscopy (SEM) image of representative MWCNT films in unsuspended and suspended forms, respectively [17]. Unlike their SWCNT counterparts, the MWCNT films leave substantial portions of the substrate uncovered. In addition, some minor recess deformation is visible on the suspended MWCNT films, which are in the same thickness range as the SWCNT films.

In **Figure 9(b)**, a transmission electron microscopy (TEM) image of an individual representative MWCNT is shown. This MWCNT has a large hollow center ~10 nm in diameter and contains approximately 40–50 shells. **Figure 9(c)** presents the dense "forest-like" growth of oriented MWCNTs with good length/diameter uniformity [16]. Here the CNT growth is easily distinguishable from the substrate.

All the MWCNT films studied show semiconductive resistance-temperature (R-T) behavior characterized by the representative curve depicted in **Figure 10** [17]. It is seen that the increase in resistivity of the MWCNT films with decreasing temperature is much less than that of the SWCNT films, which is not unexpected considering the much smaller bandgap of MWCNTs. This reduced temperature dependence implies smaller absolute TCR values for the MWCNTs. For example, the absolute TCR value at room temperature for the MWCNT films is about 0.07%/K, in contrast to 0.17%/K for the SWCNT films.

Two notable differences are discernable between the MWCNT and SWCNT films: the former have significantly higher $\Delta R/R_0$ and much shorter response times compared to the latter. The $\Delta R/R_0$ for MWCNT samples is typically in the range of a few percent, which is above an order of magnitude higher than that of SWCNT films suspended in an aqueous solution and two orders of magnitude higher than that of unsuspended SWCNT films at comparable IR power.

Figure 11 compares the photoresponse R/R_0 of MWCNT films in unsuspended and suspended cases, where R_0 is the sample resistance before IR radiation was turned on and the change in the resistance ΔR caused by IR radiation is given as $R–R_0$. Physical suspension of the MWCNT films (**Figure 11(b)**) and SWCNT films (**Figure 11(d)**) leads to further improvement in R/R_0 compared to that of their unsuspended counterparts in **Figure 11(a)** and **(c)**, respectively [2]. Considering the lower absolute TCR values of MWCNTs, the much enhanced photoresponse of these MWCNT films can be attributed to the naturally suspended inner CNT shells, which may provide an ideal configuration to enhance the bolometric effect by improving light absorption and reducing thermal transfer.

Carbon nanotubes as absorbing materials in microbolometers show much promise for providing greater TCR values, and thus improved IR detection and imaging performance. Nevertheless, additional work is needed in the development, testing, and optimization of microbolometer arrays that can offer superior performance to current well-established Si- and VOx-based technologies. The other nanostructure
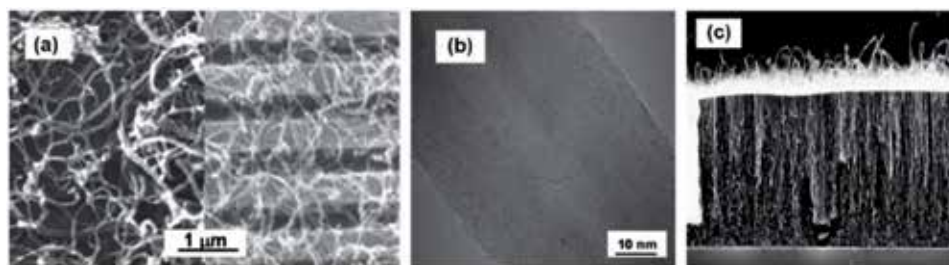
Figure 9.
(a) SEM images of unsuspended (left) and suspended (right) MWCNT films. (b) TEM image of a representative MWCNT, for which the shell number is estimated to be in the range of 40–50 [17]. (c) Dense oriented MWCNT growth [16].
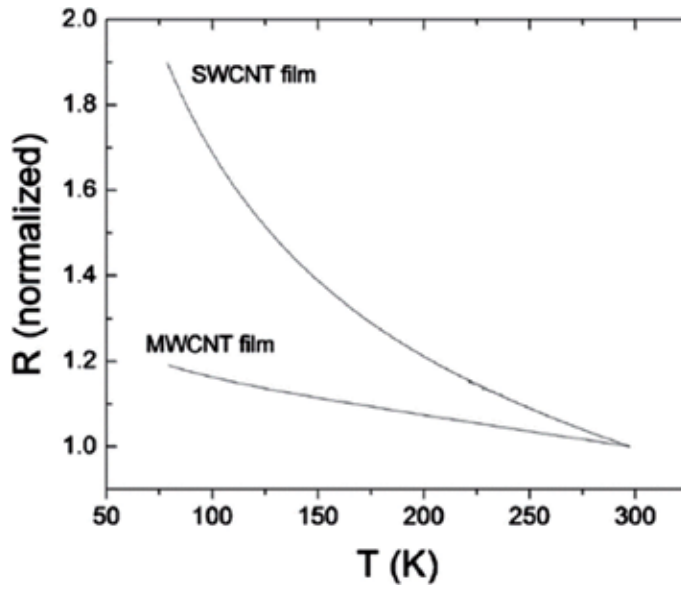
Figure 10.
Resistance vs. temperature curves for SWCNT and MWCNT films [17].
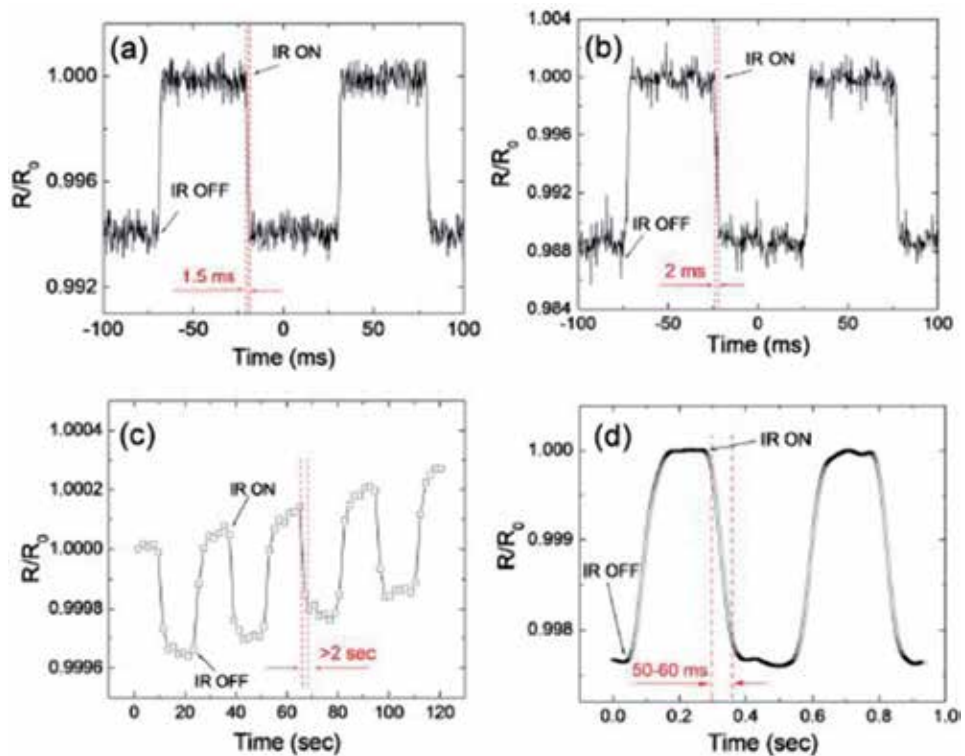
Figure 11.
Photoresponse of unsuspended and suspended CNT films. (a) Unsuspended MWCNT film (f = 10 Hz in IR, P = 3.0 mW/mm²); (b) suspended MWCNT film (f = 10 Hz in IR, P = 3.0 mW/mm²); (c) unsuspended SWCNT film (f = 1/30 Hz in IR, P = 3.5 mW/mm²); (d) suspended SWCNT film (f = 2 Hz in IR, P = 3.5 mW/mm²) [2].

technology we shall now discuss, though comprising an applied rather than a core component, has demonstrated the capability to extend and enhance the performance of a wide range of electro-optical and infrared systems and devices.

3. Nanostructured antireflection coatings for optical sensor applications

3.1 Overview of nanostructured AR coating technology

Reducing optical reflections from surfaces, which is important to many optical applications including optical lenses, windows, photovoltaic devices, and photodetectors, has commonly been achieved through coating, or texturing, the surfaces of interest. Nanostructures that minimize reflection loss have been investigated for the development of high performance antireflection (AR) coatings. Such nanostructured AR coatings having optimal index profiles can demonstrate broadband AR properties, particularly with air as the ambient medium.

Glass, a dielectric material widely used in a variety of optical applications including lenses, windows, and as a cover or encapsulation for semiconductor optoelectronic devices, is basically transparent to wavelengths longer than 400 nm. However, due to Fresnel reflection losses glass reflects about 4% of the incident light from its front surface, or ~8% from both surfaces. This undesired reflection in certain applications can degrade the efficiency of the underlying device (e.g., sensor or photovoltaic cell), reduce its signal-to-noise ratio (e.g., in the case of a photodetector), and cause glare (e.g., from electronic displays). For such applications, it is important not only to reduce reflectance but also to improve the transmittance through the surface. This requires that the coating material be nonabsorbent, and the coating surface be specular.

AR coatings have conventionally been composed of single layers having optical thicknesses equal to one quarter of the wavelength ($\lambda/4$) of interest. Ideally, such a single-layer $\lambda/4$ AR coating should have a refractive index $n_{\lambda/4}$ given by [18]:

$$n_{\lambda/4} \approx \sqrt{n_{substrate} \times n_{air}} \tag{10}$$

However, due to the unavailability of materials having the precise desired refractive index, the performance of $\lambda/4$ AR coatings often deviates from the optimum, which is especially the case for low-index substrates such as glass. For example, an ideal single-layer $\lambda/4$ AR coating on a glass surface in an air ambient would require a material with a refractive index of $(1.46)^{1/2} \approx 1.21$. Due to the unavailability of optical materials with very low ($n < 1.4$) refractive indexes, near-perfect graded-index AR coatings for glass substrates have not been practically achievable.

Recently, however, a new class of optical thin film materials consisting of tunable nanostructures has enabled the realization of very low refractive index materials [9, 19]. Using these nanostructured materials, AR coatings can greatly minimize reflection losses and enhance the sensitivity and performance of detection and imaging systems.

The multilayer AR coatings feature step-graded refractive indexes which decrease in discrete steps from that of the substrate (e.g., ~1.5 for SiO_2 or ~3.5 for Si) to a value of close to that of air (e.g., 1.18). These AR coatings with specular surfaces comprising multiple discrete layers of non-absorbing materials exploit thin film interference effects to reduce reflectance and maximize transmittance. Such discrete multilayer AR coatings, which have been shown outperform continuously-graded AR coatings, offer very effective antireflection performance [20].

Figure 12(a) shows the measured and calculated refractive index of deposited SiO$_2$ vs. deposition angle following a formula developed by Poxson et al. [20]. This plot demonstrates the potential to tune the refractive index of a given material to virtually any value between its bulk value and that of air (~1.0) through controlling the deposition angle. The SEM images in **Figure 12(b)** show the gradual decrease in density of SiO$_2$ nanocolumns transitioning from a dense bulk film deposited at an angle of 0° to a nanostructured film deposited at 75°.

3.2 Growth of nanostructured AR coating layers

The nanostructured optical layers are fabricated using a scalable physical vapor deposition (PVD) self-assembly process, which allows them to be processed on almost any type of substrate. This process involves the formation of a highly directional vapor flux, which can be implemented through melting various optical coating materials. Surface diffusion and self-shadowing effects during the growth process enable the formation of the nanostructured thin films.

As illustrated in **Figure 13**, random growth fluctuations on the substrate produce a shadow region that incident vapor flux cannot reach and a nonshadow region where incident flux deposits preferentially, creating rod-like structures with lower effective refractive indexes [21]. The deposition angle, the angle between the normal to the sample surface and the incident vapor flux, results in the formation of nanostructures tilted relative to the sample surface. This process offers advantages such as tunability of the refractive index, flexibility in choice of materials, simplicity of the growth process, and ability to optimize the coatings for any substrate-ambient material system.

Since the gaps between the nanostructures are typically much smaller than the wavelengths of visible and IR light, the nanostructured layer acts as a single homogenous film having a refractive index intermediate in value between that of the ambient air and of the nanostructure material that decreases in density with increasing gap size. Nanowires and other types of nanostructures grown by the self-assembly process provide a pathway for fabricating high-quality broadband AR coatings for a variety of nanosensor applications.
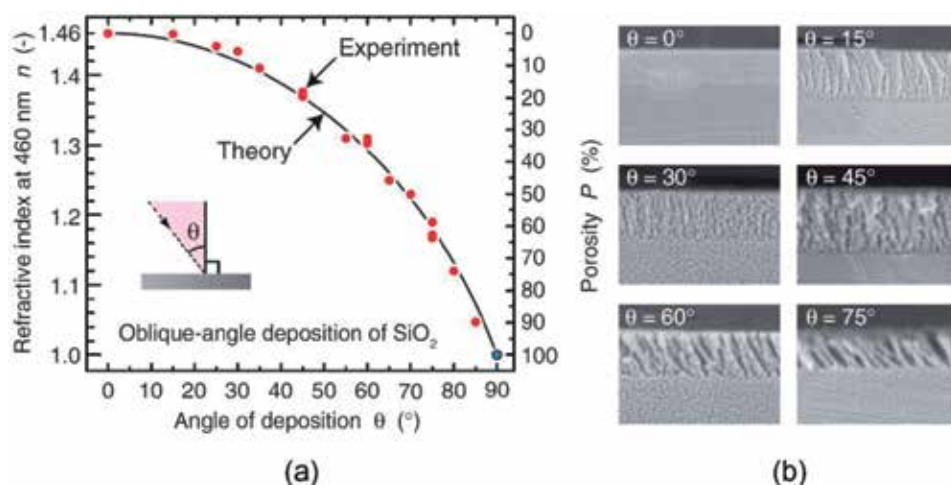
Figure 12.
(a) Refractive index of oblique-angle-deposited SiO$_2$ as a function of deposition angle. (b) SEM images showing a gradual decrease in density of SiO$_2$ nanocolumns for nanostructured AR coatings transitioning from a dense bulk film at 0° deposition angle to a nanostructured film at 75° deposition angle [20].

Figure 14 presents the measured refractive index dispersion curve as a function of wavelength from a nanostructured SiO_2 layer deposited at a highly oblique angle [22, 23]. This low-index nanostructured SiO_2 film was deposited on a Si substrate and measured by ellipsometry. Also shown is a comparison of experimental reflectivity data with theoretical calculations. These results illustrate that the nanostructures grown by the self-assembly process provide a pathway for fabricating high quality broadband AR coatings for a variety of sensing and imaging applications.

Figure 15 demonstrates the use of SiO_2 and TiO_2 nanostructures to achieve high performance, step-graded AR coatings on AlN substrates [10, 23]. In the following sections recent efforts are summarized to extend this technology to different substrates and lenses and to other bands of interest spanning the visible to the infrared for next-generation sensors.

3.3 Nanostructured AR coatings for visible EO applications

We have fabricated and tested various step-graded AR structures comprising layers of nanostructured SiO_2 using the PVD self-assembly process [17, 21, 24].
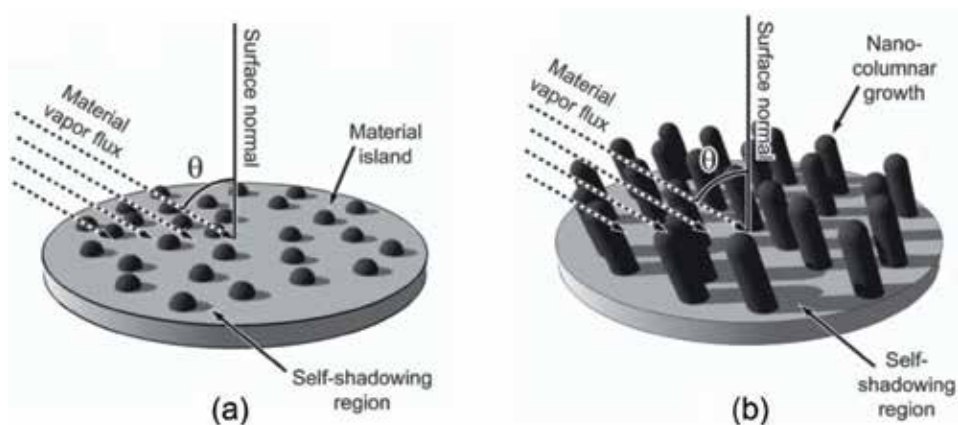
Figure 13.
(a) Schematic of self-assembly process for synthesis of nanostructured films, showing (a) initial formation of material islands at random locations across the substrate, followed by (b) formation of self-shadowed regions and nanocolumnar growth when the material vapor flux arrives at a non-normal deposition angle θ to the substrate [21].
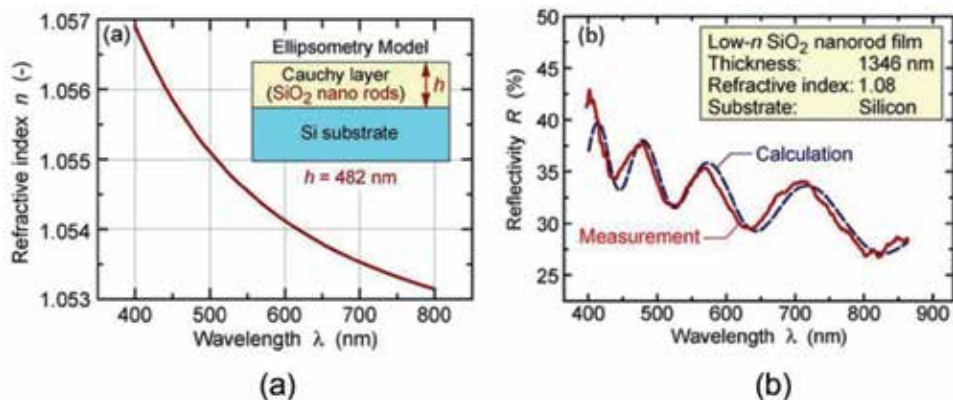
Figure 14.
(a) Refractive index dispersion curve of low-index SiO_2 nanostructure thin film on a Si substrate, with (b) comparison of the measured and calculated reflectivity spectra [22, 23].

(b) Layer No.	1	2	3	4	5
Source	TiO_2			SiO_2	
Deposition angle	25°	40°	65°	−68°	−87°
Thickness (nm)	77.4	80.2	99.3	145.0	223.0
Refractive index, n	2.03	1.97	1.67	1.27	1.05
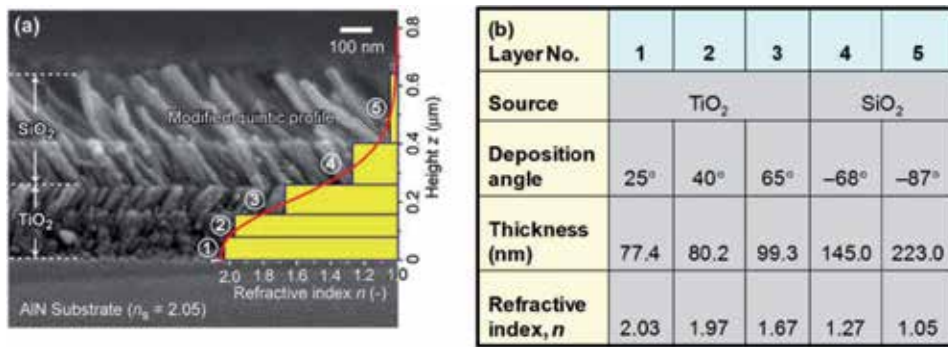
Figure 15.
(a) Cross-sectional SEM image of TiO_2 and SiO_2 step-graded index nanostructure coatings that approximate a modified quintic profile. The graded-index coating consists of three TiO_2 nanostructured layers and two SiO_2 nanostructured layers and (b) deposition angles, thicknesses, and refractive indexes for each layer in the graded index coating [10, 23].

These multilayer nanostructured AR coatings have been deposited on both sides of glass substrates, and the corresponding transmittance characterized as a function of wavelength and incident angle. The nanostructured AR coatings have likewise been successfully demonstrated on the curved surfaces of converging and diverging optical lenses, which are key components that manipulate the optical pathways in optical and infrared systems.

3.3.1 Glass substrates

Figure 16 compares the measured broadband performance of an uncoated glass slide to one coated on both sides with a multilayered, nanostructured SiO_2 coating, where the transmittance is characterized as a function of wavelength and light incidence angle [10]. The inset in **Figure 16** shows a representative cross-sectional SEM image of the two-layer structure. The nanostructured coatings were prepared in an electron beam evaporator using different deposition angles to form distinct layers with step-graded refractive index profiles.

The transmittances of the coated and uncoated glass slides were measured using an angle-dependent transmittance measurement setup consisting of a xenon lamp light source and Ando AQ6315A optical spectrum analyzer calibrated for detection of transmitted photons over the 400–800 nm wavelength range. The measured peak broadband transmittance at normal incidence of the uncoated glass slide was 92%, corresponding to ~4% reflection loss at each glass/air interface.

The peak transmittance was 98.3% for the double-sided, nanostructure-coated glass, implying an average broadband reflection loss of less than 1% at each glass/air interface. As shown in **Figure 16**, the transmittance through the nanostructured SiO_2 coated glass was also significantly higher than that through the uncoated glass across a wide range of incident angles. While the transmittance of the uncoated glass slide falls below 80% at an incident angle of 65°, the glass slide with the double-sided coating still maintains a transmittance above 95% at this angle of light incidence.

The transmittances of coated and uncoated glass slides have also been measured at normal incidence as functions of wavelength using a JASCO V-570 spectrophotometer. As shown in **Figure 17**, the average measured broadband transmittance between 350 nm and 1800 nm increases from 92.2% for the uncoated glass to 98.6% for the double-sided nanostructured coated glass [9]. This transmittance exceeds 97.8% at all wavelengths between 440 and 1800 nm, corresponding to a glass-air
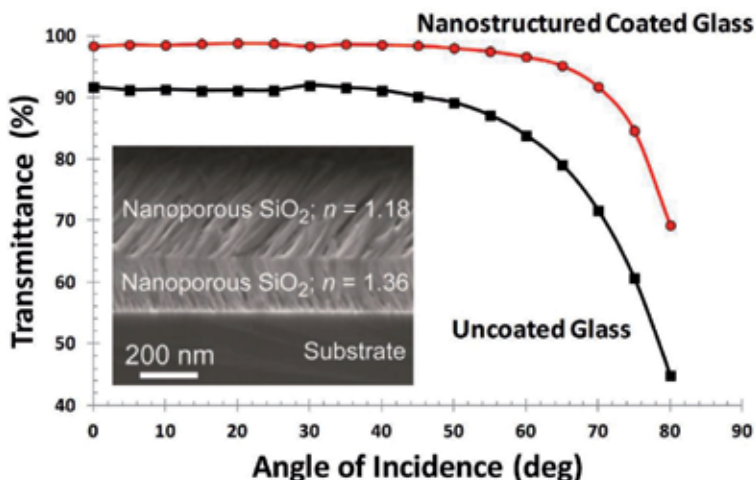
Figure 16.
Incident angle dependent broadband transmittance through glass slide coated on both sides with a step-graded, nanostructured SiO₂ AR coating, along with that for an uncoated glass slide. A representative cross-sectional SEM image of the dual-layer nanostructured coating is shown in the inset [10].
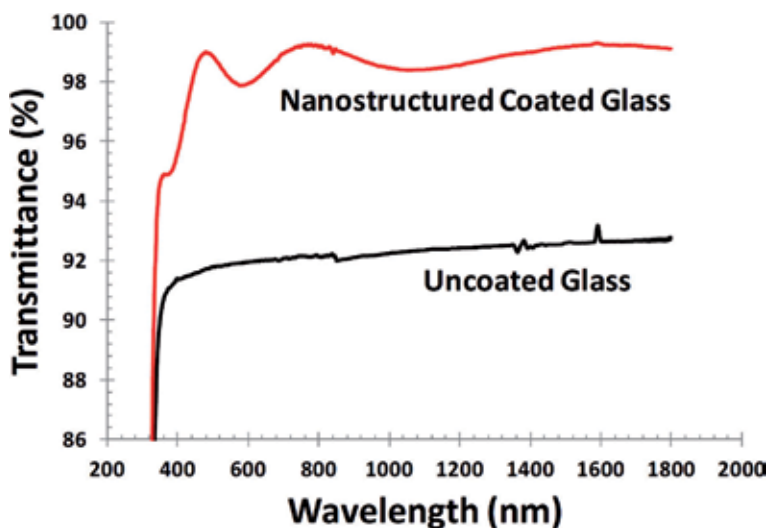
Figure 17.
Wavelength-dependent transmittance measurement of step-graded, nanostructured SiO₂ AR coating on glass substrate [9].

interface reflectivity below 1.1% over this relatively wide spectrum. These optimized nanostructured AR coatings have been shown to outperform ideal quarter-wavelength MgF$_2$ coatings over all visible wavelengths and incident angles [21].

3.3.2 Optical lenses

Light passing through an uncoated lens will suffer reflection losses at both the input and output lens interfaces. These losses add up and can limit the performance of detector devices. Demonstration of AR coatings on curved lens surfaces extends their benefits for optical system applications.

We have designed and optimized step-graded index profiles for optical lenses, as well as for ZnSe IR lenses which are covered in the following section. Multilayer

step-graded AR coating index profiles were created and optimized for glass lenses by controlling the refractive index profiles and thicknesses of the individual layers. Nanostructured SiO_2 layers of the desired refractive index were deposited on the entire surface of the optical lens by the self-assembly process. **Figure 18** compares the transmittance of uncoated and nanostructured SiO_2 multilayer AR-coated optical lenses [10].

The nanostructured AR coating significantly improves the optical transmittance through the lens from 94% to nearly 100%, which is maintained over the entire visible and majority of the NIR spectra. AR-coated lenses can thus transmit a virtually unattenuated optical signal to a sensor over a broader spectrum through eliminating unwanted reflections, enabling more effective detector devices with significantly higher responsivities. This approach can be expanded to benefit various IR components, significantly improving the detection, sensing, and imaging capabilities of electro-optical and infrared systems.

3.3.3 Flexible substrates

Broadband and high-performance AR coatings have been demonstrated on flexible substrates such as polycarbonate films. Polycarbonate is a useful material for commercial products including display filters, plastic lenses, and face shields, and is commonly utilized for defense applications as well. Polycarbonate also provides high impact resistance and has an excellent flammability rating.

Nanostructured multilayer SiO_2 AR coatings having optimized step-graded index profiles have been deposited on both sides of polycarbonate sheets. **Figure 19** compares the optical transmittance spectra of uncoated and AR-coated polycarbonate sheets [9]. The expanded transmittance spectrum over the visible (~400–800 nm) band is plotted in the inset of **Figure 19**. As seen in the inset, the uncoated polycarbonate sheet shows approximately 90% transmittance over the visible spectrum. For the AR-coated polycarbonate sheet, however, the transmittance rises to nearly 100%, and this enhancement is observed for the entire visible and part of the NIR band. Such high AR performance demonstrated over the entire visible spectrum makes the nanostructure AR coatings potentially beneficial for certain electro-optical applications including CMOS image sensors.
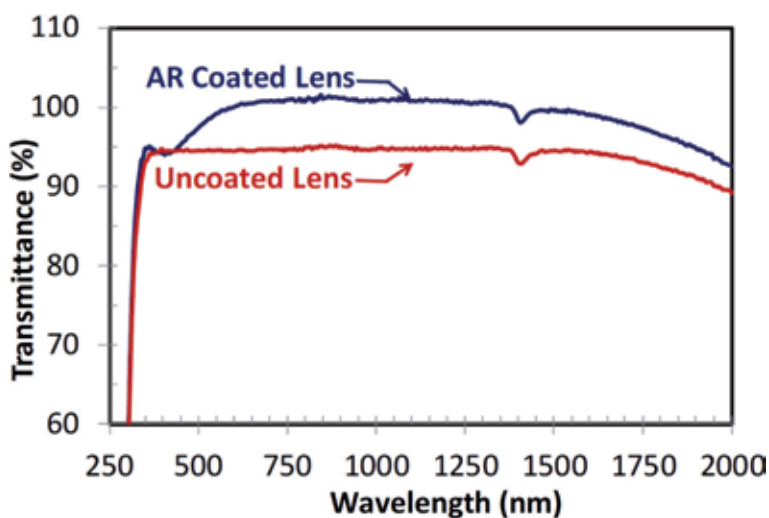
Figure 18.
Measured wavelength-dependent transmittance of nanostructured SiO_2 coated lens compared to an uncoated lens. The AR coating provides nearly 100% transmittance, which is maintained over a wide spectrum of light [10].
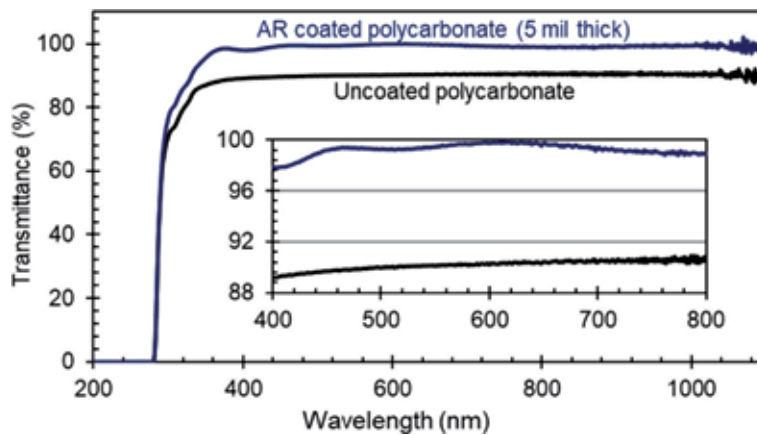
Figure 19.
Optical transmittance spectrum of transparent polycarbonate film (5 mil thickness) before and after application of nanostructured AR coating. The AR coating provides nearly 100% transmittance at 610 nm [9].

3.4 IR applications of nanostructured AR coatings

Infrared detection technology plays a critical role in various terrestrial and space applications. In order to extend the application of the AR coatings to MWIR and LWIR spectral bands, nanostructured AR coatings have been fabricated on silicon wafers by sequentially growing multiple nanostructured Si and SiO_2 layers with desired graded-index profiles through control of the deposition angle. These AR coatings minimize the reflection loss from approximately 30% to less than 1.5% over IR bands.

3.4.1 MWIR applications

The measured wavelength-dependent reflectance of multilayer AR-coated and uncoated Si substrates are shown plotted in **Figure 20** [9]. The multilayer AR coating has been synthesized with graded-index profiles optimized for the 3–5 μm MWIR band. As seen in the figure, the average measured reflectance for the multilayer AR-coated Si wafer is less than 1.5%, while the average measured reflectance for the uncoated silicon <211> wafer is ~35% over the 3–5 μm MWIR spectral band.

3.4.2 LWIR applications

The measured wavelength-dependent reflectance of an uncoated Si substrate and AR-coated Si <211> substrate having an index profile specifically designed for the 6–11 μm LWIR spectral band is plotted in **Figure 21** [25]. This dual-layer AR coating was synthesized by sequentially growing two nanostructured Si layers each at different deposition angles.

The average reflectance from 6 to 11 μm for the two-layer AR-coated Si wafer is less than 1.5%, while that of the uncoated Si <211> wafer is ~28%. These results clearly demonstrate that the multilayer AR coating significantly minimizes incident IR signal losses over the LWIR band.

Infrared optical components such as windows and lenses typically reflect a significant portion of the incoming IR signal to be detected. The incorporation of AR coatings on these IR components can greatly enhance overall system performance. We have demonstrated the nanostructured AR coatings on various components for improved IR performance, including ZnSe lenses for LWIR applications.
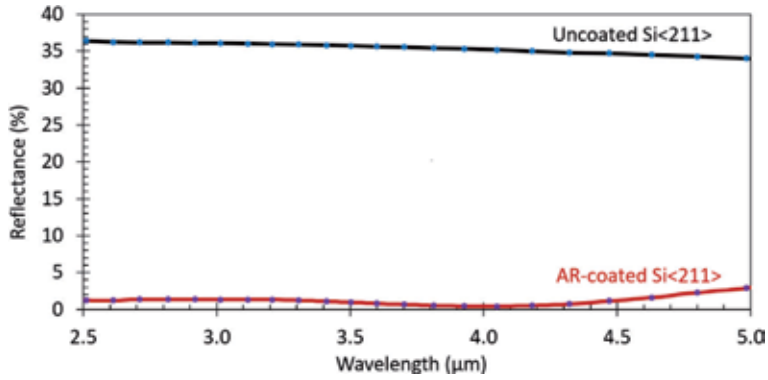
Figure 20.
Measured wavelength-dependent reflectance of multilayer AR-coated and uncoated Si <211> wafers. The multilayer AR coating on Si <211> wafers offers significantly lower reflectance over the 3–5 μm MWIR spectral band [9].
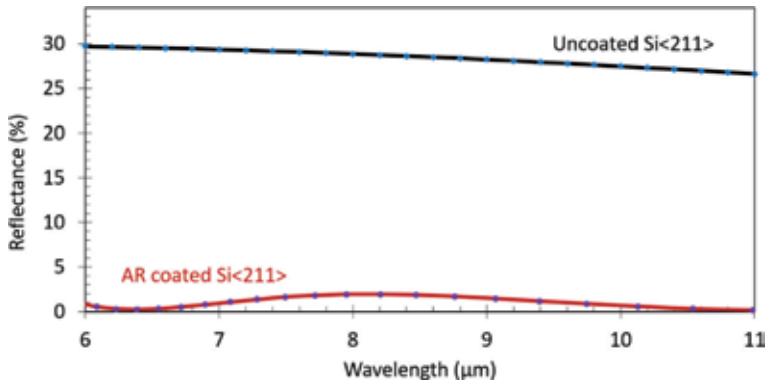
Figure 21.
Measured LWIR wavelength-dependent reflectance of two-layer AR coating structure on Si <211> substrate with that for an uncoated substrate. The AR coating significantly reduces reflection over this range compared to the uncoated Si substrate [25].
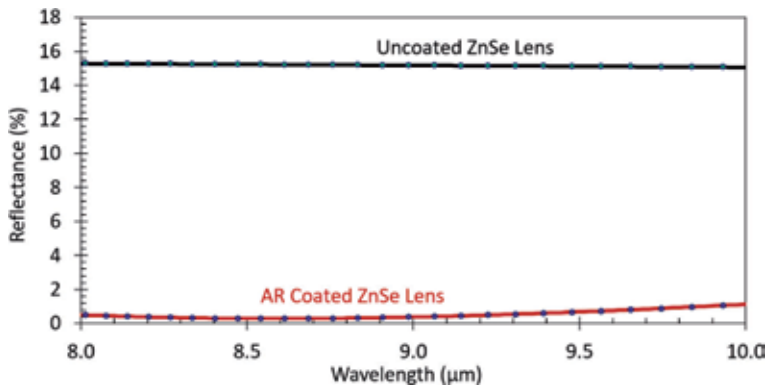
Figure 22.
Measured wavelength-dependent reflectance of uncoated and single-layer nanostructure AR-coated ZnSe lenses. The AR-coated ZnSe lens demonstrates an average reflectance of 0.6%, compared to 15.2% for the uncoated ZnSe lens, over the 8–10 μm spectral band [9].

Single-layer nanostructured AR coatings have been applied to ZnSe lenses that significantly enhance performance by minimizing the reflection of incident IR signals at the lens surfaces. **Figure 22** compares the measured reflectance spectra of ZnSe lenses with and without the AR coatings [9]. The AR-coated ZnSe lens reflects on average ~0.6% of the incident signal over the 8–10 μm band, compared to reflectance of ~15% for the uncoated lens. The performance of the nanostructured AR coatings may be further improved by implementing multilayer rather than single-layer structures.

4. Summary and conclusions

In this chapter we have first discussed recent efforts towards the design, modeling, and experimental development of next-generation carbon nanotube-based bolometers for IR sensing and imaging. The goal in the development and advancement of this technology is to enable high performance, high frame rate, uncooled microbolometers for MWIR and LWIR bands. We have presented recent results of growing variously oriented SWCNT and MWCNT films that demonstrate the promise of using CNTs for developing high performance and small pixel microbolometer arrays.

The growth and application of nanostructured layers for developing high quality antireflection coatings likewise offers an innovative approach for minimizing reflection losses in state-of-the-art sensors and optical windows for both defense and commercial applications. The step-graded multilayer antireflection technology has been shown to be both broadband and omnidirectional in nature. These nanostructure-based AR coatings have demonstrated high performance over spectral bands spanning the visible to the IR with the potential to include larger area substrates to benefit next-generation sensors.

Optical sensing technology is critical for various defense and commercial applications including optical communication and IR imaging. Advances in detector materials and technologies have been achieved over a broad spectrum using Si and SiO_2 based nanostructures and novel carbon nanotube-based materials. These technological advances are opening doors for new approaches to apply device design methodologies that can offer enhanced performance and low-cost optical sensors and systems benefitting a wide range of infrared and electro-optical applications.

Acknowledgements

Author details

Ashok K. Sood[1], John W. Zeller[1]*, Gopal G. Pethuraja[1], Roger E. Welser[1],
Nibir K. Dhar[2] and Priyalal S. Wijewarnasuriya[3]

1 Magnolia Optical Technologies, Inc., Woburn, MA, USA

2 U.S. Army Night Vision and Electronic Sensors Directorate, Fort Belvoir, VA, USA

3 U.S. Army Research Laboratory, Adelphi, MD, USA

*Address all correspondence to: jwzeller@magnoliaoptical.com

IntechOpen

References

[1] Sood AK, Richwine RA, Puri YR, Dhar NK, Polla DL, Wijewarnasuriya PS. Multispectral EO/IR sensor model for evaluating UV, visible, SWIR, MWIR and LWIR system performance. In: Proceedings of SPIE; 1 May 2009; Orlando. Bellingham: SPIE; 2009. p. 73000H

[2] Sood AK, Zeller JW, Welser RE, Puri YR, Lewis JS, Dhar NK, et al. Overview of detector technologies for EO/IR sensing applications. In: Proceedings of SPIE; 26 May 2016; Baltimore. Bellingham: SPIE; 2016. p. 98540A

[3] Dhar NK, Dat R, Sood AK. Advances in infrared detector array technology. In: Pyshkin SL, Ballato JM, editors. Optoelectronics: Advanced Materials and Devices. London: IntechOpen; 2013. pp. 149-190. DOI: 10.5772/51665

[4] Sood AK, Puri YR, Dhar NK, Polla DL. Recent advances in EO/IR imaging detector and sensor applications. In: Vaccca JR, editor. Handbook of Sensor Networking: Advanced Technologies and Applications. 1st ed. Boca Raton: CRC Press; 2015. pp. 18-21. DOI: 10.1201/b18001-5

[5] Sood AK, Lund I, Puri YR, Efstathiadis H, Haldar P, Dhar NK, et al. Review of graphene technology and its applications for electronic devices. In: Ebrahimi F, editor. Graphene: New Trends and Developments. London: IntechOpen; 2015. pp. 59-89. DOI: 10.5772/61316

[6] Sood A. K, Lund I, Zeller J. W, Puri Y. R, Efstathiadis H, Haldar P, et al. Development of graphene based detectors for EO/IR applications. In: Proceedings of SPIE; 26 May 2016; Baltimore. Bellingham: SPIE; 2016. p. 98540D

[7] Fernandes GE, Kim JH, Xu J, Sood AK, Dhar NK, Dubey M. Unleashing giant TCR from phase changes in carbon nanotube composites. In: Proceedings of SPIE; 19 September 2013; Baltimore. Bellingham: SPIE; 2013. p. 88680S

[8] Fernandes GE, Kim JH, Sood AK, Xu J. Giant temperature coefficient of resistance in carbon nanotube/phase-change polymer nanocomposites. Advanced Functional Materials. 2013;**23**:4678-4683. DOI: 10.1002/adfm.201300208

[9] Pethuraja GG, Zeller JW, Welser RE, Sood AK, Efstathiadis H, Wijewarnasuriya PS. Nanostructured antireflection coatings for infrared sensors and applications. In: Proceedings of SPIE; 18 September 2018; San Diego. Bellingham: SPIE; 2018. p. 107660I

[10] Pethuraja GG, Zeller JW, Welser RE, Sood AK, Efstathiadis H, Haldar P, et al. Development of nanostructured antireflection coatings for electro-optic infrared technologies. Sensors & Transducers Journal. 2017;**214**:46-52

[11] Jariwala D, Srivastava A, Ajayan P. Graphene synthesis and band gap opening. Journal of Nanoscience and Nanotechnology. 2011;**11**:6621-6641. DOI: 10.1166/jnn.2011.5001

[12] Sood AK, Lund I, Puri YR, Efstathiadis H, Haldar P, Dhar NK, et al. A review of growth, functionalization, and use of graphene for detection applications. International Journal of Nanoscience and Nanotechnology. 2014;**5**:133-150

[13] Sood AK, Egerton EJ, Puri YR, Fernandes G, Xu J, Akturk A, et al. Design and development of carbon nanotube-based microbolometer for IR imaging applications. In: Proceedings of SPIE; 31 May 2012; Baltimore. Bellingham: SPIE; 2012. p. 83533A

[14] Tîlmaciu CM, Morris MC. Carbon nanotube biosensors. Frontiers in Chemistry. 2015;**59**:1-21. DOI: 10.3389/fchem.2015.00059

[15] Razeghi M. Current status and future trends of infrared detectors. Opto-Electronics Review. 1998;**6**:155-194

[16] Sood AK, Egerton JE, Puri YR, Fernandes G, Kim JH, Xu J, et al. Carbon nanotube based microbolometer development for IR imager and sensor applications. In: Proceedings of SPIE; 16 September 2011; San Diego. Bellingham: SPIE; 2011. p. 815513

[17] Sood AK, Welser RE, Puri YR, Dhar NK, Polla DL, Wijewarnasuriya P, et al. Nanostructured detector technologies for optical sensing applications. In: Proceedings of SPIE; 4 June 2014; Baltimore. Bellingham: SPIE; 2014. p. 91000N

[18] Sood AK, Welser RE, Pethuraja GG, Sood AW, Puri YR, Shubert EF, et al. Nanostructured antireflection (AR) coatings of optoelectronic applications. In: Aliofkhazraei M, editor. Comprehensive Guide for Nanocoatings Technology. Vol. 4. Hauppauge: Nova Science Publishers; 2015. pp. 183-216

[19] Pethuraja GG, Welser RE, Zeller JW, Puri YR, Sood AK, Efstathiadis H, et al. Nanostructured antireflection coatings for optical detection and sensing applications. In: MRS Proceedings; 10 July 2015; San Francisco. Warrendale: MRS; 2015. p. mrss15-2137947

[20] Chhajed S, Poxson DJ, Yan X, Cho J, Schubert EF, Welser RE, et al. Nanostructured multilayer tailored-refractive-index antireflection coating for glass with broadband and omnidirectional characteristics. Applied Physics Express. 2011;**4**:052503. DOI: 10.1143/apex.4.052503

[21] Welser RE, Sood AW, Pethuraja GG, Sood AK, Yan X, Poxson DJ, et al. Broadband nanostructured antireflection coating on glass for photovoltaic applications. In: Proceedings of the 38th IEEE Photovoltaic Specialists Conference; 3-8 June 2012; Austin. New York: IEEE; 2012. pp. 003339-003342

[22] Xi JQ, Schubert MF, Kim JK, Schubert EF, Chen M, Lin SY, et al. Optical thin-film materials with low refractive index for broadband elimination of Fresnel reflection. Nature Photonics. 2007;**1**:176-179. DOI: 10.1038/nphoton.2007.26

[23] Pethuraja GG, Zeller JW, Welser RE, Efstathiadis H, Haldar P, Wijewarnasuriya PS, et al. Development of nanostructured antireflection coatings for infrared technologies and applications. In: Proceedings of SPIE; 19 September 2017; San Diego. Bellingham: SPIE; 2017. p. 104040S

[24] Sood A K, Pethuraja G, Welser R. E, Puri Y. R, Dhar N. K, Wijewarnasuriya P. S, et al. Development of large area nanostructured antireflection coatings for EO/IR sensor applications. In: Proceedings of SPIE; 28 August 2015; San Diego. Bellingham: SPIE; 2015. p. 96090D

[25] Pethuraja GG, Zeller JW, Welser RE, Sood AK, Efstathiadis H, Wijewarnasuriya P. Nanostructured antireflection coatings for infrared sensors and applications. In: Proceedings of the 2018 U.S. Workshop on the Physics and Chemistry of II-VI Materials; 22-25 October 2018; Pasadena. New York: Palisades; 2018. p. 117

Metallo-Dielectric Colloidal Films as SERS Substrate

Ana L. González, Arturo Santos Gómez and
Miller Toledo-Solano

Abstract

Along this chapter, we probe that the discrete dipole approximation models fairly well the optical response of periodic systems. Herein, we use it to model the reflectance and transmittance, at normal incidence, of colloidal films made of SiO_2 spheres. As the thickness increases from 1 to 12 layers, the photonic band gap shifts to the blue tending to the value corresponding to a 3D opal, 442 nm. A film with more than eight layers resembles the bulk properties of a 3D opal. Our results are compared to a real sample. Besides, we show that taking advantage of the wide and asymmetrical absorbance spectrum of an opal with Au NPs is possible to identify the contribution of each component in the overall spectrum, through a deconvolution analysis. Finally, we present the electric field intensity as the content of metal NP increases in a monolayer. We consider NPs one order of magnitude smaller than the silica spheres, and then, 6, 9, and 17 NPs are hosted in the void. Similar average electric field intensities, about 11 times the incident intensity, are obtained with Au and Ag NPs. But, the spots with these intensities cover a bigger area with Ag NPs than with Au NPs.

Keywords: metal nanoparticles, SiO_2 spheres, colloidal thin films, discrete dipole approximation, photonic band gap, near field intensity

1. Introduction

A crystal is defined as the solid formed by a long range periodic array of atoms or molecules. Its periodic lattice originates a potential with the same periodicity, and as outcome, the energy levels give rise to allowed and forbidden bands. In consequence, the physical properties of crystals depend on the band structure. For instance, an electromagnetic wave with a frequency in the interval of the forbidden band will be reflected or absorbed by the crystal. In nature, other entities instead of atoms or molecules can conform to ordered arrangements. For example, Tobacco mosaic virus is a virus that infects plants, especially tobacco plant (where its name comes from); it has a rod-shape with the ability of self-assembling naturally creating a bi-dimensional triangular structure. This assembly has been exploited to increase the capacity of batteries [1] and as a template for the fabrication of functional devices [2]. Other periodic structures, found in nature or produced artificially, are the named colloidal crystals. A colloidal crystal is an assembly of colloid particles with a periodic structure. Its bulk properties depend on composition,

particle size, and packing arrangement. Opals are an example of colloidal crystals, in nature and under specific conditions of pressure and temperature; silicon dioxide (SiO_2) spheres accommodate in a close-packed array. Probably its most well-known optical property is the constructive interference of light either at its surface or interior producing certain colors as the angle of incident light changes, and this property is named iridescence.

Artificially, opals can be formed in a liquid medium or during drying/evaporation of particle suspension. Nowadays, it is possible to synthesize them with dielectric spheres of porous silica, polymethyl methacrylate, polystyrene, and others, of diameter of hundreds of nanometers. The main impressive characteristic of artificial opals is its optical response in the visible range [3, 4], and this has technological implications that place them as photonic band gap (PBG) materials. A bidimensional ordered array (thin film) can be used as coatings of several substrates, allowing to optimize or even modify some of the physical and chemical properties of the substrate. Its optical response may depend on the geometry of the periodic array, defects, and thickness. Some artificial opals have been reported with a face centered cubic (FCC) or close-packed hexagonal (HCP) structure with sequences ABCABC and ABAB, respectively [5, 6].

On the other hand, nanocomposite materials often exhibit exceptional properties compared to their constituents. Consequently, the incorporation of metal nanoparticles (NPs) into colloidal crystals is a subject of study that emerges naturally [7]. Some of the methods to achieve the incorporation of the NPs are based on self-assembling, electroplating process, and photolysis [8–10]. The applications of these composite thin films cover catalysis, optical devices, solar cell, and sensors [11–15], among others.

Particularly, composite periodic structures constructed by using colloidal crystals as templates and Au NPs have been tested as surface enhanced Raman scattering (SERS) substrates. These SERS substrates are simple and inexpensive to prepare and, moreover, offer the benefit of being highly stable. However, the SERS enhancement factor (EF) depends on several factors such as the probe molecule, concentration and shape of Au NPs, and thickness of the substrate. One may think that only the NPs in the top layer of the thin film are illuminated by the excitation laser and hence contribute to the SERS signal [16]. Nevertheless, larger SERS signal has been detected using thin composite substrates (less than 10 silica layers) rather than thick ones (more than 10 silica layers), and more surprising is the fact that the SERS enhancement falls down when substrates with a thickness between 1 and 2 mm are used [17]. Therefore, it seems that the SERS EF is thickness dependent, but the origin of this behavior is not completely understood.

This chapter is dedicated to the study of the optical response of colloidal thin films (multilayers of SiO_2 spheres), with and without metal nanoparticles. In Section 2, we briefly describe the discrete dipole approximation method to model the reflectance (R), transmittance (T), and near electric field intensity. Section 3 contains an analysis of R and T of colloidal thin films as the thickness increases from 1 to 12 layers of SiO_2 spheres. Section 4 focuses on a composite thin film and its role as SERS substrate; first, the absorbance spectra are proposed as a tool to verify the inclusion of Au NP, and second, the near electric field intensity as the amount of Au NP increases is shown.

2. Discrete dipole approximation for periodic targets

Nowadays, there are several methods with their respective numerical implementations to enquire into the optical response of single targets, one of them

is the discrete dipole approximation (DDA). This method has been widely used to study the absorbed and scattered light of several systems and materials as nanoparticles, human blood, bacteria, and interstellar dust, among others [18–23]. Herein, we place attention to DDA's extended version, proposed by Draine and Flatau, for modeling R and T of infinite 2D periodic systems [24]. Recently, DDA was employed to study R and T of periodic arrays of dielectric and metal spheres [25].

In **Figure 1**, a section of a bi-dimensional periodic array of solid spheres is exemplified, each one discretized by N_{dip} dipoles represented by tiny spheres. As an analogy of atoms in a solid crystalline structure, the definition of a convenient unit cell is helpful. The target unit cell (TUC) is the entity located at the origin and that is repeated along the yz plane with an L_y and L_z periodicity. (m,n) is a pair of integers that defines the position of the TUC's replica at m units along the y axis and n units along the z axis.

The position and dipole moment of the dipole j of the (m,n) TUC replica are expressed as

$$\mathbf{r}_{jmn} = \mathbf{r}_{j00} + m\mathbf{L}_y + n\mathbf{L}_z, \tag{1}$$

$$\mathbf{p}_{jmn} = \mathbf{p}_{j00} \exp\left[i\left(m\mathbf{k}_0 \cdot \mathbf{L}_y + n\mathbf{k}_0 \cdot \mathbf{L}_z\right)\right] \quad \text{for each } j = 1, \ldots, N_{dip}, \tag{2}$$

$\mathbf{L}_y$ and $\mathbf{L}_z$ are the vectors that define the periodicity of the array; $\mathbf{r}_{j00}$ is the position vector of the j dipole that belongs to the TUC (the one at the origin), and $\mathbf{k}_0$ is the incident wave vector.

The dipole moment $\mathbf{p}_{j00}$ of the j dipole in the TUC satisfies the equation

$$\mathbf{p}_{j00} = \overleftrightarrow{\alpha}_j \cdot \left[\mathbf{E}_{\text{inc}}\left(\mathbf{r}_j\right) - \sum_{k \neq j} \tilde{\mathbf{A}}_{j,k}\mathbf{p}_{k00}\right], \tag{3}$$

where $\overleftrightarrow{\alpha}_j$ is the polarizability tensor, $\mathbf{E}_{\text{inc}}\left(\mathbf{r}_j\right)$ is the field of an incident plane wave at the position $\mathbf{r}_j$, and $\tilde{\mathbf{A}}_{j,k}$ is a matrix that takes into account the interaction
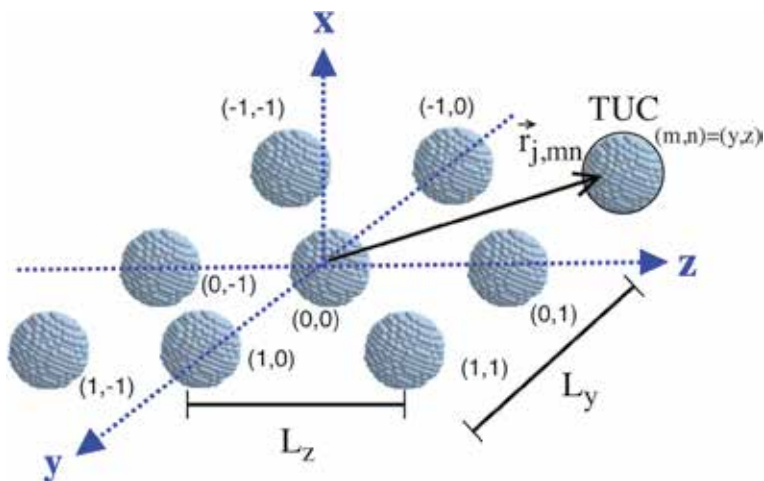
Figure 1.
A section of an infinite bidimensional periodic array of spheres. Each sphere is discretized by an array of N_{dip} dipoles. $\mathbf{r}_{j,mn}$ is the position of the j dipole of the target unit cell (TUC) replica located at m units along the y axis and n units along the z axis. Figure taken with permission from Ref. [25].

between the dipole located at $\mathbf{r}_{j00}$ and the field induced by the dipoles of the TUC and its replicas at the $\mathbf{r}_{kmn}$ positions; for more details, see [24].

If there are N_{dip} dipoles in the TUC with a similar equation to Eq. (3) existing for each dipole, then, a system of $3N_{dip}$ complex coupled equations needs to be solved for $\mathbf{p}_{j00}$ values. Once the equation system is solved, then far and near field optical response of the periodic target can be calculated.

Usually, N_{dip} dipoles are of the order of $10^5 - 10^6$; hence, numerical tools are necessary to solve the system of $3N_{dip}$ equations. A robust numerical implementation of DDA is the DDSCAT code [26] that assumes an incident plane wave along the positive direction of x axis and a bidimensional target resting on the yz plane. Among other interesting physical quantities, the 2×2 scattering amplitude matrix elements S_i can be calculated, and consequently, the 4×4 scattering intensity matrix elements $S_{\alpha\beta}$ [27].

For the specific case of unpolarized incident light, R and T are related to the $S_{\alpha\beta}$ elements through the next expressions:

$$R = S_{11} \quad \text{for } (k_{sx}k_{0x} < 0), \tag{4}$$

$$T = S_{11} \quad \text{for } (k_{sx}k_{0x} > 0), \tag{5}$$

where k_{sx} and k_{0x} are the wave vector components of the scattered light and of the incident light, respectively. Both of them are along the direction of the incident light. The S_{11} value is related to S_i elements by:

$$S_{11} = \frac{1}{2} \left(|S_1|^2 + |S_2|^2 + |S_3|^2 + |S_4|^2 \right). \tag{6}$$

3. Colloidal films of SiO$_2$ spheres: effect of thickness

This section is devoted to the effect of thickness of a colloidal film on its optical response. We consider a film built by N layers made of SiO$_2$ spheres with a diameter of 200 nm, ordered in HCP structure (AB sequence). A scheme of the thin film is shown in **Figure 2**; there, the film is on the yz plane and its thickness goes along the x axis. Also, the incident electromagnetic (EM) plane wave has a wave vector $\mathbf{K}$ in direction of the positive x axis.

The TUC for each N layer thin film, with N from 1 to 12, is conveniently built. The TUC for the monolayer contains two spheres, for the bilayer four spheres, for
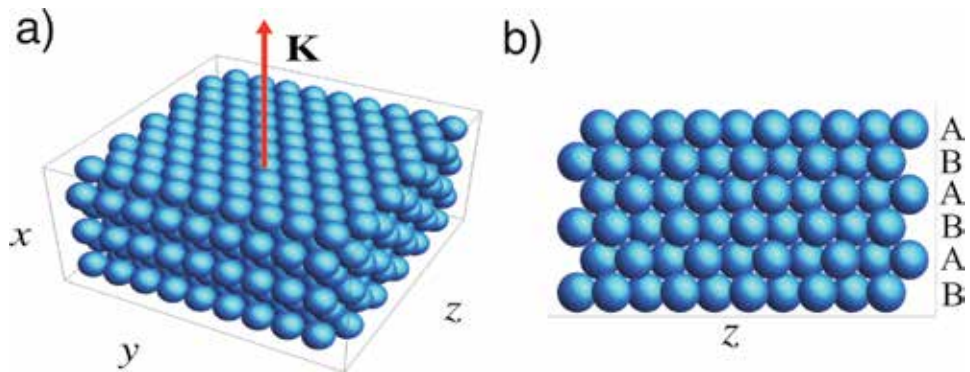
Figure 2.
*(a) The wave vector **K** of the incident EM plane wave, perpendicular to the thin film. (b) Lateral view of a thin film composed of 6 layers of SiO$_2$ spheres in an ABAB sequence.*

the three-layer six spheres, and so on. A 10 nm separation distance between two adjacent dipoles is used, implying about 4600 dipoles per sphere.

In the visible range, the refractive index of the silica, n_{SiO_2}, is almost constant, and its variations go from 1.48 to 1.45 for wavelengths from 400 to 700 nm [28, 29]. For simplicity and without loss of information, we choose $n_{SiO_2}(\lambda) = 1.46$. It is noteworthy to mention that in the visible the imaginary part of n_{SiO_2} is negligible compared to the real part. However, in the ultraviolet interval, special care needs to be taken as the imaginary part comes to be significant and it is associated to the absorption coefficient.

R and T of a thin film composed of *N* layers, when light comes parallel to the normal of the surface, are shown in **Figure 3**. As the number of layers increases from 1 to 12, that is, as the film becomes thicker, a maximum of R emerges defining a photonic band, getting sharper around 450 nm. The optical spectrum to the left and right of the PBG is not symmetric because we have chosen the wavelength as the independent variable and not the wave number. The thickness, wavelength of the BG center (λ_c), width of the BG (ΔBG), effective refractive index of the thin film (n_{eff}), and optical path length (L) of each thin film are given in **Table 1**. Each quantity is estimated as follows:

The thickness is determined by considering the diameter of the sphere, *D*, and geometrical aspects of the AB sequence, as is explained next. The base of a tetrahedron is formed by the center of three spheres on a layer A, its height goes from its base to the center of a sphere of layer B, and the last is resting on the void left by the three spheres on layer A. The height of the tetrahedron coincides with the separation distance, d(1 1 1), between two adjacent planes with Miller indices (1 1 1). Then, the thickness of a film with *N* layers is $(N-1)\mathrm{d}(1\,1\,1) + D$, with $\mathrm{d}(1\,1\,1) = \sqrt{(2/3}D$.

λ_c is extracted from the calculated R(λ) spectrum, noting that it moves to the blue as the thickness increases, stopping around 444 nm. Latter, we compare this stop value to the λ_c of a 3D opal, and with experimental results. ΔBG is associated to the full width at the half maximum (FWHM) of the spectrum, and to estimate it, a Gaussian centered at the Bragg peak (the maximum of the R spectrum) was
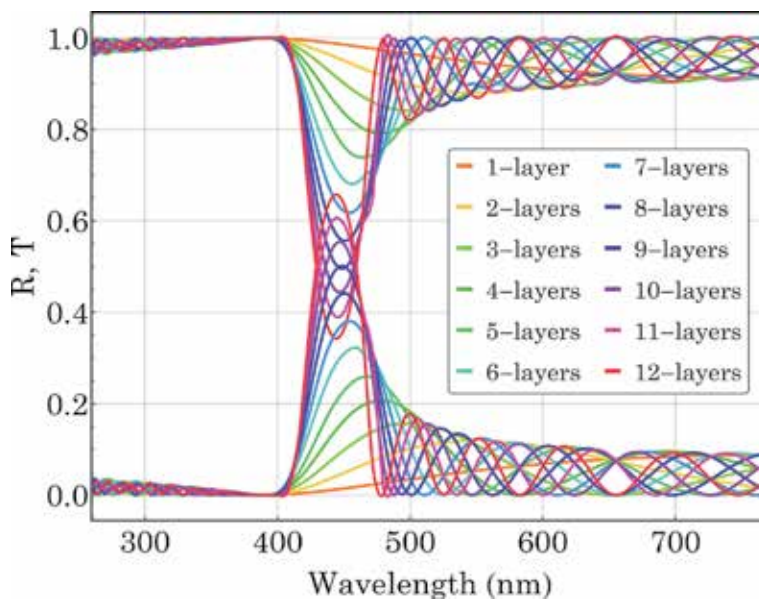
Figure 3.
Reflectance and transmittance of a thin film composed of N layers of 200 nm SiO₂ spheres. The incident light comes normal to the surface and is unpolarized.

Number of layers	Thickness (nm)	λ_c (nm)	ΔBG (nm)/(eV)	n_{eff}	L (nm)
1	200	650	—	1.29	251.9
2	363.3	549.7	—	1.3	211.4
3	526.4	499	—	1.33	187.6
4	689.9	476	—	1.34	177.6
5	853.2	465	73.64/16.7	1.34	173.5
6	1016.5	457	62.96/19.54	1.34	170.5
7	1179.8	453	55.39/22.21	1.35	169.0
8	1343.1	450	50.04/24.58	1.35	166.7
9	1806.4	449	46.05/26.71	1.35	166.3
10	1669.9.	447	43.28/28.42	1.35	165.5
11	1833.0	444.7	42.47/28.96	1.35	164.7
12	1996.3.	444.3	37.57/32.74	1.35	164.5

Table 1.
Thickness of the thin film composed of N layers, BG center position (λ_c), width of the BG (ΔBG), effective refractive index (n_{eff}), and optical path length (L).

adjusted. The trend is that the PB becomes narrow as the film is getting thicker. In **Table 1,** the ΔBG values are given in nm and eV.

Because the film is a heterogeneous material composed of SiO$_2$ spheres with air at the interspace, a refractive index can be assigned to it in order to treat the film as a homogeneous material with an effective property, n_{eff}. This can be done relating the refractive index of each involved material and its filling fraction (ff)[1], that is, the fraction of volume occupied by the spheres and air. n_{eff} is deduced using [30]:

$$n_{\text{eff}}^2(\lambda) = n_{\text{air}}^2(1 - \text{ff}) + n_{\text{SiO}_2}^2(\lambda)\text{ff}. \tag{7}$$

$n_{\text{eff}} = 1.35$ for more than seven layers (see **Table 1**), the same value of a 3D opal with HCP structure.

In the last column of **Table 1**, the optical path length (L) associated to the inhomogeneous thin film is determined simply using the generalized Bragg equation at normal incidence [31]:

$$L = \frac{\lambda_c}{2n_{\text{eff}}}, \tag{8}$$

L is interpreted as the path that follows the light when going through the heterogeneous film in order to produce constructive interference.

Now, Let's keep in mind the trend observed by the position of λ_c as the thickness of the film increases: a shift to the blue stopping at a value around 444 nm. On the other hand, consider a 3D opal with an HCP structure and a ff = 0.74. Then, using (Eq. 7) and generalized Bragg's law

$$\lambda_{c,\text{opal}} = 2d_{(111)}\sqrt{n_{\text{eff}}^2 - \sin^2\theta}, \tag{9}$$

---

[1] The ff is calculated considering a cell of a hexagonal base with a length side D and a high defined by the thickness of the N layers. Then, ff= $mV_{\text{sphere}}/V_{\text{cell}}$, with V_{sphere} and V_{cell} being the volume of a sphere and the cell, respectively. m is the number of spheres in the cell.

the wavelength of the center of the PBG, $\lambda_{c,opal}$, can be estimated. For the specific case of normal incidence and constructive interference due to planes (111), $\lambda_{c,opal}$ = 442.7 nm, a value very close to 444 nm. Then, the PBG of films with more than eight layers resembles that of a 3D artificial opal (see **Figure 4**). Excluding thin films with less than three layers, the best fitting for λ_c as a function of the number of layers is a polynomial of third order: $\lambda_c\,(N) = 600.57\,nm - 48.04\,N + 5.11\,N^2 - 0.18\,N^3$.

In **Figure 5**, the reflectance of an opal of 200 nm SiO_2 spheres has a PBG with a maximum around 474 nm [17], agreeing to our results shown in **Figure 3**. The
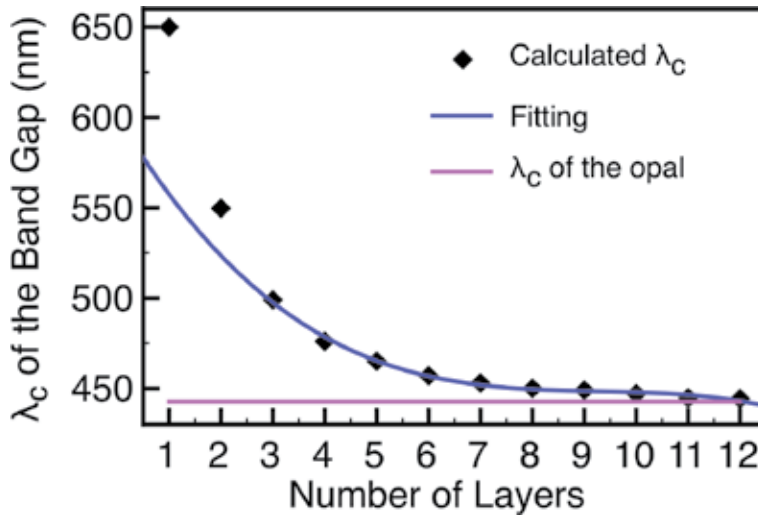
Figure 4.
Wavelength position of the center of the band gap, λ_c, as the number of layers increases. λ_c of a 3D opal is about 442.7 nm.
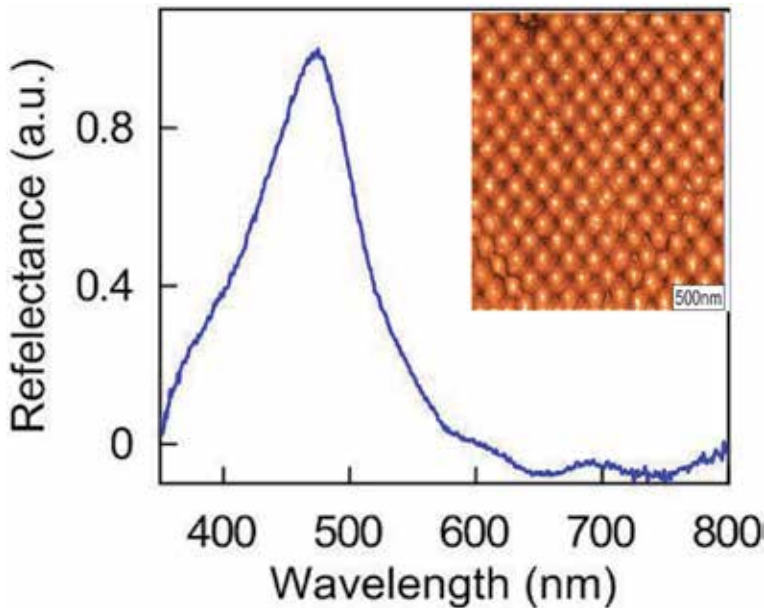
Figure 5.
Reflectance of an opal of 200 nm silica spheres; its PBG has a maximum around 474 nm. In the AFM image, some defects are noticed in the orderliness. Image modified with permission from Ref. [17].

asymmetry of the spectrum and difference in position of the gap center is presumably due to the presence of defects and polydispersity of the synthesized thin film.

4. Composite thin film: effect of metal NPs' concentration

Composite colloidal films are an option for having a substrate with the advantages of rough, periodic and plasmonic material. Its performance depends on the concentration, shape, and size of the metal NPs; type of probe molecule; and thickness of the film. Consequently, the large amount of variables involved makes difficult to establish the trend that may follow a good SERS substrate.

Au and Ag are the most plasmonic materials used to boost the SERS signal. However, it is easier to incorporate Au on crystal colloids than Ag. From the several interesting reports about the synthesis and characterization of composite colloidal thin films with Au, we can highlight the following aspects [7, 17, 32]:

- When the size of the plasmonic NPs is smaller than the size of the dielectric spheres, the lattice of the opal is not distorted.

- The photonic band of the composite shows a red shift, a reduction of its width and intensity upon increasing NP doping level.

- Even for large loads of Au NPs, evidence of the plasmon resonance is not noticeable in the reflectance spectrum of the composite.

4.1 Evidence of incorporation of metal NPs

Recently, we reported SERS-substrate films with the advantage of a rough surface provided by a periodic array of SiO_2 spheres and Au NPs [32]. The synthesis of colloidal SiO_2 spheres was performed following the methods of Stöber [33] and Razo [5], while Au NP colloid was prepared adopting the method introduced by Turkevich [34, 35]. The size of silica spheres and Au NPs is 275 and 22 nm, respectively. Besides, the surface plasmon resonance of the NPs is located at 522 nm (see Ref. [32]). The as-synthesized SiO_2 spheres and Au NPs were used to obtain composite films with low, medium, and high volume concentrations of Au NPs (composite 1, 2, and 3, respectively), accordingly to the procedure reported by Cong et al. [36], and that previously has been employed by some of us to prepare the opal/Fe_3O_4 colloidal crystal [37]. The films were deposited on a glass substrate, and to make evidence of their functionality as SERS substrates, methylene blue (MB) was employed as the molecular probe. An EF of the order of 10^5 was reached with the composite 3.

Figure 6(a) exhibits the surface of the SiO_2 opal where some internal planes are appreciated. Despite the presence of some vacancies, an FCC array is recognized. Scanning electron microscopy (SEM) image of composite 3 reveals that Au NPs are located at the interstitial sites (see **Figure 6(b)**). Moreover, the center-to-center distance between adjacent spheres in the composite is almost the same as that of the bare SiO_2 opal (panels (c) and (d) of **Figure 6**). Hence, the lattice of the opal is not distorted even using a relatively high volume concentration of Au NPs. As the concentration of Au NPs increases, more NPs cover the SiO_2 spheres and the consequent visual effect is SiO_2 spheres of smaller diameter (as it is well noticed in **Figure 6(b)**). A similar tendency has been perceived with nonspherical Au NPs, and at low concentrations, Au nanorods reside in the voids, but as the concentration increases, they start to cover the surface of the spheres [17].
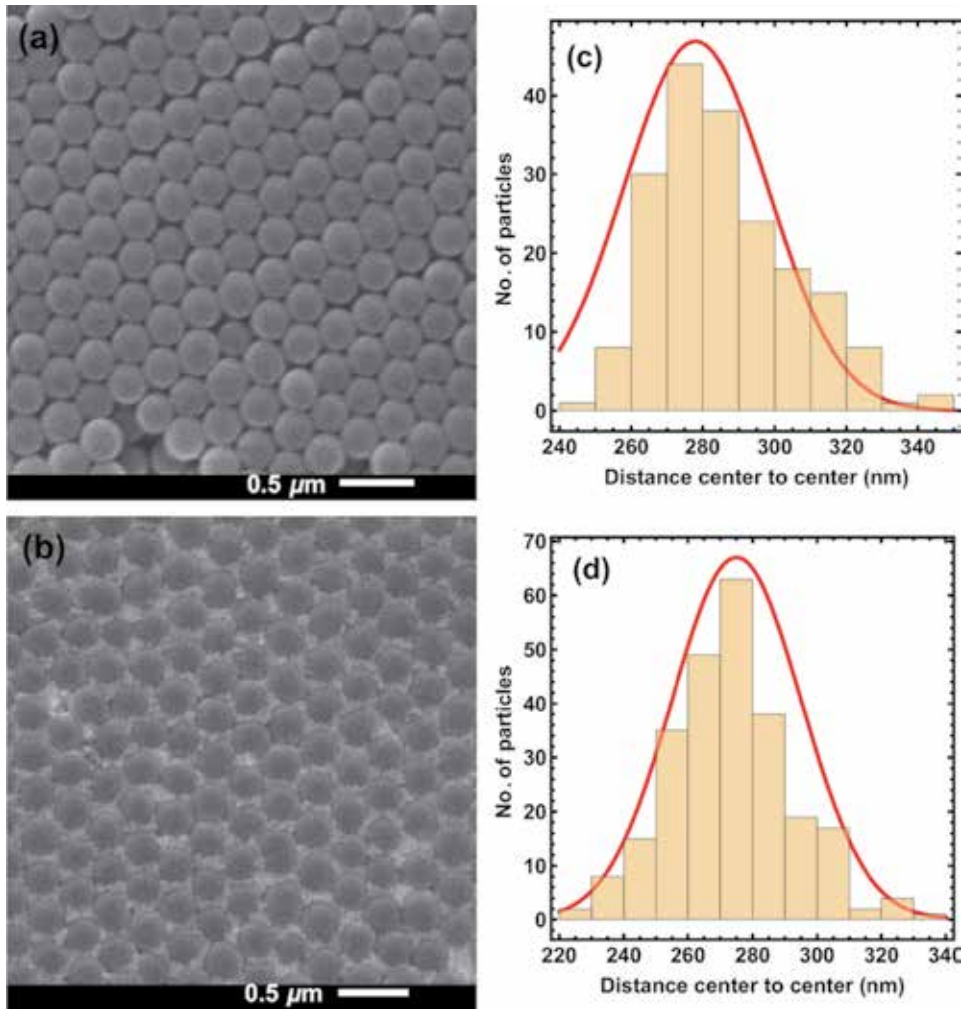
Figure 6.
Micrographs by SEM of films made of SiO₂ spheres before (a) and after infiltration of Au NPs (b). (c) and (d) show the center to center distance distribution histograms between adjacent spheres. The average distance corresponds to 278 ± 20 nm (opal) and 275 ± 20 nm, respectively. Image modified with permission from Ref. [32].

In **Figure 7**, UV–vis absorbance (*A*) spectrum of the films made of SiO₂ spheres before and after infiltration (composite 1, 2, and 3) is presented. The blue non–soft lines correspond to the measured spectra. For the opal, the peak is attributed to the PB, which originates from the diffraction of the 3D ordered structure of the colloidal crystal. With the naked eye, a wider and asymmetric spectrum of the composites compared to that of the opal is appreciated. To enquire the effect of each component of the composite on the overall spectrum, a deconvolution analysis may be carried out. Considering a Gaussian curve associated to the silica opal and other to the Au NPs, the general expression is of the form:

$$A(\lambda) = E + B_{\text{opal}} \exp\left(-(\lambda - \lambda_{\text{opal}})^2/2\sigma_{\text{opal}}^2\right) + C_{\text{Au}} \exp\left(-(\lambda - \lambda_{\text{Au}})^2/2\sigma_{\text{Au}}^2\right),$$

(10)

where *E* is a fitting value that moves the curve along the dependent variable axis; B_{opal} and C_{Au} are real values related to the highest point of each Gaussian curve;
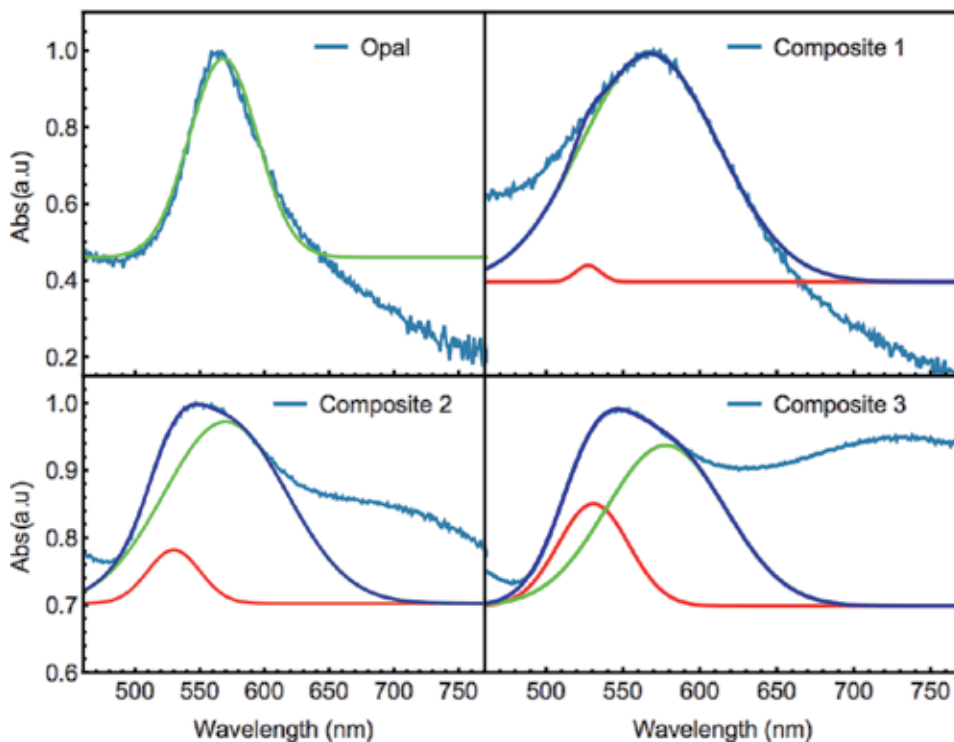
Figure 7.
UV–Vis absorbance spectrum of the films made of SiO₂ spheres before and after infiltration with low (composite 1), medium (composite 2), and high (composite 3) degree of Au NP loading. Blue non–soft line is the experimental measurement; red and blue lines are the Gaussian curves associated to the Au and silica arrays, respectively; blue soft line is the sum of blue and green lines.

Film	λ_{opal}	σ_{opal}	λ_{Au}	σ_{Au}
SiO₂	568 nm	26 nm		
Composite 1	567 nm	44 nm	527 nm	8 nm
Composite 2	570 nm	48 nm	530 nm	20 nm
Composite 3	578 nm	39 nm	532 nm	23 nm

Table 2.
Gaussian fitting parameters for absorbance bands.

λ_{opal} and λ_{Au} are the central wavelengths; and σ_{opal} and σ_{Au} are the respective FWHM. The corresponding fitting values are presented in **Table 2**. The addition of the two Gaussians give rise to a distribution (blue soft line) that fits the experimental distribution, see panels of **Figure 7**. The red and green lines are the Gaussian curves attributed to the contribution of Au and silica arrays in the composite, respectively.

SiO₂ film spectrum is very well adjusted to a Gaussian with a peak around 568 nm and a FWHM of 26 nm (see **Figure 7**). Meanwhile, when relatively low, medium, or high Au NPs concentration is incorporated in the opal, an asymmetrical and wide absorbance spectrum is noticed. At low concentration (composite 1), apparently still dominates the band assigned to the SiO₂ array and the outcome is a distribution with a slightly negative asymmetry. At medium (composite 2) and high (composite 3) concentration, it seems that the Au NP signal starts to predominate and the result is a distribution with a positive asymmetry.

As the concentration of Au NPs in the opal film increases, the center of the respective Gaussian curve (red line) is red shifted, compared to the surface plasmon resonance of the colloidal solution of Au NPs (located at 522 nm). Meanwhile, the center of the respective Gaussian curve assigned to the silica signal (green line) is slightly red shifted. The last statement agrees with the apparent reduction of the size of the silica spheres when their surface becomes to be covered by Au NPs. These indicatives confirm the increasing Au NPs' content in the composites.

4.2 Effect of metal NPs' load on the SERS EF

Opals with inclusions of Au NPs offer several of the following features: [16, 17, 32]:

- The SERS signal is more intense compared to a disordered template.

- The uniformity/periodicity of the Au NPs' spatial distribution may be controlled by the template.

- A thin layer of Au NPs is enough to increase the SERS signal.

- They are simple and inexpensive to prepare.

- The roughness increases the effective surface of the SERS substrate.

- Less than a milligram of NPs is required to coat a surface of tens of square millimeters.
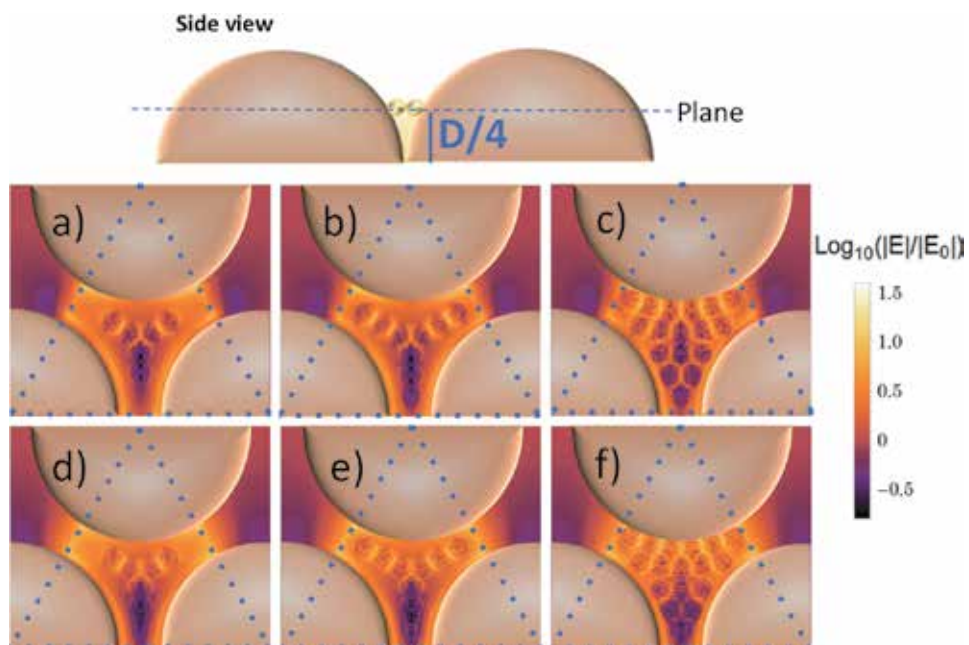
Figure 8.
Electric field intensity of (a) 6, (b) 9, and (c) 17 Au NPs at the intersite of three SiO₂ spheres. The lower panels (d), (e), and (f) are the same systems but with Ag NPs.

The thickness of the colloidal film and load of Au NPs are factors that have been exploited to succeed in the fabrication of an SERS substrate with high qualities. With inverse opal templates, nanoparticle film thickness has proved to have little effect on SERS signal intensity for substrates thicker than a monolayer. On the other hand, opals with Au NPs show a larger enhancement when the film has less than 10 silica layers compared to the thicker ones, and a possible explanation for this is a contribution of multiple scattering within the opal.

Limiting ourselves to the contribution to the SERS enhancement due to the top layer of the composite film, we study the effect of NP concentration. For illustrating low, medium, and high content of metal NPs in the surface layer of the thin film, 6, 9, and 17 metal NPs in the interspace among three dielectric spheres have been considered. An estimation of the single molecule SERS EF can be done through the SERS EF $\approx E^4$ approximation [38], with E being the intensity of the local field. Usually, the size of the metal NPs is one order of magnitude smaller than the size of the dielectric spheres; therefore, we have considered metal NP diameter of 20 nm and SiO_2 dielectric sphere of 200 nm. The spatial configuration of E values for Au and Ag NPs is presented in **Figure 8**. To decrease computational cost, only the area limited by the triangular zone was considered as the target in DDA calculation. The incident EM plane wave is parallel to the plane and travels from left to right, and its wavelength is of 633 nm (red laser). Notice that the SiO_2 spheres apparently are not touching one each other, and the reason is that the plane that is presented is the one that crosses the array as depicted in the side view drawn. In general, the average electric field intensity is of the same order of magnitude for all cases, reaching values 10–12 times the incident electric field, the field being more intense in the spots among NPs, and in the region between the SiO_2 spheres surface and the Au NPs close to it.

5. Conclusions

Along this chapter, we have proved that DDA is a good option to study the optical response of periodic systems. Herein, we use it to model the reflectance and transmittance, at normal incidence, of colloidal films made of SiO_2 spheres with a specific diameter of 200 nm. We show that as the thickness increases from 1 to 12 layers, the center of the photonic band gap shifts to the blue tending to the value of 444 nm. This value is very close to the one corresponding to a 3D opal with HCP structure, 442 nm. Analyzing the trend of the position of the BG, a film with more than eight layers resembles that of a 3D artificial opal. We also compared our results with a 3D artificial opal made with silica spheres of the same size as the one studied by us. We found a good qualitative agreement, and the differences are attributed mainly to the presence of defects in the sample.

Artificial opals with Au NPs are of interest due to their many applications, and one of them is as SERS substrate. A main issue is how to be sure the NPs are being incorporated in the sample. Usually, reflectance spectrum does not show an evident contribution due to the presence of the plasmonic NPs. However, we present here that the absorbance spectrum is wider and asymmetrical compared to the opal without Au NPs. Furthermore, with a deconvolution analysis, it is possible to identify the contribution due to the Au NPs and the silica spheres in the overall spectrum.

For SERS applications, the calculation of electric field intensity gives an idea of the enhancement factor that can be reached by the substrate. At the end of the chapter, we present the spatial distribution of electric field intensity as the amount of metal NPs increases in a monolayer. Taking advantage of the periodicity of the

system, we limited ourselves to the section defined by three silica spheres with N NPs in the void among them. The NPs considered here are one order of magnitude (diameter of 20 nm) smaller than the silica spheres. Therefore, it is possible to host 6, 9, and 17 NPs in the void. Same configuration was used for Au and Ag NPs, finding similar electric field intensities for both of them, about 11 times the incident intensity. But, the spots with these intensities cover a bigger area with Ag NPs than with Au NPs. This indicates that the SERS EF of a specific concentration of molecules would be larger using Ag NPs than Au NPs.

Acknowledgements

Conflict of interest

The authors declare no conflict of interest.

Thanks

Special thanks are given to Dr. Enrique Sánchez, from the Institute of Physics at the Benemerita Universidad Autonoma de Puebla, for his comments and facilities for the synthesis and characterization of the materials presented in **Figures 6** and 7.

Abbreviations

DDA	discrete dipole approximation
NPs	nanoparticles
PBG	photonic band gap
SEM	scanning electron microscopy
FCC	face centered cubic
HCP	hexagonal compact packing
SERS	surface enhanced Raman scattering
EF	enhancement factor
R	reflectance
T	transmittance
EM	electromagnetic

Author details

Ana L. González[1*], Arturo Santos Gómez[1,2] and Miller Toledo-Solano[3]

1 Instituto de Fisica, Benemerita Universidad Autonoma de Puebla, Puebla, Pue., Mexico

2 Instituto Tecnologico Superior de San Martin Texmelucan, San Martin Texmelucan, Puebla, Mexico

3 Facultad de Ciencias Fisico-Matematicas, CONACYT-Benemerita Universidad Autonoma de Puebla, Puebla, Pue., Mexico

*Address all correspondence to: anagr@ifuap.buap.mx

IntechOpen

References

[1] Gerasopoulos K, McCarthy M, Royston E, Culver JN, Ghodssi R. Microbatteries with tobacco mosaic virus templated electrodes. In: 2008 IEEE 21st International Conference on Micro Electro Mechanical Systems; IEEE. 2008. pp. 960-963

[2] Atanasova P, Rothenstein D, Schneider JJ, Hoffmann RC, Dilfer S, Eiben S, et al. Virus-templated synthesis of ZnO nanostructures and formation of field? Effect transistors. Advanced Materials. 2011;**23**(42):4918-4922. DOI: 10.1002/adma.201102900

[3] López C. Materials aspects of photonic crystals. Advanced Materials. 2003;**20**:1679-1704. DOI: 10.1002/adma.200300386

[4] García PD, Sapienza R, López C. Photonic glasses: A step beyond white paint. Advanced Materials. 2010;**22**(1):12-19. DOI: 10.1002/adma.200900827

[5] Razo DA, Pallavidino L, Garrone E, Geobaldo F, Descrovi E, Chiodoni A, et al. A version of Stöber synthesis enabling the facile prediction of silica nanospheres size for the fabrication of opal photonic crystals. Journal of Nanoparticle Research. 2008;**10**(7): 1225-1229. DOI: 10.1007/s11051-008-9373-4

[6] Waterhouse GI, Waterland MR. Opal and inverse opal photonic crystals: Fabrication and characterization. Polyhedron. 2007;**26**(2):356-368

[7] Morandi V, Marabelli F, Amendola V, Meneghetti M, Comoretto D. Colloidal photonic crystals doped with gold nanoparticles: Spectroscopy and optical switching properties. Advanced Functional Materials. 2007;**17**(15): 2779-2786. DOI: 10.1002/adfm.200600764

[8] Lu L, Randjelovic I, Capek R, Gaponik N, Yang J, Zhang H, et al. Controlled fabrication of gold-coated 3D ordered colloidal crystal films and their application in surface-enhanced Raman spectroscopy. Chemistry of Materials. 2005;**17**(23):5731-5736. DOI: 10.1021/cm051473d

[9] Nishio M, Moronuki N, Abasaki M. Fabrication of patterned Ag and Au inverse opal structures through repeated self-assembly of fine particles. International Journal of Automation Technology. 2014;**8**(5):755-760. DOI: 10.20965/ijat.2014.p0755

[10] Li W, Xie F, Sun T, Liao Y. Fabrication of gold/silica composite artificial opal by a multiple-step electroplating process. Asia-Pacific Journal of Chemical Engineering. 2008; **3**(3):269-274. DOI: 10.1002/apj.145

[11] Wakayama H, Setoyama N, Fukushima Y. Size-controlled synthesis and catalytic performance of Pt nanoparticles in micro- and mesoporous silica prepared using supercritical solvents. Advanced Materials. 2003; **15**(9):742-745. DOI: 10.1002/adma.200304408

[12] Li H, Wang R, Hong Q, Chen L, Zhong Z, Koltypin Y, et al. Ultrasound-assisted polyol method for the preparation of SBA-15-supported ruthenium nanoparticles and the study of their catalytic activity on the partial oxidation of methane. Langmuir. 2004; **20**(19):8352-8356. DOI: 10.1021/la049290d

[13] Bachan N, Asha A, Jeyarani WJ, Kumar DA, Shyla JM. A comparative investigation on the structural, optical and electrical properties of SiO_2-Fe_3O_4 core-shell nanostructures with their single components. Acta Metallurgica Sinica. 2015;**28**(11):1317-1325. DOI: 10.1007/s40195-015-0328-3

[14] Holtz JH, Asher SA. Polymerized colloidal crystal hydrogel films as intelligent chemical sensing materials. Nature. 1997;**389**(6653):829-832. DOI: 10.1038/39834

[15] Lee YJ, Pruzinsky SA, Braun PV. Glucose-sensitive inverse opal hydrogels: Analysis of optical diffraction response. Langmuir. 2004;**20**(8): 3096-3106. DOI: 10.1021/la035555x

[16] Kuncicky DM, Prevo BG, Velev OD. Controlled assembly of SERS substrates templated by colloidal crystal films. Journal of Materials Chemistry. 2006; **16**(13):1207-1211. DOI: 10.1039/ B512734C

[17] Tsvetkov MY, Khlebtsov BN, Khanadeev VA, Bagratashvili VN, Timashev PS, Samoylovich MI, et al. SERS substrates formed by gold nanorods deposited on colloidal silica films. Nanoscale Research Letters. 2013; **8**(1):250. DOI: 10.1186/1556-276X-8-250

[18] González AL, Noguez C. Influence of morphology on the optical properties of metal nanoparticles. Journal of Computational and Theoretical Nanoscience. 2007;**4**(2):231-238. DOI: 10.1166/jctn.2007.2309

[19] Noguez C, Villagómez CJ, González AL. Plasmonics of multifaceted metallic nanoparticles, field enhancement, and TERS. Physica Status Solidi (B). 2015;**252**(1):56-71. DOI: 10.1002/pssb.201350416

[20] Yurkin MA, Semyanov KA, Tarasov PA, Chernyshev AV, Hoekstra AG, Maltsev VP. Experimental and theoretical study of light scattering by individual mature red blood cells by use of scanning flow cytometry and a discrete dipole approximation. Applied Optics. 2005;**44**(25):5249-5256. DOI: 10.1364/AO.44.005249

[21] Bronk BV, Druger SD, Czege J, Van de Merwe WP. Measuring diameters of rod-shaped bacteria in vivo with polarized light scattering. Biophysical Journal. 1995;**69**(3):1170-1177. DOI: 10.1016/S0006-3495(95)79991-X

[22] Draine BT. The discrete-dipole approximation and its application to interstellar graphite grains. The Astrophysical Journal. 1988;**333**: 848-872. DOI: 10.1086/166795

[23] Lazarides AA, Kelly KL, Schatz GC. Effective medium theory of DNA-linked gold nanoparticle aggregates: Effect of aggregate shape. MRS Online Proceedings Library Archive. 2001;**635**. DOI: 10.1557/PROC-635-C6.5

[24] Draine BT, Flatau PJ. Discrete-dipole approximation for periodic targets: Theory and tests. JOSA A. 2008; **25**(11):2693-2703. DOI: 10.1364/ JOSAA.25.002693

[25] Santos Gómez A, González AL. Far field optical properties of a monolayer of SiO_2 spheres and small Au nanoparticles. MRS Advances. 2018; **3**(64):3917-3923. DOI: 10.1557/ adv.2019.128

[26] DDSCAT code. User guide, download options and more are available from: http://ddscat.wikidot.c om [Accessed: 2019-08-02]

[27] Bohren CF, Huffman DR. Absorption and Scattering of Light by Small Particles. Wiley-VCH; 1998. 530 p. DOI: 10.1002/9783527618156

[28] Malitson IH. Interspecimen comparison of the refractive index of fused silica. JOSA. 1965;**55**(10): 1205-1209. DOI: 10.1364/ JOSA.55.001205

[29] Brixner B. Refractive-index interpolation for fused silica. JOSA. 1967;**57**(5):674-676. DOI: 10.1364/ JOSA.57.000674

[30] Braun MM, Pilon L. Effective optical properties of non-absorbing nanoporous thin films. Thin Solid Films.

2006;**496**(2):505-514. DOI: 10.1016/j.
tsf.2005.08.173

[31] Vos WL, Sprik R, van Blaaderen A,
Imhof A, Lagendijk A, Wegdam GH.
Strong effects of photonic band
structures on the diffraction of colloidal
crystals. Physical Review B. 1996;
53(24):16231. DOI: 10.1103/
PhysRevB.53.16231

[32] Romero-Cruz LA, Santos-Gómez A,
Palomino-Ovando MA, Hernández-
Cristobal O, Sánchez-Mora E,
González AL, et al. Surface enhanced
Raman scattering due to interstitial gold
nanoparticles into SiO_2 spheres array.
Superlattices and Microstructures. 2018;
123:71-80. DOI: 10.1016/j.spmi.
2018.02.022

[33] Stöber W, Fink A, Bohn E.
Controlled growth of monodisperse
silica spheres in the micron size range.
Journal of Colloid and Interface Science.
1968;**26**(1):62-69. DOI: 10.1016/
0021-9797(68)90272-5

[34] Turkevich J, Stevenson PC, Hillier J.
A study of the nucleation and growth
processes in the synthesis of colloidal
gold. Discussions of the Faraday Society.
1951;**11**:55-75. DOI: 10.1039/
DF9511100055

[35] Kimling J, Maier M, Okenve B,
Kotaidis V, Ballot H, Plech A. Turkevich
method for gold nanoparticle synthesis
revisited. The Journal of Physical
Chemistry B. 2006;**110**(32):
15700-15707. DOI: 10.1021/jp061667w

[36] Cong H, Yu B. Fabrication of
superparamagnetic macroporous Fe3O4
and its derivates using colloidal crystals
as templates. Journal of Colloid and
Interface Science. 2011;**353**(1):131-136.
DOI: 10.1016/j.jcis.2010.09.040

[37] Carmona-Carmona AJ, Palomino-
Ovando MA, Hernández-Cristobal O,
Sánchez-Mora E, Toledo-Solano M.
Synthesis and characterization of
magnetic opal/Fe_3O_4 colloidal crystal.

Journal of Crystal Growth. 2017;**462**:
6-11. DOI: 10.1016/j.jcrysgro.
2016.12.105

[38] Le Ru E, Etchegoin P. Principles of
Surface-Enhanced Raman Spectroscopy
and Related Plasmonic Effects. 1st ed.
Amsterdam: Elsevier; 2009. p. 688

Nanocomposites

Kinetic Features of Synthesis of Epoxy Nanocomposites

Vadim Irzhak

Abstract

Kinetic features of the formation of epoxy nanocomposites with carbon (nanotubes, graphene, and graphite), metal-containing, and aluminosilicate (montmorillonite and halloysite) fillers are considered. In contrast to linear polymers, epoxy nanocomposites are obtained only via the curing of epoxy oligomers in the presence of filler or the corresponding precursor. These additives may affect the kinetics of the process and the properties of the resulting matrix. A high reactivity of epoxy groups and a thermodynamic miscibility of epoxy oligomers with many substances make it possible to use diverse curing agents and to accomplish curing reactions under various technological conditions. The mutual effect of both a matrix and nanoparticles on the kinetics of the composite formation is discussed.

Keywords: polymer nanocomposites, epoxy matrices, nanoparticles, synthesis of composites, epoxy oligomers

1. Introduction

Since around the mid-1990s, polymer nanocomposites have become the subject of considerable attention, as evidenced by monographs, and a great number of reviews [1]. The application of nanocomposites is associated with their unique properties related to a huge specific surface and high surface energy of nanoparticles. Nanosized particles, as opposed to microinclusions and coarser inclusions, are not stress concentrators, and this circumstance facilitates a marked improvement in the mechanical properties of nanocomposites. Compared with the respective polymers, the transparency of nanocomposites does not decrease, because nanoparticles do not scatter light because of their small sizes. Depending on the type of nanoparticles introduced in polymeric materials even at a low concentration, nanocomposites acquire remarkable chemical (primarily catalytic), electrophysical, and biomedical properties, thereby opening wide potential for their use [1].

Among polymer nanocomposites, it would appear that composites based on an epoxy matrix occupy an insignificant place—nearly 10% as to the number of publications—but an ever-increasing number of papers appear annually. Moreover, the interest in them grows almost exponentially, as evidenced by the number of citations [2].

Epoxy polymers in terms of a set of properties stand out among other polymeric materials and play an important role in aerospace, automotive, shipbuilding, and other industries. Their wide application in engineering is associated, firstly, with a high processability of epoxy resins and, secondly, with the unique combination of performance characteristics of their curing products [3–5].

A high reactivity of epoxy groups and a thermodynamic miscibility of epoxy oligomers with many substances make it possible to use diverse curing agents and to accomplish curing reactions under various technological conditions [6–8]. Of no small importance are the features of synthesis processes, such as the absence of volatile products and low level of shrinkage.

Epoxy polymers have high values of static and shock strength, hardness, and wear resistance. They possess marked thermal stability and heat resistance. Many solid surfaces form strong adhesive bonds with epoxy polymers [2, 3]. This circumstance determines their use as compounds, glues, paint and lacquer materials, and coatings, including in aerospace engineering. Epoxy nanocomposites are designed to realize the unique functional properties of nanoparticles: electric, magnetic, optical, chemical, and biological.

Information about epoxy nanocomposites is contained most completely in [2]. Reviews [9, 10] are devoted to epoxy nanocomposites with carbon nanotubes (CNTs). Some aspects of epoxy nanocomposites containing graphene were covered in [11].

Taking into consideration the urgency of the issue and the presence of recent studies not covered in the mentioned reviews, author took a chance to consider epoxy nanocomposites containing metal and mineral nanoparticles, graphene, and CNTs and to discuss kinetic features of the processes of their formation.

2. Feature of synthesis of epoxy nanocomposites

The generally accepted scheme of the amino-epoxy cure involves two main reactions of the glycidyl ether:
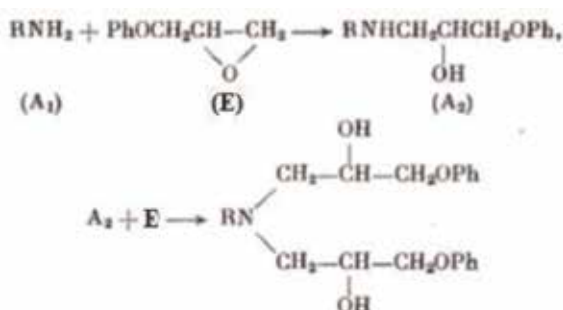
Epoxy-amine cure reactions scheme.

In principle, a reaction of esterification is possible—the resulting hydroxyls with epoxy groups.

The ratio of the rate constant of the secondary amine in addition to the corresponding constant of the primary one depends on electron-donating properties of an amine and may vary with temperature. Normally this ratio varies within 0.1–0.6. It is because of accumulation of hydroxyl groups during the reaction that the process of curing epoxy oligomers under the action of amines has autocatalytic character. Kinetics is often analyzed using empirical Eq. (1):

$$\frac{d\alpha}{dt} = (k_1 + k_2\alpha^m)(1 - \alpha)^n \tag{1}$$

$$\frac{d\alpha}{dt} = (k_1 + k_2\alpha)(1 - \alpha)^n \tag{2}$$

where α is the degree of conversion of epoxy groups; the sum of exponents $m + n$ defines the overall reaction order, which is usually two. Sometimes it is assumed

that $m = 1$ (Eq. (2)). Constants k_1 and k_2 reflect the autocatalytic character of the process.

From the standpoint of formation of epoxy nanocomposites, there are two types of fillers: fillers belonging to the first type are chemically unchanged and should be reduced to the desired size in one way or another. An example is provided by CNTs, diverse minerals, and graphene. Compounds whose chemical nature changes during composite formation belong to the second type. These are, in particular, metal salts, in which cations should be reduced to the zero-valence state.

In contrast to linear polymers, epoxy nanocomposites are obtained only via the curing of epoxy oligomers in the presence of filler or the corresponding precursor. It is evident that these additives may affect the kinetics of the process and the properties of the resulting matrix. The mechanism of curing of epoxy resins is fairly complicated, because many reactions occur simultaneously and depend on such phenomena as gelation and glass transition [6, 7]. After incorporation of nanoparticles into the epoxy resin, the process of its curing becomes even more complicated. A considerable number of papers concern the kinetics of curing of epoxy systems with various types of nanoparticles.

Most of kinetic studies are using DSC. DSC analysis has shown that etherification occurs at elevated temperatures once all the primary amines are exhausted. In this case, the data are analyzed as a rule in terms of the generalized formula:

$$\frac{d\alpha}{dt} = k(T)f(\alpha) \tag{3}$$

For nonisothermal conditions the temperature varies with time with a constant heating rate, $\beta = dT/dt$.

Isoconversional kinetic analysis has shown that the reaction rate at constant conversion depends only on the temperature. In other words,

$$E_a = -Rd\ln\left(\frac{d\alpha}{dt}\right)/dT^{-1} \tag{4}$$

where E_α is the effective activation energy at a given conversion. The energy of activation was determined by varying the rate of scanning. Multistage processes show the dependence of E_α on α, the analysis of which helps not only to reveal the complexity of the process but also to identify its kinetic scheme. So, for example, starting from Eq. (1), we get [12]

$$E_a = -(k_1E_1 + \alpha^m k_2 E_2)/(k_1 + \alpha^m k_2) \tag{5}$$

The analysis performed in [12] showed that the calculation can be reconciled with the experiment by specifying the values of E_2 and m. Thus, we can assume that Eq. (1) adequately describes the experimental data. Namely, this approach is used to study the effect of various additives on the kinetics of epoxy nanocomposites' formation.

3. Influence of the fillers on the nanocomposite synthesis process

3.1 Carbon fillers: CNTs, graphene, graphite, and carbon fiber

Taking into consideration the molecular structure of carbon nanoparticles, in particular, graphene and CNTs [13–17], it may be stated that their influence on the

kinetics of the process of curing of epoxy oligomers will be similar. Indeed, graphene, CNTs, and other compounds with the sp^2-hybridized carbon can catalyze diverse organic reactions [18–20]. Their surface energy is fairly high; therefore, the adsorption of various molecules is typical of them [21–24]. The components of epoxy binders are not exceptional in this respect. Adsorbed molecules may be involved in the process of matrix formation in a certain manner.

In work [25] the high-temperature isothermal curing of tetraglycidyl-4,4′-diamino-diphenylmethane with 4,4′-diaminodiphenyl sulfone (DDS) in the presence of multi-wall CNTs was investigated.

The typical technique used to prepare the reaction mixture for kinetic studies of the process will be described below, and the techniques described in other papers may differ from the typical one only in some details.

A mixture of an epoxy resin with preliminarily purified multi-wall CNTs was sonificated for 2 h and placed in an oil bath at temperature of 120°C, and the stoichiometric amount of a curing agent was slowly added under continuous mechanical stirring until formation of a homogeneous mixture. This process took nearly 10 min.

The kinetics was analyzed using Eq. (1). It was found that with the increase in concentration of CNTs, constant k_1, which defines the initial rate of reaction, grows, while the corresponding activation energy drops. The autocatalytic constant k_2 is practically unaffected by the presence of tubes. Xie et al. [25] believe that these effects may be attributed to the catalytic effect of surface hydroxyl groups that arise as a result of oxidation during the purification of CNTs.

The initial acceleration of the reaction under the action of single-wall CNTs was also observed [26], but the magnitude of this effect was insignificant. At the same time, the glass-transition temperature T_g decreased, thus suggesting a reduction in the degree of cross-linking of the matrix [6].

The effect of concentration and type of CNTs (single-, double-, and multi-wall) on the kinetics of reaction between low-viscosity mixture of epoxy oligomers and amine curing agents was studied by Esmizadeh et al. [27]. The analysis was conducted in terms of the equation:

$$\frac{d\alpha}{dt} = k(T)\alpha^m(1 - \alpha)^n \tag{6}$$

It was shown that the type of CNTs exerts almost no effect on kinetic parameters possibly because of their low concentration (0.01%). At a concentration of 0.1, 0.2, and 0.5%, the rate constant changes nonmonotonically, but on the whole it is lower than that in the absence of CNTs. The energy of activation increases from ~6 to ~9 kJ/mol. The heat of reaction decreases, indicating the incompletion of the process. This is also evidenced by a decrease in the high-elasticity modulus, i.e., matrix network density. In accordance with [27], the observed effects may be explained by the increase in the viscosity and thermal conductivity of the system in the presence of CNTs, although these properties were not estimated.

Multi-wall CNTs, when taken at low concentrations (0.5%), slightly accelerate the reaction of amine curing of bisphenol F diglycidyl ether, while at higher concentrations (1.5%) decelerate this reaction as shown by Visco et al. [28]. They believe that the rate of the process is controlled by viscosity of the system.

The curing of an epoxy resin is regarded as a heterogeneous phase formation process, and the role of multi-wall CNTs is discussed from this viewpoint by Susin et al. [29]. They believe that the tubes restrict the local free volume and assist in the development of the heterogeneous morphology in resin, especially at high content of multi-wall CNTs. At the same time, with the increase in their concentration

(to 1%), the ultimate heat of reaction increases, while the energy of activation decreases.

Most of kinetic studies are aimed at gaining insight into the effect of functionalized CNTs using DSC. Rahaman and Mohanty [30] presented the data of the influence of multi-wall CNTs carrying COOH groups on the process of curing of epoxy resin EPOLAM with anhydride of 1,2,3,6-tetrahydroxymethyl-1,3,6-methanephthalic acid. According to these authors, this dependence provides evidence that in the presence of multi-wall CNTs, the degree of cross-linking increases; as a result, the mobility of unreacted groups declines. The closeness of the curves at the beginning of the curing process indicates that the addition of CNTs does not affect the value of E_1. From the form of the divergence of the curves in the course of the reaction, it follows that the entrainment of the filler leads to an increase in E_2.

Note that methods using the dependence of a change in the exothermal peak on the rate of heating cannot provide reasonable isothermal predictions for the kinetics of curing of epoxy compounds because of the autocatalytic character of the process [6, 7]. The presence of at least two kinetic constants, as in Eq. (1), should be taken into account.

In this context, deserve attention other methods, which, depending on the type of study or the nature of epoxy resins, can be successfully used [31]. Among them, for example, the method of luminescence spectroscopy makes it possible to determine the degree of conversion with high accuracy at the final stage of reaction. This is hardly achievable by other methods. Analysis with the aid of a rheometer provides information about the time of gelation which cannot be obtained by another method.

The DSC studies [32] showed that multi-wall CNT with COOH functionalization act as catalysts, stimulating the initial stage of curing of bisphenol A diglycidyl ether (BADGE). This accelerating effect is noticeable even at a 1% content of multi-wall CNTs. Nonfunctionalized multi-wall CNTs decrease the degree of cross-linking, as evidenced by a lower overall heat of reaction and lower glass-transition temperatures of the nanocomposites compared with the neat epoxy resin. At the same time, the functionalization of multi-wall CNTs increases the degree of cross-linking.

Compared with the neat epoxy resin, 1% of carboxylated multi-wall CNTs decreases the heat of reaction and increases the energy of activation [33]. Fluorinated tubes insignificantly influence the value of E_a but lower the ultimate degree of conversion Q_{lim}.

The grafting of butylamine onto plasma- and CF_4-treated single-wall CNTs markedly improves the ultimate conversion, whereas clean tubes, when the reaction is accomplished in the nonisothermal regime, have no effect on this parameter, while in the case of the isothermal regime (30°C), they decrease it [34].

There was another conclusion [35] that clean and aminated single-wall CNTs reduce the ultimate heat of reaction. Tubes with the grafted epoxy groups give almost the same value of heat as that obtained in the curing of resin without any filler: 355 versus 362 J/g. It is possible that different results may be attributed to different concentrations of single-wall CNTs.

The kinetic analysis of the curing process in terms of Eq. (1) does not reveal marked differences in the values of constants and exponents for the systems of interest. However, it was shown [36] that the introduction of 3% of clean multi-wall CNTs does not influence the kinetics of reaction, but tubes with grafted amino groups decrease the constant k_1 by factor of almost 2.5, increase k_2 by factor of 3, and decrease exponent m from 0.53 to 0.27.

Multi-wall CNTs with amino groups decelerate the curing of BADGE with 2-ethyl-4-methylimidazole at concentrations of 0.5 and 1 wt % [37], but the deceleration effect vanishes at a concentration of nanoparticles of 3%. However, in this

case, the value of ultimate reaction heat decreases as well. Note that clean multi-wall CNTs accelerate curing of the same reaction system [32].

The impact of multi-wall CNTs carrying acidic and amino groups on the process of curing was studied by Raman and luminescence spectroscopy [38]. Throughout the reaction conducted in the presence of nanoparticles, the rates were higher than the neat resin. The difference in the rates of curing was explained by homogeneity of the sample and the presence of chemical groups.

The kinetics of the amine curing of BADGE in the presence of multi-wall CNTs functionalized by oxygen-containing groups using viscometry and transmission electron microscopy along with calorimetry was analyzed [39]. The samples of multi-wall CNTs had different values of specific surface S. This factor was found to be decisive in the kinetic study of reaction: if at the onset the rates were equal, then, by the time of attaining the maximum rate W_{max}, the higher the value of S, the more pronounced the deceleration of the process, so that the time of attaining W_{max} increased. Afterward, the inverse effect was observed, namely, acceleration, so that the higher the value of S, the more pronounced the final heat release. The rheokinetic study demonstrated that the time of a sharp gain in viscosity of the system (the gel point) also shifts to longer times with an increase in S. However, variation in the concentration of multi-wall CNTs (to 5%) insignificantly influences the kinetics of reaction.

The kinetic features of the process may become understandable if the micrograph of the epoxy composition which is measured at the initial stage of curing performed in the presence of multi-wall CNTs is examined (**Figure 1**). It is seen that compact polymer structures grow along the tube. Evidently, hydroxyl groups grafted on the surface catalyze the reaction of epoxy groups with amine [7] to give rise to new hydroxyl groups accelerating this reaction. In doing so, the process of polymer formation is localized, and the reaction assumes the frontal character. The natural consequence of the localization process is the formation of ineffective cross-links. Therefore, the value of critical conversion increases, and correlation is observed between the time of a sharp gain in viscosity and the specific surface of multi-wall CNTs.

It was shown that graphene oxide (GO) accelerates the curing of tetraglycidyl-4,4′-diaminodiphenylmethane with 4,4′-diaminodiphenyl sulfone [40]. According to this work, this effect is related to the presence of hydroxyl and carboxyl groups on the surface of GO.

The kinetics of the nonisothermal curing of BADGE with liquid poly(amido-amine) in the presence of amine-functionalized GO using Eq. (6) was investigated [41]. It is seen that for the systems without any filler and in the presence of GO containing NH_2 groups, the parameters of this equation are similar. At the same time, GO slightly decelerates the process.

The mixture of BADGE and 1,1,2,2-tetra(p-hydroxyphenyl)ethane tetraglycidyl ether with diethyltoluenediamine in the presence of graphene was cured [42]. It was shown that the latter somewhat accelerates the reaction and increases T_g by 15–25°C. Previously, the same authors showed using Eq. (1) that this effect is

Figure 1.
Initial stage of curing of the epoxy matrix in the presence of COOH-functionalized CNTs. Reprinted with permission from IAPC "Nauka" [39].

associated with an increase in constant k_1 and the functionalization of graphene by amine enhances the effect of the filler [43].

The IR spectral analysis of the curing of BADGE with 4,4'-diaminodiphe-nylmethane in the presence of GO permitted to obtain kinetic curves for both epoxy groups and primary, secondary, and tertiary amino groups [44]. These studies made a considerable contribution to gaining insight into the mechanism of reaction. It was shown that the original GO has no effect on the overall kinetics of the process and even decelerates the consumption of primary amino groups. But after autoclave purification, GO increases the rate of reaction of epoxy groups by more than factor of 2 and the rate of reaction of primary amino groups by factor of 1.8. As was shown by X-ray photoelectron spectroscopy, purification leads to a marked reduction in the amount of oxygen-containing groups on the surface of GO. The glass-transition temperature of a nanocomposite based on the crude GO is much lower than that of the epoxy matrix, whereas the purification of GO causes an increase in this parameter, although T_g does not attain the T_g value of the matrix.

The influence of various graphite fillers (graphite with a high surface area, graphite oxide, and exfoliated graphite oxide) on the reaction of epoxy ring opening of BADGE by amines—primary (benzylamine and cyclohexylamine) and secondary (dibenzylamine)—and hydroxyl (benzyl alcohol) was studied [45]. These data indicate the strong catalytic effect of fillers on the reaction with amines. This effect is the most pronounced for the exfoliated graphite oxide. In the case of benzyl alcohol, interaction with epoxy groups was observed only for graphite oxide. A similar effect was caused by fillers on the process of matrix formation: in the presence of graphite fillers, the rate and heat effect of the reaction grow, and the gel point shifts to smaller times.

In essence, analogous data were reported by Mauro et al. [46]. These authors believe that a marked rise in the T_g of nanocomposites compared with the neat matrix is an evidence of the catalytic effect of graphite with a high surface area (308 m^2/g) and graphite oxide. The catalytic effect of graphite was confirmed using the reaction of epoxystyrene with benzylamine.

On the other hand, it was found that the samples of graphite oxide with carboxyl or amino groups have almost no effect on the kinetics of nonisothermal curing of BADGE with 4,4'-diaminodiphenylmethane [47]. Possibly, this is related to a low concentration of the fillers (0.5%).

The effect of carbon nanofibers (diameter of 100–200 nm and length of 30–100 μm) oxidized in a solution of nitric acid and then treated with 3-glycidox-ypropyltrimethoxysilane on the kinetics of curing of epoxy resin Cycom 977 described by Eq. (1) was studied [48]. It was shown that all kinds of fibers exert a catalytic effect which manifests itself as an increase in ultimate conversion and growth of kinetic constants k_1 and k_2. Note that E_{a1} decreases, while E_{a2} increases. In terms of catalytic efficiency growth, the fibers may be arranged in the following sequence: untreated, oxidized (COOH groups on the surface), and treated with silane (epoxy groups on the surface).

The catalytic effect of a carbon nanofiber was observed: the ultimate conversion and the kinetic constants in Eq. (1) increase, while the respective activation energies decrease [49]. The higher activity is exhibited by fiber whose surface is modified through the oxidative polymerization of aniline (in accordance with the authors, the "nanograssy" coating).

The above results are rather contradictory, which is probably caused by ambiguity in the concentration of the filler, uncertainty in the degree of dispersion, and the magnitude and structure of its surface.

3.2 Noncarbon fillers: oxides of metals and silicon

The effect of Al_2O_3 nanoparticles on the kinetics of polycondensation of BADGE under the action of diethylenetriamine using modulated DSC was explored [50]. As a result, not only the rate of the process was registered, but also variation in the heat capacity of the system during the process was monitored. It was shown that the filler increases the rate of reaction but decreases the ultimate heat. Viscosity measurements confirmed that the formation of the polymer network accelerates in the presence of nanoparticles, and the gel point shifts not only with time but also with conversion. This implies that nanoparticles are directly involved in the formation of intermolecular bonds. At the same time, experiments with water additives revealed that nanoparticles affect the kinetics of the curing reaction in qualitatively the same manner as Al_2O_3 nanoparticle [51]. The authors inferred that water adsorbed by nanoparticles is responsible for the catalytic effect.

DSC was used to examine the effect of additives of Al_2O_3 and ZnO nanoparticles on the curing of BADGE with *o*-tolylbiguanidine [52]. Both oxides decelerate the reaction but increase the ultimate limiting degree of conversion. Exponents *m* and *n* in Eq. (6) remain almost unchanged, whereas the activation energy decreases. Note that in the case of ZnO, this decrease is considerable.

At a fairly low concentration (1 and 5%), ZnO nanoparticles accelerate the reaction of BADGE with 2,2'-diamino-1,1'-binaphthyl; at concentration of 10%, their catalytic efficiency declines, while at content of 15%, retardation is observed [53]. Compared with the neat matrix, nanocomposites feature higher values of ultimate heat and glass-transition temperature with the maximum values corresponding to 5% content of nanoparticles. Probably, reduction in the catalytic activity of nanoparticles with increasing concentration may be attributed to their aggregation; as a result, the effective surface decreases.

Ghaffari et al. [54] studied how the size of ZnO nanoparticles affects the kinetics of BADGE curing with poly(aminoamide). Nanoparticles were sheets with a thickness of nearly 20–40 nm, while microparticles were rods with a length of $\sim$1 μm. Analysis was performed using Eq. (5). It was found that the autocatalysis of reaction is absent; that is, *m* = 0 and *n* is somewhat above unity. For both composites, compared with the neat matrix, the energy of activation decreases, but the rate constant slightly grows in the case of the microcomposite and declines in the case of the nanocomposite.

BADGE with the propylenimine dendrimer carrying eight end groups -NH_2 in the presence of Fe_2O_3 nanoparticles was cured [55]. The latter manifested the catalytic effect. The higher the concentration of nanoparticles, the more pronounced the increase in ultimate conversion and glass-transition temperature. It is shown that the kinetics of formation of the nanocomposite containing 10% Fe_2O_3 is adequately described by Eq. (2). No data are available for other systems, including the neat matrix. A similar result was reported in [56]. It was shown that the kinetics of curing of glycerol diglycidyl ether with 3,3'-dimethylglutaric anhydride in the presence of Al_2O_3 obeys Eq. (2).

Nanoparticles of metal oxides are able to adsorb components of the reaction system to one extent or another [57]. Possibly, their kinetic role is associated with this property.

Direct measurements of the complex specific heat capacity demonstrated that the interaction of SiO_2 nanoparticles and BADGE molecules is very weak [58]. At all stages of polymer network formation, the interaction of nanoparticles and matrix is of a physical origin. The effect of the filler on the kinetics of curing was insignificant.

In contrast, acceleration of the process was observed [59, 60]. The kinetic studies revealed that the catalytic effect of SiO_2 nanoparticles is related to the presence

of hydroxyl groups on their surface [61]. When the latter groups are changed for epoxy groups, the effect of nanoparticles on the kinetics of BADGE reaction with *m*-phenylenediamine is eliminated.

3.3 Minerals

For polymer nanocomposites, the most popular fillers from the class of minerals are layered silicates [62], which are sometimes called nanoclays, in particular, montmorillonite (MMT). The structure of its crystal lattice is such that it can adsorb various ions (mostly cations) and swell in polar liquids owing to their penetration into the interlayer space [63, 64].

At the nanometer scale, MMT is composed of three-layer stacks ~0.7 nm in thickness and several hundred nanometers in length and width. At micron level, these stacks are united into primary particles with interlayer distance of about 1.35 nm. At higher level, they form aggregates. During formation of nanocomposites, stacks should be exfoliated in order to reach a high area of contact with the matrix. In order to facilitate exfoliation, the surface of stacks should be treated for the purpose of changing their hydrophilic nature to hydrophobic, because the hydrophilic character of the silicate surface hampers the dispersion of MMT. Neutral organic compounds may form complexes with interlayer cations; for example, alkylamines are transformed into alkylammonium cations. These properties of MMT govern the kinetic features of formation of epoxy nanocomposites.

In the absence of the curing agent (1,3-phenylenediamine), the modified MMT and even the unmodified MMT promote the homopolymerization of BADGE at a high temperature [65]. Depending on the nature of the intercalated modifier (octadecyl-, trimethylstearyl-, methyldihydroxyethylammonium), MMT may either catalyze the reaction of the epoxy oligomer or react with a prepolymer or a curing agent.

At the same time, it was found that MMTs modified with alkylamines weakly accelerate [66–68], retard [69], or do not affect at all [70] the kinetics of curing of epoxy oligomers with amines. A weak acceleration was also observed for the unmodified MMT and MMT with intercalated 3-aminopropylethoxysilane [71].

Thus, it should be stated that the rate of curing of epoxy oligomers is almost insensitive to the presence of MMT. However, the kinetics of formation of polymers is not reduced only to a change in the concentration of reactants: structure formation should be taken into account. Even to a higher extent, this applies to a nanocomposite, whose properties are determined not only by structural levels of polymer matrix but also by the structure of nanoparticles and the character of their distribution in the material bulk.

As was noted above, MMT requires exfoliation. Namely, this process occurs during the chemical reaction, and its efficiency depends on the reaction conditions. For example, it was shown [72] that the cationic polymerization of triglycidyl-*p*-aminophenol occurs within the interlayer space, which entails the exfoliation of MMT, whereas with DDS the epoxy oligomer reacts outside the interlayer cavity. An increase in temperature is favorable for the former reaction: ultimate conversions inside and outside the cavity are 0.19 and 0.74, respectively, at 120°C or 0.76 and 0.77 at 180°C.

The optimum structure of epoxy composites was achieved when BADGE was cured with poly(ester diamine) in the nonisothermal regime at low rise in temperature (2.5 and 5 K/min) [73]. Small-angle X-ray scattering studies revealed the exfoliation of MMT in the matrix. The authors of [74] used hyperbranched polyethylenimine with end amino groups as a curing agent and attained effective exfoliation. A comparison of three systems, such as

triglycidyl-*p*-aminophenol + DDS, BADGE + poly(ester diamine), and BADGE + hyperbranched polyethylenimine, showed [75] that the exfoliation ability of MMT decreases in the mentioned sequence.

As was reported in [76], the nonisothermal curing of epoxy oligomers with amines in the presence of MMT includes four different reactions: formation of the matrix via the interaction of epoxy groups with the diamine curing agent, intracavity homopolymerization, and two homopolymerization reactions outside MMT which are catalyzed by onium ions of organically modified clay and tertiary amines.

X-ray diffraction was used to probe the exfoliation of MMT intercalated by octadecylammonium during the isothermal curing of BADGE with DDS [77]. It was shown that this process may be divided into three different stages (**Figure 2**).

The first stage is related to the penetration of BADGE into the interlayer space of MMT; at the second stage, the cationic polymerization of the epoxy resin catalyzed by ammonium takes place; and at the third stage, BADGE sorbed by MMT is cured with amine.

In order to identify the intracavity polymerization, mixture of MMT and triglycidyl-*p*-aminophenol was held at various temperatures for tens of days in the absence of the amine curing agent. Afterward, DDS was added and the curing process was conducted in the nonisothermal regime [78]. A similar procedure was employed for the system BADGE-MMT-poly(ester diamine) [79]. At the first stage, the epoxy equivalent and the glass-transition temperature increased. This technology makes it possible to improve both the degree of dispersion of MMT in the epoxy resin and the subsequent exfoliation of the clay during formation of epoxy nanocomposites. The period of the intracavity polymerization was reduced to tens of minutes by the use of complex $BF_3 \cdot C_2H_5NH_2$ as a catalyst [80].

An attempt to accomplish the intracavity polycondensation was made by Jagtap et al. [81]. In contrast to the commonly used MMT modifiers, i.e., polyalkylamines, they used half-neutralized salt of poly(ester diamine), which was intercalated via ionic exchange in an aqueous-organic solution, assuming that these macromolecules, when fixed by the ionic end on the walls of the cavity, will react with epoxy groups of the binder via its free amine end. However, no direct evidence for this reaction is available [81].
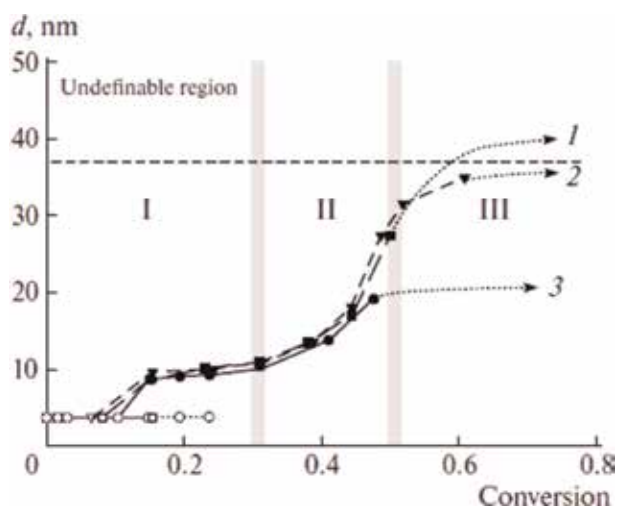

Figure 2.
Change in distance d between MMT sheets during the isothermal curing of BADGE at (1) 140, (2) 130, and (3) 120°C. Roman numerals denote stages of the exfoliation process. Arrows indicate the expected tendency of exfoliation. Reprinted with permission from Am. Chem. Soc. [77].

3.4 Metal-containing nanoparticles synthesized in situ

The synthesis of metal-containing nanoparticles for producing nanocomposites may be accomplished by various physical processes on the preformed matrix containing molecules of appropriate precursors [82–87]. Physical methods of obtaining metal-containing nanoparticles (photolysis, radiolysis, and thermolysis) are as a rule accompanied by chemical reactions leading to their formation. An important factor is the diffusion of preformed substances (metal atoms): the glassy state of the matrix provides a considerable obstacle to diffusion. For example, *N*-cetylpyridinium tetrachloroaurate was dissolved in methyl methacrylate and, after polymerization of the latter, was subjected to UV radiation. However, the formation of gold nanoparticles was registered only at temperatures above T_g of the polymer [88].

A substantially different method involves the combination of processes of formation of matrix and metal-containing nanoparticles, i.e., formation of nanocomposites in situ.

The main chemical method used at moderate temperatures includes the reduction of chemically bound metal atoms in nonpolar media. These methods of chemical reduction are the subject of most publications [83, 87, 89–93]. Mechanisms controlling formation of metal-containing nanoparticles in situ are highlighted in the review [94].

The transformation of the resulting single-valence atoms, or monomers, into nanoparticles includes nucleation stages with formation of primary clusters or stable particles, their growth by addition of monomers, possible subsequent coagulation, and/or Ostwald ripening. The kinetics of all these stages determines the size distribution function which strongly affects the ways and possibilities of the nanoparticles and corresponding nanocomposites' application. An important role in this is played by a polymer medium in which chemical reactions take place, including the ability of its components or fragments of macromolecules to be adsorbed on the particles, as well as the possibility of formation of micelle-type structures.

With rapid decay of the precursor, there will be a supersaturation of the system with a monomer. In this case, in the first approximation, nucleation will be described by Gibbs-Volmer-Frenkel thermodynamic theory [95, 96], according to which the radius of the critical nucleus is determined by the formula:
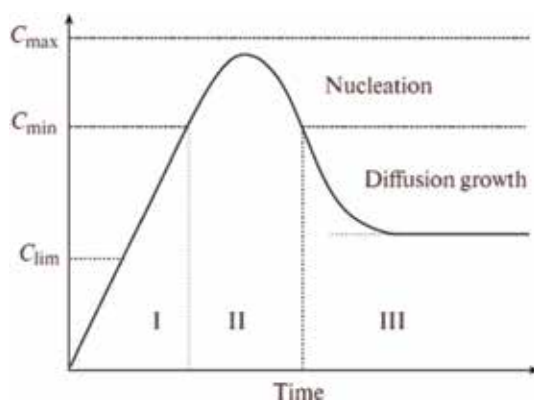
$$r_c = \frac{2\sigma V_m}{RT \ln S} \tag{7}$$

Figure 3.
LaMer pattern (see text for explanations).

where r_c, σ, and V_m are radius, surface tension, and molar volume of the critical nucleus, R is the gas constant, T is temperature, and S is the supersaturation. In this case, the nucleus will be unstable if $r < r_c$, and it stabilizes when $r \geq r_c$.

A qualitative picture of nucleation kinetics on the basis of the classic thermodynamic notions was proposed by LaMer and Dinegar [97]. The pattern illustrating their idea is shown in **Figure 3**.

Rapid increase in the concentration of monomer will lead to the achievement of the critical value of C_{min} (region I, the stage of prenucleation) and then overcome C_{min}. Exceeding this value gives rise to proper nucleation. Because of the balance between the rate of formation of the monomer and its expenditure consumption on nucleation and growth of the generated nuclei, the concentration will reach a peak, C_{max}, and then begin to decrease due to an increase in consumption for growth and again reach the critical level of C_{min}, marking the end of the nucleation stage (region II). After that, the concentration of the monomer will continue to decrease to the equilibrium value of C_0, expending on the growth of nucleus without renucleation, due to the fact that the supersaturation is below the critical level (region III).

Although short spatial and temporal scales of the nucleation stage hamper the direct observation of the classic process, to trace the time-resolved formation of silver CNs using small-angle X-ray scattering in situ was managed [98]. Silver perchlorate was reduced with sodium boron hydride in an aqueous solution. As shown in **Figure 4**, the nanoparticles' nucleation kinetics corresponds to the LaMer pattern: the number of particles initially grows without any appreciable change in their sizes, attaining a maximum in fractions of a second. Further, the number of nanoparticles descends, and their radius increases. This corresponds to stage III in the pattern, and nanoparticles interact with each other alongside with their simple growth via the reaction with monomers, i.e., the aggregation mechanism is engaged.

However, under conditions of formation of composites, it is hardly possible to implement such a mechanism. An alternative variant was obtained in [99]. When studying the synthesis of gold by reducing $HAuCl_4$ with sodium citrate, it was shown that rapid nucleation is not observed; on the contrary, the kinetic curve of accumulation of critical nuclei is S-shaped with a more or less extended induction period. The authors suggested that such features of the process are due to redox reactions leading to the conversion of gold cations to a zero-valent atom and citrate ion to acetone dicarboxylic acid. In this case, the supersaturation of the system by
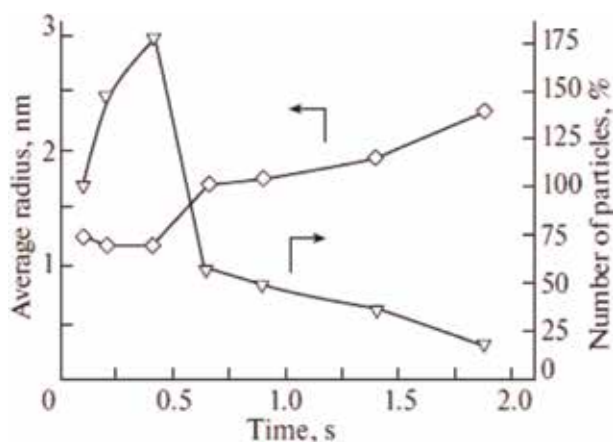

Figure 4.
Kinetics of change in the average radius and number of particles for first 2 s. Reprinted with permission from Am. Chem. Soc. [98].

the monomer, Au(0), is absent. Obviously, in this case the concept of a critical nucleus becomes meaningless.

Later it was established that S-shaped kinetics is inherent in many metals with variable valence (see, e.g., the review [100]). To describe such processes, a rather simple two-step scheme was proposed by Watzky and Finke [101]:

$$A \xrightarrow{\quad k_1 \quad} B$$
$$A + B \xrightarrow{\quad k_2 \quad} B_2 \tag{8}$$

The first stage is the slow nucleation of "kinetically efficient" clusters B from precursor A, and the second stage is the particle's fast growth reaction. In the original studies, in particular in [99], A represented complex $[(n\text{-}C_4H_9)_4N]_5Na_3[(1,5\text{-}cyclooctadiene)Ir\,P_2W_{15}Nb_3O_{62}]$, and B was the catalytic surface of a $Ir_n(0)$ nanocluster.

Studies of a wide range of systems show (see [94]) that the value depends on the number of catalytic active nuclei, namely, their ratio with increasing ratios k_2A_0/k_1 for practically unchanged diameters of the order of 2 nm. These factors—the medium, active additives, and temperature—make it possible to achieve the formation of an almost monodisperse distribution (width not exceeding 15%) of the nanoparticles with a size determined, as a rule, by a "magic number" (number of atoms in the outer filled nanoparticle shell: 13, 55, 147, 309, etc.).

The processes of formation of zero-valence atoms or other monomers inevitably lead to their clustering. To stabilize clusters in a nonpolar solution, it is necessary to have amphiphilic molecules capable of forming adsorption layers and thereby form inverse micelles from the nanoparticles.

At the same time, when the epoxy nanocomposite films are stored under light for a while, the optical density D_{max} in the region of the surface plasmon resonance of silver nanoparticles decreases. Similar changes are observed in the spectra and at storage of films in the dark [102] (**Figure 5**). The kinetic curves are described by the first-order equation (**Figure 5a**, straightening in **Figure 5b**)

$$D_{max} = D_{lim} + A \exp\{-kt\} \tag{9}$$

in which D_{lim} = 0.534 (in the dark) and 0.42 (in the light).

Accordingly, the value of the limiting conversion of nanoparticles under light is higher than in dark: the conversion under light is 0.29, while in dark, the conversion is 0.11.

The decrease in D_{max} in time means a drop in the total concentration of metallic silver, apparently due to its "dissolution." The relatively recent discovery of digestive ripening (DR), which represents the transfer of atoms from large metal nanoparticles to smaller ones [94, 103], indicates the possibility of such a process.

Although the mechanism of the DR process is not fully understood, there are grounds believe that the equation proposed in [104, 105] for describing the kinetics of Ostwald ripening (OR) is applicable to DR. The latter is one of the options for the growth of the nanoparticles, when large particles grow at the expense of small particles. According to the theory, the change in the radius r of a spherical particle in time will obey the equation:

$$\frac{dr}{dt} = \frac{K_D}{r^2}\left(\frac{r}{r_c} - 1\right) \tag{10}$$

where $K_D = \frac{2\sigma V^2 D C_0}{RT}$, D is diffusion coefficient, V is molar volume, and C_0 is solubility of the monomer; R is the gas constant and T is temperature; r_c is determined by equation (7).
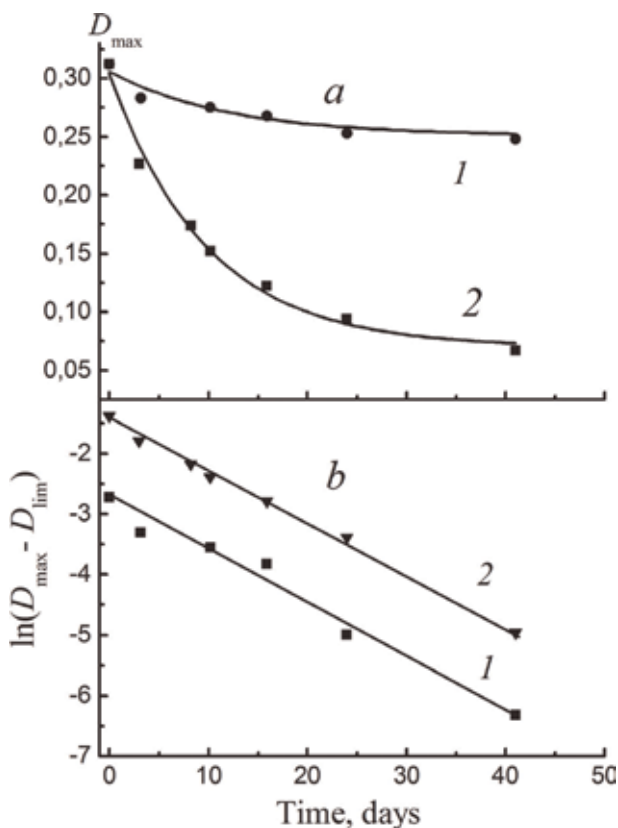
Figure 5.
Kinetics of the decrease in the concentration of silver nanoparticles in dark (1), in light (2), in natural (a), and in semi-logarithmic (b) coordinates. Reprinted with permission from IAPC "Nauka" [102].

As can be seen, the particles grow if $r \geq r_c$, and their dimensions decrease otherwise. This is the physical meaning of the phenomenon of OR.

A vivid example of reversible OR and DR was demonstrated by Xin and Zheng [106]. They observed fluctuating growth of bismuth nanoparticles in the absence of precursor at 180°C. The reaction system consisted of a limited number of large Bi nanoparticles (80–150 nm in diameter) in a solution of oleylamine (surfactant) and dichlorobenzene. The Bi nanoparticles served as a source of monomeric Bi(0).

The process includes formation and growth of small particles due to large ones (DR) with simultaneous OR. The total number of particles increased for a while and then changed to the fluctuation mode. The total volume of content fluctuated near a certain level evidently given by the total volume of initial Bi nanoparticles. The size of each of the observed particles and their assemblies experienced similar fluctuations.

Obviously, the first stage of the DR process is the disassembly of small nanoparticles on zero-valence atoms and metal clusters. Under normal conditions, they subsequently lead to formation of nanoparticles, which require their diffusion displacement. But under the conditions of a glassy matrix, diffusion is difficult, if not forbidden at all. Therefore, the entire process is reduced to the first stage, i.e., "dissolution" of large nanoparticles with the formation of zero-valence atoms and silver clusters. The presence of a limit, apparently, is due to the saturation of the boundary zone surrounding the particle by the zero-valence atoms and clusters of silver formed.

As precursors soluble in organics, complexes of univalent gold $[O(AuPR_3)_3]$ (CF_3SO_3) (R = Ph or CH$_3$) [107], $[RN(CH_3)_3][Au(SC_{12}H_{25})_2]$ (R = C$_8$H$_{17}$, C$_{12}$H$_{25}$, and C$_{14}$H$_{29}$), and $[(C_{18}H_{37})_2N(CH_3)_2][Au(SC_{12}H_{25})_2]$ were proposed by Nakamoto et al. [108]; salts of organic acids with a fairly bulky (even high-molecular-mass [109–111]) radical, 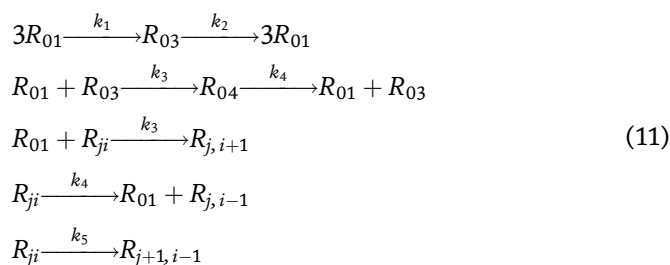such as silver myristate $C_{13}H_{27}COOAg$, copper oleate $(C_{18}H_{33}COO)_2Cu$, silver oleate, silver octanoate $C_7H_{15}COOAg$, silver stearate $C_{17}H_{35}COOAg$, silver 2-hexyldecanoate $p\text{-}C_8H_{17}CH(n\text{-}C_6H_{13})COOAg$, *cis*9-octadecanoate $p\text{-}C_8H_{17}CH=CH(CH_2)_7COOAg$, and silver neodecanoate $CH_3(CH_2)_3C(CH_3)_2COOAg$, have enjoyed popularity [107, 112–117].

However, the nonideal state of solutions of these compounds should be taken into account. This implies that, when a certain concentration is exceeded, precursors in solution are united into associates, i.e., are clustered. Evidently, this circumstance cannot be disregarded when considering feasible mechanisms governing formation of metal-containing nanoparticles.

The silver nanoparticles by the reduction of alkyl carboxylates in trimethylamine at 78°C were synthesized [118, 119]. It was found that the induction period grows and the maximum rate decreases in the following sequence: decanoate, myristate, and stearate. But in this sequence, the length of the hydrocarbon radical of carboxylates (C$_9$, C$_{13}$, and C$_{17}$) increases. It is reasonable to assume that solubility grows in the same sequence and, hence, the possibility of formation of clusters decreases. Thus, there is a direct relationship between the rate of formation of nanoparticles and the concentration of precursor clusters.

This idea underlies the theory of formation of metal-containing nanoparticles from precursors of the silver carboxylate type via their reduction which was put forth [120].

The model adopted for the formation of metal-containing nanoparticles may be presented as follows. Carboxylates reversibly form triangular and tetrahedral clusters. The development of larger clusters is not allowed because of steric reasons. The reduction of cation in them occurs. As a result, the adsorption of new salt molecules becomes possible. Indeed, if for carboxylates the tetrahedral structure is limiting, then the metal atom in the limit may be surrounded by 12 molecules (the icosahedron structure). It is assumed that the concentration of the reducing agent is high, so that the corresponding reaction is pseudo first order. Thus, the kinetic scheme may be written as follows:

$$3R_{01} \xrightarrow{k_1} R_{03} \xrightarrow{k_2} 3R_{01}$$
$$R_{01} + R_{03} \xrightarrow{k_3} R_{04} \xrightarrow{k_4} R_{01} + R_{03}$$
$$R_{01} + R_{ji} \xrightarrow{k_3} R_{j,\,i+1} \tag{11}$$
$$R_{ji} \xrightarrow{k_4} R_{01} + R_{j,\,i-1}$$
$$R_{ji} \xrightarrow{k_5} R_{j+1,\,i-1}$$

where (i = 0, 1, 2, …; j = 3, 4,…).

Here R_{ji} denotes clusters composed of i carboxylate molecules and j atoms of the zero-valence metal. Accordingly, R_{01} is the initial carboxylate, R_{03} is the cluster of the triangular carboxylate, and R_{04} is the cluster of the tetrahedral carboxylate. Reactions with constants k_1 and k_2 are responsible for the formation and dissociation of associates consisting of three carboxylate molecules, and reactions with constants k_3 and k_4 correspond to the addition of one molecule to cluster R_{ji} and its detachment. The reaction with constant k_5 involves reduction of the bound metal in a cluster.

A system of equations corresponding to scheme (11) was analyzed with a wide variation in kinetic constants. It was shown that the values of k_2, k_4, and k_5 have a slight effect on kinetics of the process. The decisive role is played by constants k_1 and k_3, that is, those constants that determine reactions giving rise to clusters, including mixed clusters.

The kinetics of the process is characterized by the existence of the induction period in the reaction of carboxylate consumption and an almost linear growth of average sizes of metal-containing nanoparticles with conversion. With the increase in constant k_1, the maximum rate increases, the induction period shortens, and the sizes of resulting particles decrease. After a certain period of growth, the number of particles reaches a limiting value which is lower than the greater the value of k_1 (**Figure 6**). At the same time, the mass of nanoparticles varies in proportion to conversion, irrespective of the constant (insert in **Figure 6**). At the same time, the narrow size distribution is typical of these particles.

Papers addressing methods of in situ obtainment of epoxy nanocomposites with metal nanoparticles are scarce.

Under UV radiation, 2,2'-dimethoxy-2-phenylacetophenone decomposes into radicals. A dimethoxyphenyl-carbonium radical reacts with $AgSbF_6$ and reduces a silver cation to Ag(0) via the transfer of electron, and then the radical transforms into the carbonium cation able to initiate the polymerization of diepoxide. Hence, silver nanoparticles and network matrix are formed simultaneously [121]. With increasing concentration of silver salt, the rate of polymerization and the ultimate conversion decrease, but the glass-transition temperature increases.

The silver nanoparticles with the same precursor, $AgSbF_6$, were obtained but in the presence of degradable under irradiation with visible light 3,5-bis(4-methoxyphenyl)-dithieno[3,2-b;2,3d]-thiophene [122]. A similar technique was employed to synthesize epoxy nanocomposites with nanoparticles of silver [123] and gold [124], but 2,3-bornadione (camphorquinone) was used as a source of radicals; in the case of gold, the precursor was $HAuCl_4$.

The silver nanoparticles in situ via the reduction of $AgNO_3$ in the epoxy resin by Triton-100, which simultaneously functioned as a stabilizer of nanoparticles, were
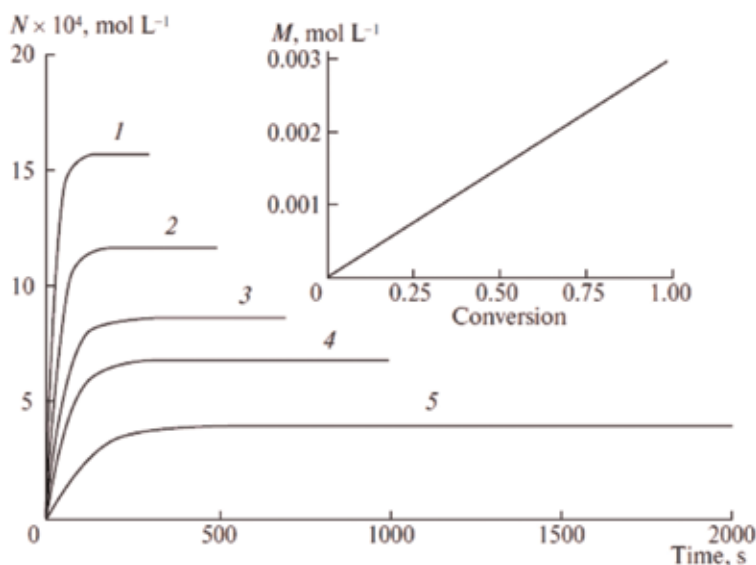

Figure 6.
Variation in N-value and mass M (insert) of nanoparticles; k_1, $L^2 \cdot mol^{-2} \cdot s^{-1}$ = (1) 10, (2) 30, (3) 50, (4) 100, and (5) 200. Reprinted with permission from IAPC "Nauka" [120].

synthesized [125]. A cycloaliphatic epoxy resin, hexahydro-4-methylphthalic anhydride as a curing agent, a reducing agent, and a precursor were dissolved in acetonitrile and exposed to UV radiation. After completion of the process, the solvent was removed at a reduced pressure.

A complex of silver acetate and 2-ethyl-4-methylimidazole was synthesized in an epoxy resin, and during its curing Ag^+ was reduced to $Ag(0)$ as a result of thermal decomposition of the complex [126]. In such a manner, silver nanoparticles were generated in situ. The imidazole product of complex decomposition served as a curing agent.

The epoxy resin ED-20 with triethylamine in the presence of silver myristate was cured [127–129]. The reduction of the latter and the formation of silver nanoparticles occurred simultaneously during polymerization. Reduction agents were both amine and the epoxy group. Carboxylate groups compatible with the medium functioned as stabilizers of particles.

4. Conclusion

It has been shown that, regardless of whether a filler is introduced in the reaction system or is formed in situ during the process of matrix formation, its structure changes to a greater or lesser extent than the unfilled cured epoxy binder. In addition, the matrix influences the character of distribution of nanoparticles over volume. This effect is especially important in the case of graphene and MMT, when exfoliation is the case in point. The matrix governs the size and shape of the resulting nanoparticles. They interact with the epoxy matrix through the resulting interfacial layers. There is no doubt that all these factors affect the properties of the epoxy nanocomposites.

The application areas of composites are defined by both the physicomechanical parameters of the epoxy matrix, its strength, thermomechanical stability, and adhesion ability and the unique properties of nanoparticles.

Nanoparticles of gold, silver, copper, TiO_2, ZnO, fullerene, and CNTs demonstrate effective antibacterial properties; therefore, composites containing these nanoparticles may be used for the microbiological control and purification of water, disinfection of surfaces, and creation of germicidal coatings, protective films, etc. Silver shows anti-inflammatory behavior and features antiviral and antifungal abilities. Its application in the form of nanoparticles (compared with the ionic form) decreases the cellular toxicity rather than the antibacterial efficiency [130].

Dielectric and magnetic epoxy nanocomposites have found wide use in such fields as Fourier spectroscopy, NMR, data storage, and absorption of electromagnetic radiation from other objects. The role of nanoparticles shows itself as improvement of electric strength and stress durability, suppression of space charge, and increase in the stability of dielectric discharge. For example, in the case of built-in planar capacitors, the insertion of dielectric films between copper sheets makes it possible to efficiently reduce the number of assembly devices. This not only leads to the miniaturization of circuit boards and electric wiring but also improves the characteristics of devices (e.g., promotes reduction in electromagnetic interference and switching noises) [131–133].

Epoxy resins are often employed in anti-wear applications. The use of such fillers as graphene oxide [134] or complexes MMT + SiO_2 [135], even at their very low content, decreases the rate of material wear by almost an order of magnitude.

The epoxy binders modified with carboxylated carbon nanotubes are more resistant to the action of aging factors. The presence of aggregates of carboxylated carbon nanotubes in the epoxy matrix positively influences the preservation of

physicomechanical properties of the composite subjected to heat and humidity aging. Microscopic examination revealed structural features of the epoxy nanocomposite and their effect on the resistance of the composite to the heat and humidity aging [136].

As for the use of epoxy nanocomposites in aerospace science and technology, this important problem, in author view, should be devoted to a special work. In short, it can be formulated as follows: structural nanocomposites, which are reinforcement structures based on carbon or glass fibers embedded in a polymer matrix modified with nanofillers, are the most important application of nanocomposites in the aerospace field [137], laminates, and sandwich structures. In addition, they can be used as anti-lightning [138], anti-radar [139] protection devices, flame retardant, and heat-resistant paints [140], ameliorating anti-corrosion performances [141].

Author details

Vadim Irzhak
Institute of Problems of Chemical Physics Russian Academy of Sciences, Chernogolovka, Moscow Region, Russian Federation

*Address all correspondence to: irzhak@icp.ac.ru

IntechOpen

References

[1] Ramdani N. editor. Nanotechnology in Aerospace and Structural Mechanics. Hershey PA: IGI Global; 2019

[2] Irzhak TF, Irzhak VI. Epoxy nanocomposites. Polymer Sciences, A. 2017;**59**(6):791-825

[3] Lee H, Neville K. Handbook of Epoxy Resins. New York: McGraw-Hill; 1967

[4] Chernin IZ, Smekhov FM, Zherdev YV. Epoxy Polymers and Compositions. Moscow: Khimiya; 1982. [in Russian]

[5] Khozin VG. Reinforcement of Epoxy Polymers. Kazan: Dom Pechati; 2004. [in Russian]

[6] Irzhak VI, Rozenberg BA, Enikolopyan NS. Network Polymers: Synthesis, Structure, Properties. Moscow: Nauka; 1979. [in Russian]

[7] Rozenberg BA. Kinetics, thermodynamics and mechanism of reactions of epoxy oligomers with amines. Advances in Polymer Science. 1986;**75**:113-165

[8] Okabe T, Takehara T, Inose K, Hirano N, Nishikawa M, Uehara T. Curing reaction of epoxy resin composed of mixed base resin and curing agent: Experiments and molecular simulation. Polymer. 2013; **54**(17):4660-4668

[9] Irzhak VI. Epoxide composite materials with carbon nanotubes. Russian Chemical Reviews. 2011;**80**(8): 787-806

[10] Kablov EN, Kondrashov SV, Yurkov GY. Prospects of using carbonaceous nanoparticles in binders for polymer composites. Nanotechnologies in Russia. 2013;**8**(3-4):163-185

[11] Song SH, Park KH, Kim BH, Choi YW, Jun GH, Lee DJ, et al. Enhanced thermal conductivity of epoxy/graphene composites by using non-oxidized graphene flakes with non-covalent functionalization. Advances in Materials. 2013;**25**(5):732-737

[12] Vyazovkin S, Sbirrzaauoli N. Mechanism and kinetics of epoxy-amine cure studied by differential scanning calorimetry. Macromolecules. 1996; **29**(6):1867-1873

[13] D'yachkov PN. Carbon Nanotubes: Structure, Properties, Application. Moscow: Binom; 2006. [in Russian]

[14] Grayfer ED, Makotchenko VG, Nazarov AS, Kim SJ, Fedorov VE. Graphene: Chemical approaches to the synthesis and modification. Russian Chemical Reviews. 2011;**80**(8):751-704

[15] Ivanovskii AL. Graphene-based and graphene-like materials. Russian Chemical Reviews. 2012;**81**(7):571-605

[16] Rakov EG. Nanotubes and Fullerenes. Moscow: Universitetskaya Kniga; 2006. [in Russian]

[17] Rakov EG. Carbon nanotubes in new materials. Russian Chemical Reviews. 2013;**82**(1):27-47

[18] Schaetz A, Zeltner M, Stark WJ. Carbon modifications and surfaces for catalytic organic transformations. ACS Catalysis. 2012;**2**(6):1267-1284

[19] Navalon S, Dhakshinamoorthy A, Alvaro M, Garcia H. Carbocatalysis by graphene-based materials. Chemical Reviews. 2014;**114**(12):6179-6212

[20] Chua CK, Pumera M. Carbocatalysis: The state of "Metal-Free" catalysis. Chemistry–A European Journal. 2015;**21**(36):12550-12562

[21] Liang Z, Gou J, Zhang C, Wang B, Kramer L. Investigation of molecular

interactions between (10, 10) single-walled nanotube and epon 862 resin/DETDA curing agent molecules. Materials Science and Engineering A. 2004;**365**(1–2):228-234

[22] Britz DA, Khlobystov AN. Noncovalent interactions of molecules with single walled carbon nanotubes. Chemical Society Reviews. 2006;**35**(7): 637-659

[23] Shen B, Zhai W, Tao M, Lu D, Zheng W. Enhanced interfacial interaction between polycarbonate and thermally reduced graphene induced by melt blending. Composites Science and Technology. 2013;**77**:87-110

[24] Xue B, Zhu J, Liu N, Li Y. Facile functionalization of graphene oxide with ethylenediamine as a solid base catalyst for knoevenagel condensation reaction. Catalysis Communications. 2015;**64**:105-109

[25] Xie H, Liu B, Yuan Z, Shen J, Cheng R. Cure kinetics of carbon nanotube/tetrafunctional epoxy nanocomposites by isothermal differential scanning calorimeter. Journal of Polymer Science, Part A: Polymer Chemistry. 2004;**42**(20):3701-3712

[26] Tao K, Yang S, Grunlan JC, Kim YS, Dang B, Deng Y, et al. Effects of Carbon Nanotube Fillers on the Curing Processes of Epoxy Resin-Based Composites. Journal of Applied Polymer Science. 2006;**102**(6):5248-5254

[27] Esmizadeh E, Yousefi A, Naderi G. Effect of type and aspect ratio of different carbon nanotubes on cure behavior of epoxy-based nanocomposite. Iranian Polymer Journal. 2015;**24**(1):1-12

[28] Visco A, Calabrese L, Milone C. Cure rate and mechanical properties of a DGEBF epoxy resin modified with carbon nanotubes. Journal of Reinforced Plastics and Composites. 2009;**28**(8): 937-949

[29] Susin SB, Pistor V, Amico SC, Coelho LAF, Pezzin SH, Zattera AJ. Investigation of cure kinetics in epoxy/multi-walled carbon nanotube nanocomposites. Journal of Applied Polymer Science. 2014;**131**(3): 39857-39862

[30] Rahaman A, Mohanty A. Effect of carbon nanotubes on the curing and thermomechanical behavior of epoxy/carbon nanotubes composites. Polymer Composites. 2014;**35**(29):441-449

[31] Cividanes LS, Simonetti EA, Moraes MB, Fernandes FW, Thim GP. Influence of carbon nanotubes on epoxy resin cure reaction using different techniques: A comprehensive review. Polymer Engineering and Science. 2014;**54**(11): 2461-2469

[32] Zhou T, Wang X, Wang T. Cure reaction of multi-walled carbon nanotubes/diglycidyl ether of bisphenol A/2-ethyl-4-methylimidazole (MWCNTs/DGEBA/EMI-2,4) nanocomposites: Effect of carboxylic functionalization of WCNTs. Polymer International. 2009;**58**(4):445-452

[33] Abdalla M, Dean D, Robinson P, Nyairo E. Cure behavior of epoxy/MWCNT nanocomposites: The effect of nanotube surface modification. Polymer. 2008;**49**(16):3310-3317

[34] Valentini L, Puglia D, Carniato F, Boccaleri E, Marchese L, Kenny JM. Use of plasma fluorinated single-walled carbon nanotubes for the preparation of nanocomposites with epoxy matrix. Composites Science and Technology. 2008;**68**(3–4):1008-1014

[35] Qiu J, Wang S. Reaction kinetics of functionalized carbon nanotubes reinforced polymer composites. Materials Chemistry and Physics. 2010; **121**(1–2):295-301

[36] Choi WJ, Powell RL, Kim DS. Curing behavior and properties of epoxy nanocomposites with amine functionalized multiwall carbon nanotubes. Polymer Composites. 2009;**30**(4):415-421

[37] Yang K, Gu M, Jin Y, Mu G, Pan X. Influence of surface treated multi-walled carbon nanotubes on cure behavior of epoxy nanocomposites. Composites Part A Applied Science and Manufacturing. 2008;**39**(10):1670-1678

[38] Cividanes LS, Brunelli DD, Antunes EF, Corat EJ, Sakane KK, Thim GP. Cure study of epoxy resin reinforced with multiwalled carbon nanotubes by raman and luminescence spectroscopy. Journal of Applied Polymer Science. 2013;**127**(1):544-553

[39] Grachev VP, Kondrashov SV, Akatenkov RV, Aleksashin VN, Deev IS, Anoshkin IV, et al. Modification of epoxy polymers by small additives of multiwall carbon nanotube. Polymer Science, Series A. 2014;**56**(3):330-336

[40] Qiu SL, Wang CS, Wang YT, Liu CG, Chen XY, Xie HF, et al. Reaction kinetics of functionalized carbon nanotubes reinforced polymer composites. eXPRESS Polymer Letter. 2011;**5**(9):809-818

[41] Ryu SH, Sin JH, Shanmugharaj AM. Study on the effect of hexamethylene diamine functionalized graphene oxide on the curing kinetics of epoxy nanocomposites. European Polymer Journal. 2014;**52**:88-97

[42] Park JK, Kim DS. Effects of an aminosilane and a tetra-functional epoxy on the physical properties of di-functional epoxy/graphene nanoplatelets nanocomposites. Polymer Engineering and Science. 2014;**54**(4):969-976

[43] Park JK, Kim DS. Preparation and physical properties of an epoxy

nanocomposite with amine-functionalized graphenes. Polymer Engineering and Science. 2014;**54**(5):985-991

[44] Galpaya DGD, Fernando JFS, Rintoul L, Motta N, Waclawik ER, Yan C, et al. The effect of graphene oxide and its oxidized debris on the cure chemistry and interphase structure of epoxy nanocomposites. Polymer. 2015;**71**:122-134

[45] Acocella MR, Corcione CE, Giuri A, Maggio M, Maffezzoli A, Guerra G. Graphene oxide as a catalyst for ring opening reactions in amine crosslinking of epoxy resins. RSC Advances. 2016;**6**(28):23858-23866

[46] Mauro M, Acocella MR, Corcione CE, Maffezzoli A, Guerra G. Catalytic activity of graphite-based nanofillers on cure reaction of epoxy resins. Polymer. 2014;**55**:5612-5615

[47] Li L, Zeng Z, Zou H, Liang M. Curing characteristics of an epoxy resin in the presence of functional graphite oxide with amine-rich surface. Thermochimica Acta. 2015;**614**:76-102

[48] Seyhan AT, Sun Z, Deitzel J, Tanoglu M, Heider D. Cure kinetics of vapor grown carbon nanofiber (VGCNF) modified epoxy resin suspensions and fracture toughness of their resulting nanocomposites. Materials Chemistry and Physics. 2009;**118**(1):234-242

[49] Cai ZQ, Movva S, Chiou NR, Guerra D, Hioe Y, Castro JM, et al. Effect of polyaniline surface modification of carbon nanofibers on cure kinetics of epoxy resin. Journal of Applied Polymer Science. 2010;**118**(4):2328-2335

[50] Sanctuary R, Baller J, Zielinski B, Becker N, Krüger K, Philipp U, et al. Influence of Al_2O_3 nanoparticles on the isothermal cure of an epoxy resin.

Journal of Physics: Condensed Matter. 2009;**21**(3):035118-035126

[51] Balle J, Becker N, Ziehmer M, Thomassey M, Zielinski B, Müller U, et al. Interactions between silica nanoparticles and an epoxy resin before and during network formation. Polymer. 2009;**50**(14):3211

[52] Karasinski EN, Da Luz MG, Lepienski CM, Coelho LAF. Nanostructured coating based on epoxy/metal oxides: Kinetic curing and mechanical properties. Thermochimica Acta. 2013;**569**:167-211

[53] Zabihi O, Mostafavi SM, Ravari F, Khodabandeh A, Hooshafza A, Zare K, et al. The effect of zinc oxide nanoparticles on thermo-physical properties of diglycidyl ether of bisphenol A/2,2-diamino-1,1-binaphthalene nanocomposites of surface treated multi-walled carbon nanotubes on cure behavior of epoxy nanocomposite. Thermochimica Acta. 2011;**521**(1–2):49-58

[54] Ghaffari M, Ehsani M, Vandalvand M, Avazverdi E, Askari A, Goudarzi A. Studying the effect of micro- and nano-sized ZnO particles on the curing kinetic of epoxy/polyaminoamide system. Progress in Organic Coatings. 2015;**89**: 277-283

[55] Zabihi O, Hooshafza A, Moztarzadeh F, Payravand H, Afshar A, Alizadeh R. Isothermal curing behavior and thermo-physical properties of epoxy-based thermoset nanocomposites reinforced with Fe_2O_3 nanoparticles. Thermochimica Acta. 2012;**527**:190-198

[56] Omrani A, Rostami AA, Ravari F, Mashak A. Curing behavior and structure of a novel nanocomposite from glycerol diglycidyl ether and 3,3-dimethylglutaric anhydride. Thermochimica Acta. 2011;**517**(1–2): 9-15

[57] Hong SG, Tsai JS. The adsorption and curing behavior of the epoxy/amidoamine system in the presence of metal oxides. Journal of Thermal Analysis and Calorimetry. 2001;**63**(1): 31-46

[58] Baller J, Thomassey M, Ziehmer M, Sanctuary R. The catalytic influence of alumina nanoparticles on epoxy curing. Thermochimica Acta. 2011;**517**(1–2): 34-39

[59] Ghaemy M, Amini Nasab SM, Barghamadi M. Nonisothermal cure kinetics of diglycidylether of bisphenol-A/amine system reinforced with nanosilica particles. Journal of Applied Polymer Science. 2007;**104**(6): 3855-3863

[60] Rosso P, Ye L. Epoxy/silica nanocomposites: Nanoparticle-induced cure kinetics and microstructure. Macromolecular Rapid Communications. 2007;**28**(1):121-126

[61] Alzina C, Sbirrazzuoli N, Mija A. Epoxy-amine based nanocomposites reinforced by silica nanoparticles. Relationships between morphologic aspects, cure kinetics, and thermal properties. Journal of Physical Chemistry C. 2011;**115**(46):22789-22795

[62] Pavlidou S, Papaspyrides CD. A review on polymer–layered silicate nanocomposites. Progress in Polymer Science. 2008;**33**(12):1119-1198

[63] Becker O, Simon PG. Epoxy layered silicate nanocomposites. Advances in Polymer Science. 2005;**179**:29-82

[64] Paiva LB, de Morales AR, Valenzuela Diaz FR. Organoclays: Properties, preparation and application. Applied Clay Science. 2008;**42**(1–2): 8-24

[65] Alzina C, Mija A, Vincent L, Sbirrazzuoli N. Effects of incorporation of organically modified montmorillonite

on the reaction mechanism of epoxy/amine cure. The Journal of Physical Chemistry. B. 2012;**116**(19):5786-5794

[66] Ivankovic M, Brnardic I, Ivankovic H, Mencer HJ. DSC study of the cure kinetics during nanocomposite formation: Epoxy/poly(oxypropylene) diamine/organically modified montmorillonite system. Journal of Applied Polymer Science. 2006;**99**(2): 550-557

[67] Román F, Calventus Y, Colomer P, Hutchinson JM. Effect of carbon nanotubes on the curing and thermomechanical behavior of epoxy/carbon nanotubes composites. Thermochimica Acta. 2012;**541**:76-85

[68] Alzina C, Sbirrazzuoli N, Mija A. Hybrid Nanocomposites: Advanced nonlinear method for calculating key kinetic parameters of complex cure kinetics. The Journal of Physical Chemistry. B. 2010;**114**(39): 12480-12487

[69] Li L, Zou H, Liang M, Chen Y. Study on the effect of poly(oxypropylene) diamine modified organic montmorillonite on curing kinetics of epoxy nanocomposites. Thermochimica Acta. 2014;**597**:93-100

[70] Ferdosian F, Ebrahimi M, Jannesari A. Curing kinetics of solid epoxy/DDM/nanoclay: Isoconversional models versus fitting model. Thermochimica Acta. 2013;**568**:67-73

[71] Shanmugharaj AM, Ryu SH. Study on the effect of aminosilane functionalized nanoclay on the curing kinetics of epoxy nanocomposites. Thermochimica Acta. 2012;**546**:16-23

[72] Shiravand F, Hutchinson JM, Calventus Y. Influence of the isothermal cure temperature on the nanostructure and thermal properties of an epoxy layered silicate nanocomposite. Polymer Engineering and Science. 2014;**54**(1):51-58

[73] Montserrat S, Román FM, Hutchinson J, Campos L. Analysis of the cure of epoxy based layered silicate nanocomposites: Reaction kinetics and nanostructure development. Journal of Applied Polymer Science. 2008;**108**(2):923-938

[74] Cortés P, Fraga I, Calventus Y, Román F, Hutchinson JM, Ferrando F. A new epoxy-based layered silicate nanocomposite using a hyperbranched polymer: Study of the curing reaction and nanostructure development. Materials. 2014;**7**(3):1830-1849

[75] Shiravand F, Fraga I, Cortés P, Calventus Y, Hutchinson JM. Thermal analysis of polymer layered silicate nanocomposites: Identification of nanostructure development by DSC. Journal of Thermal Analysis and Calorimetry. 2014;**118**(2):723-729

[76] Shiravand F, Hutchinson JM, Calventus Y. Non-isothermal cure and exfoliation of tri-functional epoxy-clay nanocomposites. Express Polymer Letters. 2015;**9**(8):695-708

[77] Kong D, Park CE. Real time exfoliation behavior of clay layers in epoxy-clay nanocomposites real time exfoliation behavior of clay layers in epoxy-clay nanocomposites. Chemistry of Materials. 2003;**15**(2):419-424

[78] Hutchinson JM, Shiravand F, Calventus Y. Intra- and extra-gallery reactions in tri-functional epoxy polymer layered silicate nanocomposites. Journal of Applied Polymer Science. 2013;**128**(5):2961-2970

[79] Pustkova P, Hutchinson JM, Román F, Montserrat S. Homopolymerization effects in polymer layered silicate nanocomposites based upon epoxy resin: Implications for exfoliation. Journal of Applied Polymer Science. 2009;**114**(2):1040-1447

[80] Hutchinson JM, Shiravand F, Calventus Y, Fernández-Francos X,

Ramis X. Highly exfoliated nanostructure in trifunctional epoxy/clay nanocomposites using boron trifluoride as initiator. Journal of Applied Polymer Science. 2014;**131**(6): 40020-40029

[81] Jagtap SB, Rao VS, Barman S, Ratna D. Nanocomposites based on epoxy resin and organoclay functionalized with a reactive modifier having structural similarity with the curing agent. Polymer. 2015;**63**:41-71

[82] Pomogailo AD, Rozenberg AS, Dzhardimalieva GI. Metal-Polymer Nanocomposites. Hoboken: Wiley; 2005

[83] Wilcoxon JP, Abrams BL. Synthesis, structure and properties of metal nanoclusters. Chemical Society Reviews. 2006;**35**(4):1162-1194

[84] Gusev AI. Nanomaterials, Nanostructures, Nanotechnologies. Moscow: Fizmatlit; 2007. [in Russian]

[85] Suzdalev IP. Nanotechnology: Physics and Chemistry of Nanocrystals, Nanostructures and Nanomaterials. Moscow: Kom Kniga; 2006. [in Russian]

[86] Faraji M, Yamini Y, Rezaee M. Magnetic nanoparticles: Synthesis, stabilization, functionalization, characterization, and applications. Journal of the Iranian Chemical Society. 2010;**7**(1):1-37

[87] Lu Y, Chen W. Sub-nanometre sized metal clusters: From synthetic challenges to the unique property discoveries. Chemical Society Reviews. 2012;**41**(9):3594-3624

[88] Agareva NA, Aleksandrov AP, Smirnova LA, Bityurin NM. Synthesis of block polymethylmethacrylate containing precursor for photoinduced formation of gold nanoparticles. Perspektivnye Materialy. 2009;**1**:5-12

[89] Rozenberg BA, Tenne R. Polymer-assisted fabrication of nanoparticles and nanocomposites. Progress in Polymer Science. 2008;**33**(1):40-112

[90] Wuithschick M, Paul B, Bienert R, Sarfraz A, Vainio U, Sztucki M, et al. Size-controlled synthesis of colloidal silver nanoparticles based on mechanistic understanding. Chemistry of Materials. 2013;**25**(24):4679-4689

[91] Wang F, Richards VN, Shields SP, Buhro WE. Kinetics and mechanisms of aggregative nanocrystal growth. Chemistry of Materials. 2014;**26**(1):5-21

[92] Yan S, Wu Z, Yu H, Gong Y, Tan Y, Du R, et al. Time-resolved small-angle X-ray scattering study on the growth behavior of silver nanoparticles. The Journal of Physical Chemistry. 2014;**118**(21):11454-11463

[93] Völkle CM, Gebauer D, Cölfen H. High-resolution insights into the early stages of silver nucleation and growth. Faraday Discussions. 2015;**179**:59-69

[94] Irzhak VI. The mechanisms of the formation of metal-containing nanoparticles. Review Journal of Chemistry. 2016;**6**(4):370-404

[95] Volmer M. Kinetik der Phasenbildung. Dresden: Steinkopff; 1939

[96] Frenkel' YI. Kineticheskaya Teoriya Zhidkostei (Kinetic Theory of Liquids). Leningrad: Nauka; 1975

[97] LaMer VK, Dinegar RH. Theory, production and mechanism of formation of monodispersed hydrosols. Journal of the American Chemical Society. 1950;**72**(11):4847-4854

[98] Polte J, Tuaev X, Wuithschick M, Fischer A, Thuenemann AF, Rademann K, et al. Formation mechanism of colloidal silver nanoparticles: Analogies and differences to the growth of gold

nanoparticles. ACS Nano. 2012;**6**(7): 5791-5802

[99] Turkevich J, Stevenson PC, Hillier J. A study of the nucleation and growth processes in the synthesis of colloidal gold. Faraday Discussions of the Chemical Society. 1951;**11**:55-75

[100] Finney EE, Finke RG. Nanocluster nucleation and growth kinetic and mechanistic studies: A review emphasizing transition-metal nanoclusters. Journal of Colloid and Interface Science. 2008;**317**(2):351-374

[101] Watzky MA, Finke RG. Nanocluster size-control and "Magic Number" investigations. Experimental tests of the "Living-Metal Polymer" concept and of mechanism-based size-control reductions leading to the syntheses of Ir(0) nanoclusters centering about four sequential magic numbers. Chemistry of Materials. 1997; **9**(12):3083-3095

[102] Bogdanova LM, Shershnev VA, Spirin MG, Irzhak VI, Dzhardimalieva GI. Evolution of silver nanoparticles synthesized in situ in a polycondensation epoxy matrix. Russian Journal of Physical Chemistry A. 2019; **93**(7):1043-1047

[103] Irzhak VI. Digestive ripening of nanoparticles. Russian Journal of Physical Chemistry A. 2017;**91**(8): 1502-1506

[104] Lifshits M, Slezov VV. Kinetics of diffusive decomposition of supersaturated solid solutions. Journal of Experimental and Theoretical Physics. 1959;**35**(2):479-492

[105] Wagner Z. Theorie der alterung von niderschlagen durch umlösen (ostwald reifung). Zeitschrift für Elektrochemie. 1961;**65**:581-591

[106] Xin HLL, Zheng HM. In situ observation of oscillatory growth of

bismuth nanoparticles. Nano Letters. 2012;**12**(3):1470-1474

[107] Bardaji M, Uznanski P, Amiens C, Chaudret B, Laguna A. Aurophilic complexes as gold atom sources in organic media. Chemical Communications. 2002;**6**:598-599

[108] Nakamoto M, Kashiwagi Y, Yamamoto M. Synthesis and size regulation of gold nanoparticles by controlled thermolysis of ammonium gold(I) thiolate in the absence or presence of amines. Inorganica Chimica Acta. 2005;**358**(14):4229-4236

[109] Gur'eva LL, Tkachuk AI, Kuzub LI, Estrina GA, Knerel'man EI, Khodos II, et al. Synthesis of silver nanoparticles with polystyrylcarboxylate ligands. Journal of Polymer Science, Series B. 2013;**55**(3–4):139-146

[110] Kuzub LI, Gur'eva LL, Grishchuk AA, Estrina GA, Estrin YI, Badamshina ER. Regularities of the formation of silver nanoparticles with oligostyrylcarboxylate ligands. Journal of Polymer Science, Series B. 2015;**57**(6): 608-615

[111] Kuzub LI, Gur'eva LL, Khodos II, Grishchuk AA, Estrin YI, Badamshina ER. Regularities of the formation of silver nanoparticles with oligostyrylmonocarboxylate ligands in ED-20 oligomer. Journal of Polymer Science, Series B. 2017;**59**(5):537-543

[112] Yamamoto M, Nakamoto M. Novel preparation of monodispersed silver nanoparticles via amine adducts derived from insoluble silver myristate in tertiary alkylamine. Journal of Materials Chemistry. 2003;**13**(9):2064-2065

[113] Yamamoto M, Kashiwagi Y, Nakamoto M. Size-controlled synthesis of monodispersed silver nanoparticles capped by long-chain alkyl carboxylates from silver carboxylate and tertiary

amine. Langmuir. 2006;**22**(20): 8581-8586

[114] Kashiwagi Y, Yamamoto M, Nakamoto M. Facile size-regulated synthesis of silver nanoparticles by controlled thermolysis of silver alkylcarboxylates in the presence of alkylamines with different chain lengths. Journal of Colloid and Interface Science. 2006;**300**(1):169-175

[115] Khanna PK, Kulkarni D, Beri RK. Synthesis and characterization of myristic acid capped silver nanoparticles. Journal of Nanoparticle Research. 2008;**10**(6):1059-1062

[116] Clary DR, Mills G. Photochemical generation of nanometer-sized Cu particles in octane. The Journal of Physical Chemistry, C. 2011;**115**(30): 14656-14663

[117] Clary DR, Nabil M, Sedeh MM, El-Hasadi Y, Mills G. Photochemical generation of Ag, Pd, and Pt particles in octane. The Journal of Physical Chemistry, C. 2012;**116**(16):9243-9250

[118] Kuzub LI, Bogdanova LM, Kurkin TS, Torbov VI, Gur'eva LL, Rozenberg BA, et al. Investigation of the Regularities of Synthesis of Monodisperse Silver Nanoparticles with Chemically Bound Organic Ligands: Proceeding of Articles "Structure and Dynamics of Molecular Systems", 2009, Yal'chik, Russia. Ioshkar-Ola: MarGTU; 2009. Part 2, No 16, pp. 134-139

[119] Kuzub LI, Bogdanova LM, Kurkin TS, Buzin PV. Principal Aspects of the Synthesis of Silver Nanoparticles with Carboxylate Ligands: Proceeding of Articles "Structure and Dynamics of Molecular Systems", 2010, Yal'chik, Russia. Ioshkar-Ola: MarGTU; 2010. Part 1, No 17. pp. 340-345

[120] Solov'ev ME, Irzhak TF, Irzhak VI. Kinetics of formation of nanoparticles from first group metal carboxylates.

Russian Journal of Physical Chemistry A. 2015;**89**(3):1642-1647

[121] Sangermano M, Yagci Y, Rizza G. In situ synthesis of silver-epoxy nanocomposites by photoinduced electron transfer and cationic polymerization processes. Macromolecules. 2007;**40**(25): 8827-8829

[122] Yagci Y, Sahin O, Ozturk T, Marchi S, Grassini S, Sangermano M. Synthesis of silver/epoxy nanocomposites by visible light sensitization using highly conjugated thiophene derivatives. Reactive and Functional Polymers. 2011; **71**(7):857-862

[123] Yagci Y, Sangermano M, Rizza GA. Visible light photochemical route to silver–epoxy nanocomposites by simultaneous polymerization–Reduction approach. Polymer. 2008; **49**(24):5195-5198

[124] Yagci Y, Sangermano M, Rizza G. Synthesis and characterization of gold-epoxy nanocomposites by visible light photoinduced electron transfer and cationic polymerization processes. Macromolecules. 2008;**41**(20): 7268-7270

[125] Lu J, Moon KS, Wong CP. Silver/ polymer nanocomposite as a high-*k* polymer matrix for dielectric composites with improved dielectric performance. Journal of Materials Chemistry. 2008;**18**(40):4821-4826

[126] Gao H, Liu L, Luo Y, Jia D. In-situ preparation of epoxy/silver nanocomposites by thermal decomposition of silver–imidazole complex. Materials Letters. 2011;**65** (23–24):3529-3532

[127] Bogdanova L, Kuzub L, Dzhavadjan E, Rabenok E, Novikov G, Pomogailo A. In situ synthesis and properties of epoxy nanocomposites.

Macromolecular Symposia. 2012;
317–318:117-122

[128] Bogdanova LM, Kuzub LI, Dzhavadyan EA, Torbov VI, Dremova NN, Pomogailo AD. Mechanical properties of epoxy composites based on silver nanoparticles formed in situ. Journal of Polymer Science, Series A. 2014;**56**(3):304-310

[129] Bogdanova LM, Kuzub LI, Spirin MG, Dzhardimalieva GI, Irzhak VI. Features of the synthesis of silver nanoparticles in a curing epoxy matrix. Vestnik KGTU. 2015;**18**(16):10-15

[130] Gu H, Tadakamalla S, Huang Y, Colorado HA, Luo Z, Haldolaarachchige N, et al. Polyaniline stabilized magnetite nanoparticle reinforced epoxy nanocomposites. ACS Applied Materials & Interfaces. 2012;**4**(10):5613-5624

[131] Huang X, Xie L, Yang K, Wu C, Jiang P, Li S, et al. Role of interface in highly filled epoxy/BaTiO$_3$ nanocomposites. Part I-correlation between nanoparticle surface chemistry and nanocomposite dielectric property. IEEE Transactions on Dielectrics and Electrical Insulation. 2014;**21**(2): 467-479

[132] Novikov GF, Rabenok EV, Bogdanova LM, Irzhak VI. Temperature dependence of direct current conductivity in Ag-ED20 nanocomposite films. Russian Journal of Physical Chemistry A. 2017;**91**(10): 1971-1975

[133] Novikov GF, Rabenok EV, Bogdanova LM, Irzhak VI. Dielectric properties of films of Ag-ED20 epoxy nanocomposite synthesized in situ. Temperature dependence of direct current conductivity. Journal of Polymer Science: Part A. 2017;**59**(5): 741-750

[134] Shen XJ, Pei XQ, Fu SY, Friedrich K. Significantly modified tribological performance of epoxy nanocomposites at very low graphene oxide content. Polymer. 2013;**54**(3):1234-1242

[135] Thind KS, Singh J, Saini JS, Bhunia H. Mechanical and wear properties of hybrid epoxy nanocomposites. Indian Journal of Engineering and Materials Science. 2015;**22**(4):421-428

[136] Kondrashov SV, Merkulova YI, Marakhovskii PS, D'yachkova TP, Shashkeev KA, Popkov OV, et al. Degradation of physicomechanical properties of epoxy nanocomposites with carbon nanotubes upon heat and humidity aging. Russian Journal of Applied Chemistry. 2017;**90**(5):788-796

[137] Dinca I, Ban C, Stefan A, Pelin G. Nanocomposites as advanced materials for aerospace industry. INCAS Bulletin. 2012;**4**(4):73-83

[138] Katunin A, Krukiewicz K, Turczyn R, Sul P, Łasica A, Bilewicz M. Synthesis and characterization of the electrically conductive polymeric composite for lightning strike protection of aircraft structures. Composite Structures. 2017; **159**:773-783

[139] Govindaraj B, Sarojadevi M. Microwave-assisted synthesis of nanocomposites from polyimides chemically cross-linked with functionalized carbon nanotubes for aerospace applications. Polymers for Advanced Technologies. 2018;**29**(6): 1718-1726

[140] Meenakshi KS, Sudhan EPJ. Development of novel TGDDM epoxy nanocomposites for aerospace and high performance applications—Study of their thermal and electrical behavior. Arabian Journal of Chemistry. 2016; **9**(1):79-85

[141] Monetta T, Acquesta A, Bellucci F. Graphene/epoxy coating as multifunctional material for aircraft structures. Aerospace. 2015;**2**(3):423-434

Graphene-Like Nanocomposites

Zahra Rafiei-Sarmazdeh and Seyed Javad Ahmadi

Abstract

After discovering graphene and its extraordinary intrinsic, other graphene-like nanomaterials (GLNs) became a topic of interest to many scientists of the time. Recently, GLNs, nanosheets of sp^2-hybridized atoms arranged in a two-dimensional lattice with impressive thermal, mechanical, and electrical properties, has attracted both academic and industrial interest because it can produce dramatic improvements in properties at very low filler content. Many studies have been performed on GLNs with various applications, including boron nitride nanosheets, transition metal dichalcogenides, and other two-dimensional (2D) nanomaterials. This rapid advance provides a strong appetence for further research on properties of GLNs, including mechanical, electrical and thermal properties and their potential applications in the nanocomposites industry.

Keywords: graphene-like, nanocomposite, boron nitride, two-dimensional, nanomaterials, polymer

1. Introduction

Composite is a combination of at least two components (or phases) that are chemically distinctly different, and these components are not dissolvable. Properties and performance of composites strongly depend on their components. In general, in the composite, there is at least one non-interconnected component, called filler or reinforcement, surrounded by a continuous phase, called matrix [1].

Recently, nanocomposites have attracted a lot of attention. Nanocomposite is actually a composite that at least one of its constituents, typically filler, is in dimensions ranging from 1 to 100 nm. The nanomaterials are incorporated within the matrix for particular purposes such as strength, resistance, electrical conductivity, magnetic properties etc.

A great effort is being made to control nanoscale structures through new approaches. The physical, chemical, and biological properties of nanomaterials are different from the properties of atoms and molecules or even bulk materials. However, the properties of nanocomposites depend not only on the properties of filler and matrix, but also on the morphological and interfacial characteristics of these materials. Nanomaterials have a high surface-to-volume ratio, which makes them ideal for use in nanocomposite materials [2].

There are several categories for composite and nanocomposite classification. One of these categories is based on the type of matrix material. On this basis, there are various composites including [3, 4]:

- Polymer matrix composites (PMCs): In commercial applications, these composites have a high rating compared to other types of composites. Various

filler materials can be used in this type of composite. The matrix can be made of thermo-plastic and thermo-set polymers.

• Metal matrix composites (MMCs): This category, which is considered an advanced building material, consists of non-metal fillers in a metal matrix. MMCs are mainly used in engineering applications, in cases where the operating temperature is in the range of 250–750°C. Copper, aluminum, titanium and super alloys are widely used to make these composites.

• Ceramic matrix composites (CMCs): This category is considered an advanced building material made of metal/non-metallic fillers in a ceramic matrix. CMCs are used in engineering applications with the operating temperature is in the range of 800–1650°C.

The use of polymer composites due to its inherent properties has grown considerably compared to other composites. High strength and modulus, fatigue resistance, high flexibility, multi-functional performance, easy to process, low weight of structure and low cost processing are the features of this category of composites than other composites.

In recent years, two-dimensional (2D) nanomaterials have drawn considerable interest for exploring potential applications. 2D nanomaterials are laminated crystals that exhibit unusual physical-chemical properties in thicknesses of atomic layers (**Figure 1**). Graphene as a famous member of the family of 2D nanomaterial is a honeycomb network of carbon atoms, co-located with sp^2 hybridize and forming a single graphene atomic layer [5, 6]. Graphene is indubitably one of the most important nanomaterials in the world, which the combination of unique properties in it makes a long way to discover a wide range of applications from
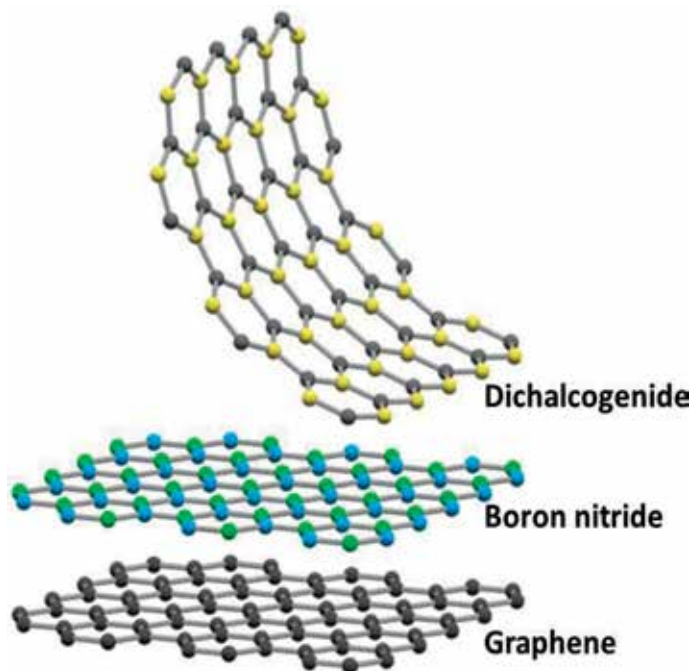

Figure 1.
Schematic view of 2D nanomaterials, a single layer of graphene, boron nitride and transition metal dichalcogenide [15].

electronics to optics [7, 8], sensors [9, 10], biology [11], coating, composite [12, 13] and etc.

Since 2004, when a single layer graphene was discovered by Novoselov [14], for the first time, various studies were carried out on a variety of graphene-like nanomaterials (GLNs), their properties and application. One of the most important uses of GLNs is the usage as filler in polymer composites due to their unique mechanical, electrical and thermal properties.

The scientists and researchers are encouraged to use other 2D nanomaterials such as boron nitride nanosheets (BNNSs) and metal dichalcogenide nanosheets for producing nanocomposite when observed amazing properties of graphene as reinforcement material for polymer-based composites. Generally, 2D nanomaterials have unique properties for using as reinforcement in nanocomposites, which include: (i) ultrathin 2D nanosheets have high special surface area, (ii) they have high surface-to-volume atomic ratio, therefore are chemically suitable for functionalizing and so their dispersion improves in polymer matrix. (iii) They have unique mechanical, thermal and electrical characteristics, which make them an ideal candidate for reinforcement of nanocomposites [16].

In comparison to the zero-dimensional (0D) nanomaterials such as BN nanoparticles or one-dimensional (1D) nanomaterials, such as boron nitride nanotubes (BNNTs), due to the special structure of 2D nanomaterials, contacting or overlapping nanosheets with each other throughout polymeric matrix could form an interconnected network of 2D layers. As a result, the percolation threshold of 2D nanocomposite is lower than other nanocomposites. This means that better properties can be achieved at much lower amounts of reinforcement, which decreases the cost of composite construction.

The other important advantage of the 2D nanosheets is their high surface area, which allows for the proper interaction of filler with polymeric matrix. This interaction results in a dramatic improvement in the properties of the matrix. However, the mentioned properties could be diminished, if the filler is not suitably dispersed or the conditions are created to allow the particles to agglomerate together during the nanocomposite manufacturing. The van der Waals force (vdW) between the layers can lead to agglomeration of nanosheets, which has a negative effect on the properties. On an industrial scale, maintaining the cost of competitive production with a high degree of dispersion and low content of filler is the goal, and therefore the manufacturing processes of these nanocomposites with unique properties that have the capacity to scale up is very valuable.

GLNs are instant and important nanomaterials that have outlandish mechanical and functional properties. Due to their extraordinary properties, these materials have the potential to be recognized as generations of next generation composites with maximum structural and/or functional reinforcement in a minimum amount of filler. Adding these nanomaterials significantly improves the mechanical properties of the polymer matrix. Thermal, electrical conductivity and dimensional stability of nanocomposite significantly change. In addition, the unique properties of each of these nanosheets will appear in the final nanocomposite.

However, the research on GLNs polymer-based nanocomposites is still in its early stages. Little research has been done on the properties of these nanocomposites, such as optical properties, irradiation properties and biocompatibility. The reason is not that these studies are not important or interesting, but rather, the production of GLNs nanocomposite is difficult due to low-yield and high-cost methods to synthesis of GLNs. This prevents the rapid progress of research on properties and application of GLNs polymer-based nanocomposites.

In this chapter, we focus on a summary of recent developments in 2D graphene-like nanomaterials in the manufacture of polymer nanocomposites. We have also

reviewed the synthesis methods of GLNs and the processing polymer-based nanocomposites. Some applications of these nanomaterials have been investigated. Ultimately, we have studied the problems and limitations facing this category of nanocomposites.

2. Synthesis approach of graphene-like nanomaterials

2D nanosheets are synthesized using a variety of methods based on two top-down and bottom-up approaches. In top-down approach, the bulk of the parent material is used and the final 2D nanosheets are produced during the processes. This approach can be cost-effective depending on the material used. In this view, 2D nanomaterials are produced by methods such as separation, peeling, cleavage and exfoliation. Micromechanical cleavage, ball milling, liquid/chemical exfoliation and functionalization (covalent and non-covalent) are common methods in this category [17–25].

In the bottom-up, the precursor materials are used for producing of GLNs, with methods such as chemical synthesis, chemical vapor deposition (CVD) and plasma-enhanced chemical vapor deposition (PECVD). However, there are the main challenges facing researchers in this field. One of them is the need for high amounts of nanomaterials and low yield synthesis methods of these nanomaterials. A great effort is being made for improvement the efficiency of the synthesis of these nanosheets [26–28].

In general, interfacial interaction is believed to play an important role in determining the final properties of polymer nanocomposites. Interfacial interaction between the polymer matrix and the filler materials includes van der Waals interactions, hydrous bonds, covalent bonds, and ionic bonds [29]. Hence, many efforts have been made to develop and improve interfacial interactions of nanocomposites including filler or matrix. The functionalization of the filler surface and the use of compatibilizer are common to be modified the surface of filler in terms of polar/nonpolar nature and to be able to interact with the polymeric matrix due to the hydrophobic/hydrophilic nature of polymers used in the composite and coating industry.

3. Graphene-like nanocomposites and their importance

Due to inherent and impressive properties of mechanical, electronic and thermal conductivity of GLNs, these compounds are considered as a promising candidate for using in polymer nanocomposites as fillers. Compared to conventional composites, these nanocomposites show a dramatic increase in properties, even in a low content of filler. Hence, the 2D nanomaterials and GLNs based-nanocomposites are not only lighter, but also have more and stronger multi-functional properties. As mentioned in the previous section, due to the high surface area of GLNs, the physicochemical interaction of the filler with the polymeric matrix enhances. This helps strengthen and enhancement of interfacial bonding between layers of GLNs and polymer matrix [30].

According to the interaction between filler and polymer matrix, polymer composites are divided into three groups; conventional or immiscible composites, intercalated composites, and exfoliated or miscible composites (**Figure 2**). In conventional composites, 2D nanosheets remain as agglomerates in the polymer matrix and retain their original structure. The diffraction pattern of conventional composites is the same as that for the first powder of these nanosheets. In intercalated
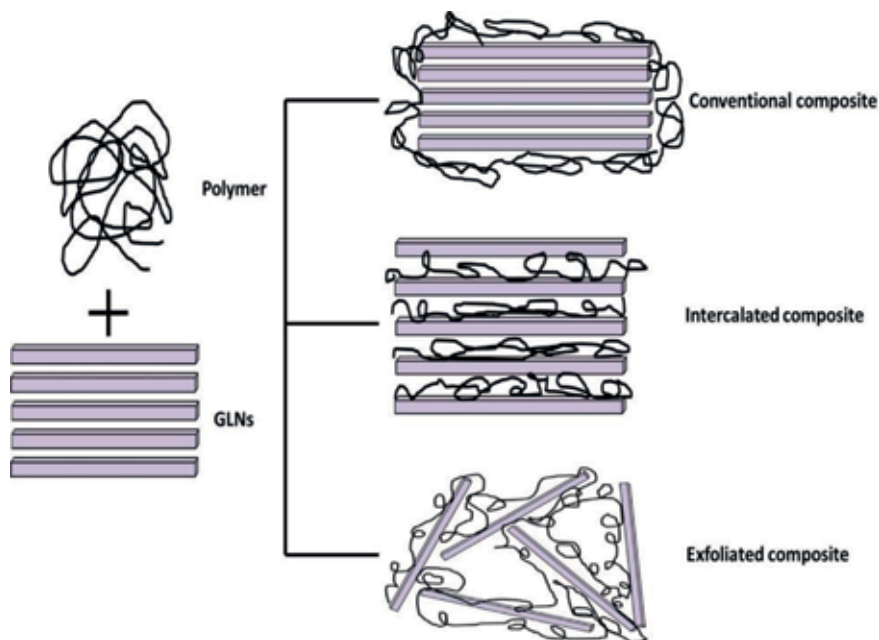
Figure 2.
Schematic view of different groups of composites; conventional, intercalated and exfoliated nanocomposites.

nanocomposites, polymer chains are intercalated between 2D layers, which partially open the layers. The characteristic peak displacement of these nanosheets to lower angles represents intercalating. In the third group, the suitable interaction between filler and the polymer matrix leads to the complete exfoliation of the layers by the polymer chains. The characteristic peak related to these nanosheets disappears in the diffraction pattern of these nanocomposites. In practice, however, it is rarely possible to achieve complete exfoliation [31, 32].

4. Processing

The final properties of nanocomposites depend on the method and processing conditions. Most polymer composites are processed using the following methods: (i) melt processing (ii) solvent processing (iii) *In-situ* polymerization; (iv) electrospinning and (v) layer by layer (LBL) assembly (**Figure 3**).

The melt mixing method is one of the most economical and environmentally friendly methods used to make nanocomposites. In fact, this process is the choice of most industries. The mixing of materials is often done through a single or double extruder, in such a way that the reinforcement is mixed with the molten polymer. The mixer uses shear force to separate the filler agglomerates and disperse them throughout the polymeric matrix (**Figure 3(a)**). Another point of this method is the lack of any solvent for processing. Most polymers used in this method include low-density polyethylene (LDPE), high-density polyethylene (HDPE), polypropylene (PP), polystyrene (PS), poly(methyl methacrylate) (PMMA), polyamide polyester and polycarbonate [30, 33–37].

Solution mixing is another way of producing nanocomposites containing GLNs. In this method, the nanomaterials and polymers are dissolved in the solvent before being molded and then the solvent is evaporated (**Figure 3(b)**). In this method, both thermoset and thermoplastic polymers can be used. Polymers such as PMMA,
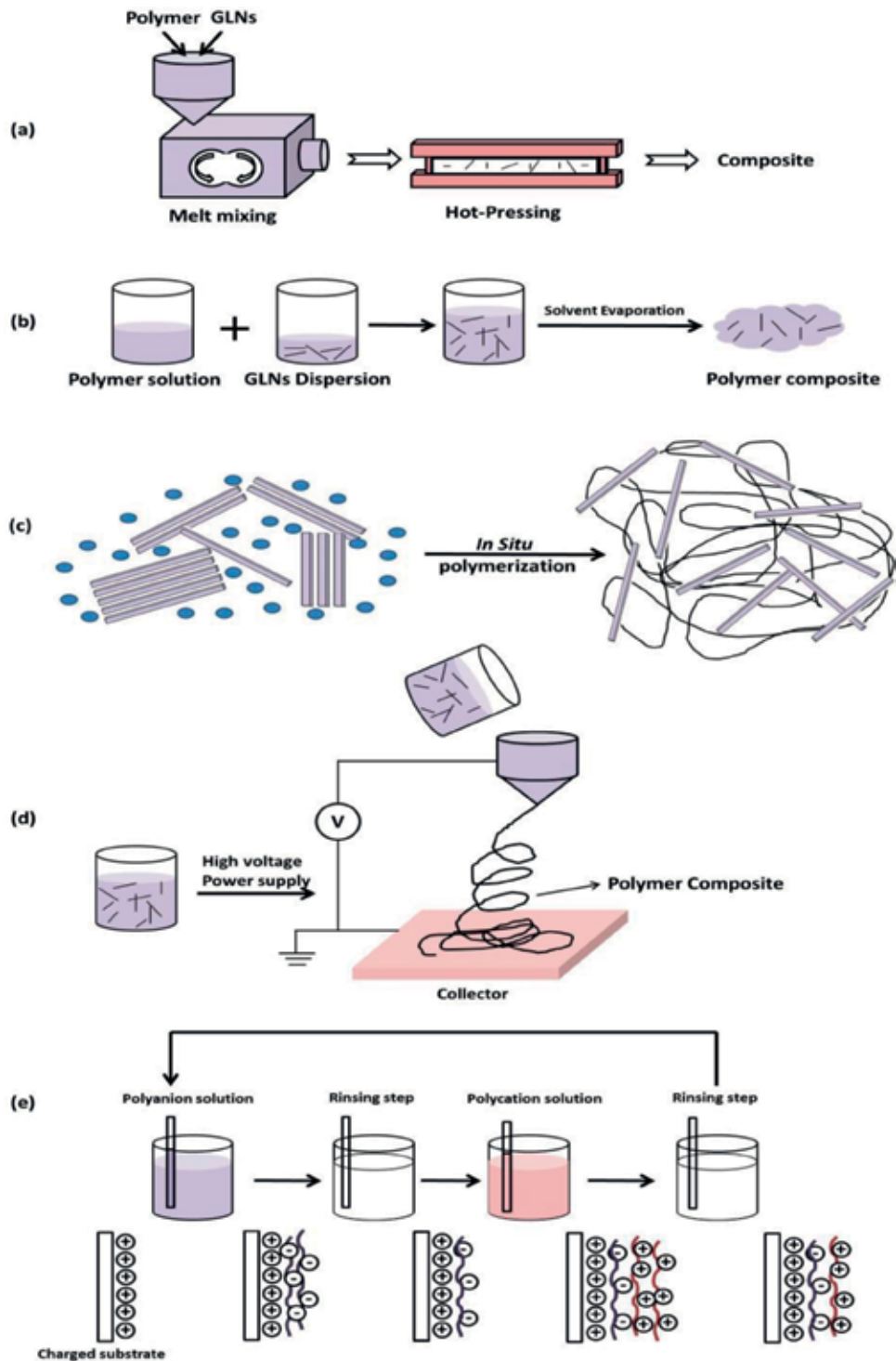
Figure 3.
Schematic image of basic set-up of processing methods of composites (a) melt processing, (b) solvent processing, (c) in-situ *polymerization, (d) electrospinning and (e) layer by layer (LBL) assembly.*

polyvinyl alcohol, poly(hydroxy amino ether), PS, polyethylene (PE), polyethylene oxide (PEO) and epoxy can be used. Low viscosity of polymer in the solution (contrary to the molten method) with mechanical stirring or ultrasonic waves can help the

better dispersity of nanosheets in the polymeric matrix [16]. Different solvents can be put in this category such as chloroform, acetonitrile and toluene [38–40].

Another technique is *in situ* polymerization that both thermoset and thermoplastic polymers can be used. The filler should be dispersed in the monomer that is supposed to polymerize (**Figure 3(c)**). Polymerization begins with the use of a chemical that initiates the reaction or the mixing of the two monomers or with the help of temperature. One of the advantages of this method is the ability to graft polymer molecules to the filler surface and better dispersion of nanosheets. This technique can be used to make polymer composites that are not soluble in common solvents or are thermally unstable (for melt mixing). This method has been used in the development of PE [41], PP [42], PMMA [43], nylon 6 [44], PU [45], polylactic acid (PLA) [46], etc. composites.

Another method used to make this type of nanocomposite is electrospinning, which has been reported with the use of polymers such as polyimide, polyurethane (PU) [47], poly(vinyl alcohol) (PVA) [48], gelatin [49], nylon 6 [50], polyaniline (PANI) [51]. In this method, nanosheets orientation is possible along the axis of the fibers (**Figure 3(d)**). Electrospun diameter of polymer fibers can be controlled in the range of tens of nanometers to several micrometers [16].

Another possible way to achieve the proper dispersion of GL nanosheets in the polymeric matrix is layer by layer (LBL) assembly while to maintain the unique properties of the components (**Figure 3(e)**). This technique is obtained by sequential absorption of the charged components in opposite direction by attractive forces such as electrostatic, hydrogen bonding, etc. Therefore, multi-layer structures using the LBL assembly can be manufactured reproducibly, so that it is possible to control the thickness and composition of hybrid nanocomposite at the nanoscale level [52].

Despite the successful use of various methods in the synthesis of these nanocomposites, there is still a lack of information about: (1) the use of a suitable method for a particular compound of a matrix and reinforcement; (2) the maximum reinforcement content for achieving an optimal combination of properties and the low costs [16]. Therefore, it is still necessary to use the simulation and modeling method to achieve the answer to these unbeknownst.

5. Application of graphene-like nanocomposite

Depending on the type of GLNs and its inherent properties, the designed properties of nanocomposite can be received. Extraordinary properties of GLNs, such as BNNSs, including high thermal properties, structural stability, good mechanical properties, and antioxidant ability, have attracted the attention of researchers to use as a filler [53, 54]. A summary of the application of GLNs nanocomposites is shown in **Figure 4**.

Fillers with a high aspect ratio and crystallinity can improve thermal conductivity and reduce Kapitza resistance [55, 56]. For example, most thermoplastic polymers, such as polyethylene, polypropylene, polyamide and thermosets such as epoxy, are insulating and have very low thermal conductivity, but these properties can be improved by adding fillers such as boron nitride. The use of BN in insulating polymer matrix is the solution if both of electrical properties and thermal conductivity are needed in an electronic device [57]. So far, few studies have been carried out on the thermal conductivity of thermoplastics filled with 2D boron nitride [58–65]. Therefore, researchers focus the investigation on the effect of filler (chemical composition, morphology, surface characteristics, shape and size) on electrical conductivity.
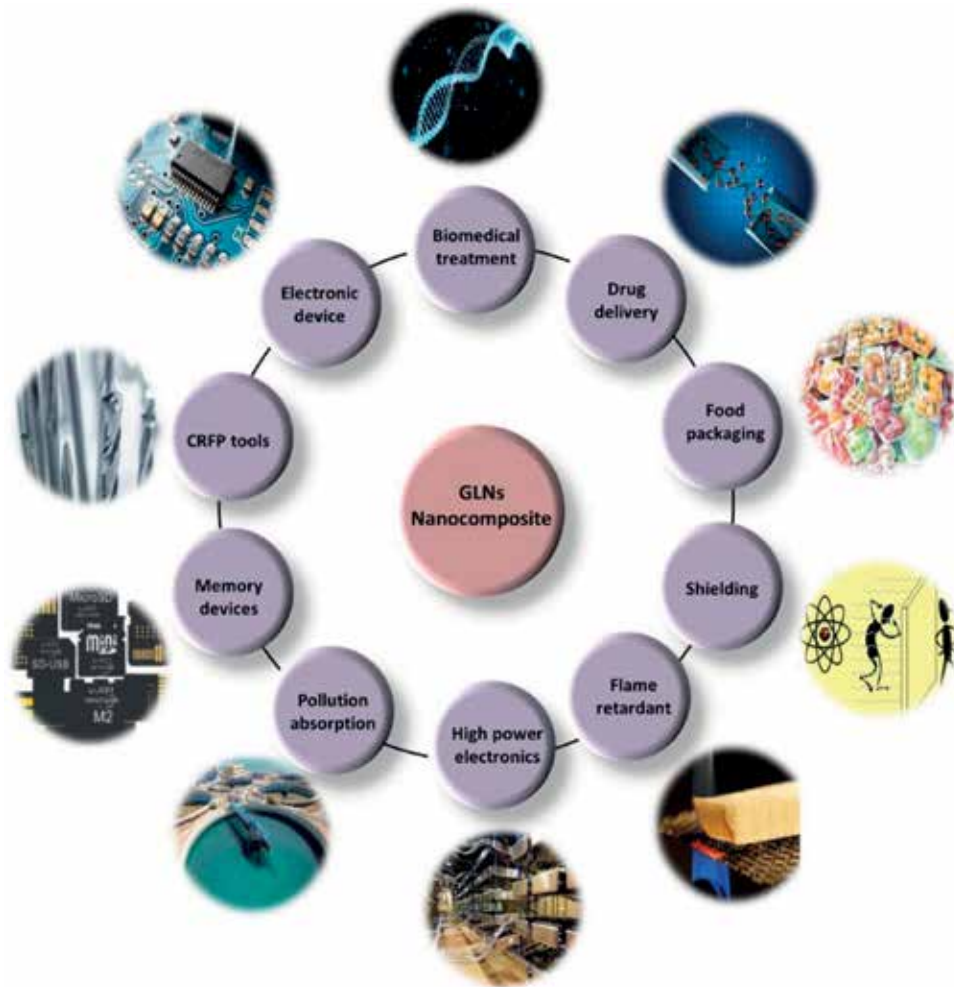
Figure 4.
A summary of the application of GLNs nanocomposites.

The application of epoxy as a thermoset polymer is highly sought-after due to high chemical resistance, corrosion and significant mechanical properties. However, due to very low thermal conductivity (0.15–0.35 W/mK), its use in electronic tools and carbon fiber reinforced plastic (CFRP) tooling is limited. Hence, researchers have used BNNSs to improve the thermal conductivity of this polymer [66, 67].

PVA/BNNSs can be used to make memory devices, due to the huge potential of trapping charge carriers and to perceive the non-volatile memory effect. In these devices, a thin film of hybrid nanocomposite is used as a sandwiched active layer between two conductive electrodes to form the memristor structure [68].

Flexible insulation nanocomposites such as PU/BN nanocomposites show high thermal conductivity that are a desirable option for miniaturization of high-power electronics and portable devices [69].

Polymer materials are widely used in most important industries. However, these materials are high-risk materials to burn, and most of them are decomposed with the emission of toxic gases. Therefore, nanocomposite modification is necessary to reduce their flammability. There are three common strategies to achieve this: the use of inherently flame resistant polymers, flame retardant materials and surface/coating modifications. Usually, a small amount of filler can improve the thermal

properties of the nanocomposite. 2D graphene-like nanomaterials as inorganic fillers, if they are well spread on the polymer matrix, can create a physical barrier inside the polymer and prevent the penetration of heat and degradation of polymeric materials. Totally, the addition of 2D nanosheets results in the thermal stability of polymers. This effect can be due to the thermal stability of filler and the barrier effect of these nanomaterials, which leads to the resistance of the nanocomposite to thermal degradation and prevents the penetration of degradation products from the polymer matrix to the gas phase. Several studies have been carried out on the effects of these nanomaterials on the thermal stability of various polymers [61, 70].

GL nanomaterials are capable of separating, organic pollution absorption, water and wastewater treatment, contaminant elimination from oil, due to the nanosheet structure, the polarity of bonds and the high surface area. In practical application and in different situations, these nanosheets due to their powdery state and the ease of collection after separation require for the embedding in a substrate. Therefore, polymer-based nanocomposites of GLNs such as polyvinylidene fluoride (PVDF) (due to high chemical resistance) are used [71–73].

One of the special applications of BNNSs is the neutron shielding property, due to intrinsic property of boron in absorbing neutrons. The placement of boron nitride in a polymeric matrix can produce a multifunctional nanocomposite that exhibits structural, radiation protection, and even resistance to flame. These polymer nanocomposites can be used in spacecraft and nuclear reactors. NASA has focused on the protective properties of nanocomposites containing BNNSs in a polyethylene matrix [74, 75].

Since graphene and graphene oxide have been successfully used in biomedical applications, much attention has been paid to GLNs due to their 2D structure, which is similar to graphene. Polymers, on the other hand, were used in bio-detecting research because of low weight, ease of fabrication, and relatively low cost of processing. The simultaneous use of 2D materials and polymers offers a lot of potential to the researchers. BN has a high biocompatibility due to its excellent chemical stability, good process—ability and good biology activity [76]. For example, chitosan/BN nanocomposites have been used as protective coating for stainless steel. Also, BN is used to strengthen polypropylene as a bio-composite for bone prosthesis [77].

The water-soluble polymers have a widespread in biomedical science. The polyethylene glycol (PEG) nanocomposite containing MoS_2 nanosheets has been used as a multi-functional drug carrier for combined cancer therapy [78]. Also, PEG nanocomposites containing WS_2 have been used as a multifunctional agent for dual-modal CT/photoacoustic imaging in photo-thermal therapy [79]. Also, MoS_2-based nanocomposites are used in DNA sensors to detect DNA molecules [80].

Another application of GLNs nanocomposites are the increasing the impermeability of nanocomposites against oxygen that used in the food packaging industry. Most polymers used in this industry suffer from the problem of oxygen penetration. 2D nanosheets form a strong barrier against oxygen penetration due to their layered structure. For example, the nanocomposites based on cellulose nanofibers containing BNNSs prevent the penetration of oxygen. In addition, GLNs improve the mechanical properties of the nanocomposite and does not alter the brittleness [81].

6. Future outlook

The fillers based on GL nanomaterials are at the beginning of their path to expand. However, there are several fundamental challenges that must be considered before fully understanding their effects in polymer composites.

1. Distribution of fillers in the polymeric matrix is important to achieve the properties of nanocomposites. However, most of the composite processing methods are not economically optimal. Solvent processing, LBL assembly and electrospinning have a better result in dispersion of the filler but are not economically affordable. The melt processing method is economical, but the filler has no proper dispersion and the final properties are less than optimal.

2. GL nanomaterials can act as nucleating sites and affect the polymer's crystallinity. Therefore, the degree of dependence of the crystallinity value on the mechanical properties of the composites should be investigated.

3. The development and quality of nanocomposites containing GL nanomaterials depend on several factors, including the type of filler, the number of layers, the purity of the filler, the amount of dispersion in the polymer, and the interaction between the filler and the polymer matrix. However, so far, no systematic study has been done to compare the effect of aspect ratio, filler purity, functionalization degree, and the types of functional groups on the properties of nanocomposites.

7. Conclusions

Graphene-like nanomaterials and polymer-based nanocomposites demonstrate the increasing growth in technology and applications. In this study, recent advances in the production of polymer-filled nanocomposites with GLNs were investigated, properties and applications of these materials. Although these materials are in the early stages of development, their value added and their ability to address them is quite evident. Of course, one should take into account the unfulfilled expectations of graphene nanocomposites and consider the challenges and problems involved in the development of these materials that need to be solved and used them to develop polymer-filled with GLNs.

The first challenge is the production of GLNs. On the other hand, high-quality and large-scale of GLNs preparation at affordable cost is still not possible. Although recent steps have been taken for this purpose seriously, but new synthesis methods should be created to reduce the use of acid and solvent.

The second major challenge is the nanocomposite production process. The full utilization of GLNs-filled nanocomposites with the good dispersion of GLNs increases the cost-effectiveness of final nanocomposite production. Many efforts have been made to improve and enhance the properties of nanocomposites by modifying the interfacial interaction of filler and polymer matrix through functionalization or use the compatibilizers. Several studies use the functionalization of filler in order to create strong interaction between GLNs with a polymer matrix. This improves bonding between GLNs and polymer, which improves stress transfer, increases thermal stability and other properties. Efforts in this field can lead to the production of nanocomposites that have widespread use in the field of bio-detecting, drug delivery, food packaging, thermal shields, contamination absorption, electronics device etc.

Conflict of interest

The authors declare that they have no conflict of interest.

Author details

Zahra Rafiei-Sarmazdeh[1*] and Seyed Javad Ahmadi[2]

1 Plasma and Nuclear Fusion Research School, Nuclear Science and Technology Research Institute, Tehran, Iran

2 Nuclear Fuel Cycle School, Nuclear Science and Technology Research Institute, Tehran, Iran

*Address all correspondence to: zrafiei@alumni.ut.ac.ir

IntechOpen

References

[1] Papageorgiou DG, Kinloch IA, Young RJ. Mechanical properties of graphene and graphene-based nanocomposites. Progress in Materials Science. 2017;**90**: 75-127. DOI: 10.1016/j.pmatsci.2017. 07.004

[2] Okpala CC. Nanocomposites—An overview. International Journal of Engineering Research and Development. 2013;**8**(11):17-23. e-ISSN: 2278-067X

[3] Wan RM, Zheng SR, Zheng Y. Polymer Matrix Composites and Technology. 1st ed. Cambridgeshire, England: Woodhead Publishing Limited; 2011

[4] Beaumont PWR, Zweben CH. Comprehensive Composite Materials II. 2nd ed. Amsterdam, Netherlands: Elsevier; 2018

[5] Nag A, Raidongia K, Hembram KPSS, Datta R, Waghmare UV, Rao CNR. Graphene analogues of BN: Novel synthesis and properties. ACS Nano. 2010;**4**(3):1539-1544. DOI: 10.1021/ nn9018762

[6] Wang J, Ma F, Sun M. Graphene, hexagonal boron nitride, and their heterostructures: Properties and applications. RSC Advances. 2017;**7**: 16801-16822. DOI: 10.1039/ C7RA00260B

[7] Avouris P. Graphene: Electronic and photonic properties and devices. Nano Letters. 2010;**10**(11):4285-4294. DOI: 10.1021/nl102824h

[8] Antonio T, Patrick GS. Graphene: From functionalization to devices. Journal of Physics D: Applied Physics. 2014;**47**(9):090201. DOI: 10.1088/ 0022-3727/47/9/090201

[9] Shao Y, Wang J, Wu H, Liu J, Aksay IA, Lin Y. Graphene based electrochemical sensors and biosensors: A review. Electroanalysis. 2010;**22**(10):

1027-1036. DOI: 10.1002/elan. 200900571

[10] Justino CIL, Gomes AR, Freitas AC, Duarte AC, Rocha-Santos TAP. Graphene based sensors and biosensors. Trends in Analytical Chemistry. 2017; **91**:53-66. DOI: 10.3390/s17102161

[11] Pumera M. Graphene in biosensing. Materials Today. 2011;**14**(7):308-315. DOI: 10.1016/S1369-7021(11)70160-2

[12] Deshmukh K, Joshi GM. Embedded capacitor applications of graphene oxide reinforced poly(3,4-ethylenedioxythiophene)-tetramethacrylate (PEDOT-TMA) composites. Journal of Materials Science: Materials in Electronics. 2015;**26**(8): 5896-5909. DOI: 10.1007/s10854-015-3159-0

[13] Luong ND, Hippi U, Korhonen JT, Soininen AJ, Ruokolainen J, Johansson L-S, et al. Enhanced mechanical and electrical properties of polyimide film by graphene sheets via in situ polymerization. Polymer. 2011;**52**(23): 5237-5242. DOI: 10.1016/j. polymer.2011.09.033

[14] Novoselov KS, Geim AK, Morozov SV, Jiang D, Zhang Y, Dubonos SV, et al. Electric field effect in atomically thin carbon films. Science. 2004;**306**(5696): 666. DOI: 10.1126/science.1102896

[15] New Devices and New Physical Effects with Automically Thin Stacks. Arkansas: Churchill Lab. Available from: http://churchill-lab.com/research/

[16] Bhattacharya M. Polymer nanocomposites—A comparison between carbon nanotubes, graphene, and clay as nanofillers. Materials. 2016; **9**(4):262-296. DOI: 10.3390/ma9040262

[17] Streletskii AN, Permenov DG, Bokhonov BB, Kolbanev IV, Leonov AV,

Berestetskaya IV, et al. Destruction, amorphization and reactivity of nano-BN under ball milling. Journal of Alloys and Compounds. 2009;**483**(1–2): 313-316. DOI: 10.1016/j.jallcom. 2008.08.088

[18] Li LH, Chen Y, Behan G, Zhang H, Petravic M, Glushenkov AM. Large-scale mechanical peeling of boron nitride nanosheets by low-energy ball milling. Journal of Materials Chemistry. 2011;**21**(32):11862-11866. DOI: 10.1039/ C1JM11192B

[19] Pu F. High yield production of inorganic graphene-like materials (MoS_2, WS_2, BN) through loquid exfoliation testing key parameters [thesis]. Department of Materials Science and Engineering, Massachusetts Institute of Technology; 2012

[20] Cao L, Emami S, Lafdi K. Large-scale exfoliation of hexagonal boron nitride nanosheets in liquid phase. Materials Express. 2014;**4**(2):165-171. DOI: 10.1166/mex.2014.1155

[21] André C, Guillaume YC. Boron nitride nanotubes and their functionalization via quinuclidine-3-thiol with gold nanoparticles for the development and enhancement of the HPLC performance of HPLC monolithic columns. Talanta. 2012;**93**:274-278. DOI: 10.1016/j.talanta.2012.02.033

[22] Lin Y, Williams TV, Cao W, Elsayed-Ali HE, Connell JW. Defect functionalization of hexagonal boron nitride nanosheets. Journal of Physical Chemistry C. 2010;**114**:17434-17439. DOI: 10.1021/jp105454w

[23] Magda GZ, Pető J, Dobrik G, Hwang C, Biró LP, Tapasztó L. Exfoliation of large-area transition metal chalcogenide single layers. Scientific Reports. 2015;**5**: 14714-14718. DOI: 10.1038/srep14714

[24] Costa MCF, Ribeiro HB, Kessler F, Souza EAT, Fechine GJM.

Micromechanical exfoliation of two-dimensional materials by a polymeric stamp. Materials Research Express. 2016;**3**(2):025303-025307. DOI: 10.1088/2053-1591/3/2/025303

[25] Brent JR, Savjani N, O'Brien P. Synthetic approaches to two-dimensional transition metal dichalcogenide nanosheets. Progress in Materials Science. 2017;**89**:411-478. DOI: 10.1016/j.pmatsci.2017.06.002

[26] Lin Z, McCreary A, Briggs N, Subramanian S, Zhang K, Sun Y, et al. 2D materials advances: From large scale synthesis and controlled heterostructures to improved characterization techniques, defects and applications. 2D Materials. 2016;**3**(4): 042001-042038. DOI: 10.1088/ 2053-1583/3/4/042001

[27] Yu J, Hu X, Li H, Zhou X, Zhai T. Large-scale synthesis of 2D metal dichalcogenides. Journal of Materials Chemistry C. 2018;**6**(17):4627-4640. DOI: 10.1039/C8TC00620B

[28] Wang H, Zhao Y, Xie Y, Ma X, Zhang X. Recent progress in synthesis of two-dimensional hexagonal boron nitride. Journal of Semiconductors. 2017;**38**(3):031003-031016. DOI: 10.1088/1674-4926/38/3/031003

[29] Bhuvana S, Prabakaran M. Synthesis and characterisation of polyamide/ halloysite nanocomposites prepared by solution intercalation method. Nanoscience and Nanotechnology. 2014;**4**:44-51. DOI: 10.3390/ma9040262

[30] Dhand V, Rhee KY, Ju Kim H, Ho Jung D. A comprehensive review of graphene nanocomposites: Research status and trends. Journal of Nanomaterials. 2013;**2013**:1-14. DOI: 10.1155/2013/763953

[31] Paul DR, Robeson LM. Polymer nanotechnology: Nanocomposites.

Polymer. 2008;**49**(15):3187-3204. DOI: 10.1016/j.polymer.2008.04.017

[32] Chen B, Evans JRG, Greenwell HC, Boulet P, Coveney PV, Bowden AA, et al. A critical appraisal of polymer-clay nanocomposites. Chemical Society Reviews. 2008;**37**(3):568-594. DOI: 10.1039/B702653F

[33] Coleman JN, Khan U, Blau WJ, Gun'ko YK. Small but strong: A review of the mechanical properties of carbon nanotube-polymer composites. Carbon. 2006;**44**(9):1624-1652. DOI: 10.1016/j.carbon.2006.02.038

[34] Kim H, Abdala AA, Macosko CW. Graphene/polymer nanocomposites. Macromolecules. 2010;**43**(16):6515-6530. DOI: 10.1021/ma100572e

[35] Salavagione HJ, Castelaín M, Shuttleworth PS, Martínez G, Gómez-Fatou MA, Marco C, et al., editors. Graphene based polymer nanocomposites: Chemical incorporation strategies and property enhancement. In: 16th European Conference on Composite Materials, ECCM 2014. 2014

[36] Jiang X, Drzal LT. Improving electrical conductivity and mechanical properties of high density polyethylene through incorporation of paraffin wax coated exfoliated graphene nanoplatelets and multi-wall carbon nano-tubes. Composites Part A: Applied Science and Manufacturing. 2011;**42**(11):1840-1849. DOI: 10.1016/j.compositesa.2011.08.011

[37] El Achaby M, Qaiss A. Processing and properties of polyethylene reinforced by graphene nanosheets and carbon nanotubes. Materials and Design. 2013;**44**:81-89. DOI: 10.1016/j.matdes.2012.07.065

[38] Aranda P, Ruiz-Hitzky E. Poly (ethylene oxide)-silicate intercalation materials. Chemistry of Materials. 1992;

4(6):1395-1403. DOI: 10.1021/cm00024a048

[39] Shen Z, Simon GP, Cheng Y-B. Comparison of solution intercalation and melt intercalation of polymer-clay nanocomposites. Polymer. 2002;**43**(15):4251-4260. DOI: 10.1016/S0032-3861(02)00230-6

[40] Furuichi N, Kurokawa Y, Fujita K, Oya A, Yasuda H, Kiso M. Preparation and properties of polypropylene reinforced by smectite. Journal of Materials Science. 1996;**31**(16):4307-4310. DOI: 10.1007/BF00356454

[41] Zhang H, Zhang H-X, Yoon K-B. Synthesis of polyethylene/exfoliated MoS_2 nanocomposites by in situ exfoliation polymerization using Ziegler-Natta catalyst intercalated MoS_2. RSC Advances. 2017;**7**(82):52048-52052. DOI: 10.1039/C7RA10853B

[42] Huang Y, Qin Y, Zhou Y, Niu H, Yu Z-Z, Dong J-Y. Polypropylene/graphene oxide nanocomposites prepared by In situ Ziegler-Natta polymerization. Chemistry of Materials. 2010;**22**(13):4096-4102. DOI: 10.1021/cm100998e

[43] Aldosari AM, Othman AA, Alsharaeh HE. Synthesis and characterization of the in situ bulk polymerization of PMMA containing graphene sheets using microwave irradiation. Molecules. 2013;**18**(3):3152-3167. DOI: 10.3390/molecules18033152

[44] Xu Z, Gao C. In situ polymerization approach to graphene-reinforced nylon-6 composites. Macromolecules. 2010;**43**(16):6716-6723. DOI: 10.1021/ma1009337

[45] Wang X, Hu Y, Song L, Yang H, Xing W, Lu H. In situ polymerization of graphene nanosheets and polyurethane with enhanced mechanical and thermal properties. Journal of Materials

Chemistry. 2011;**21**(12):4222-4227. DOI: 10.1039/C0JM03710A

[46] Qiu Z, Guan W. In situ ring-opening polymerization of poly (l-lactide)-graft-graphene oxide and its effect on the crystallization kinetics and morphology of biodegradable poly(l-lactide) at low loadings. RSC Advances. 2014;**4**(19):9463-9470. DOI: 10.1039/C3RA46656F

[47] Jing X, Mi H-Y, Salick MR, Cordie TM, Peng X-F, Turng L-S. Electrospinning thermoplastic polyurethane/graphene oxide scaffolds for small diameter vascular graft applications. Materials Science and Engineering: C. 2015;**49**:40-50. DOI: 10.1016/j.msec.2014.12.060

[48] Bao Q, Zhang H, Yang J-x, Wang S, Tang DY, Jose R, et al. Graphene-polymer nanofiber membrane for ultrafast photonics. Advanced Functional Materials. 2010;**20**(5):782-791. DOI: 10.1002/adfm.200901658

[49] Panzavolta S, Bracci B, Gualandi C, Focarete ML, Treossi E, Kouroupis-Agalou K, et al. Structural reinforcement and failure analysis in composite nanofibers of graphene oxide and gelatin. Carbon. 2014;**78**:566-577. DOI: 10.1016/j.colsurfa.2012.05.018

[50] Pant HR, Park CH, Tijing LD, Amarjargal A, Lee D-H, Kim CS. Bimodal fiber diameter distributed graphene oxide/nylon-6 composite nanofibrous mats via electrospinning. Colloids and Surfaces A: Physicochemical and Engineering Aspects. 2012;**407**:121-125. DOI: 10.1016/j.colsurfa.2012.05.018

[51] Wang Y, Tang J, Xie S, Liu J, Xin Z, Liu X, et al. Leveling graphene sheets through electrospinning and their conductivity. RSC Advances. 2015;**5**(52):42174-42177. DOI: 10.1039/C5RA01922B

[52] Lee T, Min SH, Gu M, Jung YK, Lee W, Lee JU, et al. Layer-by-layer assembly for graphene-based multilayer nanocomposites: Synthesis and applications. Chemistry of Materials. 2015;**27**(11):3785-3796. DOI: 10.1021/acs.chemmater.5b00491

[53] Yu C, Zhang J, Tian W, Fan X, Yao Y. Polymer composites based on hexagonal boron nitride and their application in thermally conductive composites. RSC Advances. 2018;**8**:21948-21967. DOI: 10.1021/acsami.5b03007

[54] Yuan C, Duan B, Li L, Xie B, Huang M, Luo X. Thermal conductivity of polymer-based composites with magnetic aligned hexagonal boron nitride platelets. ACS Applied Materials and Interfaces. 2015;**7**(23):13000-13006. DOI: 10.1021/cm504550e

[55] Shtein M, Nadiv R, Buzaglo M, Kahil K, Regev O. Thermally conductive graphene-polymer composites: Size, percolation, and synergy effects. Chemistry of Materials. 2015;**27**(6):2100-2106. DOI: 10.1021/cm504550e

[56] Hu J, Huang Y, Yao Y, Pan G, Sun J, Zeng X, et al. Polymer composite with improved thermal conductivity by constructing a hierarchically ordered three-dimensional interconnected network of BN. ACS Applied Materials and Interfaces. 2017;**9**(15):13544-13553. DOI: 10.1021/acsami.7b02410

[57] Guerra V, Wan C, McNally T. Thermal conductivity of 2D nano-structured boron nitride (BN) and its composites with polymers. Progress in Materials Science. 2019;**100**:170-186. DOI: 10.1021/jp0607014

[58] Takahashi S, Imai Y, Kan A, Hotta Y, Ogawa H. Dielectric and thermal properties of isotactic polypropylene/hexagonal boron nitride composites for high-frequency applications. Journal of Alloys and Compounds. 2014;**615**:

141-145. DOI: 10.1016/j.jallcom. 2014.06.13

[59] Zhang X, Shen L, Wu H, Guo S. Enhanced thermally conductivity and mechanical properties of polyethylene (PE)/boron nitride (BN) composites through multistage stretching extrusion. Composites Science and Technology. 2013;**89**:24-28. DOI: 10.1016/j. compscitech.2013.09.017

[60] Zhou W, Qi S, Li H, Shao S. Study on insulating thermal conductive BN/HDPE composites. Thermochimica Acta. 2007;**452**(1):36-42. DOI: 10.1016/j.tca.2006.10.018

[61] Shin YK, Lee WS, Yoo MJ, Kim ES. Effect of BN filler on thermal properties of HDPE matrix composites. Ceramics International. 2013;**39**:S569-SS73. DOI: 10.1016/j.ceramint.2012.10.137

[62] Muratov DS, Kuznetsov DV, Il'inykh IA, Mazov IN, Stepashkin AA, Tcherdyntsev VV. Thermal conductivity of polypropylene filled with inorganic particles. Journal of Alloys and Compounds. 2014;**586**: S451-S4S4. DOI: 10.1016/j. jallcom.2012.11.142

[63] Kim K, Ju H, Kim J. Filler orientation of boron nitride composite via external electric field for thermal conductivity enhancement. Ceramics International. 2016;**42**(7):8657-8663. DOI: 10.1016/j.ceramint.2016.02.098

[64] Kemaloglu S, Ozkoc G, Aytac A. Thermally conductive boron nitride/SEBS/EVA ternary composites: "Processing and characterization". Polymer Composites. 2010;**31**(8): 1398-1408. DOI: 10.1002/pc.20925

[65] Cheewawuttipong W, Fuoka D, Tanoue S, Uematsu H, Iemoto Y. Thermal and mechanical properties of polypropylene/boron nitride composites. Energy Procedia. 2013;**34**:

808-817. DOI: 10.1016/j.egypr.2013. 06.817

[66] Hou J, Li G, Yang N, Qin L, Grami ME, Zhang Q, et al. Preparation and characterization of surface modified boron nitride epoxy composites with enhanced thermal conductivity. RSC Advances. 2014;**4**:44282-44290. DOI: 10.1021/cm504550e

[67] Xu Y, Chung DDL. Increasing the thermal conductivity of boron nitride and aluminum nitride particle epoxy-matrix composites by particle surface treatments. Composite Interfaces. 2000;**7**:243-256. DOI: 10.1163/156855 400750244969

[68] Siddiqui GU, Rehman MM, Yang Y-J, Choi KH. A two-dimensional hexagonal boron nitride/polymer nanocomposite for flexible resistive switching devices. Journal of Materials Chemistry C. 2017;**5**:862-871. DOI: 10.1039/C6TC04345C

[69] Yu C, Gong W, Tian W, Zhang Q, Xu Y, Lin Z, et al. Hot-pressing induced alignment of boron nitride in polyurethane for composite films with thermal conductivity over 50 $Wm^{-1}K^{-1}$. Composites Science and Technology. 2018;**160**:199-207. DOI: 10.1016/j.compscitech.2018.03.028

[70] Wenelska K, Maślana K, Mijowska E. Study on the flammability, thermal stability and diffusivity of polyethylene nanocomposites containing few layered tungsten disulfide (WS_2) functionalized with metal oxides. RSC Advances. 2018; **8**:12999-13007. DOI: 10.1039/C8RA01527A

[71] Liu D, He L, Lei W, Klika KD, Kong L, Chen Y. Multifunctional polymer/porous boron nitride nanosheet membranes for superior trapping emulsified oils and organic molecules. Advanced Materials Interfaces. 2015; **2**(12):1500228. DOI: 10.1002/admi.201500228

[72] Moradi R, Shariaty-Niassar M, Pourkhalili N, Mehrizadeh M, Niknafs H. PVDF/h-BN hybrid membranes and their application in desalination through AGMD. Membrane Water Treatment. 2018;**9**:221-231. DOI: 10.12989/mwt.2018.9.4.221

[73] Kamble AR, Patel CM, Murthy ZVP. Modification of PVDF membrane by two-dimensional inorganic additive for improving gas permeation. Separation Science and Technology. 2018:1-18. DOI: 10.1080/01496395.2018.1496118

[74] Harrison C, Burgett E, Hertel N, Grulke E. Polyethylene boron composites for radiation shielding applications. American Institute of Physics. 2008;**969**:484-491. DOI: 10.1063/1.2845006

[75] Harrison C, Weaver S, Bertelsen C, Burgett E, Hertel N, Grulke E. Polyethylene/boron nitride composites for space radiation shielding. Journal of Applied Polymer Science. 2008;**109**: 2529-2538. DOI: 10.1002/app.27949

[76] Lu F, Wang F, Cao L, Kong CY, Huang X-C. Hexagonal boron nitride nanomaterials: Advances towards bioapplications. Nanoscience and Nanotechnology Letters. 2012;**4**: 949-961. DOI: 10.1166/nnl.2012.1444

[77] Chan WK, Wong MH, Yeung WK, Tjong CS. Polypropylene biocomposites with boron nitride and nanohydroxyapatite reinforcements. Materials. 2015;**8**(3):992-1008. DOI: 10.3390/ma8030992

[78] Liu T, Wang C, Gu X, Gong H, Cheng L, Shi X, et al. Drug delivery with PEGylated MoS_2 nano-sheets for combined photothermal and chemotherapy of cancer. Advanced Materials. 2014;**26**(21):3433-3440. DOI: 10.1002/adma.201305256

[79] Cheng L, Liu J, Gu X, Gong H, Shi X, Liu T, et al. PEGylated WS_2 nanosheets as a multifunctional theranostic agent for in vivo dual-modal CT/photoacoustic imaging guided photothermal therapy. Advanced Materials. 2014;**26**(12):1886-1893. DOI: 10.1002/adma.201304497

[80] Zhu C, Zeng Z, Li H, Li F, Fan C, Zhang H. Single-layer MoS_2-based nanoprobes for homogeneous detection of biomolecules. Journal of the American Chemical Society. 2013; **135**(16):5998-6001. DOI: 10.1021/ja4019572

[81] Nguyen H-L, Hanif Z, Park S-A, Choi BG, Tran TH, Hwang DS, et al. Sustainable boron nitride nanosheet-reinforced cellulose nanofiber composite film with oxygen barrier without the cost of color and cytotoxicity. Polymers. 2018;**10**:501-516. DOI: 10.3390/polym10050501

Polymer Nanocomposite-Based Electrochemical Sensors and Biosensors

Baiju John

Abstract

Polymer nanocomposites (PNCs) play a significant role in modern day life and are widely studied for extensive properties which make them appealing to numerous applications. They are synthesized with scalable processing procedures with several nanoscale variations of fillers and forms leading to specific sensing applications. In this chapter, PNC-based electrochemical sensors and biosensors like DNA biosensors and immunosensors are discussed. These sensors related PNC applications uses nanofillers of various combinations like conductive polymers with graphene (Grp), carbon nanotubes (CNTs), and metal nanoparticles, which endow high electrical conductivity, effective surface area, and fast electron transfer rate. Currently, wearable devices based on electrochemical Sensors and biosensors have been of great interest in the detection of both physiological and environmental analytes.

Keywords: polymer nanocomposites, electrochemical sensors, biosensors, DNA sensors, immunosensors

1. Introduction

Polymer nanocomposites (PNCs) have electrochemical properties as transducers which can be used for the manufacturing of electrochemical sensors and biosensors. They possess significant variations in responsiveness, synthesis, and morphology, which help in a significant level of variations in conductivity [1]. Afar from the economic aspect of the PNC-based sensors, the improved performance on the electronic side stands apart among its peers through the basal plane ratio of the nanofillers, method of doping, kinetic properties of the electrode, biological response and environmental impact [1]. The impact of nanofillers in PNCs plays a significant role in sensing, processing, and actuating capabilities of the electrodes of electrochemical and biosensing applications [2].

The "active states of PNCs" rests on three pillars: high electrical conductivity rate, large surface area and fast electron rate which leads to best electricidal sensor outcomes. PNCs helps in the material technological advancement of electrochemical sensors which have high sensitivity and selectivity, lower detection limits, reproducibility and stability as shown in **Figure 1**. All these increased used the PNCs in electrochemical sensor research which were manufactured through chemical synthesis or polymerization methods and could be easily scaled up for
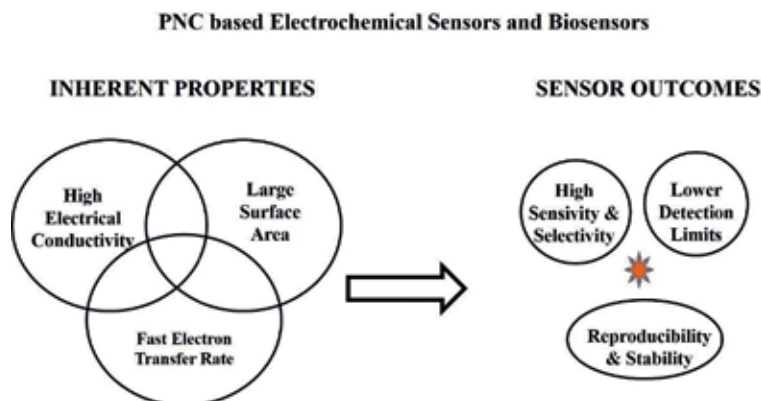
PNC based Electrochemical Sensors and Biosensors

INHERENT PROPERTIES

SENSOR OUTCOMES

High Electrical Conductivity

Large Surface Area

Fast Electron Transfer Rate

High Sensivity & Selectivity

Lower Detection Limits

Reproducibility & Stability

Figure 1.
Key properties of PNC based electrochemical sensors and biosensors. With permission from Elsevier [1].

various applications [3]. The electrochemical sensors along with the immunosensors and biosensors are becoming the norm of the day. Detections limits and sensing technologies are improved consistently due to developments happening in the unique properties of PNCs especially conductivity and electrochemical activity. The interactive fillers facilitate ion diffusion that impacts the sensing applications through intercalation into the PNC matrices leading to better stability of active electron transfer sites and detection limits. These active fillers help in reducing the layer thickness in PNC leading to ultrathin electrochemical detector technology. PNCs stand as an outstanding leader with significant advantages in large specific interaction surface area, reduced dimension of fillers and efficient electron transfer rate [3].

2. Electrochemical sensors

PNCs are widely used in the development of electrochemical sensors. The electrochemical sensors are based on three categories of PNCs. PNCs of conductive polymers and inorganic nanomaterials, PNCs of conductive polymers and Grp, and PNCs of conductive polymers and CNTs. Once interaction has occurred between the PNC-based electrochemical sensors and the target analyte, an electronic signal is detected by the transduction system. The applications of PNC-based electrochemical sensors different materials are shown in **Table 1**.

2.1 Polymer nanocomposites based on conductive polymers and inorganic nanomaterials

Metal and metal oxide nanoparticles have been extensively studied as electrochemical sensing materials due to such beneficial features as their small size; unique chemical, physical, and electronic properties; flexibility in fabricating novel and improved sensing devices; and good sensitivity to the ambient conditions are shown in **Table 1**. The assimilation of nanoparticles of metals into PNC matrices set the stage for enhanced electrocatalytic electrode detection leading to multiple modern-day applications. For example, a Zinc oxide nanoparticle intercalated into polypyrrole (ZnO-PPy) PNC showed excellent Xanthine detection by through xanthine oxidase enzyme immobilization [4]. A glassy carbon electrode (GCE) modified with ultrathin polypyrrole nanosheets decorated with Ag nanoparticles was fabricated for the detection of hydrogen peroxide (H_2O_2). The modified device showed

Sensory material	Analyte	Detection limit
PPy-ZnO-Pt	Xanthine	0.8 μM
PPy-Pt-GCE	Hydrogen peroxide	0.6 μM
PANI-TiO$_2$-GCE	Glucose	0.5 μM
PANI-NiCo$_2$O$_4$-GCE	Glucose	0.3833 μM
PANI-Grp-GCE	4-aminophenol	6.5×10^{-8} M
PANI-Grp-ITO	Artesunate	0.012 ng mL^{-1}
PANI-Grp-GCE	Lercanidipine	1.94 ng mL^{-1}
PANI-Grp-GCE	Nitazoxanide	2.2 μg mL^{-1}
PPy-Grp-GCE	Adenine	0.02 μM
	Guanine	0.01 μM
PPy-PIL-GO-GCE	Dopamine	73.3 nM
PEDOT-rGO-GCE	Dopamine	39.0 nM
PEDOT-Grp-GCE	Ascorbic acid	2.0 μM
PANI-Grp-Bi$_2$O$_3$-GCE	Etodolac	10.03 ng mL^{-1}
PANI-rGO-MIP-AuNP-GCE	Serotonin	11.7 nmol L^{-1}
PPy-MWCNT-ITO	Cholesterol	0.04 mM L^{-1}
PPy-MWCNT-GCE	Pemetrexed	3.28×10^{-9} M
PEDOT-CNT-CPE	Hydroquinone	0.3 μM
PEDOT-CNT-CPE	Dopamine	20.0 nM
PEDOT-CNT-CPE	Nitrobenzene	83.0 nM

Table 1.
Electrochemical sensors based on polymer nanocomposites [1].

high sensitivity toward the reduction of H$_2$O$_2$ [5]. Similar electrochemical sensor based on polypyrrole–platinum (PPy-Pt) PNC was fabricated for the detection of H$_2$O$_2$ [6]. Another voltammetric sensor based on a polyaniline-gold nanoparticle (PANI-AuNP) PNC deposited on GCE was used for the detection of epinephrine (EP) and uric acid (UA) [6]. Exploiting the advantages of PNCs, two GCEs modified with PANI-TiO$_2$ and PANI-NiCo$_2$O$_4$ PNC-based electrochemical sensors were developed for the detection of glucose [7]. TiO$_2$ nanotubes (TNTs) was intercalated into a PANI-TNT PNC composite for through hydrothermal method for the detection (a reported sensitivity of 11.4 μA mM^{-1}) of glucose (a reported sensitivity of 11.4 μA mM^{-1}) by the immobilization of glucose oxidase (GOD) [7].

2.2 Polymer nanocomposites based on conductive polymers and graphene

Graphene (Grp), an allotrope of carbon, has become the new material of interest and widely integrated into the sensor research from the beginning of this millennium due to its unique properties of electrical conduction and 2-dimensional existence. Grp-PNC-based electrochemical sensors are used for electroanalytical detection of target molecules with high precision of selectivity and sensitivity as shown in **Table 1**, which showed spectacular detection limits over a wide range. An electrochemical sensor fabricated for the detection of 4-aminophenol (4-AP) using a PANI-Grp-GCE-modified device showed a detection limit of 6.5×10^{-8} M and sensitivity of 604.2 μAmM^{-1} [8]. A sensor was fabricated with a PANI-Grp-based PNC onto an ITO plate with immobilized horseradish peroxidase enzyme with a

sensitivity limit of 0.15 mA ng mL^{-1} [9]. A PANI-Grp-GCE-based PNC sensor for the elimination of calcium antagonist lercanidipine in pharmaceutical formulations for medical purposes showed a detection limit in the range from 5 to 125 ng mL^{-1} [10]. The same PANI-Grp-GCE-based PNC sensor showed the detection of nitazoxanide compound which was an added advantage [11]. Electrochemical sensors based on PPy-based PNC are becoming popular these days due to their specific applications through their overoxidized form polypyrrole (PPyox). Fabrication of polypyrrole-graphene (PPyox/Grp) helped in the simultaneous detection of adenine and guanine through an electrodeposition method. PPy-Grp composite was electro-polymerized with pyrrole and graphene oxide (GO), followed by electrochemical reduction of GO composite. The electrochemical sensor's significant improvement in the sensing of adenine and guanine is due to the specific structure of the nanocomposite. The adenine and guanine showed strong π-π interactions, and cationic selectivity [12].

The detection of Dopamine (DA) using PNCs was the holy grail in neurochemical studies ad it is a prominent neurotransmitter, which plays a role in neurological disorders such as Parkinson's disease and schizophrenia [13]. A poly(ionic liquid)-functionalized polypyrrole-graphene oxide (PIL-PPy-GO)-based PNC electrochemical sensor was fabricated by the polymerization of 1-vinyl-3-ethyl-imidazolium bromide on N-vinyl imidazolium-modified PPy-GO films. The PILs helped in changing the surface charge which dispersibility of the PIL-PPy-GO composite and helped in the detection of DA [14]. Another sensor used for the detection of DA was a PNC-based poly (3,4-ethylene dioxythiophene)-graphene oxide (PEDOT-GO) fabricated by electrodeposition showed significant sensing capabilities [15]. A one-step electrochemical redox synthesis process of PEDOT-Grp PNC film was done using simultaneous electrodeposition of PEDOT and electrochemical reduction of GO on a GCE with high detection sensing of the ascorbic acid molecules. In this sensor PEDOT-Grp thin film PNC mediated the electron transfer between AO and electrode interface resulting in significant improvement in electrocatalytic activity and sensitivity of ascorbic acid molecules [16]. Jain et al. [5] introduced the combination of Grp and a conducting PANI-Bi$_2$O$_3$ PNC, the synergic effect of which enhanced the performance of sensors used for the electrocatalytic oxidation of etodolac in pharmaceutical formulations.

In recent years, molecularly imprinted polymers (MIPs) with high selectivity, affinity, chemical stability, and easy preparation for the template molecule are a promising candidate for developing a new generation of recognition elements for sensors. A double-layered membrane-sensing interface was fabricated based on rGO-PANI nanocomposites and MIPs embedded with AuNPs for sensitive and selective detection of serotonin (5-hydroxytryptamine, 5-HT). The obtained sensor showed remarkable selectivity to serotonin against the interferences caused by ascorbic acid and other interferents with a good detection limit of 11.7 nmol L^{-1} [17].

2.3 Polymer nanocomposites based on conductive polymers and carbon nanotubes

PNCs based on conductive polymers helped in improving the sensing properties of the electrochemical sensors with enhanced selectivity and stability. Some of the popular CNT-based PNC reported in the literature are shown in **Table 1**. A PPy-multiwalled carbon nanotube (MWCNT)-toluene sulfonic acid-based PNC was fabricated fr the detection of cholesterol with ITO-coated glass was the substrate for the sensor. The sensor showed high sensitivity and a fast response time of 9 s [18]. Sodium dodecyl sulfate-doped PPyox) with carboxylic acid functionalized MWCNT-modified GCE were reported for the detection of the anticancer drug

pemetrexed (PMX). The results showed that overoxidation of the PPy film conferred a negative charge density on the porous layer, which in turn enhances the adsorption of PMX [19]. Xu et al. fabricated a carbon paste electrode (CPE) modified with a PEDOT-CNT nanocomposite. They used this electrode for the analysis of hydroquinone, DA, and nitrobenzene [20].

3. DNA biosensors

PNCs are widely used these days in DNA biosensors. The medico biological field is growing leaping and bounds. In this era of 23 and me everything possible with DNA is bouncing through the boundaries of technology like DNA CRISPR editing, gene mapping. Biological agents for nefarious purposes and forensics. A basic DNA sensor work on a simple principle. You plant a DNA probe on a surface and this planted DNA chain hybridizes with its complementary pair. This hybridization technically called transduction can be detected optically and electrochemically. The electrochemical detection of transducers through electrochemical sensors leads us to DNA biosensors and are now extremely popular. The recent progress in the studies is summarized in **Table 2** and discussed in the section below.

The schematic illustration of the most popular DNA biosensor based on polyaniline-gold nanoparticle-chitosan-graphene sheet (PANI-AuNP-Cts-GS) composite with a functional capture probe for the detection of BCR/ABL fusion gene in chronic myelogenous leukemia (CML) is shown in **Figure 2**. The capture probe used a hairpin structure and was dually labeled with a 5′-SH and a 3′-biotin. The biotin electrode probe was used for the detection of streptavidin–alkaline phosphatase (AP) enzyme which in turn cause an electrochemical signal caused by the catalytic reduction of 1-naphthyl phosphate to 1-naphthol picked up by Diffuse Pulse Voltammetry (DPV) with a detection range of 10–1000 pM [21]. A DNA biosensor fabricated with PANI–AuNP PNC was used for the detection of Ag^+. It works on the following principle: the electrochemical biosensor regenerates cysteine leading to the release of Ag^+ from the cytosine to Ag^+-Cytosine complex and reused again. The fabricated biosensor showed excellent selectivity with a good detection limit for silver ions [22]. Another DNA electrochemical biosensor was developed using polyaniline nanofibers (PANI-nf) enrapturing AuNPs making (PANI-nf-AuNP), a PNC. Gold was used as the electrode for the detection of *Staphylococcus aureus* DNA from the PANI-nf-AuNPs sensor, where the detection concentration varied from 150×10^{-12} to 1×10^{-6} mol L^{-1} [23]. A DNA biosensor based on the PANI-Fe_3O_4-CNT PNC was manufactured for sensing *Neisseria gonorrhoeae* through a DNA probe. The fabricated biosensor showed sensing in the range from 1×10^{-19}

Sensor	Analyte	Detection limit
PANI-AuNP-GS-Cts-GCE	BCR/ABL fusion gene	2.11 pM
PANI-AuNP-Au	Silver ions	10 pM
PANI-AuNP-Au	DNA sequence associated with *S. aureus*	150 pM^{-1} μM
PPy-PANI-AuNP-Au	15-mer DNA oligonucleotides	1.0×10^{-13} M
PPy-PEDOT-AgNP-GCE	27-mer DNA oligonucleotides	$5.4 \pm 0.3 \times 10^{-15}$ M
PANI-Fe_3O_4-CNT-ITO	*Neisseria gonorrhoeae*	1×10^{-19} M
PANI-AuNP-GSPE	microRNA-16	0.1 nM

Table 2.
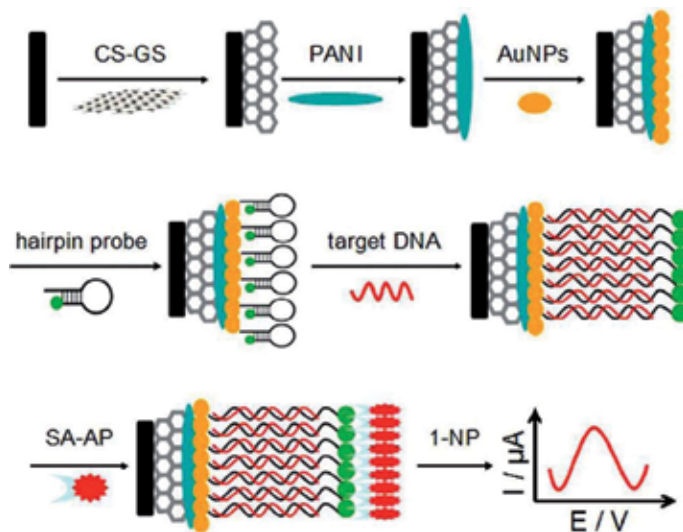*Polymer nanocomposite-based DNA sensors [1].*

Figure 2.
Schematic illustration of the DNA sensor construction process. With permission from Elsevier [1].

to 1×10^{-6} M through DPV measurements [24]. The most recent DNA biosensor based on PANI-AuNPs PNC detected the microRNA-16 using a streptavidin-AP conjugate to biotinylated target sequences through transduction with a detection limit of 0.1 nM [25]. DNA biosensor made with polypyrrole-polyaniline-gold (PPy-PANI-Au) PNC responded to the target DNA through transduction, non-complementary and single- and double-base-mismatched target DNA-chains with a detection limit between 1×10^{-6} and 1×10^{-13} M [26]. Nanotube DNA biosensor based on polypyrrole and poly(3,4-ethylenedioxythiophene) (PPy-PEDOT) PNC, which was functionalized with Ag nanoparticles sensed DNA transduction through EIS detection. The DNA chains used for detection were thiol-capped on the modified sensor [27].

4. Electrochemical immunosensors

PNCs are superior candidates for the fabrication of electrochemical Immunosensors, where the antibodies are the probes which form ionic complexes with the corresponding antigen pair with a specific target. Electrochemical Immunosensors are becoming widely used in clinical diagnosis applications, doping or impurities or detecting biological components in the food industry and detecting the biomolecules of environmental origin and impact. The most widely reported are discussed in this section and shown in **Table 3**. The immunosensors based on CNT-PPy-goat IgGs showed the interaction between the goat IgGs and its anti-goat IgGs, which changes the charges at the sensor surface with changes in conductance level. The response time for the anti-goat IgG was 1 min [28]. A label-free impedance immunosensor for human chorionic gonadotropin (hCG) detection using a PPy-PPa-hCG-modified carbon ink electrode was fabricated by the deposition of a PPy-pyrole-2-carboxylic acid copolymer. The hCG antibody was immobilized via the COOH groups of pyrrole-2-carboxylic acid, as a linker for covalent biomolecular immobilization. This immunosensor has a detection limit of the hCG antigen was in the range of 100 pg mL^{-1} to 40 ng mL^{-1} [29]. The next progress was PANI-AuNP hybrid electrochemical immunosensor with the gold electrode for the detection of prostate antigen (PSA). The immunosensor showed effective immobilization

Sensor	Analyte	Detection limit
CNT-PPy-microelectrode	Anti-goat IgG	0.05 µg mL^{-1}
PPy-PPa-carbon ink	hC	2.3 pg mL^{-1}
PANI-AuNP-Au	Prostate-specific antigen	0.6 pg mL^{-1}
Grp-DPB-AuNP-Au	Aflatoxin B1	1.0 fM
Au-PPy-GCE	Ofloxacin	0.03 ng mL^{-1}
Grp-AuNP-DPB-AuNPs-IL-GCE	Microcystin-LR	3.7×10^{-17} M
Grp-PANI-GCE	Estradiol	0.02 ng mL^{-1}
PANI-GO-CdSe-GCE	Interleukin-6	0.17 pg mL^{-1}
PEDOT-AuNP-ZnSe-Azure I-Pt	Alpha-Fetoprotein	1.1 fg mL^{-1}
PANI-AuNP-PWE	Carcinoembryonic antigen	0.50 pg mL^{-1}
	α-fetoprotein	0.80 pg mL^{-1}
pPPA-MWCNT-GCE	Prolactin	3 pg mL^{-1}
Pt(MPA)NP-PPy-ITO	C-reactive protein (αCRP)	4.54 ng mL^{-1}
PPy-PPa-rGO	Aflatoxin B1	10 fg mL^{-1}
PANI-Au-AMNP-NPG	Carbohydrate antigen 72-4	0.10 U mL^{-1}
AuNP-FC-PANI-GCE	Carcinoembryonic antigen	0.1 pg mL^{-1}

Table 3.
Electrochemical immunosensors based on polymer nanocomposite [1].

of anti-PSA with excellent sensing performance (1.4 µA M^{-1}) and detection limit (0.6 pg mL^{-1}) through effective electron transport [30]. For the detection of aflatoxin B1, an electrochemical immunosensor based on a Grp-CP-AuNP-IL composite film was used. The fabrication was in a five-part series mode as Grp-CP-AuNP-IL pattern. Poly(DPB), 2,5-di-(2-thienyl)-1-pyrrole-1-(p-benzoic acid) helped in the electrochemical stability as a CP. The covalent bonding through the antibody immobilization via carbonyl groups of the polymer helped in preventing the antibody loss, resulting in a detection limit of 1.0 fM [31]. For ofloxacin detection, an immunosensor was fabricated based on a dual-amplification mechanism resulting from Au nanoclusters embedded in the pre-synthesized PPy film as the sensor platform and multienzyme antibody-functionalized gold nanorods as the label. The electrochemical response was in the range of 0.08 and 410 ng mL^{-1} with a low detection limit of 0.03 ng mL^{-1} [32].

An electrochemical immunosensor was fabricated a PNC-based Grp-AuNP-poly-DPB-AuNP-IL for the detection of microcystin-LR through electrodeposition method on GCE. In this electrochemical sensor, the Grp-gold helped in the electron transfer of [Fe(CN)$_6$]$^{3-}$, and the poly 2,5-di-(2-thienyl)-1-pyrrole-1-(p-benzoic acid)- gold nanoparticle (poly-DPB-AuNP) enhanced the electrical conduction and subsequent immobilization of the microcystin-LR antibody [33]. A Grp-PANI-based PNC electrochemical sensor for the estradiol using horseradish peroxidase-graphene oxide-antibody (HRP-GO-Ab) was designed where carboxylated GO serves the antibody carrier property while the horseradish peroxidase helped in catalytic hydrogen reduction on the electrode. This estradiol immunosensor detected the estradiol in tap water and milk samples, with average recoveries of 97.25% and 96.6%, respectively [34]. The electrochemical immunosensors with electrochemiluminescence (ECL) sensing property was achieved through Quantum dots (QDs). This was based on graphene oxide nanosheet–polyaniline nanowire-CdSe quantum dot (GO-PANI-CdSe) which detected human interleukin-6 (IL-6) [35]. A ZnSe QD-Azure

I-AuNP-PEDOT-modified Pt electrode electrochemical immunosensor helped in the detection of alpha-fetoprotein (AFP) through electrochemiluminescence (ECL) sensing (detection limit ~1.1 fg mL^{-1}). The sensing mechanism was as follows: ZnSe QDs immobilize the antibody, the nanoAu-PEDOT facilitated the electron transfer, and Azure I did the catalytic reduction of redox dye with two active amino groups [36].

PANI-AuNP-modified paper working electrodes (PANI-AuNP PWEs) were fabricated for the simultaneous determination of two tumor markers, carcinoembryonic antigen (CEA) and AFP, in real human serum samples [37]. An electrochemical immunosensor for prolactin hormone was also constructed by immobilizing the antigen onto poly (pyrrolepropionic acid) CP and carbon nanotube (pPPA/CNT) hybrids deposited onto a GCE and labeled with AP enzyme with a reported detection limit of 104 ng mL^{-1} [38]. Polypyrrole (PPy)-based PNC was used to manufacture a bioelectrode for the detection of human C-reactive protein antigen (Ag-αCRP). This was made possible with the inorganic nanoparticles (3-mercaptopropionic acid (MPA)-capped Pt nanoparticles. First, the Ab-αCRP was immobilized covalently through specific carboxyl groups linkages through Pt(MPA)- NPs within the polypyrrole (PPy)-based PNC film by carbodiimide coupling. The resulted electrochemical immunosensor showed excellent fine probe orientation with a detection capacity of 10 ng mL^{-1}–10 μg mL^{-1} [39]. Another label-free impedimetric immunosensor based on multifunctional PNCs was based on (polypyrrole–pyrrolepropylic acid–reduced graphene oxide (PPy-PPa-rGO)) for the detection of mycotoxin aflatoxin B1 [40]. An enzyme-free electrochemical immunosensor modeled on the *sandwich* pattern was used for the detection of carbohydrate antigen 72–4 (CA72–4). The sensing electrode was nanoporous gold (NPG) film and asymmetric multicomponent (AMNPs) nanoparticles based on PANI-Au was used as labels. The NPG helped in the creased immobilization of Ab1 on the electrode, while the PANI-Au AMNPs impacted on the reduction capability of the electrochemical immunosensor [41]. The doping of AuNPs and PANI films with potassium ferricyanide over a gold electrode was used to detect a carcinoembryonic antigen (CEA). This PNC-based biocompatible electrochemical immunosensor showed excellent conductivity and redox electroactivity. The detection of CEA was analyzed through electrode response of $[Fe(CN)_6]^{3-}$ as the redox mediator [42].

5. Conclusion

PNCs have been explored for the construction of novel biosensors using PNC like materials as sensing elements. The efficient combination of different nanoscaled materials with good conductive polymers open a new avenue for utilizing novel PNCs as enhanced elements for constructing electrochemical sensing platforms with high performance. Health monitoring wearable tech like Fitbit or Apple Watch are all based on the PNC electrochemical sensors are of great interest in the health industry for the detection of physiological parameters of the human body. The progress of PNC-based wearable electrochemical sensors to analyses biochemical fluids other than blood such as interstitial fluids, sweat, tears, and saliva invoked interests in Silicon Valley echelons like Google, OrSense, and NovioSense which made the sector more interesting. Another significant challenge is the technical challenges to the wearability of the PNC-based material for manufacturing the same which includes analytical performance and biocompatibility. There is significant progress reported on the PANI-based wearable immunosensor used for epidermal pH monitoring. With all these advances the future of PNC-based devices is promising and applications shall reach out to commercial sensing applications like military, health-care and community fitness initiatives.

Author details

Baiju John[1,2,3]

1 Advanced Polymeric Nanostructured Materials Engineering, Graduate School of Engineering, Toyota Technological Institute, Nagoya, Japan

2 The Center for Biomedical Engineering, UTMB Galveston, Galveston, Texas, USA

3 Duann Innovations and Systems, Houston, TX, USA

*Address all correspondence to: jonsbaiju@gmail.com

IntechOpen

References

[1] Shrivastava S, Jadon N, Jain R. Next-generation polymer nanocomposite-based electrochemical sensors and biosensors: A review. Trends in Analytical Chemistry. 2016;**82**:55-67. DOI: 10.1016/j.trac.2016.04.005

[2] Wallace GG, Smyth M, Zhao H. Conducting electroactive polymer-based biosensors. Trends in Analytical Chemistry. 1999;**18**:245-251. DOI: 10.1016/S0165-9936(98)00113-7

[3] Gangopadhyay R, Amitabha D. Conducting polymer nanocomposites: A brief overview. Chemistry of Materials. 2000;**12**:608-622. DOI: 10.1021/cm990537f

[4] Devi R, Thakur M, Pundir CS. Construction and application of an amperometric xanthine biosensor based on zinc oxide nanoparticlespolypyrrole composite film. Biosensors & Bioelectronics. 2011;**26**:3420-3426. DOI: 10.1016/j.bios.2011.01.014

[5] Xing L, Rong Q, Ma Z. Non-enzymatic electrochemical sensing of hydrogen peroxide based on polypyrrole/platinum nanocomposites. Sensors and Actuators B: Chemical. 2015;**221**:242-247. DOI: 10.1016/j.snb.2015.06.078

[6] Yu Z, Li H, Zhang X, Liu N, Tan W, Zhang X, et al. Facile synthesis of $NiCo_2O_4$@Polyaniline core-shell nanocomposite for sensitive determination of glucose. Biosensors & Bioelectronics. 2016;**75**:161-165. DOI: 10.1016/j.bios.2015.08.024

[7] Fan Y, Liu JH, Yang CP, Yu M, Liu P. Graphene-polyaniline composite film modified electrode for voltammetric determination of 4-aminophenol. Sensors and Actuators B: Chemical. 2011;**157**:669-674. DOI: 10.1016/j.snb.2011.05.053

[8] Radhapyari K, Kotoky P, Das MR, Khan R. Graphene-polyaniline nanocomposite based biosensor for detection of antimalarial drug artesunate in pharmaceutical formulation and biological fluids. Talanta. 2013;**111**:47-53. DOI: 10.1016/j.talanta.2013.03.020

[9] Jain R, Tiwari DC, Shrivastava S. A sensitive voltammetric sensor based on synergistic effect of graphene-polyaniline hybrid film for quantification of calcium antagonist lercanidipine. Journal of Applied Polymer Science. 2014;**131**:40959-40965. DOI: 10.1149/2.018404jes

[10] Jain R, Tiwari DC, Karolia P. Electrocatalytic detection and quantification of nitazoxanide based on graphene-polyaniline (Grp-Pani) nanocomposite sensor. Journal of the Electrochemical Society. 2014;**161**:H1-H6. DOI: 10.1039/C4RA08543D

[11] Gao YS, Xu JK, Lu LM, Wu LP, Zhang KX, Nie T, et al. Overoxidized polypyrrole/graphene nanocomposite with good electrochemical performance as novel electrode material for the detection of adenine and guanine. Biosensors & Bioelectronics. 2014;**62**:261-267. DOI: 10.1016/j.bios.2014.06.044

[12] Zhang W, Yuan R, Chai YQ, Zhang Y, Chen SH. A simple strategy based on lanthanum-multiwalled carbon nanotube nanocomposites for simultaneous determination of ascorbic acid, dopamine, uric acid and nitrite. Sensors and Actuators B: Chemical. 2012;**166-167**:601-607. DOI: 10.1016/j.snb.2012.03.018

[13] Mao H, Liang J, Zhang H, Pei Q, Liu D, Wu S, et al. Poly(ionicliquids) functionalized polypyrrole/graphene oxide nanosheets for electrochemical sensor to detect dopamine in the presence of ascorbic acid. Biosensors & Bioelectronics. 2015;**70**:289-298. DOI: 10.1016/j.bios.2015.03.059

[14] Wang W, Xu G, Cui XT, Sheng G, Luo X. Enhanced catalytic and dopamine sensing properties of electrochemically reduced conducting polymer nanocomposite doped with pure graphene oxide. Biosensors & Bioelectronics. 2014;**58**:153-156. DOI: 10.1016/j.bios.2014.02.055

[15] Lu L, Zhang O, Xu J, Wen Y, Duan X, Yu H, et al. A facile one-step redox route for the synthesis of graphene/poly(3,4-ethylenedioxythiophene) nanocomposite and their applications in biosensing. Sensors and Actuators B: Chemical. 2013;**181**:567-574. DOI: 10.1016/j.snb.2013.02.024

[16] Jain R, Shrivastava S. A graphene-polyaniline-Bi_2O_3 hybrid film sensor for voltammetric quantification of anti-inflammatory drug etodolac. Journal of the Electrochemical Society. 2014;**161**:H189-H194. DOI: 10.1149/2.043404jes

[17] Xue C, Wang X, Zhu W, Han Q, Zhu C, Hong J, et al. Electrochemical serotonin sensing interface based on double-layered membrane of reduced graphene oxide/polyaniline nanocomposites and molecularly imprinted polymers embedded with gold nanoparticles. Sensors and Actuators B: Chemical. 2014;**196**:57-63. DOI: 10.1016/j.snb.2014.01.100

[18] Singh K, Solanki PR, Basu T, Malhotra BD. Polypyrrole/multiwalled carbon nanotubes based biosensor for cholesterol estimation. Polymers for Advanced Technologies. 2012;**23**:1084-1091. DOI: 10.1002/pat.2020

[19] Karadas N, Ozkan SA. Electrochemical preparation of sodium dodecylsulfate doped over-oxidized polypyrrole/multi-walled carbon nanotube composite on glassy carbon electrode and its application on sensitive and selective determination of anticancer drug: Pemetrexed. Talanta.

2014;**119**:248-254. DOI: 10.1016/j.talanta.2013.10.065

[20] Xu G, Li B, Wang X, Luo X. Electrochemical sensor for nitrobenzene based on carbon paste electrode modified with a poly(3,4-ethylenedioxythiophene) and carbon nanotube nanocomposite. Microchimica Acta. 2014;**181**:463-469. DOI: 10.1007/s00604-013-1136-y

[21] Wang L, Hua E, Liang M, Ma C, Liu Z, Sheng S, et al. Graphene sheets, polyaniline and AuNPs based DNA sensor for electrochemical determination of BCR/ABL fusion gene with functional hairpin probe. Biosensors & Bioelectronics. 2014;**51**:201-207. DOI: 10.1016/j.bios.2013.07.049

[22] Yang Y, Zhang S, Kang M, He L, Zhao J, Zhang H, et al. Selective detection of silver ions using mushroom-like polyaniline and gold nanoparticle nanocomposite-based electrochemical DNA sensor. Analytical Biochemistry. 2015;**490**:7-13. DOI: 10.1016/j.ab.2015.08.010

[23] Spain E, Kojima R, Kaner RB, Wallace GG, Grady JO, Lacey K, et al. High sensitivity DNA detection using gold nanoparticle functionalized polyaniline nanofibres. Biosensors & Bioelectronics. 2011;**26**:2613-2618. DOI: 10.1016/j.bios.2010.11.017

[24] Singh R, Verma R, Sumana G, Srivastava AK, Sood S, Gupta RK, et al. Nanobiocomposite platform based on polyaniline-iron oxide-carbon nanotubes for bacterial detection. Bioelectrochemistry. 2012;**86**:30-37. DOI: 10.1016/j.bioelechem.2012.01.005

[25] Saberi RS, Shahrokhian S, Marrazza G. Amplified electrochemical DNA sensor based on polyaniline film and gold nanoparticles. Electroanalysis. 2013;**25**:1373-1380. DOI: 10.1002/elan.201200434

[26] Wilson J, Radhakrishnan S, Sumathi C, Dharuman V. Polypyrrole-polyaniline- Au (PPy-PANi-Au) nano composite films for label-free electrochemical DNA sensing. Sensors and Actuators B: Chemical. 2012;**171-172**:216-222. DOI: 10.1016/j.snb.2012.03.019

[27] Radhakrishnan S, Sumathi C, Umar A, Kim SJ, Wilson J, Dharuman V. Polypyrrole-poly(3,4-ethylenedioxythiophene)-Ag (PPy-PEDOT-Ag) nanocomposite films for label-free electrochemical DNA sensing. Biosensors & Bioelectronics. 2013;**47**:133-140. DOI: 10.1016/j.bios.2013.02.049

[28] Tam PD, Hieu NV. Conducting polymer film-based immunosensors using carbon nanotube/antibodies doped polypyrrole. Applied Surface Science. 2011;**257**:9817-9824. DOI: 10.1016/j.apsusc.2011.06.028

[29] Truong LTN, Chikae M, Ukita Y, Takamur Y. Labelless impedance immunosensor based on polypyrrole-pyrolecarboxylic acidcopolymer for HCG detection. Talanta. 2011;**85**:2576-2580. DOI: 10.1016/j.talanta.2011.08.018

[30] Dey A, Kaushik A, Arya SK, Bhansali S. Mediator free highly sensitive polyaniline-gold hybrid nanocomposite based immunosensor for prostatespecific antigen (PSA) detection. Journal of Materials Chemistry. 2012;**22**:14763-14772. DOI: 10.1039/C2JM31663C

[31] Linting Z, Ruiyi L, Zaijun L, Qianfang X, Yinjun F, Junkang L. An immunosensor for ultrasensitive detection of aflatoxin B1 with an enhanced electrochemical performance based on graphene/conducting polymer/gold nanoparticles/the ionic liquid composite film on modified gold electrode with electrodeposition. Sensors and Actuators B: Chemical. 2012;**174**:359-365. DOI: 10.1016/j.snb.2012.06.051

[32] Zang S, Liu Y, Lin M, Kang J, Sun Y, Lei H. A dual amplified electrochemical immunosensor for ofloxacin: Polypyrrole film-Au nanocluster as the matrix and multi-enzyme-antibody functionalized gold nanorod as the label. Electrochimica Acta. 2013;**90**:246-253. DOI: 10.1016/j.electacta.2012.12.021

[33] Ruiyi L, Qianfang X, Zaijun L, Xiulan S, Junkang L. Electrochemical immunosensor for ultrasensitive detection of microcystin-LR based on graphene-gold nanocomposite/functional conducting polymer/goldnanoparticle/ionic liquid composite film with electrodeposition. Biosensors & Bioelectronics. 2013;**44**:235-240. DOI: 10.1016/j.bios.2013.01.007

[34] Li S, Liu JY, Lian W, Cui M, Xu W, et al. Electrochemical immunosensor based on graphene-polyaniline composites and carboxylated graphene oxide for estradiol detection. Sensors and Actuators B: Chemical. 2013;**188**:99-105. DOI: 10.1016/j.snb.2013.06.082

[35] Liu PZ, Hu XW, Mao CJ, Niu HL, Song JM, Jin BK, et al. Electrochemiluminescence immunosensor based on graphene oxide nanosheets/polyaniline nanowires/CdSe quantum dots nanocomposites for ultrasensitive determination of human interleukin-6. Electrochimica Acta. 2013;**113**:176-180. DOI: 10.1016/j.electacta.2013.09.074

[36] Liu K, Zhang J, Liu Q, Huang H. Electrochemical immunosensor for alpha-fetoprotein determination based on ZnSe quantum dots/azure I/gold nanoparticles/poly(3,4-ethylenedioxythiophene) modified Pt electrode. Electrochimica Acta. 2013;**114**:448-454. DOI: 10.1016/j.electacta.2013.10.018

[37] Li L, Li W, Yang H, Ma C, Yu J, Yan M, et al. Sensitive origami dual-analyte electrochemical immunodevice based on polyaniline/Au-paper electrode and multi-labeled 3D graphene sheets. Electrochimica Acta. 2014;**120**:102-109. DOI: 10.1016/j.electacta.2013.12.076

[38] Serafin V, Agui L, Yanez Sedeno P, Pingarron JM. Determination of prolactin hormone in serum and urine using an electrochemical immunosensor based on poly(pyrrolepropionicacid)/carbon nanotubes hybrid modified electrodes. Sensors and Actuators B: Chemical. 2014;**195**:494-499. DOI: 10.1016/j.snb.2014.01.055

[39] Mishra SK, Srivastava AK, Kumar D, Mulchandani A, Rajesh. Protein functionalized Pt nanoparticles-conducting polymer nanocomposite film: Characterization and immunosensor application. Polymer (Guildf.). 2014;**55**:4003-4011. DOI: 10.1016/j.polymer.2014.05.061

[40] Wang D, Hu W, Xiong Y, Xu Y, Li CM. Multifunctionalized reduced graphene oxide-doped polypyrrole/pyrrolepropylic acid nanocomposite impedimetric immunosensor to ultra-sensitively detect small molecular aflatoxin B1. Biosensors & Bioelectronics. 2015;**63**:185-189. DOI: 10.1016/j.bios.2014.06.070

[41] Fan H, Guo Z, Gao L, Zhang Y, Fan D, Ji G, et al. Ultrasensitive electrochemical immunosensor for carbohydrate antigen 72-4 based on dual signal amplification strategy of nanoporous gold and polyaniline–Au asymmetric multicomponent nanoparticles. Biosensors & Bioelectronics. 2015;**64**:51-56. DOI: 10.1016/j.bios.2014.08.043

[42] He S, Wang Q, Yu Y, Shi Q, Zhang L, Chen Z. One-step synthesis of potassium ferricyanide-doped polyaniline nanoparticles for label-free immunosensor. Biosensors & Bioelectronics. 2015;**68**:462-467. DOI: 10.1016/j.bios.2015.01.018

Chapter 10

Nanocomposite-Based Graphene for Nanosensor Applications

Rumei Cheng and Shengju Ou

Abstract

Nanocomposites based on carbon nanomaterial particularly in graphene oxide, graphene quantum dots, and doped graphene quantum dots with improved biocompatibility have been increasing interests in the field of drug delivery, biosensor, energy, imaging and electronic. These nanomaterials as new kinds of fluorescent probes and electrochemical sensors all display ultrasmall size, good photostability, and excellent biocompatibility. In this chapter, we summarize an updated advance in the development of graphene and its related derivatives of synthesis methods and biomedical applications as nanosensors for detection of metal ions, inorganic ions, amino acids, proteins, saccharides and small molecules, drug molecules, and so on.

Keywords: nanocomposite, graphene oxide, graphene quantum dots, sensor, detection, application

1. Introduction

Graphene, as an atom-thick sp^2-hybridized carbon nanosheet, has been extensively studied since it was first separated and characterized by Andre Geim and Konstantin Novoselov in 2004 [1]. The graphene presents a unique property including large specific surface area, easy functionalization, unique optical properties, chemical stability, high electronic conductivity, and photonic and mechanical properties and provides a promising platform for the design and construction of useful nanomaterials. Recently, the field involving graphene nanomaterials is a rapidly developing area due to their potential applications in biomedical and clinical medicine field. One of the most valuable virtues of graphene is their applications in sensors, particularly in fluorescence sensors and electrochemical sensors [2].

Mainly graphene-based nanomaterials are graphene oxide (GO, 2-D), graphene quantum dots (GQDs, 0-D), and heteroatom (N, P, S atom)-doped graphene quantum dots (doped GQDs, 0-D). The structures of different materials are shown in **Figure 1**. GO is a layered stack of nanosheets, while GQDs are regarded as GO nanosheets cutting into nanodots in oxidation process showing excellent performance of graphene. Recently, the GQDs have greatly attracted attention of scientific workers due to the good biocompatibility, excellent water solubility, and stable photoluminescence (PL) and chemical inertness [3, 4]. The GQDs contain carboxyl group, hydroxyl group, and epoxy groups at the edge and show similar structure to graphene and can be easily functionalized by various biological and non-biological species. Meantime, heteroatom-doped GQDs showed enhanced chemical activity, higher fluorescence quantum yields, and effectively modulated performance of bandgap.
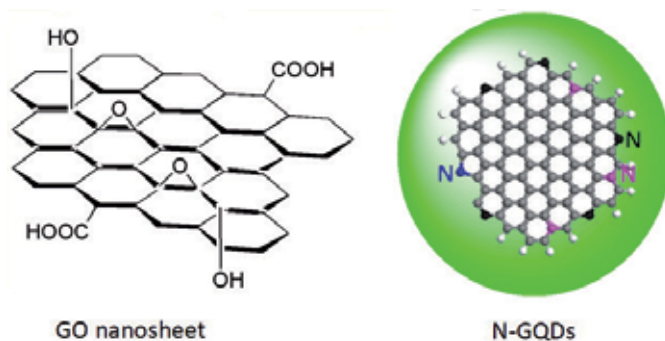
Figure 1.
Structure of graphene oxide (GO) and nitrogen-doped graphene quantum dots (N-GQDs).

In this chapter, efforts have been made on summarizing the design, synthesis, and applications of nanocomposite-based graphene. We mainly focused on the recent development of graphene-based nanocomposites as fluorescence sensors and electrochemical sensors for the detection of biological species and non-biological species in human serum, respectively.

2. Applications of nanocomposite-based graphene as nanosensors

2.1 Nanocomposite-based graphene oxide as fluorescence sensors

2.1.1 Detection of amino acids

People are very interested in the detection of amino acids due to their multiple biological functions. Cheng and co-workers designed and synthesized a turn-on fluorescent nanosensor based on the alizarin red aluminum (III) complex covalently binding to graphene oxide (GO) for the detection of lysine with high sensitivity and high selectivity [5]. The nanosensor was prepared by GO, Al(III) ions, and alizarin red (GO-Al-AR) by coordination mode. The as-prepared GO-Al-AR nanosensor was depicted in **Figure 2**. It showed weak fluorescence due to photo-induced electron transfer (PET). However, the fluorescence intensity of GO-Al-AR obviously enhanced upon addition of lysine. The fluorescence response of GO-Al-AR nanosensor exhibited good linear relationship with the concentrations of lysine within 25 mg/L to 250 mg/L. The detection limit was 2.0 mg/L. The premium pH value was between 6.5 and 7.2, suggesting the as-synthesized sensor is suitable for detection of lysine in living cells.

Another novel fluorescence sensing method was developed for the detection of tyramine based on CdSe/ZnS quantum dots-GO using imprinting technique [6]. The fluorescent sensor was synthesized by using CdSe/ZnS quantum dots, GO, 3-mercaptopropyltriethoxysilane (MPTES) (monomer), and tetraethyl orthosilicate (TEOS) (cross-linking agent) and targeted molecule tyramine for synthesizing molecularly imprinted polymers (MIPs), namely, Gra-QDs@MIPs. The as-synthesized sensor showed a high selectivity for the detection of tyramine. The fluorescence intensity of Gra-QDs@MIPs showed a good linear relationship with concentrations of tyramine between 0.07 and 12 mg/L. The Gra-QDs@MIPs can be used to detect tyramine in rice wine samples. A biosensor was constructed and reported based on reduced GO field-effect transistor (rGO-FET) modified by the cascading enzymes arginase and urease for the monitoring of ʟ-arginine [7]. The rGO-FET was employed to immobilize arginase and urease through electrostatic
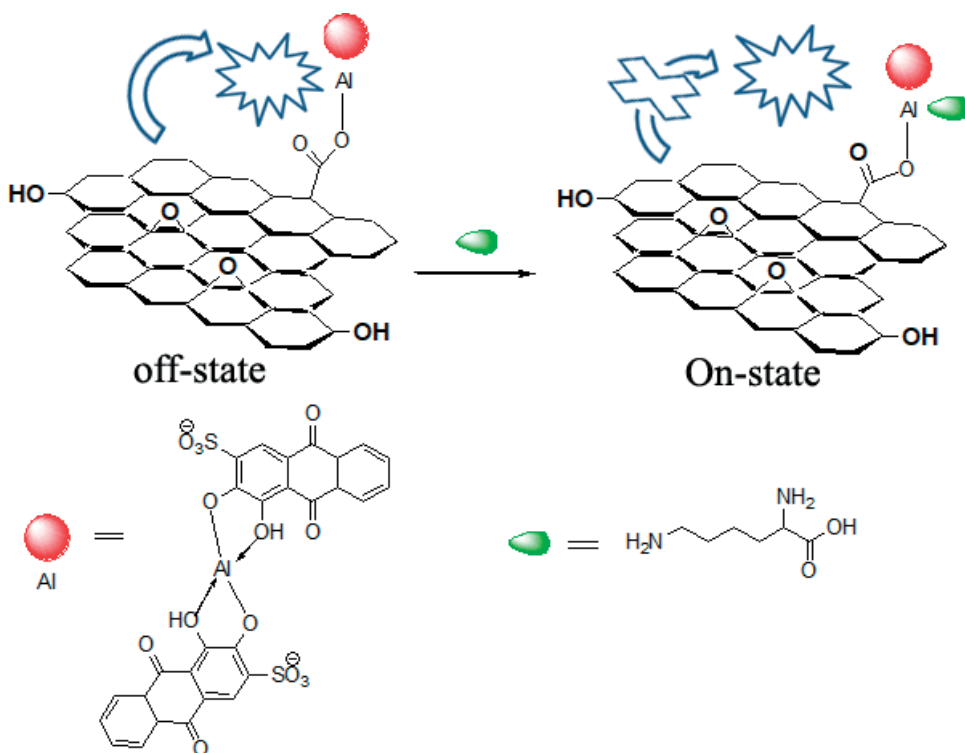
Figure 2.
A schematic illustration of a turn-off/turn-on fluorescence response of GO-Al-AR to lysine.

interaction based on cationic polyethylenimine (PEI) building block. The functionalized transistors showed high sensitivity and high selectivity for the detection of L-arginine within 10–1000 μM. The detection limit was 10 μM. The sensor showed fast response and good stability.

2.1.2 Detection of drug molecules

Bao and co-workers designed RhBPy-graphene oxide (GO) complex as a fluorescent probe for the sensitive and selective detection of doxorubicin (DOX) in MeOH/H$_2$O solution [8]. The fluorescence of RhBPy[2] rotaxane can be efficiently quenched by addition of graphene oxide (GO) due to fluorescence resonance energy transfer (FRET), while the fluorescence of RhBPy[2] rotaxane can be recovered due to different interaction forces between DOX and RhBPy[2] rotaxane toward GO. Li et al. developed a fluorescent probe for the monitoring and detection of antibiotic virginiamycin based on GO-supported carbon quantum dots (GO/C-dots) as the signal element and molecularly imprinted polymer (MIP) as the recognition template [9]. MIP with virginiamycin as the template molecule was constructed and designed using o-aminophenol as monomer on the surface of ITO electrode deposited by GO/C-dots. The specific sensor can be obtained by removing the virginiamycin from the MIP. The GO/C-dot complex displayed strong fluorescence signal, while its fluorescence intensity declined obviously upon adsorption of virginiamycin. The specific probe showed high selectivity and high sensitivity toward virginiamycin, and detection limit is 1.56×10^{-11} mol/L.

The novel doxorubicin (DOX) functionalized GO nanosensor was designed and synthesized for the detection of dopamine based on mechanism of fluorescence resonance energy transfer (FRET) [10]. The DOX showed strong property, but the

fluorescence was quenched upon addition of GO (**Figure 3**). The GO-DOX complex as sensing platform showed a high selectivity toward dopamine based on different adsorption interactions between dopamine and DOX and GO. The fluorescence intensity of DOX-GO complex was partly recovered upon addition of dopamine based on competitive adsorption of DOX and dopamine on the surface of GO. The fluorescence response of DOX-GO exhibited a linear relationship with concentrations of dopamine between 8.3×10^{-7} M and 3.3×10^{-5} M in aqueous solution and 1.44 and 11.48 μmol/L in human serum, respectively. The DOX-GO can be an efficient nanosensor for sensing dopamine in human serum and living cells.

2.1.3 Detection of the other small molecules

The hexylenediamine-functionalized high fluorescent GO was constructed and prepared for the detection of hypochlorous acid (HOCl) in aqueous solution [11]. The fluorescence of functionalized GO was quenched upon addition of HOCl based on the mechanism of intramolecular charge transfer (ICT) between GO and chloramines forming by the oxidation of amino groups of functionalized GO using HOCl. The functionalized GO showed high selectivity and sensitivity for the determination of HOCl. The detection limit was 3.5 μM. The obtained sensor can be used to detect HOCl in tap water. The water-soluble and good biocompatible nanocomposite sensor was designed and prepared based on GO, Cu^{2+}, and histidine-functionalized perylenediimide (PDI-HIS) for the determination of pyrophosphate (PPi) in biological conditions [12]. The as-synthesized sensor can be used as an efficient sensing platform in physiological conditions by fluorescence turn-on switch. The obtained sensor PDI-HIS-Cu-GO (PCG) displayed high selectivity and high sensitivity for the PPi detection with affinity constant 1.0×10^6 M^{-1}. The detection limit was 0.6×10^{-7} M. Compared to the PDI-HIS+Cu^{2+} complex, the PDI-HIS-Cu-GO nanocomposites showed higher selectivity for PPi in intracellular detection.

Cheng et al. designed a dual-output nanosensor based on GO for the detection of Ag^+ in aqueous solution with high sensitivity and high selectivity [13]. The nanosensor (**Figure 4**) was prepared by conjugation of GO with well-known fluorophore 1,8-diaminonaphthalene (DAN). The addition of Ag^+ ions significantly
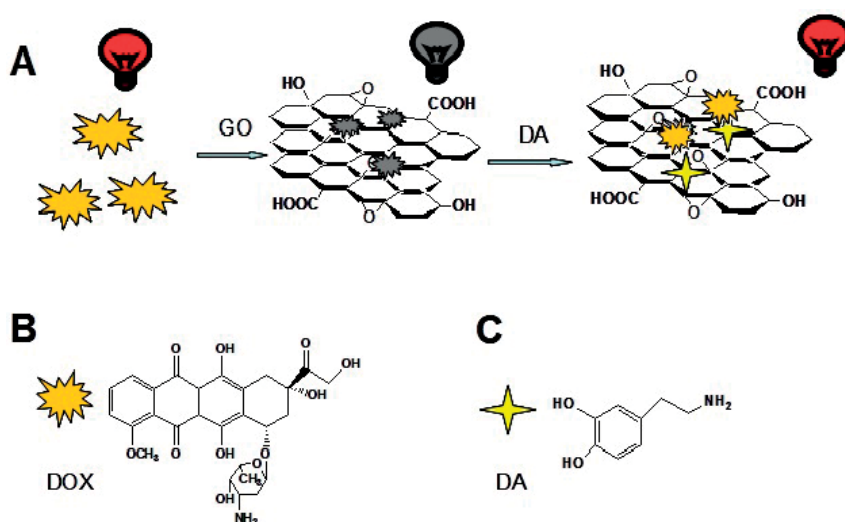
Figure 3.
A schematic illustration of the fluorescence response of a DOX-GO complex to dopamine (a); Molecular structures of DOX (b) and dopamine (c).
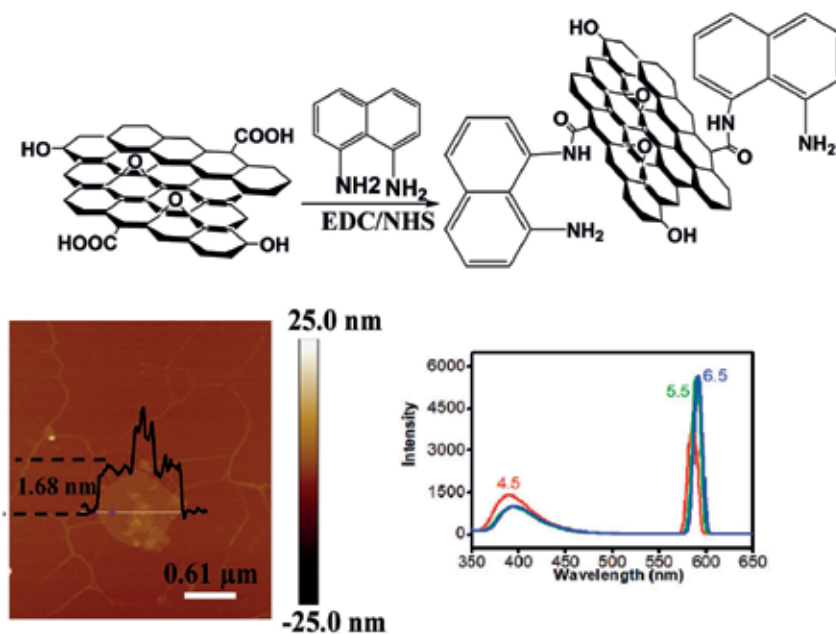
Figure 4.
Synthetic pathway and AFM images of GAP and its fluorescence response to fivefold Ag$^+$ in aqueous solutions with various pHs.

quenched the fluorescence of resultant sensor based on the mechanism of PET, while the intensity of second-order scattering obviously enhanced. Furthermore, the intensity of as-prepared sensor showed a good linear relationship with the concentrations of Ag$^+$ ranging from 6 to 12 mg/L. The fluorescent sensor showed no or weakly response to Na(I), K(I), Ca(II), Mg(II), Cr(III), Mn(II), Fe(II), Co(II), Ni(II), Cu(II), Zn(II), and Fe(III).

2.2 Nanocomposite-based graphene oxide as electrochemical sensors

2.2.1 Detection of proteins

Gevaerd et al. designed and synthesized imidazole-functionalized graphene oxide (GO-IMZ) as non-enzymatic electrochemical sensor for the detection of progesterone [14]. Progesterone (P4) plays an important role in the stabilization and maintenance of gestation as most important progestogen of mammals. The GO-IMZ complex as an artificial enzymatic active site was reported using voltammetric determination of progesterone. The as-synthesized sensor displayed a synergistic effect of GO nanosheets and imidazole showing the obvious enhancement on the electrochemical response of P4. The electrochemical response signal showed a linear relationship with concentrations of P4 between 0.22 and 14.0 μmol/L. The detection limit was 68 nmol/L. The limit of quantification was 210 nmol/L. The higher sensitivity was presented compared to the unmodified electrode.

Tomita and co-workers designed and reported the construction of high accessible and high tunable multi-fluorescent sensing system, and this sensing system presented protein fluorescent signals from a single microplate well [15]. The principal mechanism of approach was based on three single-stranded DNAs (ssDNAs) functionalized-nano-graphene oxide (nGO). The single-stranded DNAs showed different sequences and functions, and fluorophores exhibited different optical

properties. The fluorescence of three fluorophore-modified ssDNAs was quenched upon conjugation with nGO. The partial recovery of fluorescence intensity of individual ssDNAs was observed upon addition of analyte proteins.

2.2.2 Detection of drug molecules

Abdallah and Ibrahim designed and developed an imprinted potentiometric sensor for the detection of gabapentin that is an anticonvulsant agent [16]. The sensor was constructed using carbon paste electrode following three steps: (i) the GO was decorated by silver nanoparticles; (ii) silver nanoparticles modified with GO mixed physically with molecularly imprinted polymers nanoparticles with gabapentin as a template molecule and then leached the template molecule; and (iii) the abovementioned mixture deposited on carbon paste electrode. The sensor showed good selectivity and high sensitivity, and the detection limit is 4.8×10^{-11} mol/L. Yang and co-workers designed and prepared CdTe quantum dot (QD)-decorated poly(diallyldimethylammonium chloride) (PDDA)-functionalized graphene (CdTe-PDDA-Gr) nanocomposite based on the presence of PDDA and CdTe QDs using chemical reduction of exfoliated graphite oxides [17]. The CdTe-PDDA-Gr nanocomposite showed very fast electron transfer behavior and obvious absorption effect for puerarin due to high surface area and good conductivity. They exhibited very good electrocatalytic behavior toward the oxidation of puerarin. The oxidation peak current showed a good linear relationship with the concentrations of puerarin within 0.001–1.0 μM by differential pulse voltammetry (DPV). The limitation of detection was 0.6 nM (SNR of 3).

The nickel tetra-amined phthalocyanine-graphene oxide covalent compound was developed as a photoelectrochemical sensor for the detection of erythromycin with high sensitivity [18]. The graphene oxide was modified by tetra-amined phthalocyanine (NiTAPc) by covalent bonding getting the final product NiTAPc-Gr. The as-synthesized sensor exhibited a higher photoelectrochemical efficiency and showed a peak wavelength of 456 nm by irritation of visible light. Compared to that of GO/ITO, the photocurrent of NiTAPc-Gr/ITO was 50-fold at the same conditions. The photocurrent showed a good linear relationship with the concentrations of erythromycin between 0.40 and 120.00 μmol/L. The detection limit was 0.08 μmol/L. The constructed photoelectrochemical sensors have been successfully applied to detect erythromycin in human blood plasma.

2.2.3 Detection of the other small molecules

A bimetallic electrochemical sensor was designed and constructed for the sensitive detection of uric acid (UA) with high selectivity [19] as shown in **Figure 5**. The bimetallic nanoparticles (NPs) were synthesized by electrodeposition on the glassy carbon electrode (GCE) using the $HAuCl_4$ and $AgNO_3$ as precursors by co-reduction through cyclic voltammetry scanning. Firstly, the GO-TH complex was formed by electrostatic interactions between GO and thionine (TH); then, the GO-TH complex was drop-coated on Au-Ag NPs to construct Au-Ag NPs/GO/TH@GCE. The redox current peak intensity showed regular increase with the increase of concentration of UA. The good linear relationship was exhibited between I_{UA}/I_{TH} and [UA] within 1–100 μM with linearly plotted (R^2 = 0.9929). The detection limit was 0.3 μM.

A non-enzymatic sialic acid (SA) electrochemical sensor was designed and constructed based on indicator displacement assay (IDA) of dopamine with high sensitivity and high selectivity [20]. The mechanism of SA detection was based on reversible covalence with boronic acid-diol complex. In other words, the SA and DA all can covalently interact with 2-fluorophenylboronic acid (FPBA) by replacing of 1,2-diols. The electrode was constructed and synthesized based on
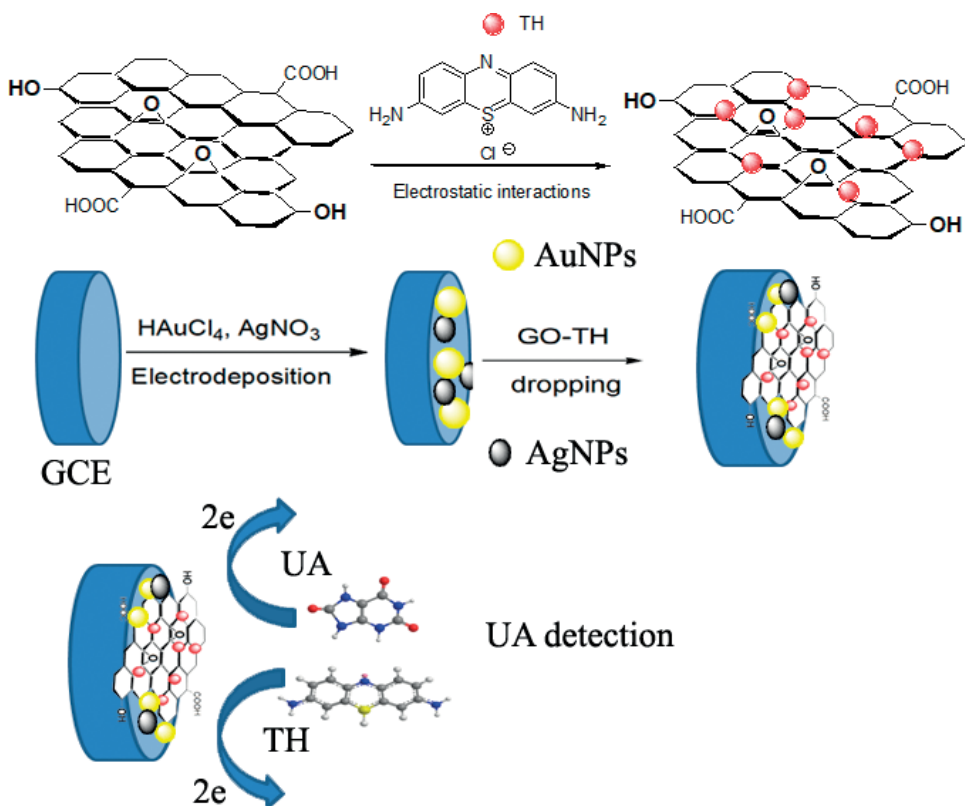
Figure 5.
Illustration of the preparation and applications of the Au-Ag NPs/GO/TH@GCE sensing platform.

tetra(4-carboxyphenyl) porphine-graphene oxide (TCPP-GO), DA, and FPBA on the surface of glassy carbon electrode (GCE), respectively. The TCPP-GO complex obviously enhanced the sensitivity of the electrochemical sensor. The recovered anodic current intensity of DA showed a good linear relationship with the concentration of SA within 0.1–7.5 mM. The detection limit was 28.5 μM. The sensor has been successfully applied to detect SA in human blood and urine samples.

The gold/silver/gold/chitosan-graphene oxide (Au/Ag/Au/CS-GO) sensor was designed and constructed for the detection of Pb^{2+} and Hg^{2+} ions with high sensitivity [21]. The higher affinity constant of Pb^{2+} binding with the CS-GO showed higher affinity than that of Hg^{2+} binding with the CS-GO. The maximum S/N was 1.53. The Au/Ag/Au/CS-GO surface plasmon resonance (SPR) sensor displayed good repeatability toward Pb^{2+} ions due to the coordination interaction. The adsorption behaviors of Pb^{2+} and Hg^{2+} ions onto the surface of CS-GO sensor fit to the Langmuir isotherm model. The affinity constant of Pb^{2+} and Hg^{2+} to bind Au/Ag/Au/CS-GO sensor was 7×10^5 M^{-1} and 4×10^5 M^{-1}, respectively. Priya et al. resigned and prepared a voltammetric sensor based on graphene oxide/κ-carrageenan/ʟ-cysteine nanocomposite (GO/κ-Car/ʟ-Cys) for the detection of Cd^{2+} and Pb^{2+} ions [22]. The GO/κ-Car/ʟ-Cys composite modified with glassy carbon electrode (GCE) was successfully synthesized. The electrochemical response of GO/κ-Car/ʟ-Cys composite showed a good linear relationship with the concentrations of Cd^{2+} and Pb^{2+} ions within 5–50 nM, and the detection limit was 0.58 and 1.08 nM for Cd^{2+} and Pb^{2+} ions, respectively. The sensitivity for Cd^{2+} and Pb^{2+} ions was 1.39 μA/nM and 1.32 μA/nM, respectively. The interference experiment results showed no affect even on the presence of other species.

2.3 Nanocomposite-based graphene quantum dots (GQDs) as fluorescence sensors

2.3.1 Detection of amino acids

The fluorescent graphene quantum dots-gold nanoparticles as nanosensor showed a high selectivity and high sensitivity for the detection of cysteine [23]. The AuNPs@r-GQDs nanocomposite was prepared by the following processes. First, nitrogen-doped graphene quantum dots (N-GQDs) were reduced to r-GQDs by $NaBH_4$ as reductant and subsequently the r-GQDs converted $HAuCl_4$ to Au nanoparticles (AuNPs) by reduction reaction and coated onto AuNPs forming core-shell-structured AuNPs@r-GQDs. The AuNPs@r-GQDs showed good dispersion behavior with an intensive surface plasma band at 525 nm. The AuNPs@r-GQDs exhibited aggregation behavior and led to their color change by using cysteine as cross-linking agent through adsorption of Ag ions onto their surface. The detection limit was 5.6 nM. Furthermore, the AuNPs@r-GQDs showed higher selectivity for cysteine than that of glutathione (GSH) even at the interfere condition of 1000-fold concentrations of GSH.

The $GQD-MnO_2$ complex as a convenient fluorescence nanosensor has been constructed and prepared for the detection of glutathione (GSH) with high selectivity and high sensitivity [24]. The fluorescence intensity of GQDs was quenched upon addition of MnO_2 nanosheet based on the mechanism of fluorescence resonance energy transfer (FRET). The fluorescent signal recovered upon GSH reducing MnO_2 nanosheets into Mn^{2+} ions and releasing GQDs. The $GQD-MnO_2$ complex as nanoprobe showed a sensitive response to GSH between 0.5 and 10 µmol/L. The fluorescence intensity showed a good linear relationship with the concentrations of GSH. The detection limit was 150 nmol/L. The $GQD-MnO_2$ complex exhibited higher selectivity for the GSH than that of other metal ions and biomolecules and successfully applied to detect GSH in living cells.

2.3.2 Detection of drug molecules

Zhou et al. designed and developed a convenient fluorescent sensor based on the molecularly imprinted polymers (MIPs)-functionalized GQDs for the detection of tetracycline (TC) with high sensitivity and high selectivity [25]. The GQDs were prepared by one-pot method, and the amino-functionalized GQDs and carboxyl-functionalized GQDs were fabricated, respectively. The GQD-MIPs were synthesized by sol-gel method. The GQD-MIPs exhibited strong fluorescence property, and the fluorescence was quenched upon addition of TC. The fluorescence quench efficiency showed a linear relationship with concentrations of TC between 1.0 and 10^4 µg/L. The detection limit was 1 µg/L.

2.3.3 Detection of inorganic ions

The sulfanilic acid and glutathione-functionalized GQDs was constructed and synthesized as fluorescent sensor for the detection of sulfide anions and ascorbic acid [26]. The sulfanilic acid and glutathione-functionalized GQDs were prepared through amide linkage using 1-(3-dimethylaminopropyl)-3-ethyl-carbodiimide hydrochloride (EDC) as catalyst, namely, SSGQDs. The SSGQDs showed strong fluorescence property. The fluorescence of SSGQDs was quenched upon addition of Cu^{2+} ions, forming SSGQD-Cu(II) complex. The S^{2-} ions showed high coordination interaction with Cu^{2+} ions from SSGQD-Cu(II) complex and induced the fluorescence recovery of SSGQDs. The ascorbic acid (AA) as a reduction can reduce Cu^{2+} into Cu^+ and induced the disaggregation of the SSGQDs, and fluorescence of

SSGQDs was recovered again. The GQDs as a green sensor were synthesized for the detection of free chlorine with high selectivity and high sensitivity [27]. The GQDs showed strong fluorescence property, and fluorescence of GQDs was quenched upon addition of chlorine-based fluorescence resonance energy transfer. The fluorescence quenching efficiency exhibited a good linear relationship with concentrations of chlorine with a wide range from 0.05 to 10 μM. The sensing system has been applied to detect chlorine in drinking water.

The europium-functionalized GQDs (Eu-GQDs) were synthesized by treatment of Eu-decorated graphene (3D Eu-graphene) through a strong acid oxidation [28]. The amount of Eu was 2.54%. The Eu-GQDs complex showed higher electron density and surface chemical activities compared to that of GQDs. The as-synthesized Eu-GQDs exhibited a sensitive response for the detection of Cu^{2+} and L-cysteine with high selectivity and high sensitivity. The fluorescence of Eu-GQDs was quenched upon addition of Cu^{2+} due to the coordination interaction between Cu^{2+} and carboxyl groups of Eu-GQDs. The fluorescence of Eu-GQDs was recovered in the presence of L-cysteine due to strong affinity of Cu^{2+} and S of L-cysteine. The good linear relationship was shown within the range of 0.1–10 μM for Cu^{2+} and 0.5–50 μM for L-cysteine, respectively. The detection limit was 0.056 μM for Cu^{2+} and 0.31 μM for L-cysteine, respectively. The proposed nanosensor can be used to detect Cu^{2+} and L-cysteine in serum samples.

A fluorescence sensor based on gold nanoparticles-functionalized GQDs has been designed and synthesized for the detection of Pb^{2+} with high sensitivity and high selectivity [29]. The GQDs showed strong fluorescence property. The fluorescence of GQDs was quenched in the presence of Au nanoparticles due to the aggregation of GQDs. The fluorescence of GQDs was recovered upon addition of Pb^{2+} ions inducing de-aggregation of gold nanoparticles-GQD complex. The fluorescence intensity exhibited a good linear relationship with the concentrations of Pb^{2+} ions within 50 nM–4 μM. The detection limit was 16.7 nM. The dopamine-functionalized GQDs (DA-GQDs) was constructed and prepared for the detection of Fe^{3+} ions with high sensitivity and high selectivity [30]. The DA-GQDs showed bright blue fluorescence, and the fluorescence of DA-GQDs was quenched in the presence of Fe^{3+} ions. The fluorescence quenching efficiency exhibited a good linear relationship with the concentrations of Fe^{3+} ions between 20 nM and 2 μM. The detection limit was 7.6 nM. The DA-GQD sensing probe displayed excellent selectivity for the detection of Fe^{3+} ions in the presence of other biomolecules. The reaction mechanism of Fe^{3+} was based on coordination interaction and oxidation of dopamine. The as-synthesized nanosensor as sensing platform can be widely used for environmental monitoring and biomedical applications.

The folic acid-functionalized GQDs (FA-GQDs) were designed and synthesized by thermal pyrolysis of maleic acid (MA) and folic acid (FA) [31]. The FA-GQDs showed obvious fluorescence behavior, and fluorescence property depends on the different ratio of FA/MA used in thermal pyrolysis. The FA-GQDs as a turn-on fluorescent sensor showed a high sensitivity for the detection of folate receptor-positive cancer cells. The resulting FA-GQDs also exhibited a fluorescence response to Hg^{2+} ions. The fluorescence quenching efficiency showed a good linear relationship to the concentrations of Hg^{2+} ions within 2.0×10^{-6} to 5.0×10^{-12} M. The detection limit was 1.7×10^{-12} M (S/N = 3). The FA-GQD nanosensor displayed excellent selectivity for the detection of Hg^{2+} ions in the presence of other metals and biomolecules.

2.3.4 Detection of proteins

The fluorescence sensor lecithin/β-CD@NR@ GQD complex was constructed and synthesized by covalence Nile red (NR) onto GQDs using

lecithin/β-cyclodextrin (lecithin/β-CD) complex as linker [32]. The GQDs connect with NR through lecithin/β-CD complex based on electrostatic interaction and hydrophobic interaction. The fluorescence of GQDs was quenched upon addition of lecithin/β-CD@NR based on Förster resonance energy transfer. Meantime, the fluorescence intensity of NR obviously enhanced. The lecithin/β-CD@NR@ GQD complex as nanosensor exhibited high sensitivity for the detection of acid phosphatase (ACP). The detection limit was 28 μU/mL. The proposed sensor has been successfully applied to monitor ACP in PC-3 M cells.

The graphene oxide quantum dots@silver (GQDs@Ag) nanocrystals with core-shell structure was designed and prepared as fluorescence sensing platform for the detection of prostate-specific antigen (PSA) [33]. The quantities of GQDs on GQDs@Ag decided the intensities of fluorescence signal. The incorporated GQDs can be released by removing of silver shell based on oxidative reaction without affecting their fluorescence performance. The anti-PSA antibody (Ab_1) and antibody (Ab_2) was immobilized onto magnetic beads (MBs) and GQDs@Ag, respectively. The GQDs@Ag showed a high sensitivity and high selectivity for the detection of PSA. The fluorescence intensity exhibited an excellent linear relationship with concentrations of PSA within 1 pg/mL to 20 ng/mL. The detection limit was 0.3 pg/mL. The as-synthesized immunosensor has been successfully applied to detect PSA in human serum. The antibody anti-cardiac troponin I (anti-cTnI) modified with amine-functionalized GQDs (afGQDs) was constructed and prepared by carbodiimide coupling reaction, namely, anti-cTnI/afGQDs [34]. The complex anti-cTnI/afGQDs exhibited sensitive response for detection of target antigen (cTnI) with high sensitivity and high selectivity. The as-synthesized complex as nanosensor showed strong fluorescence behavior, and the fluorescence of anti-cTnI/afGQDs was quenched in the presence of graphene (Gr). The fluorescence of anti-cTnI/afGQDs was recovered upon the addition of target antigen (cTnI) on anti-cTnI/afGQDs/Gr-inducing Gr apart from GQDs. The fluorescence intensity showed a good linear relationship with the concentrations of cTnI between 1.0 pg/mL and 1.0 ng/mL. The detection limit was 0.192 pg/mL.

2.4 Nanocomposites based on graphene quantum dots (GQDs) as electrochemical sensors

The functionalized glassy carbon electrode (GCE) based on composites of GQDs and β-cyclodextrins (β-CDs) was designed and synthesized as an electrochemical sensor for the detection of tyrosine (Tyr) enantiomers [35]. The as-synthesized β-CDs-GQDs/GCE exhibited an ultrasensitive response signal for the monitoring of Tyr enantiomers using GQDs as substrate and β-CDs as recognition molecule. The β-CDs-GQDs/GCE showed obvious difference in the oxidation peak current between L-Tyr and D-Tyr. The quantities of L-Tyr of healthy people showed higher than that of depression patients. The detection limit was 6.07×10^{-9} M and 1.03×10^{-7} M for L-Tyr and D-Tyr, respectively.

The gold nanoparticles/proline-functionalized GQDs (GNs/Pro-GQDs) were constructed and prepared as ultrasensitive electrochemical sensor for the monitoring of p-acetamidophenol [36]. The proline-GQDs were synthesized using pyrolysis of citric acid and proline. The GNs/Pro-GQDs were formed by directly reacting $HAuCl_4$ with proline-GQDs. The peak current (I_p) showed a good linear relationship with the concentration of p-acetamidophenol within 0.08–100 mM. The detection limit was 0.02 μM (S/N = 3).

The GQDs/riboflavin (RF) functionalized glassy carbon elec-trode (GC/GQDs/RF) was developed as a sensitive electrochemical sensor to detect persulfate ($S_2O_8^{2-}$) [37]. The modified electrode exhibited a stable redox peak between pH 1

and pH 10. The obtained GC/GQDs/RF showed a good electrochemical activity for the detection of $S_2O_8^{2-}$. The linear calibration range was from 1.0 μM to 1 mM. The detection limit and sensitivity were 0.2 μM and 4.7 nA/μM, respectively. One electrochemiluminescent (ECL) sensor was developed and synthesized to monitor Cr(VI) ions in water samples based on fluorescence signal changes of graphene quantum dots/peroxodisulfate (GQD/$S_2O_8^{2-}$) complex [38]. The fluorescence of GQD/$S_2O_8^{2-}$ complex was quenched in the presence of Cr(VI) ions based on mechanism of fluorescence resonance energy transfer (FRET). The linear response range was 50 nM–60 μM. The detection limit was 20 nM (S/N = 3). The obtained sensor has been successfully applied to detect Cr(VI) in river water.

The hybrid GQDs/TiO_2 NTs were constructed based on titanium dioxide nanotube arrays (TiO_2 NTs) infilled with GQDs as an efficient ECL sensor for detection of PSA [39]. The fabricated GQDs/TiO_2 NP composite electrode presented good stability and showed higher fluorescence intensity compared to that of pure TiO_2 NT electrode. The TiO_2 functionalized Fe_3O_4 magnetic nanoparticles (CdTe/MNPs) acted as quencher for the sensor. The GQDs/TiO_2 NT sensing platform showed high sensitivity and high selectivity for the detection of PSA. The ECL quenching efficiency exhibited a good linear relationship with log of the concentration of the PSA within 1.0 fg/mL to 10 pg/mL. The detection limit was 1 fg/mL (S/N = 3). The obtained nanosensor has been successfully applied to detect PSA in clinical human serum samples. The label-free ECL immunosensor was designed and synthesized based on GQDs [40]. The Au/Ag-rGO complex was prepared and employed to immobilize GQDs. The aminated-GQDs and carboxyl-GQDs were loaded onto electrode. The antibody of PSA was conjugated with modified electrode by absorbing Au/Ag to target proteins. The ECL quenching efficiency showed a linear relationship with log of concentrations between 1 pg/mL to 10 ng/mL. The detection limit was 0.29 pg/mL.

The chitosan-functionalized GQDs (GQD-CS) were constructed and employed to mobilize methylene blue (MB) using glass carbon electrode (GCE) based on aminohydroxy reaction [41]. The non-enzymatic sensor showed high sensitivity and high selectivity for the detection of H_2O_2. The obtained GQD-CS/MB/GCE displayed an obviously catalytic behavior toward H_2O_2 reduction. Compared with bare GCE, GQDs/GCE, and GQD-CS/GCE, the hybrid GQD-CS/MB/GCE showed higher electrochemical activities based on synergistic effect between GQD-CS and MB. The sensitivity was 10.115 μA/mM and detection limit was 0.7 μM.

The GQDs coated on hollow nickel nanospheres (hNiNS) modified with glass carbon electrode (GCE) were designed and synthesized as a molecularly imprinted electrochemical sensor (MIECS) for the monitoring of bisphenol S (BPS) with high sensitivity and high selectivity [42]. The pyrrole serves as monomer and BPS as template to polymerized molecularly imprinted polymer (MIP) film. The response signal showed linear relationship with the concentration of BPS between 0.1 and 50 μM. The detection limit was 0.03 μM. The ultrasensitive electrochemical sensor based on modified glass carbon electrode (GCE) was constructed and prepared for the determination of metronidazole (MNZ) [43]. The GQDs coated with molecularly imprinted polymers (MIPs) were synthesized. The complex of graphene nanoplatelets (GNPs) and MIPs exhibited obviously enhanced electrocatalytic property for MNZ based on good synergistic effect of GNPs and MIPs. The proposed electrochemical sensor displayed two linear ranges within 0.005–0.75 μmol/L and 0.75–10.0 μmol/L. The detection limit was 0.52 nmol/L. The electrochemical sensor has been applied to inspection of human serum samples. The GQD self-assembled monolayer-modified electrode was constructed as highly selective electrochemical sensor for the detection of dopamine (DA) [44]. The GQD-$NHCH_2CH_2NH_2$ functionalized GCE was prepared. The functionalized

electrode showed excellent electrical conductivity and displayed sensitive response to DA. The modified GCE showed a good linear relationship with the concentrations within 1–150 μM. The detection limit was 0.115 μM (S/N = 3). The obtained GQD-NHCH$_2$CH$_2$NH$_2$ functionalized GCE displayed good stability and excellent anti-interference capability.

2.5 Nanocomposite-based doped graphene quantum dots as nanosensors

The chemical doping is a common strategy and used for tailoring the properties of GQDs. The heteroatom-doped GQDs showed exceptional properties such as tunable emission, changeable spin density, and charge distribution of carbon atoms [45]. Dopants include N, sulfur (S), phosphorus (P), boron (B), fluorine (F), and chlorine (Cl).

2.5.1 Nitrogen-doped graphene quantum dots (N-GQDs) as nanosensors

The first successful synthesis of nitrogen-doped GQDs was reported by Li and co-workers in 2012 [46]. Liu et al. synthesized N-GQDs by hydrothermal method using citric acid as carbon sources and ammonia as nitrogen sources with N/C atomic ratio of ca. 4.3% emitting an obviously blue luminescence [47]. The fluorescence quantum yield of N-GQDs was 2.46% by calculation. The as-prepared N-GQDs can strongly adsorb 18 mer ssDNA (5′-ATACCAGCTTATTCAATT-3′) via π-π interaction force. The fluorescence of N-GQDs was quenched by photo-induced electron transfer mechanism between N-GQDs and ssDNA. The fluorescence of N-GQDs can be recovered upon addition of mixture of bleomycin and Fe(II) due to the noncovalent binding between bleomycin and ssDNA.

Fan and co-worker constructed N-GQD-Hg(II) complex system as a highly sensitive fluorescence sensor for cysteine detection [48]. The N-GQDs was prepared by one-pot method using citric acid as carbon source and urea as nitrogen sources. The N-GQD-Hg(II) complex as fluorescence sensor showed weak fluorescence. The fluorescence was recovered upon addition of cysteine to the complex system of N-GQD-Hg(II) due to the coordinate interaction between cysteine and Hg(II). The fluorescence intensity showed good linear relationship with the concentration of cysteine within a range of 0.05–30 μmol/L. The detection limit was 1 .3 nmol/L.

Zhao et al. prepared oxygen-rich nitrogen-doped GQDs by using one-pot synthesis strategy as pH-sensitive sensor for the detection of Hg(II) ion [49]. The oxygen-rich N-GQDs were synthesized by using citric acid (CA) and 3,4-dihydroxy-L-phenylalanine (L-DOPA) as the carbon source and the N source, respectively. The N-GQDs showed excitation-wavelength-independent fluorescent behavior, and the quantum yield was 18%. The N-GQDs as an efficient fluorescent sensor displayed the highly sensitivity and highly selectivity for the detection of Hg(II) based on the mechanism of nonradiative electron transfer. The detection limit was 8.6 nM. The fluorescence quenching efficiency showed good linear relationship with the concentration of Hg(II) within concentration from 0.04 to 6 μM. The competitive experiments showed that the N-GQDs showed high selectivity and sensitivity for the detection of Hg(II) even in the interference of other metal ions.

The strip-based fluorescence molecularly imprinted sensor was designed and constructed for monitoring thiacloprid [50]. The fluorescence molecularly imprinted sensor was synthesized based on polydopamine (PDA) polymer, thiacloprid, and N-GQDs. Firstly, the filter paper is dipped into N-GQD aqueous solution; secondly, the dopamine with thiacloprid self-polymerized on the surface of strip. The polydopamine molecularly imprinted polymer acted as an high efficient

sensor for the detection of thiacloprid. The as-prepared fluorescence molecularly imprinted sensor showed a linear relationship between 0.1 and 10 mg/L, and detection limit was 0.03 mg/L.

The hydrogen peroxide (H_2O_2) holds an important role in the biological system and is closely related with many diseases such as cancer, Parkinson disease, and so on [51]. The Pd nanoparticles decorated with N-GQDs @N-carbon hollow nanospheres was designed and synthesized as a high electrochemical sensor for the hydrogen peroxide detection [52]. The proposed NGQD@NC@Pd HNSs sensor showed highly efficient electrocatalytic activity as non-enzymatic catalyst for the reduction of H_2O_2. The NGQD@NC@Pd/GCE exhibited excellent repeatability and reproducibility by detecting eight different NGQD@NC@Pd/GCE in fixed concentration H_2O_2 with relative standard deviation (RSD) 2.7 and 3.6%, respectively. The cytotoxicity of NGQD@NC@Pd/GCE was evaluated by using Cell Counting Kit-8 (CCK8) assay. The results of CCK-8 assay displayed over 95% viability incubating NGQD@NC@Pd/GCE using MDA-MB-231 and HBL-100 cells for 4 h, indicating good biocompatibility of the NGQD@NC@Pd/GCE.

Peng and co-workers designed and reported a strategy method to detect Hg(II) ions by accelerating reaction rate between porphyrin and Mn(II) based on synergistic effect of N-GQDs and Hg(II) [53]. The reaction mechanism is based on larger Hg(II) of porphyrin-Hg(II) complex, which was replaced by smaller Mn(II) ions forming porphyrin-Mn(II) complex in a relatively faster speed. Such course was accompanied by the absorption red-shift and fluorescence quenching of porphyrins; meantime, the fluorescence intensity of N-GQDs enhanced. The CCK-8 assay showed over 90% viability by incubating 5.0 μM TMPyP, 40 μM Mn(II), or 20 μg/L N-GQDs for 24 h using A549 cells, indicative of good biocompatibility.

2.5.2 Nitrogen and phosphorus co-doped graphene quantum dots (N,P-GQDs) as nanosensors

Liu and co-workers prepared N,P-GQDs as fluorescence sensor for the detection of nitrite with high sensitivity and high selectivity [54]. The N,P-GQDs were synthesized by hydrothermal method using tetrakis(hydroxymethyl)phosphonium chloride and ethylenediamine endcapped polyethylenimine as phosphorus, carbon, and nitrogen source, respectively. The N,P-GQDs were prepared by using different temperatures (230° and 250°) and showed higher oxygen, nitrogen, and phosphorus levels at 230° compared to the those at 250°. The absolute quantum yield of N,P-GQDs was 9.4%. The N,P-GQDs showed a fast response to NO_2^- with high sensitivity and high selectivity. The fluorescence quenching efficiency exhibited a good linear relationship with concentration of NO_2^- within 5–30 nM. The detection limit was 2.5 nM. The results of MTT assays displayed over 90% cell viability by incubating N,P-GQDs with T24 cells for 24 h, suggesting good biocompatibility and imaging nitrite in live cell.

Ananthanarayanan et al. used carbonization strategy for the preparation of N,P-GQDs from biomolecule adenosine triphosphate (ATP) as nitrogen and phosphorus source [55]. Firstly, adenosine triphosphate (ATP) was carbonized for 1 h at 90° and got carbonized ATP; then the carbonized ATP was exfoliated in HNO_3 for 24 h and got final product N,P-GQDs. The results of Raman spectrum characterization of carbonized ATP exhibited prominent D and G bands, indicative of the presence of sp^3 carbon with graphitic nature. The N,P-GQDs have many advantages, such as excellent biocompatibility, good photostability, high fluorescence quantum yield (QY ~ 27.5% by calculation and ~53.0% after chemical reduction using $NaBH_4$), and low molecular weight (~1.4 kDa). The doping proportions of N and P are

6.2 (C/N = 7.0) and 6.9 (C/P = 6.3), respectively. The N,P-GQDs exhibited good two-photon upconversion properties. The strong upconverted photoluminescence phenomenon was showed with maximum emission at ~560 nm upon excitation at 800 nm. The lifetime measurements of N,P-GQDs exhibited τ_1 (A_1) and τ_2 (A_2) to be 320 ps (0.44) and 1.62 ns (0.56), respectively, where τ_1 and τ_2 are time constants and A_1 and A_2 are the corresponding amplitudes. The imaging and real-time tracking of transferrin receptors in human cervical cancer cells came true upon conjugating N,P-GQDs with a transferrin.

Mahyari and Gavgani designed and constructed cobalt porphyrin-supported N,P-GQDs/graphene (CoPP@N,P-GQDs/G) complex as noble metal-free photocatalysts [56]. Firstly, the N,P-GQDs were synthesized by carbonization of adenosine triphosphate as nitrogen source and phosphorous source; secondly, the N,P-GQDs were embedded on graphene oxide; and thirdly, the cobalt porphyrins with photoactive property were loaded through ionic interaction. The resultant product CoPP@N,P-GQDs/G showed good dispersion in the reaction medium (water). The CoPP@N,P-GQDs/G complex as recyclable photocatalysts showed high efficiency with the aerobic oxidation reaction of alcohols by using visible-light irradiation. Furthermore, CoPP@N,P-GQDs/G complex displayed the good selectivity for various alcohols by mild and green ways.

2.5.3 Nitrogen and sulfur co-doped graphene quantum dots (N,S-GQDs) as nanosensors

Mondal et al. designed and synthesized N,S-GQDs from the mixture of graphene oxide solution and thiourea by hydrothermal method [57]. The N,S-GQDs exhibited strong emission peak at 405 nm upon excitation at 320 nm. The N,S-GQDs showed a sensitive response to 2,4,6-trinitrophenol with highly selectivity, and the detection limit was 19.05 ppb. The fluorescence of N,S-GQDs significantly decreased upon addition of 2,4,6-trinitrophenol based on photo-induced electron transfer (PET) mechanism. The fluorescence quenching efficiency showed good linear relationship with concentration of 2,4,6-trinitrophenol. The N,S-GQDs showed higher quenching efficiency compared to these of N-GQDs, S-GQDs, and GQDs. Gavgani and co-workers constructed an ammonia (NH_3) sensor based on N,S-GQDs/polyaniline (PANI) hybrid with high sensitivity and high selectivity [58]. The N,S-GQDs were synthesized by hydrothermal process using citric acid as carbon source and using thiourea as sulfur source, respectively. The N,S-GQDs/PANI hybrid was prepared by using in situ chemical oxidative polymerization. The increased proportion of N,S-GQDs in N,S-GQDs/PANI hybrid showed considerable improvement of NH_3 response, such as around 42% at 100 ppm and 385% at 1000 ppm, respectively. The N,S-GQDs/PANI hybrid showed fivefold higher response compared to that of free PANI. The enhancement of sensing properties for the N,S-GQDs/PANI hybrid attributed to the synergistic effect between the N,S-GQDs and PANI.

Chen et al. synthesized N,S-GQDs by one-pot pyrolysis method with quantum yield of 67% using citric acid and cysteine as carbon source and nitrogen and sulfur source, respectively [59]. The N,S-GQDs showed an excitation-independent emission property. The fluorescence of N,S-GQDs was quenched upon addition of AgNPs, and the fluorescence of N,S-GQD-AgNPs was recovered in the presence of CN^-. The N,S-GQDs have no effect on the adsorption spectrum of AgNPs; however, addition of CN^- obviously decreased the absorbance of AgNPs. The detection limit was 0.52 μM for fluorescent sensors and 0.78 μM for colorimetric sensors. The as-synthesized N,S-GQD-AgNPs as nanosensor has been successfully applied to detect CN^- in realized water samples.

2.5.4 Sulfur-doped graphene quantum dots (S-GQDs) as nanosensors

The S-GQDs were prepared and reported by Bian and co-workers through one-pot hydrothermal method using compound 1,3,6-trinitropyrene as carbon source and 3-mercaptopropionic acid (MPA) as sulfur source [60]. The S-GQDs as fluorescent sensing probes showed highly sensitive response to the Ag^+ ions with high selectivity within a wide linear range of 0.1–130.0 μM. The detection limit was 30 nM. The fluorescence intensity of S-GQDs was obviously decreased upon addition of Ag^+ ions. The fluorescence quenching efficiency showed a good linear relationship with concentration of Ag^+ ions based on photo-induced electron transfer (PET) mechanism. The feasibility of as-synthesized S-GQDs as fluorescent sensing probe in practical application was assessed by Ag^+ detection in local lake. The detection results obtained from S-GQDs and ICP-MS were close.

Li et al. synthesized the S-GQDs by electrochemical approach using graphite electrode in sodium p-toluenesulfonate aqueous solution [61]. The S-GQDs obviously improved surface chemistry and electronic properties. The S-GQDs as fluorescent sensor showed a sensitive response to the Fe^{3+} ions with high selectivity and high sensitivity. The fluorescence intensity of S-GQDs obviously decreased upon addition of Fe^{3+} ions concentration between 0.01 and 0.70 μM. The fluorescence quenching efficiency showed good linear relationship with the concentration of Fe^{3+} ions. The detection limit was 4.2 nM. The S-GQDs as a fluorescent sensor can be reused over five times without signal lost. This fluorescence sensing probe can be successfully applied to detect Fe^{3+} ions in human serum. Dong et al. prepared S-GQDs by hydrothermal process using the mixture of 1,3,6-trinitropyrene, Na_2S, and NaOH in aqueous solution [62]. The reported S-GQDs exhibited a stable yellow-green emission. It was found that fluorescence quenching was pH-dependent and showed best quenching efficiency at pH 7.0. The as-synthesized S-GQDs showed excitation-independent photoluminescence property. The S-GQDs as a newly fluorescent probe showed high selectivity and high sensitivity for the detection of Pb(II) ions. Compared to Pb(II) ions, ions such as Na(I), K(I), Cu(II), Ca(II), Mg(II), Fe(III), Ni(II), Co(II), and Cd(II) have no obvious effect on the fluorescence intensity of S-GQDs. The fluorescence intensity of S-GQDs significantly decreased upon addition of Pb(II) ions from 0.1 to 220.0 mM in aqueous solution. The fluorescence quenching efficiency showed good linear relationship with concentrations of Pb(II) from 0.1 to 140.0 μM. The detection limit was 0.03 μM.

3. Conclusion

In this chapter, we concluded recent development of modified graphene-based nanocomposites (including of GO, GQDs, doped GQDs) as novel and convenient fluorescence nanosensors and electrochemical sensors for the detection of amino acids, proteins, metal ions, inorganic anions, drug molecules, and small molecules, pH, respectively. The obtained functionalized fluorescence sensors and electrochemical sensors as sensing platforms displayed high sensitivity and high selectivity for the detection of biomolecules, respectively.

The graphene-based composites attracted the interest of scientific workers due to its nanosize, quantum confinement, edge effects, low toxicity, and good conductivity. We comprehensively summarized the preparation, dopant element, interaction mechanism, and practical applications. The relationship between response signals and analyte concentrations was discussed in detail. The functionalized graphene-based nanocomposites showed good biocompatibility and low toxicity.

The as-synthesized fluorescence sensors and electrochemical sensors have been successfully applied for the monitoring of biomolecules in the human serum samples. The graphene-based nanocomposites showed great potential as sensing platforms for the biomedical applications and clinic research.

Acknowledgements

Conflict of interest

The author(s) declare that they have no competing interests.

Author details

Rumei Cheng[1]* and Shengju Ou[2]

1 Institute of Advanced Materials for Nano-Bio Applications, School of Ophthalmology and Optometry, Wenzhou Medical University, Wenzhou, Zhejiang, China

2 Hangzhou Zhe Da Femtosecond Test Technology Co., Ltd., Zhejiang University National Science Park, Hangzhou, Zhejiang, China

*Address all correspondence to: rumeicheng@yahoo.com

IntechOpen

References

[1] Novoselov KS, Geim AK, Morozov S, et al. Electric field effect in atomically thin carbon films. Science. 2004;**306**:666-669. DOI: 10.1126/science.1102896

[2] Parnianchi F, Nazari M, Maleki J, et al. Combination of graphene and graphene oxide with metal and metal oxide nanoparticles in fabrication of electrochemical enzymatic biosensors. International Nano Letters. 2018;**8**:229-239. DOI: 10.1007/s40089-018-0253-3

[3] Zhu S, Zhang J, Tang S, et al. Surface chemistry routes to modulate the photoluminescence of graphene quantum dots: From fluorescence mechanism to up-conversion bioimaging applications. Advanced Functional Materials. 2012;**22**:4732-4740. DOI: 10.1002/adfm.201201499

[4] Zhang M, Bai L, Shang W, et al. Facile synthesis of water-soluble, highly fluorescent graphene quantum dots as a robust biological label for stem cells. Journal of Materials Chemistry. 2012;**22**:7461-7467. DOI: 10.1039/c2jm16835a

[5] Cheng R, Peng Y, Ge C, et al. A turn-on fluorescent lysine nanoprobe based on the use of the Alizarin Red aluminum(III) complex conjugated to graphene oxide, and its application to cellular imaging of lysine. Microchimica Acta. 2017;**184**:3521-3528. DOI: 10.1007/s00604-017-2375-0

[6] Wang Q, Zhang D. A novel fluorescence sensing method based on quantum dot-graphene and a molecular imprinting technique for the detection of tyramine in rice wine. Analytical Methods. 2018;**10**:3884-3889. DOI: 10.1039/c8ay01117f

[7] Berninger T, Bliem C, Piccinini E, et al. Cascading reaction of arginase and urease on a graphene-based FET for ultrasensitive, real-time detection of arginine. Biosensors and Bioelectronics. 2018;**115**:104-110. DOI: 10.1016/j.bios.2018.05.027

[8] Bao X, Shi J, Zhu J, Wang X. A novel sensitive and selective nanocomposite sensor for doxorubicin based on graphene oxide and fluorescent [2] Rotaxane. Sensors and Actuators B. 2016;**237**:380-386. DOI: 10.1016/j.snb.2016.06.140

[9] Li S, Li J, Luo J, et al. A fluorescence switch sensor for detection of virginiamycin based on graphene oxide-supported carbon quantum dots and molecularly imprinted polymer. RSC Advance. 2017;**7**:56359-56364. DOI: 10.1039/c7ra12098b

[10] Cheng R, Ge C, Qi L, et al. Label-free graphene oxide förster resonance energy transfer sensors for selective detection of dopamine in human serums and cells. The Journal of Physical Chemistry C. 2018;**122**:13314-13321. DOI: 10.1021/acs.jpcc.7b09256

[11] Zhu H, Xu H, Yan Y, et al. Highly fluorescent graphene oxide as a facile and novel sensor for the determination of hypochlorous acid. Sensors and Actuators B. 2014;**202**:667-673. DOI: 10.1016/j.snb.2014.06.002

[12] Muthuraj B, Mukherjee S, Chowdhury SR, et al. An efficient strategy to assemble water soluble histidine-perylenediimide and graphene oxide for the detection of PPi in physiological conditions and in vitro. Biosensors and Bioelectronics. 2017;**89**:636-644. DOI: 10.1016/j.bios.2015.12.036

[13] Cheng R, Li L, Ou S, et al. Determination of Ag+ ions by a graphene oxide based dual-output nanosensor with high selectivity. RSC Advance. 2016;**6**:36218-36222. DOI: 10.1039/c6ra00048g

[14] Gevaerd A, Blaskievicz SF, Zarbin AJG, et al. Nonenzymatic electrochemical sensor based on imidazole-functionalized graphene oxide for progesterone detection. Biosensors and Bioelectronics. 2018;**112**:108-113. DOI: 10.1016/j.electacta.2018.02.132

[15] Tomita S, Ishihara S, Kurita R. A multi-fluorescent dna/graphene oxide conjugate sensor for signature-based protein discrimination. Sensors. 2017;**17**:2194-2206. DOI: 10.3390/s17102194

[16] Abdallah NA, Ibrahim HF. Potentiometric sensor of graphene oxide decorated with silver nanoparticles/molecularly imprinted polymer for determination of gabapentin. Carbon Letters. 2018;**27**:50-63. DOI: 10.5714/CL.2018.27.050

[17] Yang R, Miao D, Liang Y, et al. Ultrasensitive electrochemical sensor based on CdTe quantum dots-decorated poly(diallyldimethylammonium chloride)-functionalized graphene nanocomposite modified glassy carbon electrode for the determination of puerarin in biological samples. Electrochimica Acta. 2015;**173**:839-846. DOI: 10.1016/j.electacta.2015.05.139

[18] Peng J, Huang Q, Zhuge W, et al. Blue-light photoelectrochemical sensor based on nickel tetra-amined phthalocyanine-graphene oxide covalent compound for ultrasensitive detection of erythromycin. Biosensors and Bioelectronics. 2018;**106**:212-218. DOI: 10.1016/j.bios.2018.02.009

[19] Gao X, Gui R, Xu KQ, et al. A bimetallic nanoparticle/graphene oxide/thionine composite-modified glassy carbon electrode used as a facile ratiometric electrochemical sensor for sensitive uric acid determination. New Journal of Chemistry. 2018;**42**:14796-14804. DOI: 10.1039/c8nj02904k

[20] Liu T, Fu B, Chen J, et al. A non-enzymatic electrochemical sensor for detection of sialic acid based on a porphine/graphene oxide modified electrode via indicator displacement assay. Electrochimica Acta. 2018;**269**:136-143. DOI: 10.1016/j.electacta.2018.02.132

[21] Kamaruddin NH, Bakar AAA, Mobarak NN, et al. Binding affinity of a highly sensitive Au/Ag/Au/chitosan-graphene oxide sensor based on direct detection of Pb^{2+} and Hg^{2+} ions. Sensors. 2017;**17**:2277-2293. DOI: 10.3390/s17102277

[22] Priya T, Dhanalakshmi N, Thennarasu S, et al. A novel voltammetric sensor for the simultaneous detection of Cd^{2+} and Pb^{2+} using graphene oxide/κ-carrageenan/L-cysteine nanocomposite. Carbohydrate Polymers. 2018;**182**:199-206. DOI: 10.1016/j.carbpol.2017.11.017

[23] Hai X, Lin X, Chen X, et al. Highly selective and sensitive detection of cysteine with a graphene quantum dots-gold nanoparticles based core-shell nanosensor. Sensors and Actuators B. 2018;**257**:228-236. DOI: 10.1016/j.snb.2017.10.16

[24] Yan X, Song Y, Zhu C, et al. Graphene quantum dot—MnO_2 nanosheet based optical sensing platform: A Sensitive fluorescence "turn off—on" nanosensor for glutathione detection and intracellular imaging. ACS Applied Materials &Interfaces. 2016;**8**:21990-21996. DOI: 10.1021/acsami.6b05465

[25] Zhou T, Halder A, Sun Y. Fluorescent nanosensor based on molecularly imprinted polymers coated on graphene quantum dots for fast detection of antibiotics. Biosensors. 2018;**8**:82-93. DOI: 10.3390/bios8030082

[26] Na W, Qu Z, Chen X, et al. A turn-on fluorescent probe for sensitive detection

of sulfide anionsand ascorbic acid by using sulfanilic acid and glutathione functionalized graphene quantum dots. Sensors and Actuators B. 2018;**256**: 48-54. DOI: 10.1016/j.snb.2017.09.182

[27] Dong Y, Li G, Zhou N, et al. Graphene quantum dot as a green and facile sensor for free chlorine in drinking water. Analytical Chemistry. 2012;**84**:8378-8382. DOI: 10.1021/ac301945z

[28] Lin L, Song X, Chen Y, et al. Europium-decorated graphene quantum dots as a fluorescent probe for label-free, rapid and sensitive detection of $Cu^{2+}$and L-cysteine. Analytica Chimica Acta. 2015;**891**:261-268. DOI: 10.1016/j.aca.2015.08.011

[29] Niu X, Zhong Y, Chen R, et al. A "turn-on" fluorescence sensor for Pb2+ detection based on graphene quantum dots and gold nanoparticles. Sensors and Actuators B. 2018;**255**:1577-1581. DOI: 10.1016/j.snb.2017.08.167

[30] Chowdhury AD, Doong R. Highly sensitive and selective detection of nanomolar ferric ions using dopamine functionalized graphene quantum dots. ACS Applied Material Interfaces. 2016;**8**:21002-21010. DOI: 10.1021/acsami.6b06266

[31] Li R, Wang X, Li Z, et al. Folic acid-functionalized graphene quantum dots with tunable fluorescence emission for cancer cell imaging and optical detection of Hg^{2+}. New Journal Chemistry. 2018;**42**:435-4360. DOI: 10.1039/c7nj05052f

[32] Na W, Liu Q, Sui B, et al. Highly sensitive detection of acid phosphatase by using a graphene quantum dots-based förster resonance energy transfer. Talanta. 2016;**161**:469-475. DOI: 10.1016/j.talanta.2016.08.043

[33] Pei H, Zhu S, Yang M, et al. Graphene oxide quantum dots@silver core-shell nanocrystals as turn-on fluorescent nanoprobe for ultrasensitive detection of prostate specific antigen. Biosensors and Bioelectronics. 2015;**74**:909-914. DOI: 10.1016/j.bios.2015.07.056

[34] Bhatnagar D, Kumar V, Kumar A, et al. Graphene quantum dots FRET based sensor for early detection of heart attack in human. Biosensors and Bioelectronics. 2016;**79**:495-499. DOI: 10.1016/j.bios.2015.12.083

[35] Dong S, Bi Q, Qiao C, et al. Electrochemical sensor for discrimination tyrosine enantiomers using graphene quantum dots and β-cyclodextrins composites. Talanta. 2017;**173**:94-100. DOI: 10.1016/j.talanta.2017.05.045

[36] Zhou X, Li R, Li Z, et al. Ultrafast synthesis of gold/proline-functionalized graphene quantum dots and its use for ultrasensitive electrochemical detection of p-acetamidophenol. RSC Advance. 2016;**6**:42751-42755. DOI: 10.1039/c6ra04602a

[37] Roushani M, Abdi Z. Novel electrochemical sensor based on graphene quantumdots/riboflavin nanocomposite for the detection of persulfate. Sensors and Actuators B. 2014;**201**:503-510. DOI: 10.1016/j.snb.2014.05.054

[38] Chen Y, Dong Y, Wu H, et al. Electrochemiluminescence sensor for hexavalent chromium based on the graphene quantum dots/peroxodisulfate system. Electrochimica Acta. 2015;**151**:552-557. DOI: 10.1016/j.electacta.2014.11.068

[39] Tian C, Wang L, Luan F, et al. An electrochemiluminescence sensor for the detection of prostate protein antigen based on the graphene quantum dots infilled TiO_2 nanotube arrays. Talanta. 2019;**191**:103-108. DOI: 10.1016/j.talanta.2018.08.050

[40] Wu D, Liu Y, Wang Y, et al. Label-free electrochemiluminescent immunosensor for detection of prostate specific antigen based on aminated graphene quantum dots and carboxyl graphene quantum dots. Scientific Reports. 2016;**6**:20511-20517. DOI: 10.1038/srep20511

[41] Mollarasouli F, Asadpour-Zeynali K, Campuzano S, et al. Non-enzymatic hydrogen peroxide sensor based on graphene quantum dots-chitosan/methylene blue hybrid nanostructures. Electrochimica Acta. 2017;**246**:303-314. DOI: 10.1016/j.electacta.2017.06.003

[42] Rao H, Zhao X, Liu X, et al. A novel molecularly imprinted electrochemical sensor based on graphene quantum dots coated on hollow nickel nanospheres with high sensitivity and selectivity for the rapid determination of bisphenol S. Biosensors and Bioelectronics. 2018;**100**:341-347. DOI: 10.1016/j.bios.2017.09.016

[43] Ensafi AA, Nasr-Esfahani P, Rezaei M. Metronidazole determination with an extremely sensitive and selective electrochemical sensor based on graphene nanoplatelets and molecularly imprinted polymers on graphene quantum dots. Sensors and Actuators B. 2018;**270**:192-199. DOI: 10.1016/j.snb.2018.05.024

[44] Li Y, Jiang Y, Mo T, et al. Highly selective dopamine sensor based on graphene quantum dots self-assembled monolayers modified electrode. Journal of Electroanalytical Chemistry. 2016;**767**:84-90. DOI: 10.1016/j.jelechem.2016.02.016

[45] Zhang Y, Ma D, Zhuang Y, et al. One-pot synthesis of N-doped carbon dots with tunable luminescence properties. Journal of Materials Chemistry. 2012;**22**:16714-16718. DOI: 10.1039/C2JM32973E

[46] Li Y, Zhao Y, Cheng H, et al. Nitrogen-doped graphene quantum dots with oxygen-rich functional groups. Journal of the American Chemical Society. 2012;**134**:15-18. DOI: 10.1021/ja206030c

[47] Liu X, Na W, Liu Q, Su X. A novel label-free fluorescent sensor for highly sensitive detection of bleomycin based on nitrogen-doped graphene quantum dots. Analytica Chimica Acta. 2018;**1028**:45-49. DOI: 10.1016/j.aca.2018.04.038

[48] Liu Z, Gong Y, Fan Z. Cysteine detection using a high-fluorescence sensor based on a nitrogen-doped graphene quantum dot–mercury(II) system. Journal ofLuminescence. 2016;**175**:129-134. DOI: 10.1016/j.jlumin.2016.01.036

[49] Shi B, Zhang L, Lan C, et al. One-pot green synthesis of oxygen-rich nitrogen-doped graphene quantum dots and their potential application in pH-sensitive photo-luminescence and detection of mercury(II) ions. Talanta. 2015;**142**:131-139. DOI: 10.1016/j.talanta.2015.04.059

[50] Liu Y, Cao N, Gui W, et al. Nitrogen-doped graphene quantum dots-based fluorescence molecularly imprinted sensor for thiacloprid detection. Talanta. 2018;**183**:339-344. DOI: 10.1016/j.talanta.2018.01.063

[51] Ju J, Chen W. In situ growth of surfactant-free gold nanoparticles on nitrogen-doped graphene quantum dots for electrochemical detection of hydrogen peroxide in biological environments. Analytical Chemistry. 2015;**87**:1903-1910. DOI: 10.1021/ac5041555

[52] Xi J, Xie C, Zhang Y, et al. Pd nanoparticles decorated N-doped graphene quantum dots@Ndoped carbon hollow nanospheres with high electrochemical sensing performance in cancer detection. ACS Applied Materials & Interfaces. 2016;**8**:22563-22573. DOI: 10.1021/acsami.6b05561

[53] Peng D, Zhang L, Liang R, et al. Rapid detection of mercury ions based on nitrogen-doped graphene quantum dots accelerating formation of manganese porphyrin. ACS Sensor. 2018;**3**:1040-1047. DOI: 10.1021/acssensors.8b00203

[54] Liu R, Zhao J, Huang Z, et al. Nitrogen and phosphorus co-doped graphene quantum dots as anano-sensor for highly sensitive and selective imaging detection of nitrite in live cell. Sensors and Actuators B. 2017;**240**: 604-612. DOI: 10.1016/j.snb.2016.09.008

[55] Ananthanarayanan A, Wang Y, Routh P, et al. Nitrogen and phosphorus co-doped graphene quantum dots: Synthesis from adenosine triphosphate, optical properties, and cellular imaging. Nanoscale. 2015;**7**:8159-8165. DOI: 10.1039/c5nr01519g

[56] Mahyari M, Gavgani JN. Cobalt porphyrin supported on N and P co-doped graphene quantum dots/graphene as an efficient photocatalyst for aerobic oxidation of alcohols under visible-light irradiation. Research on Chemical Intermediates. 2018;**44**: 3641-3657. DOI: 10.1007/s11164-018-3330-3

[57] Mondal TK, Dinda D, Saha SK. Nitrogen, sulphur co-doped graphene quantum dot: An excellent sensor for nitroexplosives. Sensors and Actuators B. 2018;**257**:586-593. DOI: 10.1016/j.snb.2017.11.012

[58] Gavgani JN, Hasani A, Nouri M, et al. Highly sensitive and flexible ammonia sensor based on S and Nco-doped graphene quantum dots/polyaniline hybrid at room temperature. Sensors and Actuators B. 2016;**229**: 239-248. DOI: 10.1016/j.snb.2016.01.086

[59] Chen C, Zhao D, Hu T, et al. Highly fluorescent nitrogen and sulfur co-doped graphene quantumdots for an inner filter effect-based cyanide sensor.

Sensors and Actuators B. 2017;**241**: 779-788. DOI: 10.1016/j.snb.2016.11.010

[60] Bian S, Shen C, Qian Y, et al. Facile synthesis of sulfur-doped graphene quantum dots asfluorescent sensing probes for Ag^+ ions detection. Sensors and Actuators B. 2017;**242**:231-237. DOI: 10.1016/j.snb.2016.11.044

[61] Li S, Li Y, Cao J, et al. Sulfur-doped graphene quantum dots as a novel fluorescent probe for highly selective and sensitive detection of Fe^{3+}. Analytical Chemistry. 2014;**86**: 10201-10207. DOI: 10.1021/ac503183y

[62] Bian S, Shen C, Hua H, et al. One-pot synthesis of sulfur-doped graphene quantum dots as a novel fluorescent probe for highly selective and sensitive detection of lead(II). RSC Advance. 2016;**6**:69977-69983. DOI: 10.1039/c6ra10836a

Mechanical and Tribological Properties of Epoxy Nano Composites for High Voltage Applications

Rashmi Aradhya and Nijagal M. Renukappa

Abstract

The tribological and mechanical properties of organomodified montmorillonite (oMMT)-incorporated Epoxy (Epoxy-oMMT), vinyl ester (vinyl ester-oMMT) and titanium dioxide (TiO_2)-filled Epoxy (Epoxy-TiO_2) nanocomposites are discussed below. Implications of introducing oMMT and TiO_2 nanoparticles on mechanical and dry sliding wear properties are presented using micrographs of cast samples and through observations of wear affected surface of nanocomposites. Distribution of nanoparticles and their influence on properties are being emphasized for understanding the wear properties. The data on mechanical and tribological properties determined experimentally are compared with published literature. The main focus is to highlight the importance of nanofillers in the design of wear-resistant thermoset polymer composites. A detailed study of strength and moduli of Epoxy-oMMT, Epoxy-TiO_2 and vinyl ester-oMMT nanocomposites was taken up as a part of the investigation. A discussion on density, hardness, tensile, flexural test data, and friction and wear of nanocomposites and analysis of results by comparison with prevalent theoretical models and published results of experiments are presented.

Keywords: organomodified montmorillonite, titanium dioxide, tribological properties friction and wear d wear resistant

1. Introduction

The present day scenario is attracting the polymer nanocomposites with greater interest both in industry and academics because of significant improvement in the properties when compared to base matrix or traditional composites [1]. The important structural characteristics which give unique properties to nanocomposites are the nanosize and a huge interfacial surface area of the nanofillers.

Since 1980s, advantageous properties of polymer nanocomposites were realized at the Toyota research laboratories where they studied nylon-6 based composite system with nanoclay as the reinforcement material to improve the toughness and heat resistance of nylon-6 [2]. Since then, a large quantity of research work has been carried out on polymer composites system using nanoclays and nanoparticle fillers of metallic or nonmetallic type and remarkable enhancements and benefits in several properties have been reported. The intriguing fact is that the properties which were observed in nanocomposites were never anticipated.

Although, the broad group of nanocomposite polymer materials have been widely investigated and fairly understood, the development of thermoset polymer based nanocomposites which also belong to this group, still remains a challenge. This is mainly because of the difficulty in uniform dispersion of nanofiller particles in the thermoset polymer matrix.

Many studies shown improvements in the mechanical strength and modulus of nanoclay filled epoxy resin nanocomposites as compared to the Epoxy resin [3]. Wang and co-authors [4] reported another technique called unique "slurry compounding" to fabricated exfoliated nanoclay-Ethacure nanocomposites. This composites shows improvements in the modulus of epoxy resin by about 40% with 5 wt.% of nanoclay, but with decreased tensile strength. They attributed this partial achievement to the feeble surface interface and occurrence of air foam in the nanocomposite samples. Gefu and co-authors [5] studied vinyl ester with 1 wt.% nanoclay. They have compared five types of mixing combinations such as (i) 30 min manual stirring, (ii) 30 min manual stirring and 1 h sonification mixing, (iii) 30 min manual stirring and 1 h sonification mixing followed by three-roll mill shear mixing, (iv) 30 min manual stirring and 1 h sonification mixing followed by three-roll mill shear mixing and 1 h sonification mixing, and (v) 30 min manual stirring and 1 h sonification mixing followed by three-roll mill shear mixing with 1 h sonification mixing and three-roll mill shear mixing while holding other factors constant.

It could be generally concluded that intensive mixing improved exfoliation until a certain point (defined as optimum point) and then its positive effects diminish with further mixing efforts. Considering reduced mixing effort of method iv, it is being recommended. Kotsilkova and co-authors [6] studied the flexural strength and flexural modulus of epoxy-clay nanocomposites fabricated by direct method or without solvent method and indirect method or solvent processing techniques. Different organic modifiers were used to functionalize the clay. It has been observed that the mechanical properties are majorly dependent on nanocomposite structure and the type of solvent used. The fabricated samples by direct processing method or without using solvent technique showed increased flexural modulus. The modulus of the nanocomposites at 5 volume percentage of clay content increased significantly.

In compare, the flexural modulus of fabricated nanocomposites fabricated by adding solvent or solvent processing technique is not affected [7]. The flexural strength of the fabricated nanocomposites has increased when compared to the samples fabricated by the direct processing method or without using solvent. This is due to the strength of the solvent, acting as a plasticizer for the base resin and alters the interfacial adhesions. In earlier studies it is reported that nanoclay appears to have either the intercalated structure or the partially exfoliated structure. The maximum improvement achieved in the modulus was of the order of about 80% with 10 wt.% nanoclay [7].

While the addition of nanoclay to epoxy resin generally increases the tensile modulus, it decreases the tensile strength and fracture strain [8, 9]. This was mainly attributed to the agglomeration of nanoclay and presence of voids. Organically modified nanocly effect on the physical, structural properties of organically modified clay –epoxy nanocomposites samples was examined by Dean and co-authors [10]. They reported that different morphological structures such as intercalation, partial and full exfoliation of nanoclay. The degree of intercalation morphology varies and interlayer expansion was observed. This is related to the mechanical properties of the fabricated nanocomposite samples. With the increase in the clay content, 35% increase in tensile modulus for the 2 wt.% sample, 15% increase in tensile modulus for 4 wt.% sample and 30% increase in the tensile modulus for the sample with 6 wt.% respectively.

Isık and co-authors [11] reported the clay loading effect on the tensile strength of organically modified clay filled epoxy nanocomposites. The tensile strength decreases with increasing content of clay. This is due to the nonuniform dispersion of clay, agglomeration of clay causes stress concentration and decreased polymer clay interactions. They also observed that the tensile modulus of the nanocomposite increases with increasing amount of clay. The mechanical properties of montmorillonite filled epoxy nanocomposites were studied by Akbari and Bagheri [12]. They found a decrease in flexural strength with increasing the content of organically modified clay and this is due to the fact that intercalated structure of clay in the nanocomposites. Kaya and co-authors [13] analyzed the flexural and tensile properties of clay filled epoxy nanocomposite samples. The surface modified and unmodified montmorillonite clay were added to the epoxy matrix with increasing clay contents from 1 to 10 wt.%. The author presented that both tensile and flexural modulus values tend to increase with increasing content of unmodified and modified clay. With the increase in clay loadings, surface modified clay showed a little higher values of elastic modulus when compared to surface unmodified montmorillonite clay. This is due to the fact that the effect of surface modification causes better level of penetration of the epoxy resin into the galleries of montmorillonite clay.

From the above studies, it was found that the mechanical properties such as flexural and tensile strength reduce for the fabricated nanocomposite samples with surface modified and not modified clay when compared to pristine base matrix. This is mainly due to the creation of voids, feeble adhesion points along the filler-matrix surface interface during nanocomposite processing. Velmurugan and Mohan [14] have reported the presence and effect of quaternary ammonium modified montmorillonite clay content on the mechanical properties of clay-epoxy nanocomposites. They reported that the tensile modulus of the fabricated samples increased about three times when compared to base pristine epoxy with the accumulation of 10 wt.% surface modified clay. This is due to the fact that the exfoliation structure of clay layers and surface interfacial adhesion between the nanoclay and the epoxy matrix, whereas, the tensile strength reduced in spite of the content of the clay as compared to pristine polymer (epoxy).

Yasmin and co-authors [15] conducted studies on the mechanical characteristics of surface modified montmorillonite clay added epoxy nanocomposite samples with variation in concentration of clay from 1 to10 wt.% fabricated by shear mixing technique. Based on their report, the addition of surface modified nanoclay particles there is a significant improvement both in elastic and storage modulus of base epoxy resin. In addition, there is an increase in storage modulus with increasing in clay content. This was ascribed to intercalation or exfoliation structure of surface modified nanocly (Cloisite 30B) in base epoxy matrix. The results reconfirmed that there is a direct relation between the degree of intercalation or exfoliation and the mechanical properties of the fabricated nanocomposites samples.

Basara and co-authors [16] analyzed the presence and effect of clay substance and morphological structure on mechanical properties of nanocomposites. The organically surface modified (Cloisite 30B) and natural or unmodified (Cloisite Na+) clay with the content varying from 0.5 to 11 wt.% was reinforced into base epoxy matrix and observed that tensile modulus increased with clay content. This is attributed to stiffening effect of montmorillonite clay in two types of clay reinforced nanocomposites. Cloisite 30B and Cloisite Na+ reinforced nanocomposite samples showed utmost tensile strength at 1 and 0.5 wt.% respectively. The reason for the decrease in tensile strength at larger montmorillonite clay content is due to the stress concentration effect of the agglomerated clay particles and lesser surface interactions.

Zhu and co-authors [17] investigated PA6/TiO$_2$ nanocomposites which resulted in improved spinnability and mechanical properties. It was observed that tenacity at break and the initial modulus of PA6 with modified nano-TiO$_2$ composites showed improvement by about 10, 20%, respectively, as compared to the pure PA6.

Mina and co-authors [18] studied TiO$_2$ filled isotactic polypropylene (iPP) composites with TiO$_2$ which was first single-extruded by an extruder and then double-molded by compression molding. Micro-hardness increased rapidly and then leveled off with increasing filler content. Variations with respect to molding conditions were also observed.

According to Dean and co-authors [19] the inter-gallery spacing of surface modified montmorillonite nanoclay increased efficiently. Ha and co-authors [20] have demonstrated that the tensile strength and elastic modulus of surface modified montmorillonite nanoclay Epoxy nanocomposites are elevated than that of unmodified montmorillonite nanoclay-Epoxy composites. Ha and co-authors [21] have stated that surface modification increases the interlayer gallery expansion, in turn improves the dispersion of nanoclay into the base polymer. Wang and co-authors [22] reported that improvement in the modulus and fracture toughness of base polymer such as epoxy was achieved by adding surface modified nanoclay using silane functionalizer. Lam and co-authors [23, 24] reported the effect of bunch of nanoclay and shows there is a best nanosized clay weight percentage in the nanocomposites in order to acquire maximum mechanical properties. The highest hardness is achieved for 4 wt.% of nanoclay. Furthermore, increasing the nanoclay content affected in reducing the hardness of the nanocomposites [23, 24].

Huang and co-authors [25] fabricated the composites of TiO$_2$ and epoxy by direct solution adding method, where directly epoxy and nanosized TiO$_2$ in the liquid form were mixed with the catalystmethyl isobutylketone. Based on the results obtained from XRD, the hydrogen bonds are formed by adding TiO$_2$ nanoparticles in epoxy resin. The Scanning Electron Microscopy result recommended that TiO$_2$ nanoparticles are uniformly distributed within the epoxy nanomaterial. The nanocomposite properties degrade if the nanofillers TiO$_2$ exceeds 3 wt.%. In addition, mechanical properties are enhanced by raising the concentration of catalyst such as methyl isobutylketone.

Elansezhian and co-workers [26] studied the wear and tensile strength behavior of vinyl ester with silica, alumina and zinc oxide nano fillers and reported that the addition of silica to the vinyl ester resin significantly improved wear resistance as compared to other two fillers. The functionalized silica nanoparticles showed an improved dispersion with vinyl ester resin. Functionalization caused particle dispersion more uniformly in the polymer matrix. As-received nanoparticles show lower tensile strength whereas functionalized nanoparticles show improved tensile strength by more than 15% at 5 wt.% loading as compared to unfilled resin.

Haque and co-authors [27] reported that the flexural strength of glass-vinyl ester-clay nanocomposites containing 1 wt.% nanoclay improved by 24% in comparison to conventional composites. The improvement in the mechanical properties of the nanocomposites mostly relies on achieving proper polymer/silicate layer (intercalated) or uniformly dispersed (exfoliated) morphology in the structure. It is observed that incorporation of higher percentage of nanoclay particles (> 2 wt.%) into the resin, may not improve mechanical properties.

Apoorva and co-authors [28] reported that tensile modulus of nanocomposites with nanoclay (cloisite 10A and Vinyl monomer) increases by about 25% with organically modified clay addition. The tensile modulus improved in the nanocomposites with Cloisite in a more effective manner. Whereas, at elevated clay load, cloisite 10A and Vinyl monomer clays emerge to execute uniformly good,

the mechanical strength appears to be marginally reduces with cloisite 10A nano-composites. Vinyl monomer clay nanocomposites prove a little diverse trend [28]. The little concentration of Vinyl monomer clayin the nanocomposite system, the tensile strength show to enhance and this enhance is dedicated to the chemical link created connecting Vinyl monomer clay's surface functionalization and Vinyl ester manacles through the process of curing, which is additional useful in transfer pressure to the nanoclay platelets compared to an unreactive clay such as cloisite 10A. The succeeding small fall in tensile strength at 1 wt.% and two and half weight percentage clay content was due to lack of proper distribution of clay.

The attempts have been made to fabricate nanoparticle filled epoxy nano-composites to progress the tribological properties of the base polymers. Recently, nanosized inorganic fillers such as nanometer sized Silicon Carbide (SiC), Silicon di-oxide (SiO_2), Zinc oxide (ZnO), Zirconium di-oxide (ZrO_2), Alumina (Al_2O_3) and Titaniam di-oxide (TiO_2) be used as nanofillers in epoxy to attain excellent tribological property [29, 30]. The main benefit of nanosized filler filled composites over micro-sized filler filled composites lie down in its performance development which is attained at comparatively small percentage of the nanofillers. At higher filler loadings, due to higher percentage of particles or atoms present on the surface of the nanofillers, agglomeration takes place very easily because of nonuniform dispersion of nanofillers in the polymer by using conventional mechanical mixing techniques [31]. This results in the poor performance of the nanocomposites at higher percentage of loading than the micro filler based composites system.

Many authors reported that, polymer composites is widely used in wear applications such as cams, brakes, bearings and gears due to their self-lubrication property, low co-efficient of friction and improved resistance to wear. The inborn shortage of polymers is changed profitably by using special micro fillers and nanosized particles. More polymer micro and nanocomposites are in use as sliding devices which were formerly made of metallic materials. On the other hand, extreme improvements are in progress to find out different areas of purpose to modify their properties for higher load-carrying and ecological conditions [32, 33].

Extensive work has been approved in the development of nanofiller composites through the addition of nanosized particles namely ceramics and carbon in polymer based matrices. For example surface modified nanoclays [34], carbon nanotubes [35], alumina [36] ZnO and SiC nanoparticles [37] are incorporated in to the base polymers. Majority of these cases are on the effect of filler particle in polymer composites descending against metallic surface results in decrease of rate of wear, friction co-efficient and larger mechanical strength which is owing to incorporation of nanofillers.

Recent reports on the wear behavior of surface modified nanoclay added polyamide6 (PA6) by Srinath and Gnanmoorthy [38] and Dasari and co-authors [39] has exposed lesser friction and higher rate of wear resistance, this is dedicated to the increase of the bond between nanofiller and the polymer matrix.

Nanofillers inclined to develop a persistent transmit layer on the opposite face which defends the nanocomposite sample outside surface from straight make contact with the opposite face thus reduces rate of friction and rate of wear. The incorporation of organically modified nanoclay into the base polymer matrix to formulate the nanocomposite is an alternative way to change the properties of composite material [40]. Ng and co-authors [41] directly dispersed TiO_2 nanoparticles in to the epoxy. The resultant composites appeared not only to be tougher than the traditional micro-particle filled epoxy but also to possess a higher scratch resistance. Rong and co-authors [42] also carried out wear trial on nanotitanium-epoxy nano-composites and studied that the tribological characteristics is importantly depends on the state of dispersion and homogeneity of the filler.

Shao Rong and co-authors [43] have proved that the epoxy/SiO_2-TiO_2 nanocomposites are effective in lowering the frictional coefficient and wear rate. The results of these experiments [43] indicate that the wear mechanism of composites changed from adhesive wear to mild abrasive wear and fatigue wear with the increase of the SiO_2-TiO_2 content. Chang and co-authors [44] have proved that the addition of nanoTiO_2 apparently reduced the frictional coefficient and significantly enhanced the wear resistance of the composites, especially at contact pressures and sliding velocities.

The present study incorporates different evaluation techniques to encompass properties of mechanical and wear characteristics.

2. Results and discussion

2.1 Density of the nanocomposites

Density is an important property in several weight sensitive applications. In many applications, polymer composites are replacing traditional or conventional metals and metal based composites mainly for their low densities. Density of a composite depends on the relative proportion of matrix and the reinforcing filler. There is always a difference between the measured and the theoretical density values of a composite due to the presence of empty space and hole. These empty spaces or voids majorly affect the performance of the nanocomposites. A larger void content indicates lower value of fatigue resistance, greater susceptibility to water penetration and weathering [45]. The theoretical and measured densities of nanocomposites along with corresponding volume fraction of voids are presented in **Table 1**. The theoretical density was calculated for nanocomposite samples by weight additive principle, which states that:

$$d = w_1 d_1 + w_2 d_2 \qquad (1)$$

where d is the density of the nanocomposite, w_1 and w_2 are the weight fractions of the fillers, epoxy and hardener, d_1 and d_2 are their corresponding densities. It

Samples (wt.%)		Density (g/cm^3)		Void fraction (%)
		Theoretical	Experimental	
Epoxy-oMMT	0	1.170	1.170	-
	2	1.184	1.176	0.65
	5	1.206	1.181	2.03
	7	1.221	1.182	3.13
Epoxy-TiO$_2$	2	1.231	1.222	0.73
	5	1.323	1.284	2.91
	7	1.384	1.294	6.50
Vinyl ester-oMMT	0	1.346	1.346	–
	2	1.351	1.347	0.29
	5	1.368	1.348	1.46
	7	1.379	1.349	2.14

Table 1.
Theoretical, experimental densities and void fractions in nanocomposites.
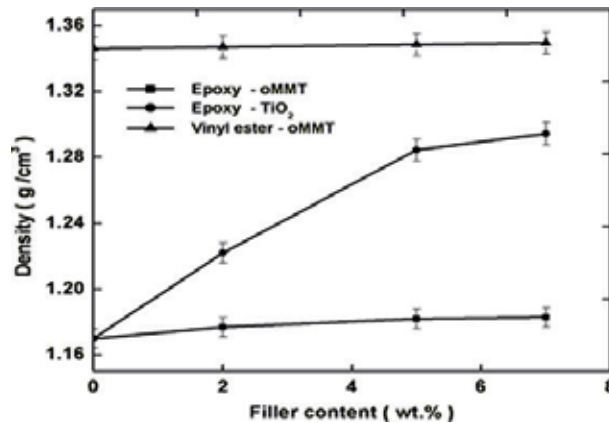
Figure 1.
Variation of density as a function of filler content for epoxy and vinyl ester nanocomposites.

may be noted from **Table 1** that density values of the nanocomposite calculated theoretically from weight fractions using Eq. (1) are not in agreement with the experimentally determined values. Theoretically calculated density values are larger when compared to equivalent experimental values due to empty space or voids and holes or pores.

The knowledge of void fraction is therefore essential for estimation of the quality of the composites. From the measured densities of Epoxy-oMMT, Epoxy-TiO_2 and Vinyl ester-oMMT nanocomposites (**Figure 1**), it is clear that pure Epoxy and Vinyl ester resin has an average density of 1.17 and 1.34 g/cm^3 with an error of ±0.0088 respectively. With the incorporation of oMMT and TiO_2 nanofillers, an increase in the density of the nanocomposites is observed. This is observed to be true in both Epoxy and Vinyl ester matrix with nanosized oMMT and TiO_2 filler inclusions.

It is evident from **Figure 1** that the density values for Epoxy-oMMT nanocomposite increases with the nanofiller loading content. However, the increase in the density was small in Epoxy-oMMT nanocomposites. With the addition of 7 wt.% oMMT, the density of Epoxy increases by 1% but the density of Epoxy-TiO_2 increases by 10%. This is due to higher density of TiO_2 as compared to oMMT. The density of Vinyl ester is higher than that of Epoxy due to the presence of bromine. Bromine is a heavy atom and there are four bromine atoms bonded in one molecule, and this result in density being higher for brominated Vinyl ester. Similar trends are noticed for Vinyl ester-oMMT nanocomposites.

2.2 Micro-hardness of the nanocomposites

Hardness is one of the significant factors that control the wear property of the composite samples. In this work, the data obtained for micro-hardness of the Epoxy and Vinyl ester composites with different types of weight percentage of fillers loading have been obtained. **Figure 2** shows the experimental results of measurements of micro-hardness of pure Epoxy and Epoxy-oMMT, Epoxy-TiO_2, pure Vinyl ester and Vinyl ester-oMMT nanocomposite samples with different weight percentage of nanofiller content.

Figure 2 indicates that the addition of oMMT nanofiller into Epoxy, Vinyl ester and TiO_2 to Epoxy results in significant improvement in hardness of nanocomposites. In general, mechanical properties of nanocomposite depend primarily on following things namely filler content, filler size and shape, the degree of interfacial
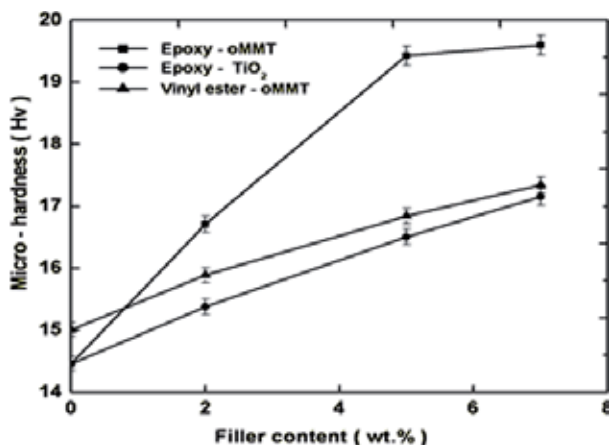
Figure 2.
Micro-hardness of epoxy and vinyl ester nanocomposites.

interaction or between the filler particles and polymer matrix and degree of dispersion of nanofiller within the polymer matrix. The improvement in the hardness property of the nanocomposites may be attributed to the intercalated and exfoliated clay platelets structure [46].

The intercalated/exfoliated clay platelets effectively restrict indentation and increase the hardness of the nanocomposites [46]. Similarly, incorporation of TiO_2 into Epoxy increases the degree of dispersion, thereby increases the hardness of nanocomposite. Organomodified montmorillonite has a much greater surface hardness because of its ceramic nature. Therefore, the contribution of oMMT to the hardness is greater as compared to TiO_2 filled nanocomposites. From the observed data it is clear that the increment in hardness is more significant up to 5 wt.% of filler loading. The increase in hardness for 5 wt.% filled polymer matrix may be partly attributed to the intrinsic hardness of nanofiller and the nanoparticles might be offering better resistance against Epoxy and Vinyl ester segmental motion under indentation.

On the other hand, increase in filler loading from 5 to 7 wt.% and the rise in value of the hardness is trivial implying that higher filler loading gives rise to undesired dispersion and agglomeration in the polymer matrix. When in comparison with the oMMT and TiO_2 nanocomposites loading is concerned, the Epoxy-oMMT nanocomposite reveal greater hardness values for the different filler loadings are concerned. Among all the nanocomposites investigated maximum micro-hardness value is recorded for Epoxy nanocomposite filled with 7 wt.% oMMT.

2.3 Mechanical properties

The measured tensile properties of Epoxy-oMMT, Epoxy-TiO_2 and Vinyl ester-oMMT nanocomposites are shown in **Table 2**. It is noticed from the **Table 2** that, lower values of tensile strength and tensile elongation are obtained for nanocomposites than those of pure Epoxy and Vinyl ester. However, the Young's moduli are evidently enhanced by the addition of fillers. As seen in **Table 2**, the tensile strength of these nanocomposites invariably decreases with increase in filler loading irrespective of the type of filler. Similar observations have been reported by some investigators [47].

The tensile strength and fracture toughness of a nanocomposite samples depend upon the filler shape, size and amount which is mixed with the polymer matrix, the strong bond between the nanofiller and the polymer matrix, the robustness of the

polymer matrix and the filler. Nanofillers affect the mechanical properties in accordance with their packing characteristics, size and interfacial interaction. The highest three dimensional packing of filler reflects the size distribution and shapes of the particles. The space between the particles is implicit to be packed with polymer matrix and no empty spaces or air bubbles are expected. With this condition, for a given nanocomposite, the matrix amount is fewer and it acts as separate segment or compartment to hold up tensile load. Properties of nanocomposites are manipulated by the individual properties of the filler and the matrix and also the filler-matrix interface.

Ability of the matrix to transfer the load to the filler particles, is its major purpose, and depends on the adhesion and compatibility between the filler and matrix. The tensile strengths of the nanoparticles filled Epoxy are less than that of pure Epoxy/Vinyl ester. The decreasing trend of adhesion with respect to relatively higher filler loading points towards the phenomenon of dewetting occurs at the interface. The figure shows a close up view of matrix region where more particles are concentrated. There can be two reasons for the decline in the strength properties of the filled nanocomposites as compared to the pure polymers which is evident from data shown in **Table 2** and discussed below;

Samples (wt.%)		Tensile strength (MPa) ± 1.5%	Tensile modulus (GPa) ± 1.5%	Elongation at break (%) ± 2%
Epoxy-oMMT	0	47.50	1.44	10.39
	2	31.56	1.73	10.50
	5	37.95	1.90	11.30
	7	33.79	2.09	9.35
Epoxy-TiO$_2$	2	32.60	1.61	10.41
	5	36.91	1.72	10.98
	7	32.47	1.82	11.18
Vinyl ester-oMMT	0	71.10	3.49	2.54
	2	69.40	3.55	2.38
	5	66.21	3.74	2.22
	7	64.10	3.91	2.08

Table 2.
Mechanical properties of polymer nanocomposites.

In the present study, the tensile strength of all nanocomposites is much lower than that of pure Epoxy and Vinyl ester may be assumed to be closely related to processing method. The compounding of oMMT in an Epoxy matrix with high shear mixing produces a highly viscous and foamy material. A higher content of oMMT leads to higher viscosity. Furthermore, the diethyltoluenediamine used to functionalize Nanomer 1.30E can voluntarily contribute in the curing reaction and delamination of the clay platelets. This results in highly viscous fluid with time and hampers the complete removing of gas before the process of curing. The nanocomposites with 7 wt.% of oMMT, the removal of gas turn out to be more critical. The presence of small gas bubbles in 2, 5 and 7 wt.% oMMT nanocomposites confirms the same.

The additional reason for voids can be air entered during transfer of the largely gelatinous material into the mold. Furthermore, the tensile strength of all the samples in the range of 30–70 MPa indicates break initiation from analogous types of defects. Consequently, it might be understood that under loading condition, breaks may begin from these tiny spaces or voids and result in sample failure at

fairly low strains [48]. The other reason is that the corner points of the irregular shape of the spherical filler namely TiO_2 particulate, may result in stress concentration in the Epoxy matrix. These two factors are perhaps responsible for significant reduction in tensile strengths of the nanocomposites. A comparison of the results reveals that the Vinyl ester-oMMT nanocomposites possess higher tensile strength confirming the effect of incorporation of oMMT filler which improves nanofiller-matrix surface adhesion or interface in the composite.

The tensile modulus shows a marked increase with increasing oMMT, TiO_2 content from 0 to 7 wt.% in Epoxy and Vinyl ester matrices. The improvement in the Young's modulus can be attributed to the exfoliation and good dispersion of nano-sized filler particles that restricts the mobility of polymer chains under loading as well as good interfacial adhesion between the particles and the polymer matrix [49]. The orientation of clay platelets and polymer chains with respect to the direction of loading can also contribute to the reinforcement effects [49]. Unlike the Young's modulus, nanocomposites of any nanoclay content show a lower tensile strength than that of pure Epoxy. Similar results are reported by Zerda and co-authors [50] but in contrast, an increase in tensile strength values of nanocomposites are also reported [51, 52].

As reported in literature, the strain at break of nanocomposites usually declines with increasing filler content. Low filler loadings cause a significant drop in fracture strain. It may be recalled that the composite is made up of partly filler and partly matrix. Due to the rigid nature of the fillers, most of the deformation comes from the polymer. The actual deformation is experienced only by the polymer matrix which is much larger than the measured deformation of the sample. With the result, that the polymer failure reaches failure strain limit at lower level of total deformation. Hence, the total composite strain-to-break decreases. However, it is interesting to observe that nanocomposites of the present study show contrary results that is strain-to-break behavior as comparable to conventionally filled composites. It tends towards slightly higher values for filler content of less than 5 wt.% (**Table 2**).

This increase suggests that the nanoparticles are able to introduce additional mechanisms of failure and energy consumption without blocking matrix deformation. Particles may induce matrix yielding under certain conditions and may furthermore act as inhibitors to crack growth by pinning the cracks [15]. Nevertheless, if the fillers exceed 5 wt.%, the failure strain undergoes a slight decrease. Such a reduction leads to that the large proportion of fillers start dominating, and they reduce the matrix deformation by mechanical restraining.

The decrease in tensile strength and the upgrading of values of hardness with the filler addition is due to the following reasons: under the action of a mechanical (tensile) force, the interface between filler and polymer matrix will tend to debonding, depending on interfacial bond strength and this can direct to a break in the nanocomposite material. On the other hand, in case of hardness, pressing stress is in act. The matrix phase and the nanofiller phase would be hard-pressed together. Thus the interfacing bond can transfer pressure more effectively and thus there is an enhancement in the values of hardness.

2.4 Flexural properties

Table 3 lists the average values of flexural modulus for different weight percentages of oMMT and TiO_2 nanofillers. The flexural modulus of Epoxy resin is 2.30 GPa. The addition of oMMT and TiO_2 to Epoxy resin is expected to reinforce the resin and increase its elastic modulus and the results are on expected lines. The flexural modulus of nanocomposites shows increase with oMMT and TiO_2 concentrations. For 7 wt.% of oMMT and TiO_2 loading, improvement in the flexural

Samples (wt.%)		Flexural modulus (GPa) ± 1.5%	% change	Flexural strength (MPa) ± 1.5%	% change
Epoxy-oMMT	0	2.30	—	89	—
	2	2.34	1.70	91	2.20
	5	2.57	10.50	95	6.31
	7	2.69	14.49	100	11.0
Epoxy-TiO$_2$	2	2.52	8.73	96	7.29
	5	2.85	24.12	102	12.74
	7	3.07	33.77	105	15.23
Vinyl ester-oMMT	0	3.56	—	99	—
	2	3.79	6.06	63	36.36
	5	4.05	12.09	56	43.43
	7	4.26	16.43	45	54.54

Table 3.
Flexural properties of the polymer nanocomposites.

modulus is 14 and 33% respectively. The addition of 7 wt.% oMMT into Vinyl ester increases the flexural modulus by 16% and the flexural strength of Epoxy resin and Vinyl ester resin are observed to be 89 and 99 MPa respectively. The maximum improvement in the flexural strength is observed with the addition of 7 wt.% oMMT and TiO$_2$ and it is 11 and 15% as compared to pure polymer. Significant improvement in the flexural strength of around 54% is observed at 7 wt.% Vinyl ester-oMMT nanocomposite.

The gradual increase in flexural strength and modulus, of nanocomposites, reveals that mechanical stresses are efficiently transferred via the interface. The significant uniqueness of nanocomposites is considered to explain this phenomenon about quality of the interface in the nanocomposites, (static adhesion strength) usually take part in significant responsibility in the materials' capability to convey stresses and elastic deformation from the base polymer matrix to nanofillers [15, 16].

This is correct for nanofillers filled composites, because they have high part of interfacing. If the interaction between filler and matrix is poor, then filler particles are not capable of carrying out any part of the outside weight. Further, the power of the nanocomposite will not be superior as compared to that of pure polymer matrix. Instead of this, if the fillers and matrix bond is strong, then the tensile strength of composite can be higher than that of polymer matrix [15, 16]. The comparison of the results reveals that Vinyl ester-oMMT nanocomposite shows higher flexural strength and modulus.

2.5 Friction and dry sliding wear behavior

In **Figure 3**, the variation of the coefficient of friction can be observed for the three nanocomposite materials, as a function of the sliding distance, for load of 30 N and sliding velocity of 1 m/s. Initially, an increase in friction coefficient is associated with the initial running-in period is observed. After the initial running-in period the friction coefficient stabilizes as a function of sliding distance. Epoxy-TiO$_2$ shows lesser coefficient of friction, followed by Epoxy-oMMT. Among the three nanocomposite systems studied, pure Epoxy shows higher coefficient of friction for all the sliding distances.
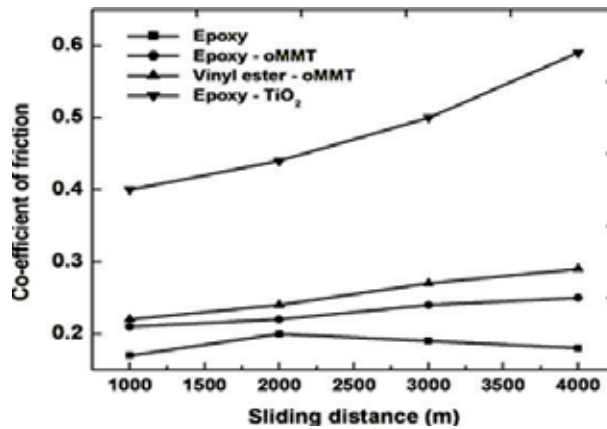
Figure 3.
Coefficient of friction of 5 wt.% filler filled polymer nanocomposites.
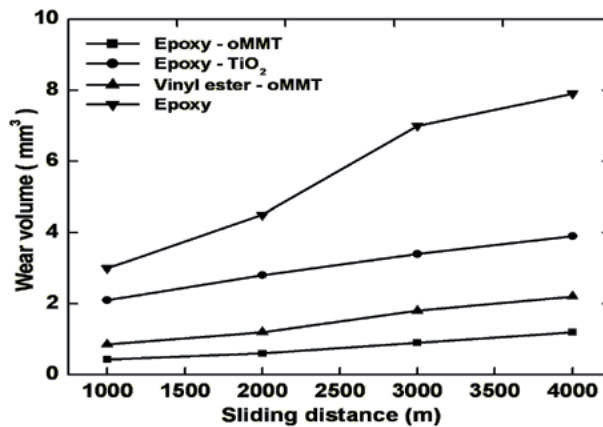
Figure 4.
Wear volume as a function of sliding distance of 5 wt.% filler filled polymer nanocomposites.

The variation of wear volume as a function of sliding distance is shown in **Figure 4**, for the three nanocomposites, for load of 30 N and sliding velocity of 1 m/s. As seen in the **Figure 4**, a linear increase of the wear volume loss as a function of the sliding distance is observed. This increase is more significant for the pure Epoxy. Nanoparticles filled polymer composites such as Epoxy-oMMT, Epoxy-TiO$_2$ and Vinyl ester-oMMT have shown a lesser wear volume loss during the sliding processes.

The wear volume and specific wear rate (K$_s$) as a function of sliding distance for pure Epoxy and oMMT filled Epoxy nanocomposites are shown in **Figures 5** and **6** respectively. From **Figure 5**, it is observed that the wear volume loss increases with increase in sliding distance for all the nanocomposites. Wear volume loss showed an upward trend in the gradient, as the sliding distances were increased in case of pure Epoxy (**Figure 5**). The sliding over a pure epoxy surface with a flat steel, the counter surface of which is ground to a roughness of 0.25–0.30 μm (arithmetic mean) under a load of 30 N and at a velocity of 1 m/s, resulted in a specific wear rate of 10.54 × 10^{-5} mm^3/Nm for 1000 m sliding distance (**Figure 6**).

The result obtained possibly may be due to enhanced temperature occurs for the duration of the process of wear. The wear resistance varies in the order of weight percentages as follows; 5 > 2 > 7 > 0% by weight of oMMT filler in polymer matrix. It is clear from the data in the **Figure 6** that the specific wear rate value of pristine
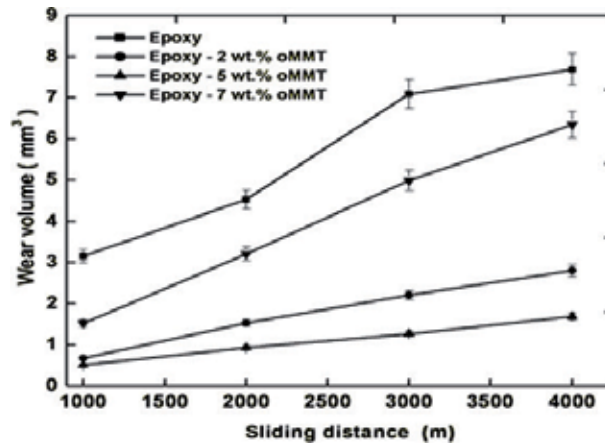
Figure 5.
Wear volume as a function of sliding distance of pure epoxy and oMMT filled epoxy nanocomposites.
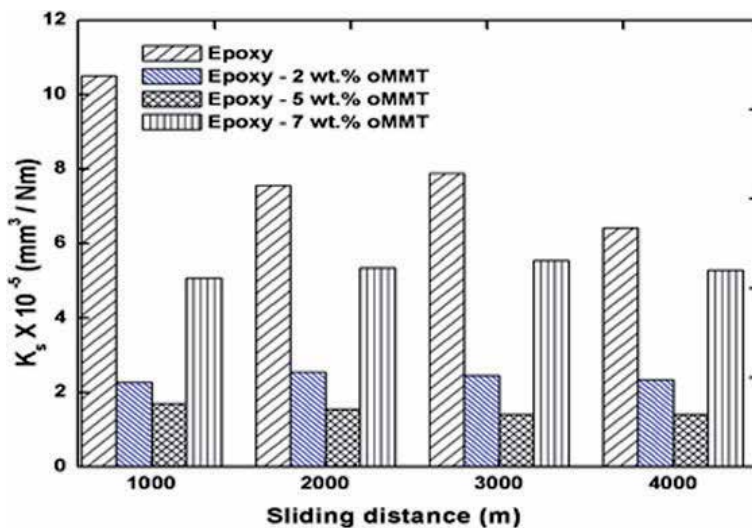
Figure 6.
Specific wear rate as a function of sliding distance of pure epoxy and oMMT filled epoxy nanocomposites.

Epoxy be linear up to 2000 m and rises nonlinearly up to 4000 m. The specific wear rate of oMMT nanofillers filled Epoxy nanocomposites decreases linearly with increase in sliding distances except in the case of 7 wt.%. Epoxy resin with 5 wt.% of nanofillers (oMMT) has the smallest specific wear rate, whereas specific wear rate of pristine Epoxy rises above 5 wt.%. This is due to the poor interaction or adhesion Epoxy matrix nano-particles and the accumulation of the nanoparticles at 7 wt.% filler content.

The incorporation of 5 wt.% of oMMT in Epoxy, results in decrease in specific wear rate by 70–80%. The tendency is in agreement with that of the tensile strength and hardness results and is listed in **Table 2** and **Figure 2** respectively. It is well known that majority of micro-fillers used are generally very successful in the reduction the wear property of different polymers. In the pristine Epoxy, wear trash consists of deformed polymer matrix containing broken down and powdered matrix particles and wear powder of the metallic opposite surface. The constituent parts can either be lost from the contact region or stay there for unchanging time as a

"transport layer." In such cases, the polymer constituent can cushion the opposite surface and reduces the toughness, but the broken matrix particles and wear powder of the metallic opposite surface will take steps as a third body abrasive guiding to increase the abrade of the opposite surface. Thus, specific wear rate of the pristine Epoxy depend on presence of various elements in the wear trash. During the process of wear, no film was formed on the opposite surface and thus maximum specific wear rate was observed in pristine Epoxy.

The wear volume loss is low for oMMT filled Epoxy nanocomposites as compared to pure Epoxy. At the beginning of sliding, the two surfaces of all the asperities are in contact with each other. When shear forces are applied, the asperities get deformed. The oMMT particles protrude out from the surface of the sample and initially, the Epoxy matrix wears out and only oMMT nanoparticles remain in contact with the countersurface. As sliding distance increases, the wear rate starts decreasing and the oMMT nanoparticles wear out the steel countersurface. Due to extreme hardness of the countersurface, oMMT nanoparticles adhere to the matrix and excess filler concentration is observed on the exposed composite surface after prolonged sliding. During sliding, a rolling effect of nanoparticles may reduce the shear stress, the frictional coefficient, and the contact temperature.

For the oMMT filled Epoxy nanocomposites, a three-body contact condition is induced by the addition of nanoparticles between the contact surfaces, which is evidenced by presence of the grooves on the worn surfaces (**Figure 8a** and **b**). Hence, it is proposed that during the sliding process, many of the hard particles are embedded in the soft polymeric transfer film on the counter surface which creates grooves on the sample surface. In this way, the distance between the countersurface and the sample gets enhanced, i.e., the particle act like as spacers. This in turn, can cause reduction in the adhesion between the contacting surfaces. Therefore, the coefficient of friction of oMMT filled Epoxy is always less than that of pure Epoxy. Moreover, as the nanoparticles are free to move and they tend to be dispersed uniformly over the transfer film during the wear process. This can result in a more uniform contact stress between the contact surfaces and in turn minimizes the stress concentration [53–55].

In the present work, the wear-resistant of Epoxy nanocomposite filled with small size oMMT particles (<40 nm) transfers well to the counterface and its transfer film is thin, uniform and adheres strongly to the countersurface. Thus, the improvement in the tribological behavior of Epoxy-oMMT nanocomposite is related to the improved characteristics of the transfer film.

2.6 Morphology of wear affected surface

SEM assessment of worn surfaces of pure base resin and organically modified montmorillonite nanoclay (oMMT) added nanocomposites against metal counter surface with a load of 30 N and sliding velocity of 1 m/s are given in **Figures 7a**, **b** and **8a, b** respectively. **Figure 7a** and **b** represents the features worn surfaces of base resin. Projectile marked depicts the direction of sliding. At lesser enlargement, the worn surface is moderately rough and allied with micro-cracks in the epoxy (**Figure 7a**). The advanced microscopy image indicates (**Figure 7b**), break to the epoxy matrix is elevated ensuing in extra base material elimination from the nanocomposite surface. The loss and contact temperature are significantly enlarged, leading to increase in fracture of the base epoxy near the region of interface.

The interface surface break extremely increases with channel by the Epoxy removed (**Figure 7b**). A comparison of results of **Figure 7a** and **b**, indicates that the damaged outside surfaces are highly smoother at the mentioned sliding conditions and separation of matrix is very much limited with the content of organically modified montmorillonite nanoclay particles. **Figure 8** indicates shape and size of the wear debris
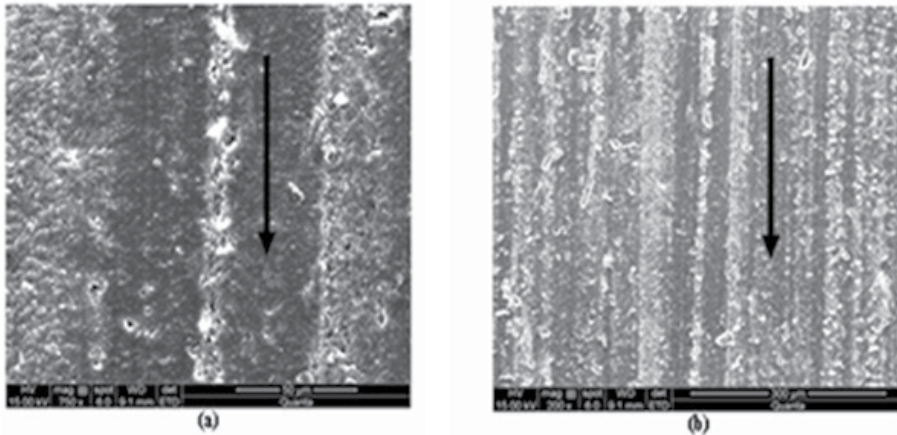
Figure 7.
Scanning electron micrograph of pure epoxy at 30 N, 1 m/s. (a) Lower magnification and (b) higher magnification.
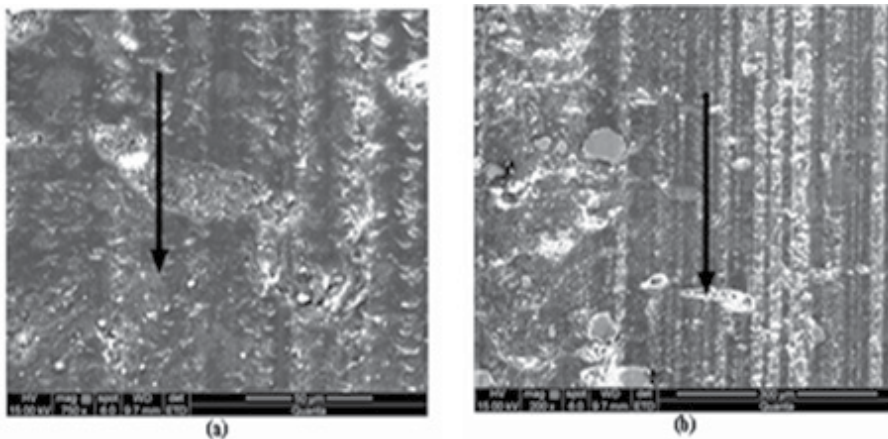
Figure 8.
Scanning electron micrograph of 5 wt.% oMMT filled epoxy at 30 N, 1 m/s. (a) Lower magnification and (b) higher magnification.

and debris shape changes for organically modified nanoclay composite. The shape of the debris changes to spherical and finer in comparison to that seen in **Figure 7** when the nanofillers were not present. These small or fine particles build up marks of dense material as seen in **Figure 8a** and **b**. Enlarged magnification (**Figure 8b**) shows the makeup of the packed material formed by addition of the wear debris.

The surface worn is comparatively soft and illustrated by surface damage due to fatigue, usually taken places at elevated temperatures and eliminates the surface deposit by microcracks. A space consists of worn out particle are held jointly by thermal and mechanical processes implicated in sliding, particularly roughing due to frictional heat, and compression due to the load applied. Consequently, due to the adding up of Organically Modified Montmorillonite nanoclay (oMMT) nanoparticles, outside surface reliability is preserved in the polymer matrix with a steady process of wear is taking place even at elevated load and velocity situations and thus guide to an increased load bearing capability of the nanocomposite. In addition, for nanocomposite samples, the width of traces of the wear for the nanocomposites throughout the process of sliding was considered using scanning electron microscope.

The highest and lowest trace width for the pristine Epoxy resin is 50 and 25.35 μm correspondingly. In the case of, 5 wt.% of organically modified Monmorillonite nano-clay (oMMT) filled Epoxy nanocomposite, the width of the trace is 27.69–18.46 μm respectively. It was accomplished from the width of the trace that organically modified Monmorillonite nanoclay (oMMT) filled Epoxy nanocomposite has the smallest width of trace and consequently observed that improved resistance to wear.

2.7 Characteristics of Wear by analysis using Taguchi method

The research results were studied by Taguchi method and important factors affecting rate of wear are identified. The results of the Taguchi analysis are listed in **Table 4** and in **Figure 9**.

Test run	Velocity (A) m/s	Load (B) N	Filler content (C) %	Distance (D) (m)	K_s (mm³/Nm) × 10^{-5}	S/N ratio (db)
1	0.5	10	0	1000	3.41	89.34
2	0.5	20	2	2000	2.97	90.54
3	0.5	30	5	3000	4.70	106.55
4	1.0	10	2	3000	2.00	94.00
5	1.0	20	5	1000	2,54	91.90
6	1.0	30	0	2000	8.40	101.51
7	1.5	10	5	2000	2.99	90.48
8	1.5	20	0	3000	8.50	101.41
9	1.5	30	2	1000	4.51	86.91

Table 4.
Experimental design (L₉ orthogonal array) with output and S/N ratio.
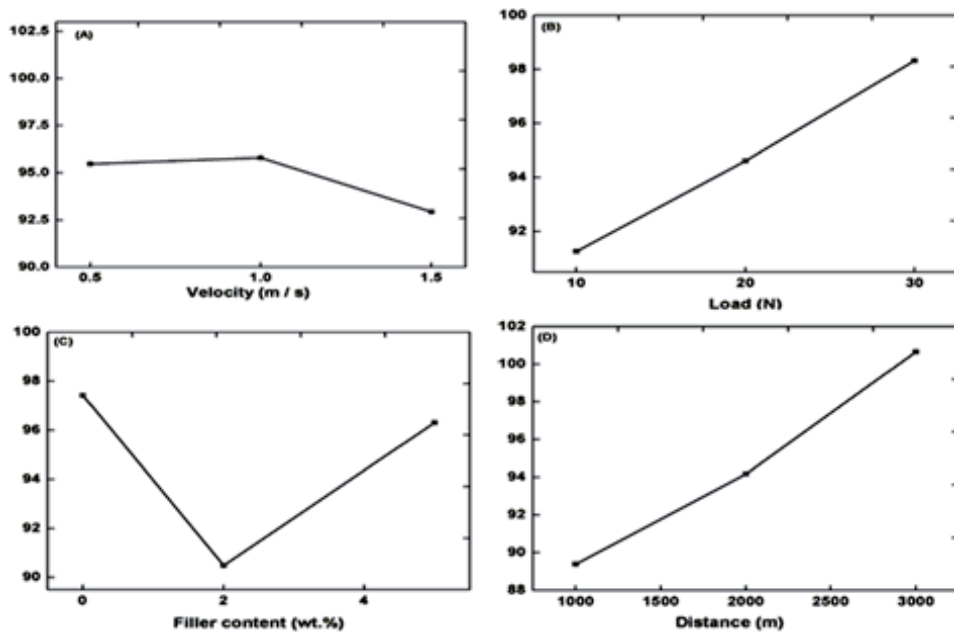
Figure 9.
Effect of control factors on specific wear rate of epoxy-oMMT nanocomposites.

Level	(A) Velocity	(B) Load	(C) Filler content	(D) Distance
1	95.48	91.27	97.42	89.94
2	95.80	94.62	90.48	94.18
3	92.94	98.33	96.32	100.65
Delta	2.86	7.05	6.94	11.26
Rank	4	2	3	1

Table 5.
Response table for signal to noise ratios.

From **Table 4** the overall mean for the S/N ratio of the wear rate is found to be 85.264 db. **Figure 9** shows the effect of the three control parameters on particular rate of wear. The analysis was made using MINITAB 15, a popular software tool particularly used for plan of experimental applications.

The probable interactions among the control parameters have to be taken into account before any effort is made to utilize this model as a predictor tool for the monitoring of performance.

The S/N ratio result are listed in **Table 5**, it is concluded from table that amid every single one of the parameters, sliding distance is mainly important factor subsequently normal load and content of the filler while the velocity of the sliding has the smallest amount to the rate of the wear of the organically modified montmorillonite nanoclay (oMMT) added nanocomposite.

Investigation of the outcomes guides to the conclusion that combination of factors A_2, B_3, C_1 and D_3 gives minimum specific wear rate as shown in **Figure 9**.

3. Conclusions

This study shows that a fair degree of success has been achieved in production of pristine base Epoxy resin and organically modified nanoclay (oMMT) and TiO_2 added base Epoxy resin and Vinyl ester nanocomposites. The mechanical and tribological properties of the pristine Epoxy and organically modified nanoclay (oMMT) and Titania (TiO_2) added nanocomposites have been analyzed by series of tests and also by means of Taguchi's design of experiment technique. The following conclusions were drawn from the research work:

i. Incorporation of nanofillers modifies the tensile and flexural strengths of the composites both for Epoxy as well as for Vinyl ester matrix.

ii. The mechanical strength, modulus, hardness and physical density of the epoxy based nanocomposites are very much influenced by the nano filler type and content.

iii. The nanoparticles filled Epoxy composites possess higher hardness values as compared to the Vinyl ester-oMMT nanocomposites.

iv. The tensile strength of the Epoxy-oMMT, Epoxy-TiO_2 and Vinyl ester-oMMT nanocomposites decreases with increase in oMMT and TiO_2 content, whereas, the hardness and modulus increased with filler loading into the matrix.

v. The oMMT filler has the ability to replace TiO_2 in some applications where high load bearing capabilities are not required.

vi. Fabrication of polymer nanocomposite of specific requirements, there is a need for the choice of appropriate nanofiller material for optimizing the properties of the composite system.

vii. The tribological results of pristine Epoxy and organically modified nanoclay (oMMT) filled nanocomposites are in the arranged susequently: Epoxy < Epoxy-7 wt.% oMMT < Epoxy-2 wt.% oMMT < Epoxy-5 wt.% oMMT. From the assessment of deviation in specific wear loss and wear rate, with larger sliding space, the abrasive wear mechanisms can control the interfacial interaction between the surfaces in contact. In this state, wear resistance of pristine polymer possibly is improved by adding the epoxy with organically modified nanoclay (oMMT) nanofiller.

viii. Evaluation are conducted on the wear behavior, where 5 wt.% of organixally modified nanoclay (oMMT) added polymer nanocomposites samples illustrate enhanced results in contrast with pristine polymer Epoxy and other samples with higher filler content.

ix. Dry sliding wear result of nanocomposites over different loads and different velocities can be effectively studied using Taguchi's experimental design technique. Taguchi's technique gives easy, organized and proficient technique for deciding the factors of control.

x. Sliding distance come out as the important factor which affects rate of wear of Organically modified nanoclay (oMMT) filled nanocomposites, other parameters such as specific load, nanofiller content and sliding distance and velocity have taken part in a considerable position in finding the specific wear rate (K_s).

Author details

Rashmi Aradhya* and Nijagal M. Renukappa
Siddaganga Institute of Technology, Tumkur, Karnataka, India

*Address all correspondence to: rash_mysore@sit.ac.in;
rash_mysore@yahoo.com

IntechOpen

References

[1] Dennis HR, Hunter DL, Chang D, Kim S, White JL, Cho JW, et al. Polymer. 2001;**42**:9513-9522

[2] Usuki A, Kojima Y, Kawasumi M, Okada A, Fukushima Y, Kurauchi T, et al. Synthesis of nylon 6-clay hybrid. Journal of Materials Research. 1993;**8**:1179-1184

[3] Messersmith PB, Giannelis EP. Synthesis and characterization of layered silicate - epoxy nanocomposites. Chemistry of Materials. 1994;**6**: 1719-1725

[4] Wang K, Chen L, Wu J, Toh ML, He C, Yee FA. Epoxy nanocomposites with highly exfoliated clay, mechanical properties and fracture mechanisms. Macromolecules. 2005;**38**:788-800

[5] Ji G, Li G. Effects of nanoclay morphology on the mechanical, thermal, and fire-retardent properties of vinyl ester based nanocomposite. Materials Science and Engineering: A. 2008;**498**:327-334

[6] Kotsilkova R. Processing-structure properties relationships of mechanically and thermally enhanced Smectite/epoxy Nanocomposites. Journal of Applied Polymer Science. 2005;**97**:2499-2510

[7] Qi B, Zhang QX, Bannister M, Mai Y. Investigation of the mechanical properties of DGEBA - based epoxy resin with nanoclay additives. Composite Structures. 2006;**75**:514-519

[8] Tsai JL, Hsu SM. Investigating mechanical properties of epoxy/ organoclay nanocomposites. Journal of the Chinese Institute of Engineers. 2008;**31**:09-16

[9] Yasmin A, Luo JJ, Abot JL, Daniel IM. Mechanical and thermal behavior of clay/epoxy nanocomposites. Composites Science and Technology. 2006;**66**:2415-2422

[10] Dean DR, Walker R, Theodore M, Hampton E, Nyairo E. Chemorheology and properties of epoxy/layered silicate nanocomposites. Polymer. 2005;**46**:3014-3021

[11] Isik I, Yilmazer U, Bayram G. Impact modified epoxy/montmorillonite nanocomposites: Synthesis and characterization. Polymer. 2003;**44**:6371-6377

[12] Akbari B, Bagheri R. Deformation mechanism of epoxy/clay nanocomposite. European Polymer Journal. 2007;**43**:782-788

[13] Kaya ED. Development of epoxy/ clay nanocomposites. IYTE Thesis of Master of Science; 2006

[14] Velmurugan R, Mohan TP. Room temperature processing of epoxy-clay nanocomposites. Journal of Materials Science. 2004;**39**:7333-7339

[15] Yasmin A, Abot JL, Daniel IM. Processing of clay/epoxy nanocomposites by shear mixing. Scripta Materialia. 2003;**49**:81-86

[16] Basara C, Yilmazer U, Bayram G. Synthesis and characterization of epoxy based nanocomposites. Journal of Applied Polymer Science. 2005;**98**:1081-1086

[17] Zhu M, Xing Q, Adler HJ. Preparation of PA6/nano titanium dioxide (TiO_2) composites and their spinnability. Macromolecular Symposia. 2004;**210**:251-261

[18] Mina F, Seema S, Matin R, Rahaman J, Sarker RB, Gafur A, et al. Improved performance of isotactic polypropylene/titanium dioxide composites, effect of processing conditions and filler content. Polymer Degradation and Stability. 2009;**94**:183-188

[19] Dean KM, Bateman SA, Simons RA. Comparative study of UV active silane grafted and ion-exchanged organo-clay for application in photocurable urethane acrylate nano and micro-composites. Polymer. 2007;**48**:2231-2240

[20] Ha SR, Ryu SH, Park SJ, Rhee KY. Effect of clay surface modification and concentration on the tensile performance of clay/epoxy nanocomposites. Materials Science and Engineering A. 2007;**448**:264-268

[21] Ha SR, Ryu SH, Park SJ, Rhee KY. Fracture performance of clay/epoxy nanocomposites with clay surface-modified using 3 aminopropyltriethoxysilane. Colloids and Surfaces, A: Physicochemical and Engineering Aspects. 2008;**313-314**:112-115

[22] Wang L, Wang L, Chen L, Zhang YW, He CB. Preparation, morphology and thermal/mechanical properties of epoxy/nanoclay composite. Composites Part A Applied Science and Manufacturing. 2006;**37**:1890-1896

[23] Lam CK, Lau KT, Cheyung HY, Ling HY. Effect of ultrasound sonication in nanoclay clusters of nanoclay/epoxy composites. Materials Letters. 2005;**59**:1369-1372

[24] Lam CK, Cheyung HY, Lau KT, Zhou LM, Ho MW, Hui D. Cluster size effect in hardness of nanoclay/epoxy composites. Composites Part B: Engineering. 2005;**36**:263-269

[25] Huang JF, Manson A, Hertzberg RW, Miller GA, Sperling LH. Structure- property relationships in rubber-toughened epoxies. Polymer Engineering and Science. 1989;**29**:1466-1476

[26] Elansezhian R, Saravanan L. Effect of nano silica fillers on mechanical and abrasive wear behavior of vinyl ester resin. The International Journal of Applied Research in Mechanical Engineering. 2011;**1**:105-108

[27] Haque A, Hussain F, Dean D, Shamsuzzoha M. S2-glass/vinyl ester polymer nanocomposites, manufacturing, structures, thermal and mechanical properties. Journal of Composite Materials. 2003;**37**: 1821-1837

[28] Shah AP, Rakesh Gupta K, Gangarao HVS, Powel CE. Moisture diffusion through vinyl ester nanocomposites made with montmorillonite clay. Polymer Engineering and Science. 2002;**42**:1852-1863

[29] Avella M, Errica ME, Martuscelli E. Novel PMMA/CaCO$_3$ nanocomposites abrasion resistant prepared by an in situ polymerization process. Nano Letters. 2003;**1**:213-217

[30] Zhao LX, Zheng LY, Zhao SG. Tribological performance of nano-Al$_2$O$_3$ reinforced polyamide 6 composites. Materials Letters. 2006;**60**:2590-2593

[31] Chang L, Zhang Z, Breidt C, Friedrich K. Tribological properties of epoxy nanocomposites, I. enhancement of the wear resistance by nano-TiO$_2$ particles. Wear. 2005;**258**:141-148

[32] Winkler J, Klinke E, Sathyanarayana MN, Dulog L. Theory for the De agglomeration of pigment clusters in dispersion machinery by mechanical forces II. Journal of Coatings Technology. 1987;**59**:45-53

[33] The PL, Mohad Ishak ZA, Hasim AS, Karger-Kocsis J, Ishiaku US. Effects of epoxidized natural rubber as a compatibilizer in melt compounded natural rubber- organoclay nanocomposites. European Polymer Journal. 2004;**40**:2513-2521

[34] Shanmuharaj AM, Bae JH, Lee KY, Noh WH, Lee SH, Ryu SH. Physical and chemical characteristics of multiwalled carbon nanotubes functionalized with aminosilane and its influence on the properties of natural rubber composites. Composites Science and Technology. 2007;**67**:1813-1822

[35] Shi G, Zhang MQ, Rong MZ, Wetzel B, Friedrich K. Sliding wear behavior of epoxy containing nano-Al_2O_3 particles with different treatments. Wear. 2004;**256**:1072-1081

[36] Zhang ZZ, Su FH, Wang H, Jiang W, Men XH, Liu WM. Study on the friction and wear properties of carbon fabric composites reinforced with micro and nanoparticles. Materials Science and Engineering A. 2005;**404**:251-258

[37] Bahadur S, Gong D, Anderegg JW. The transfer and wear of nylon and CuS-nylon composites, filler proportion and counterface characteristics. Wear. 1993;**162-164**:397-406

[38] Srinath G, Gnanmoorthy R. Effects of organoclay addition on the two body abrasive wear characteristics of polyamide 6 nanocomposites. Journal of Materials Science. 2005;**40**:8326-8333

[39] Dasari A, Yu ZZ, Mai YW, Hu GH, Varlet J. Clay exfoliation and organic modification on wear of nylon 6 nanocomposites processed by different routes. Composites Science and Technology. 2005;**65**:2314-2328

[40] LeBaron PC, Wang Z, Pinnavaia TJ. Polymer-layered silicate nanocomposites, an overview. Applied Clay Science. 1999;**15**:11-29

[41] Ng CB, Scbadler LS, Siegel RW. Synthesis and mechanical properties of TiO_2-epoxy nanocomposites. Nanostructured Materials. 1999;**12**:507-510

[42] Rong MZ, Zhang MQ, Liu H, Zeng H, Wetzel B, Friedrich K. Microstructure and tribological behavior of polymeric nanocomposites. Industrial Lubrication and Tribology. 2001;**53**:72-77

[43] Lu S-R, Jing-Hongyu H-LZ, Wang X-y. Wear and mechanical properties of epoxy/SiO2-TiO2 composites. Journal of Materials Science. 2005;**40**:2815-2821

[44] Chang L, Zhang Z, Ye L, Friedrich K. Tribological properties of high temperature resistant polymer composites with fine particles. Tribology International. 2007;**40**:1170-1178

[45] Ber BB, Agarwal LJ. Analysis and Performance of Composites. 2nd ed. John Wiley and Sons, Inc; 1990

[46] Schadler LS, Brinson LC, Sawyer WG. Polymer nanocomposites, a small part of the story. Journal of Materials. 2007;**59**:53-60

[47] Farzana H, Jihua C, Mehdi H. Epoxy-silicate nanocomposites: Cure monitoring and characterization. Materials Science and Engineering. 2007;**A445-446**:467-476

[48] Liu X, Wu Q. Modern approach for study and analysis of composite polymer materials. Polymer. 2001;**42**:10013-10019

[49] Kormann X, Berglund LA, Sterte J. Anisotropic behavioral approach for materials. Polymer Engineering and Science. 1998;**38**:1351-1358

[50] Zerda AS, Lesser AJ. Intercalated clay nanocomposites: Morphology, mechanics and fracture behavior. Journal of Polymer Science Part B: Polymer Physics. 2001;**39**:1137-1146

[51] Zhang M, Zeng H, Zhang L, Liu L, Lin G, Li RKY. Fracture characteristics of discontinuous carbon

fibre-reinforced PPS and PES-C
composites. Polymer Composites.
1993;**1**:357-365

[52] Wu CL, Zhang MQ, Rong MZ,
Friedrick K. Tensile performance
improvement of low nanoparticles
filled-polypropylene composites.
Composites Science and Technology.
2002;**62**:1327-1340

[53] Suresha B, Chandramohan G,
Sampathkumaran P, Seetharamu S.
Investigation of the friction and wear
behavior of glass–epoxy composite with
and without graphite filler. Journal of
Reinforced Plastics and Composites.
2007;**26**:81-93

[54] Suresha B, Chandramohan G,
Prakash JN, Balusamy V,
Sankaranarayanasamy K. The role
of fillers on friction and slide wear
characteristics in glass–epoxy
composite systems. Journal of Minerals
and Materials Characterization and
Engineering. 2003;**5**:87-101

[55] Suresha B, Chandramohan G,
Renukappa NM, Siddaramaiah.
Mechanical and tribological properties
of glass–epoxy composites with and
without graphite particulate filler.
Journal of Applied Polymer Science.
2007;**103**:2472-2480

Chapter 12

Copper Bimetals and Their Nanocomposites

Hussein Shokrvash, Rahim Yazdani Rad, Abouzar Massoudi and Reza Shokrvash

Abstract

This chapter deals with the study of the electrolysis synthesis of copper matrix nanocomposites developed for the fabrication of nanoparticulate Cu-bimetals. In this chapter, we describe the successful synthesis of Cu matrix nanocomposites by the electro-deoxidation method. We think that this approach will make it possible to realistically integrate a series of copper-bimetals. This study makes a significant contribution to the literature because this method opens novel opportunity to the design of nanocomposite materials. Particularly, this opens up prospects for designing the new materials from immiscible metallic elements, which is the main topic in designing of alloys as well as materials science progression.

Keywords: copper bimetals, immiscible metals, nanocomposites, nanoalloys, electrosynthesis

1. Introduction

Copper is widely used for electronic and thermal devices due to its excellent electrical and thermal conductivity, as well as corrosion resistance and ease of fabrication [1]. Its application is limited due to poor mechanical properties and high coefficient of thermal expansion [2, 3]. Along with rapidly growing technologies, demand for new materials which could meet the technological needs quickly increases. Therefore, scientists are looking for materials that are able to meet the new demands presented by operating conditions in the high-tech applications [4–7].

Some of optimal properties are the high strength-to-weight ratio, high conductivity, and thermal stability. Traditional commercial Cu alloys can achieve these functions but show limitations which include lower specific strength and high density which impact negatively on structural applications. The Cu bimetals are the foundation of high-strength materials without any compromise in electrical conductivity. They are becoming a research focus on how to extend the solubility of immiscible metallic elements in copper which will increase the strength and without losing conductivity.

The solubility of elements in bulk phases commonly limited to equilibrium states, which is defined as an element might dissolve in the structure of the metal. Since the optimum performance in multiphase materials cannot be gained, the development of synthesis methods is inevitable for improvements of the solid solubility [8–12].

Recent progress in nanoscience has led to the great breakthroughs in the material fields and broad foundation in nanomaterials and processing technologies [13–17].

The synthesis and upscaling nanomaterials to bulk products fulfilled through direct manipulation of atoms and molecules with using of new approaches and precise assembling which leads to the emergence of novel multi-component nano-structures. The capabilities of nanotechnology open up exciting new prospects for the design of monolithic materials from immiscible elements which have a positive enthalpy of formation [18–22].

2. Aspect of thermodynamics

As a thermodynamic principle, all binary systems are divided into two groups: those with positive heat and those with a negative heat of formation. The negative enthalpy of formation symbolizes a mutual solubility of elements [23]. The same applies to the intermetallic compounds. If one or more intermetallic compounds occur in the phase diagram, or if there is a significant solid solubility between the given elements, an enthalpy of negative detection is expected. If none of the conditions are satisfied, it is expected to be positive enthalpy [24]. **Figure 1** shows collections of immiscible binary systems which have a positive enthalpy of formation. Based on the Hume-Rothery rules [26], synthesis of the homogeneous bulk alloys from immiscible metals infeasible and increase one of the elements leads to the formation of a new phase.

Cu bimetals are the most important immiscible binary systems used in magnetic, mechanical, thermal, and energy systems. The strength of copper increased by adding nonsoluble elements at the expense of electrical conductivity. This can be mitigated by choosing the alloying elements with little or no solubility in copper

	Ti	V	Cr	Mn	Fe	Co	Ni	Cu	Zn	Nb	Mo	Ru	Rh	Pd	Ta	W	Re	Os	
Ti	0	37	-372	-277	-418	-386	-435	-147	-198	11	-167	-763	-790	-648	31	-82	-189	-713	Ti
V	37	0	-88	-286	-176	-199	-250	13	-51	-56	-127	-321	-393	-275	-122	-97	-148	-361	V
Cr	-372	-88	0	-110	-8	5	-30	108	44	47	42	4	-129	-82	-130	26	4	-22	Cr
Mn	-277	-286	-110	0	9	-19	-115	29	-25	-153	-138	-15	-188	-251	-254	-92	-139	-40	Mn
Fe	-418	-176	-8	9	0	-60	-97	65	-23	-2505	-484	41	-57	-116	-3468	-554	-25	11	Fe
Co	-386	-199	5	-19	-60	0	-21	54	-58	-178	-52	52	12	-10	-253	-84	-72	34	Co
Ni	-435	-250	-30	-115	-97	-21	0	-6	-256	-316	-100	40	2	-6	-746	-116	-116	32	Ni
Cu	-147	54	108	29	65	54	-6	0	-92	-29	83	108	-4	-126	28	129	83	141	Cu
Zn	-198	-51	44	-25	-23	-58	-256	-92	0	-160	-42	-150	-391	-571	-88	58	8	21	Zn
Nb	11	-56	-47	-153	-2505	-150	-316	-29	-160	0	-133	-249	-548	-435	-10	-76	-702	-276	Nb
Mo	-167	-127	42	-136	-484	-52	-100	83	-42	-133	0	-57	-248	-100	-193	-8	-2	-52	Mo
Ru	-763	-321	4	-15	41	52	40	108	-150	-249	-57	0	-8	47	-332	-66	-87	-16	Ru
Rh	-790	-393	-129	-188	-57	12	2	-4	-391	-548	-248	-8	0	37	-611	-273	-181	-8	Rh
Pd	-648	-275	-82	-251	-116	-10	-6	-126	-571	-435	-100	47	37	0	-480	-123	-57	67	Pd
Ta	31	-122	-130	-254	-3468	-253	-746	28	-88	-10	-193	-332	-611	-480	0	-114	-226	-330	Ta
W	-82	-97	26	-92	-554	-84	-116	129	58	-76	-8	-66	-273	-123	-114	0	7	-56	W
Re	-189	-148	4	-139	-25	-72	-116	83	8	-702	-2	-87	-181	-57	-226	7	0	-89	Re
Os	-713	-361	-22	-40	11	34	32	141	21	-276	-52	-16	-8	67	-330	-56	-89	0	Os
	Ti	V	Cr	Mn	Fe	Co	Ni	Cu	Zn	Nb	Mo	Ru	Rh	Pd	Ta	W	Re	Os	

Energy scale (meV/atom)

-500   -400   -300   -200   -100   -10   10   100   200   300

Figure 1.
Enthalpy matrix. Calculated enthalpies of formation of the lowest-energy structures of binary compounds relative to phase separation into pure elements. The numbers in bold blue font have been calculated with respect to the solid solution (with the permission of Troparevsky, M. C. [25]).

at thermodynamic equilibrium state which will increase the strength without any reduction in electrical conductivity. Niobium (Nb) and molybdenum (Mo) with bcc crystal structure are elements which satisfy the above criteria. The Cu-Nb and Cu-Mo bimetals are an advanced class of materials offering superior performance and defined by a unique structure, precisely engineered to overcome the limitations of bulk materials.

Thermodynamic data for reliable predictions of liquidus, phase fraction, and equilibrium and non-equilibrium solidifications behavior is required, because it is difficult to obtain these information from enthalpy of formation. The equilibrium phase diagrams of Cu-Mo and Cu-Nb are shown in **Figure 2**.

The Cu-Mo system has a very limited terminal solid solutions and the eutectic reaction $Cu_{(L)} + Mo_{(L)}$ at 1083.4°C and the monotectic reaction 2515°C [27].

In the Cu-Nb system, Nb is soluble into the structure of Cu less than 0.1% at room temperature and up to 0.98% at 1095°C. The Cu dissolution in the Nb structure is about 0.1% and up to 0.975% at 1675°C. In this system, there is also a tendency for clustering in a liquid state due to the transformation of the peritectic reaction with 0.87% of Nb at 1095°C [28].

The Cu-Nb and some binary systems of Nb were studied by Ablitzer [29]. He showed that the diffusion rate of Cu-Nb was greater than Nb/Nb. These studies showed no interdiffusion of Cu-Nb or partial diffusion in Cu-Nb pair at 1000° C for 14 days. These results show that iron, cobalt, and nickel diffuse abnormally fast in niobium, whereas the latter displays no curvature (on an Arrhenius plot) in self-diffusion (Eq. (1)). Analysis of all available data for impurity diffusion in niobium shows that the solidus rule proposed by Roux and Vignes is completely quantitative as regards both activation energies and diffusion coefficients [30]:

$$D_{Nb/Nb} = (0.81 \pm (0.57\ 0.30)e^{-\left(\frac{94900 \pm 1400}{RT}\right)}$$
$$D_{Cu/Nb} = (0.00 \pm 0.00\ 0.00)e^{-\left(\frac{000000 \pm 0000}{RT}\right)}$$
$$D_{Fe/Nb} = (0.14 \pm (0.08\ 0.05)e^{-\left(\frac{70300 \pm 1400}{RT}\right)} \qquad (1)$$
$$D_{Co/Nb} = (0.11 \pm 0.05\ 0.04)e^{-\left(\frac{65600 \pm 1200}{RT}\right)}$$
$$D_{Ni/Nb} = (0.077 \pm 0.02\ 0.016)e^{-\left(\frac{63100 \pm 800}{RT}\right)}$$
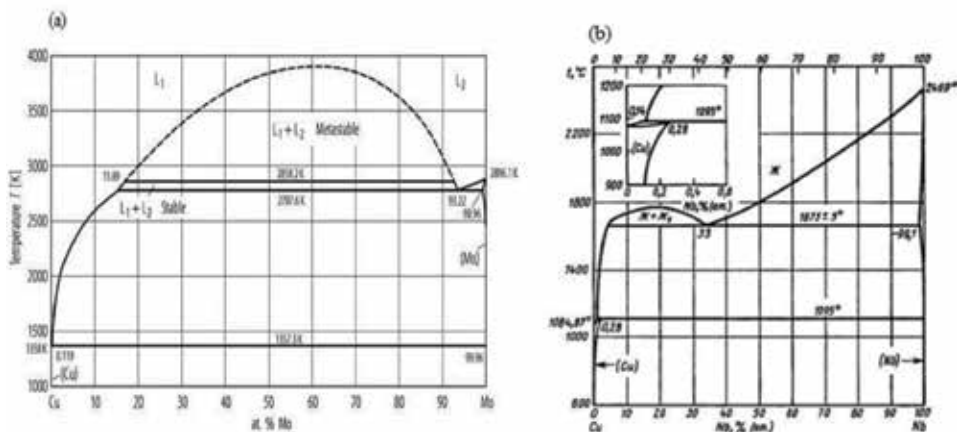
Figure 2.
The equilibrium phase diagrams of (a) Cu-Mo and (b) Cu-Nb [27, 28].

3. Fabrication techniques

Copper bimetals consist of immiscible metals with notably different melting points and are attractive due to the unique combination of their mechanical, electrical, and physical properties. It has been shown that the non-equilibrium supersaturated solid solutions can be achieved in Cu-based binary system by mechanical alloying (MA) [31, 32] rapid solidification [33, 34], and thin-film deposition [35, 36]. The fabrication of Cu-based binary system such as Cu-(Nb, Cr, W, Fe, etc.) has been reported by mechanical alloying. Despite the positive heat of mixing the alloy constituents, the complete dissolution of the minority phases into the copper fcc lattice was observed for each specimen after 16 hours of MA.

Apart from the importance of Cu-Nb system due to the outstanding properties and applications in various fields, a major restriction of this system is the immiscibility of elements in each other. Therefore, Cu and Nb do not form any alloys by conventional bulk processing techniques. These issues have been addressed in researches related to the synthesis of Cu-Nb composites. Dupouy et al. [37] have presented a method for production of nanocomposites from these materials. In this method, Nb rod was placed in the Cu tube, and the nanostructured composite was produced by drawing. Extended results of investigations into these materials are contained in the studies carried out by Funkenbusch et al. [38] as well as Hangen and Raabe [39]. However, it has been shown that non-equilibrium supersaturated solid solutions can be achieved in Cu-Nb system by mechanical alloying, rapid solidification, thin-film deposition, and accumulative roll bonding.

4. Microstructure and properties

The multidisciplinary properties of Cu-Nb materials require a coordinated, collaborative, and focused approach in addressing the immiscibility challenge. The mutual solubility of Nb and Cu is negligible, less than 0.1% for Nb in Cu lattice and 0.9% for Cu in Nb lattice near room temperature. Whereas, there are great prospects for application and their superb roles, which have ultimate tensile strength over 750 MPa, and electrical conductivity of 65% IACS and resistivity of 1.7241 μΩ cm [40–45].

Zeik used rapid solidification technique and showed high volume fraction of Nb-Cu multiphase which is distributed within a Cu-rich matrix containing Nb-rich dendrites [46]. Gluchowski used pure Cu as matrix, and fine particles of second phase with dimensions at the level of 100 nm has been observed on the borders of matrix grains [47]. Being a non-equilibrium method, film formation by sputtering deposition could result in improvement of the solid solubility, intense changes within the defect density, the formation of metastable phases (pseudo-alloys), and changes within the microstructure of alloy films. Research studies have documented the wide variety of copper-niobium nanocomposites, exhibiting the enhanced properties such as thermal stability, mechanical strength, superconductivity, and irradiation resistance **(Figure 3)** [48–53].

The fabrication of pseudo-alloys by nanoparticles has been reported for different Cu-based binary systems such as Cu-(Nb, Cr, Fe, W, Ru, etc.). One way to strengthen copper is to add immiscible metallic elements such as chromium and niobium elements to form supersaturated solid solution [31, 47], which is subsequently heat-treated to form high-strength copper alloy with fine dispersed metallic particles.

Excellent mechanical properties and good electrical conductivity are outstanding features of copper-niobium compounds. Other important features of copper-niobium compounds are superconductivity and its use in superconductor wires [49–54].
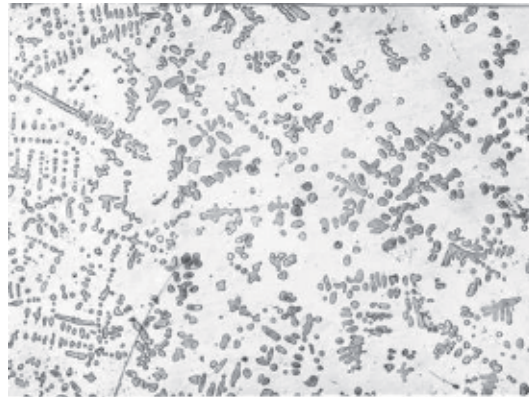
Figure 3.
The microstructure of copper-niobium coarse-grained particles is copper-rich and niobium-rich compounds dispersed in amorphous phase [46].

Cu-Nb nanocomposites have been produced with severe plastic deformation (SPD) process. The Cu-Nb composition plays a significant role in the mechanical properties of these materials. The copper-niobium interface has been studied with high-resolution transmission electron microscopy (HRTEM). Although copper and niobium have poor mechanical bonds prior to the process, they are produced with strong bonds after plastic deformation. In **Figure 4** the regular interface {111} Cu// {110} Nb is shown with a thickness of 2 nm along the wire axis [52].
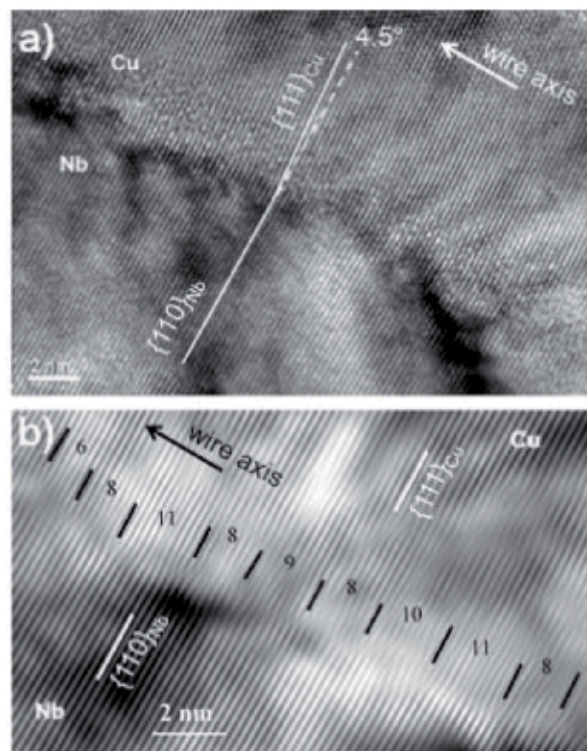
Figure 4.
HRTEM image shows the Cu-Nb interface. It is observed that a regular interface of {111} Cu//{110} Nb is formed along the wire axis with thickness of 2 nm [52].

Mara and co-workers investigated nanoparticle nanocomposites of Cu-Nb with thicknesses of 5 and 40 nm with magnetic sputtering techniques [54]. They observed the growth of layers was consistent with the planes of {111} Cu//{110} Nb and with the constant control of uniform growth of the nano-layers.

The experiments are given by three-dimensional Cu-Nb nanocomposites in which nano-sized drops of niobium are immersed into a copper matrix. The structure consists of coarse phase of copper and niobium-rich compounds, which are scattered throughout the amorphous phase. Degtyarenko showed such systems being superconducting even at Nb content lower than a percolation threshold, but its properties in comparison with the granular one fabricated at slow melt cooling have a distinction in kind [55].

The transport properties in this system are strongly affected by the size and proximity effects but free from a complicating anisotropy factor. In comparison with it, Degtyarenko et al. evaluated the Cu-Nb composites with a micron-scale structure. Samples of the first type represent the tapes prepared at extremely fast cooling of Cu-Nb melt. The niobium drops and spacing between them have a measure of about 10 nm, and the drops are immersed into the Cu matrix with low content (~1 at%) of Nb. The system is similar to a granular superconductor, but its structural sizes are less than coherence lengths of the materials forming it.

The copper-rich or niobium-rich phases exhibit a positive resistance coefficient (TCR). In the Cu-90Nb composition, the first transition temperature is superconducting (TC~4.5 K). The amorphous film exhibits high room temperature resistance as well as negative TCR, and the transfer of superconductivity is dependent on the amorphous phase composition (**Figure 5**) [55].
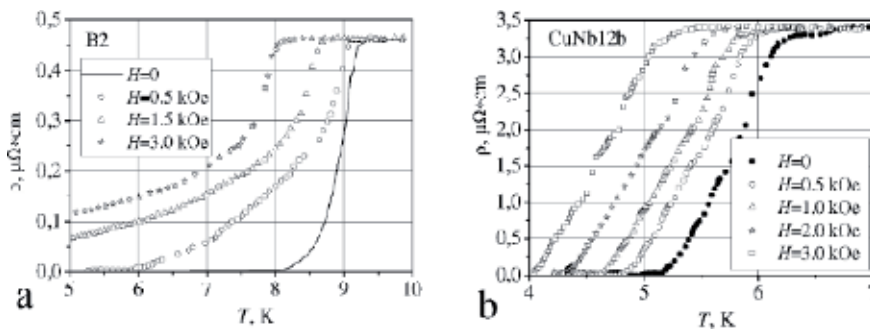
Figure 5.
The temperature dependence of the resistivity in the vicinity of the superconducting transition of the slow cooled (a) and quenched (b) samples [55].
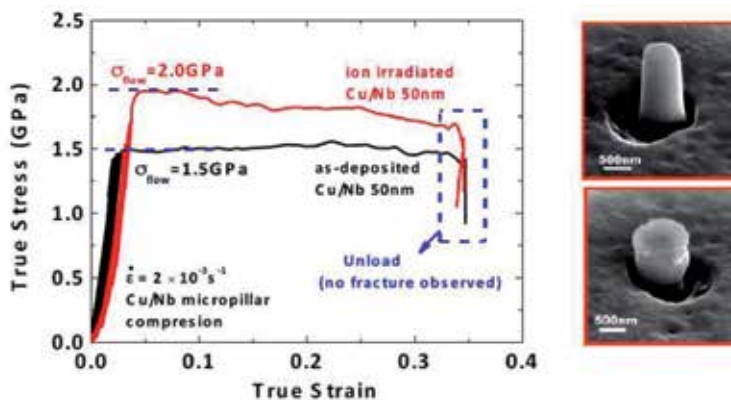
Figure 6.
The stress-strain diagram of Cu-Nb composite which is true in different circumstances [56].

Beyond the ability of conductance, superconductivity, and thermal stability, Cu-Nb nanocomposites also enable extraordinary and unusual mechanical properties after exposure to radiation [56]. The effect of radiation on mechanical properties of Cu-Nb thin-film nanocomposites was investigated by Li et al. [56]. To perform these tests, a pressure on the specimens was performed by designing micrometer diameter specimens. He described the effects of radiation on compressive strength and a slight reduction of the plastic strain, while a failure phenomenon was observed at the applied maximum strain (**Figure 6**).

5. New approaches

Early success in manufacturing Cu-Nb bimetals at scale have come as three-dimensional nanocomposites. At this scale, Shokrvash et al. [57] lined the Cu-Nb bulk nanostructure with a metal oxide precursor (Nb_2O_5) and Cu. These studies describe the successful synthesis of Cu-Nb nanocomposites by the electro-deoxidation method. Structural analysis of the obtained products reveals rapid reduction of Nb_2O_5 to Nb and the embedment of Cu and Nb within the bulk nanostructures of Nb and Cu, respectively. The authors have elaborately discussed the electrochemical route to process Cu-Nb composites. The solubility of Cu in Nb could be enhanced through this technique. They have adopted different characterization techniques to show the solubility, structure, and morphology of Cu-Nb composites synthesized by the electrochemical route. The oxygen-free nanostructured materials could be processed using this technique. This investigation deals with the study of the electrolysis synthesis of Cu-Nb nanocomposites, and developed to fabrication of nanoparticulate bulk materials with equilibrium processes to delivering improved electrical conductance (**Figures** 7 and **8**) [58].

It has been proven in the Cu-Nb system that the immiscibility can be overcome and direct alloying can be realized between the constituent elements by a local electric field between the boundaries of nanoparticles [58]. The mechanical properties of as-synthesized materials have been investigated by nanoindentation testing. The indentation hardness and modulus have been measured using a maximum load of 10 mN with a loading rate of 20 mN/minute and holding and unloading rate 20 mN/minute. The acquisition of data from five tests presented the ultimate strength for Cu-14%Nb and Cu-22%Nb nanocomposites ranging 4.42–4.82 GPa [59].

In these research, thermodynamic and kinetic model has been established for direct alloying between Cu and Nb, based on electromigration theory. Particularly, this opens up prospects for designing the new materials from immiscible metallic elements, which is the main topic in designing alloys as well as materials science progression.
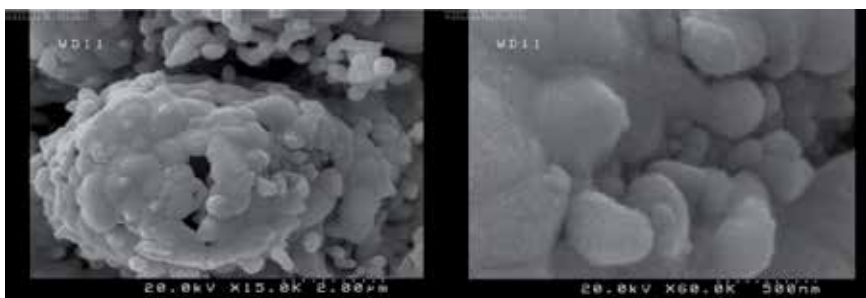
Figure 7.
FESEM image of Cu-22%Nb representing the composite structure (images by secondary electron mode) (with the permission of Shokrvash [57]).
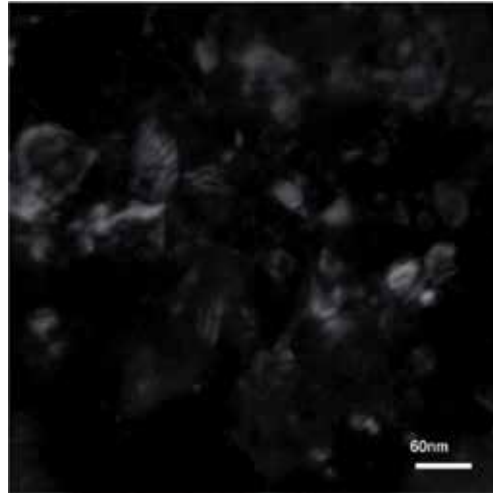
Figure 8.
The dark field TEM image of Cu-22%Nb nanocomposite (with the permission of Shokrvash [57]).

Author details

Hussein Shokrvash[1*], Rahim Yazdani Rad[2], Abouzar Massoudi[2] and
Reza Shokrvash[3]

1 Research Center for Nanotechnology and Nano-Devices (RCNN), University of
Maragheh, Iran

2 Materials and Energy Research Center, Iran

3 Electronics, Telecommunication Department, Civil Aviation Technology College,
Tehran, Iran

*Address all correspondence to: hshokrvash190@gmail.com

IntechOpen

References

[1] Davis JR. Copper and Copper Alloys. ASM International; 2001. pp. 153-163. ISBN-13: 978-0871707260

[2] Konrad JA. Kundig, copper and copper alloys, chapter 5. In: Handbook of Materials Selection. John Wiley & Sons, Inc.; 2002. ISBN: 9780471359241

[3] Konečná R, Fintová S. Copper and Copper Alloys: Casting, Classification and Characteristic Microstructures. Intech Open; 2012. DOI: 10.5772/39014

[4] Koch CC. In: Cahn RW, Haasen P, Kramer EJ, editors. Materials Science and Technology. Weinheim: VCH; 1991

[5] Oehring MY, Klassen T, Bormann R. Competition between stable and metastable phases during mechanical alloying and ball milling. Physica Status Solidi. 1992;**131**:671

[6] Johnson WL. Thermodynamic and kinetic aspects of the crystal to glass transformation in metallic materials. Progress in Materials Science. 1986;**30**:81-134

[7] Ma E. High entropy alloys. Progress in Materials Science. 2005;**50**:413

[8] Eugene V. In: Dirote, editor. Trends in Nanotechnology Research. Nova Science Publishers, Inc; 2004. ISBN 1-59454-091-8

[9] Gogotsi Y. Nanomaterials Handbook. CRC Press, Taylor & Francis Group; 2006. Chapter 1

[10] Olson GB. Science. 2002;**88**(5468): 933-998

[11] Aricò AS, Bruce P, Scrosati B, Tarascon JM, Schalkwijk W. Nature Materials. 2005;**4**:366-377

[12] Maynard A, Bowman D, Hodge G. Nature Materials. 2011;**10**:554-557

[13] Nie Z, Petukhova A, Kumacheva E. Nature Nanotechnology. 2010;**5**:15-25

[14] Lee I, Hana SW, Kim K. Chemical Communications. 2001:1782-1783

[15] Lavine M. Science. 2006;**312**(5780): 1575b-1575b

[16] Amendola V et al. Nanoalloys. Nanoscale. 2013;**5**:5611-5619

[17] Jakobi J et al. Stoichiometry of alloy nanoparticles from laser ablation of PtIr in acetone and their electrophoretic deposition on PtIr, electrodes. Nanotechnology. 2011;**22**:145601

[18] Gordon E, Karabulin A, Matyushenko V, Sizov V, Khodos I. Physical Chemistry Chemical Physics. 2014;**16**:25229-25233

[19] Guisbiers G et al. Nano Letters. 2014;**14**(11):6718-6726

[20] Lin Q, Corbett DJ. Journal of the American Chemical Society. 2007;**129**(21):6789-6797

[21] Herlach DM. Phase Transformations in Multicomponent Melts. WILEY-VCH Verlag GmbH & Co. KGaA; 2008. pp. 97-105

[22] Huang B et al. Journal of the American Chemical Society. 2017;**139**(13):4643-4646

[23] Manenc J. Structural Thermodynamics of Alloys. Springer; 1973. pp. 24-36. ISBN: 978-94-010-2605-5

[24] Lee HJ. Thermodynamics of pure metals and alloys, Chapter 2. Caltech Thesis; 2003

[25] Troparevsky MC et al. Physical Review X. 2015;**5**:011041

[26] Hume-Rothery W. Atomic Theory for Students of Metallurgy. London: The Institute of Metals; 1969

[27] Predel B. Landolt-Börnstein—Group IV Physical Chemistry. Vol. 12B. Berlin, Heidelberg: Springer; 2012. pp. 253-253. Chapter 186

[28] Okamoto H. Journal of Phase Equilibria. 1991;**12**:614

[29] Ablitzer D. Philosophical Magazine A. May 1977

[30] Roux F, Vignes A. Physical Review Applied. 1970;**5**:393

[31] Botcharova E, Freudenberger J, Schultz L. Journal of Alloys and Compounds. 2004;**365**:157-163

[32] Botcharova E, Freudenberger J, Gaganov A, Khlopkov K, Schultz L. Materials Science and Engineering A. 2006;**416**:261-268

[33] David EL, Gary MM. NASA Contractor Report 185144. Lewis Research Center Under Grant NGT-50087; 1989

[34] Munitz A, Bamberger M, Venkert A, Landau P, Abbaschian R. Journal of Materials Science. 2009;**44**:64-73

[35] Demkowicz MJ, Hoagland RG, Hirth JP. Physical Review Letters. 2008;**100**:136102

[36] Zhu XY, Luo JT, Zeng F, Pan F. Thin Solid Films. 2011;**520**:818-823

[37] Dupouy F et al. Scripta Materialia. 1996;**34**:1067-1073

[38] Funkenbusch PD. Metallurgical and Materials Transactions. 1987;**18A**:1249-1256

[39] Hangen U, Raabe D. Acta Metallurgica. 1995;**43**:4075-4082

[40] Seeger A, Schottky G. Acta Metallurgica. 1959;**7, 495**

[41] Verhoeven JD, Downing HL, Chumbley LS, Gibson ED. Journal of Applied Physics. 1989;**65**:1293

[42] Spitzig WA, Downing HL, Laabs FC, Gibson ED, Verhoeven JD. Materials Metallurgical Transactions A. 1993;**24**:7-14

[43] Heringhaus F, Raabe D, Gottstein G. Acta Metallurgica et Materialia. 1995;**43**:1467-1476

[44] Freudenberger J, Botcharova E, Schultz L. Journal of Materials Science. 2004;**39**:5343-5345

[45] Sandim MJR et al. Superconductor Science and Technology. 2006;**19**:1233-1239

[46] Zeik KL, Koss DA, Anderson IE, Howell PR. Metallurgical Transactions A. 1992;**23**:2159-2167

[47] Sheibani S, Heshmati-Manesh S, Ataie A. Journal of Alloys and Compounds. 1994;**495**(59)

[48] Głuchowski W, Stobrawa JP, Rdzawski ZM, Marszowski K. Journal of Achievements in Materials and Manufacturing Engineering. 2011;**46**

[49] Mahalingam T, Lin CH, Wang LT, Chu JP. Materials Chemistry and Physics. 2006;**100**:490-495

[50] Vidal V, Thilly L, Petegem SV, Stuhr U, Lecouturier F, Renault PO, et al. Scripta Materialia. 2009;**60**:171-174

[51] Lei RS, Pu WM, Ming-xing G, Li Z, Qi-yi D. Transactions of Nonferrous Metals Society of China. 2009;**19**:272-276

[52] Demkowicz MJ, Thilly L. Acta Materialia. 2011;**59**:7744-7756

[53] Deng L, Ke H, Hartwigc KT, Siegrist TM, Dong L, Sun Z, et al. Journal of Alloys and Compounds. 2014;**602**:331-338

[54] Mara NA, Sergueeva A, Tamayo T, Zhang X, Misra A, Mukherjee A. JOM. 2004;**56**:141

[55] Degtyarenko PN et al. Journal of Physics: Conference Series. 2008;**97**:012024

[56] Li D, Robinson M, Rathz T, Wiliams G. Acta Materailia. 1998;**42**:2849-2822

[57] Shokrvash H, Yazdani Rad R, Massoudi A. Metallurgical and Materials Transactions A. 2018;**49**(4):1355-1362

[58] Shokrvash H, Yazdani Rad R, Massoudi A. Advanced Ceramics Progress. 2018;**4**(1):32-39

[59] Shokrvash H, Yazdani Rad R, Massoudi A. Paper entitled High performance Cu-Nb nanocomposites synthesized by electrolysis approach. In: Advanced Engineering Materials; 2019

Classification of Electrospinning Methods

Muhammad Waqas Munir and Usman Ali

Abstract

Electrospun nanofibers are being used in a variety of performance apparel applications where their unique properties add to their functionality. Those properties include, small fiber diameter, high surface area, potential to combine chemistry, layer thinness, high porosity, filtration properties, and low basis weight. Electrospinning has been considered as an efficient technique for nanofiber web formation. Polymers have been electrospun into nanofibers mostly after being dissolved in solvent and melted. This chapter presents a comprehensive summary of existing electrospinning methods. Electrospinning methods are classified into different categories depend upon jet formation.

Keywords: electrospinning, spinneret, needleless electrospinning, nanofiber

1. Introduction

Nanotechnology denotes to the science and designing concerning materials, structures, and gadgets which at least one of the dimension is 100 nm or less. Electrospun nanofiber webs can be modified to a desired porous structure, and in these are a huge range of polymers that can be used to make nanofibers [1]. The unique combination of high surface area, low weight, flexibility, and porous structure enables us to control the water resistance level, vapor transmission, and air permeability rate. Consumption of nanofibers in the world is shown in **Figure 1**. Applications of electrospun nanofibers, as shown in **Figure 2**, include tissue engineering scaffolds [2], filtration [3], catalyst and enzyme carriers [4, 5], release control [6], sensors [7], energy storage [8], affinity membranes [9], recovery of metal ions [10–12], wound healing [13], reinforcement [14], protective clothing [15, 16], and energy conversion and storage [17].

1.1 Various ways to make nanofibers

Nanofibers can be processed by a number of techniques such as:

1. Drawing

2. Template synthesis

3. Phase separation
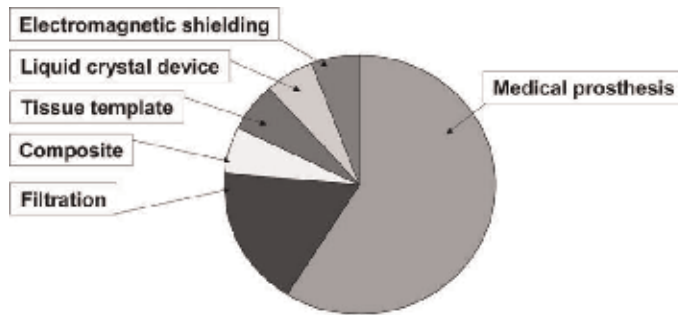
Figure 1.
Consumptions of nanofibers in world [18].
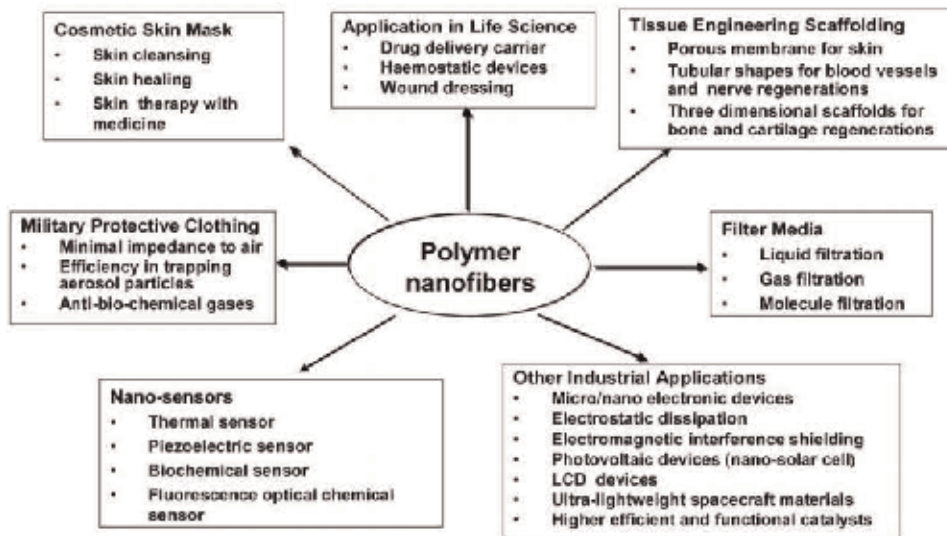
Figure 2.
Potential applications electrospun nanofibers [18].

4. Self-assembly

5. Electrospinning

Commonly nanofiber fabrication is done by electrospinning method [19].

1.1.1 Drawing

In drawing process, single nanofiber is attended by stretching of polymer that is in solution form. With this method only viscoelastic materials have been spun into nanofibers. If polymer is in melt form, then cooling system is necessary to solidify the fiber. On the other hand, if polymer is in solution form, then heating mechanism is necessary to evaporate the solvent. This is a very slow process that is suitable only for lab scale [18]. Process diagram is shown in **Figure 3**.

1.1.2 Template synthesis

In this method, nonporous membranes are used in which pores are in cylindrical form. Diameters of these pores are uniform. Solid polymers are formed
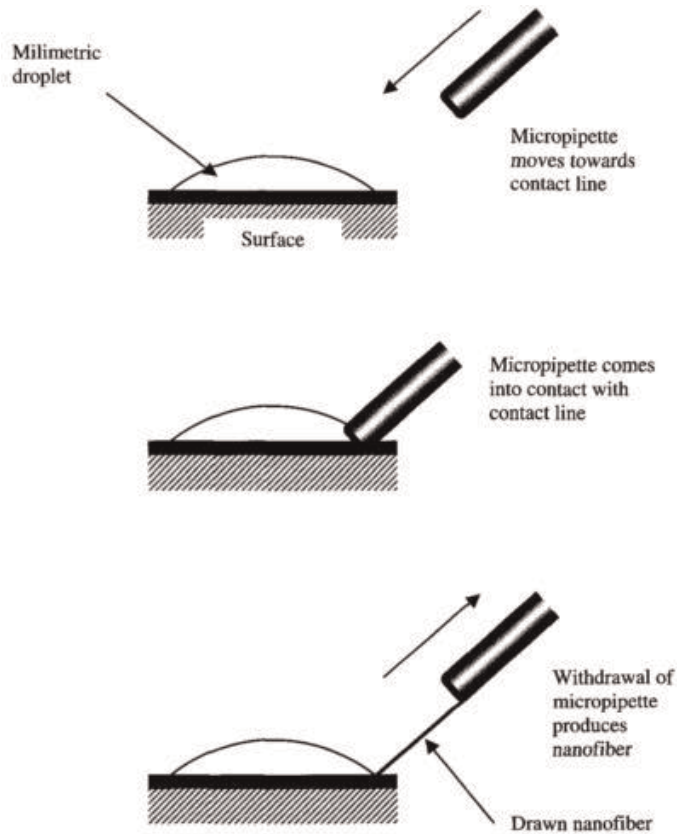
Figure 3.
Drawing in method [19].
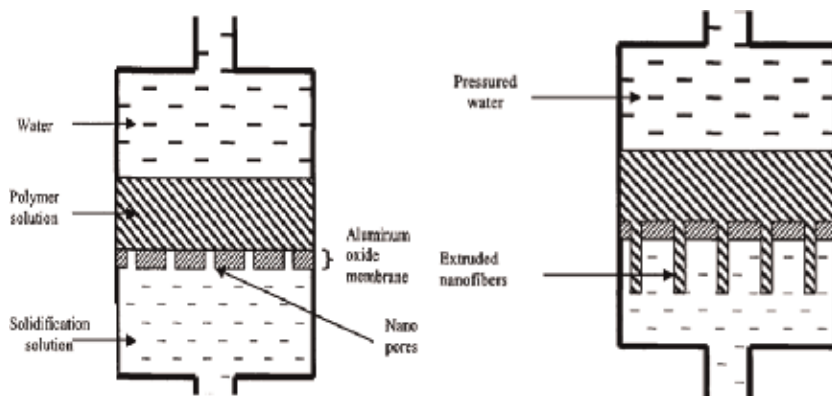
Figure 4.
Temple synthesis [20].

that have diameter equal to size of porous [20]. The process diagram is shown in **Figure 4**.

1.1.3 Phase separation

In this process, five steps are involved: polymer dissolution, polymer gelation, extraction of solvent, freezing, and freeze-drying. Fiber dimensions are not

controllable with this process. This proves only suitable for lab scale [21]. The process diagram is shown in **Figure 5**.

1.1.4 Self-assembly

Peptide nanofibers are produced from self-assembly process. This is a very complex process that is only suitable of lab-scale nanofiber production [22]. This is shown in **Figure 6**.
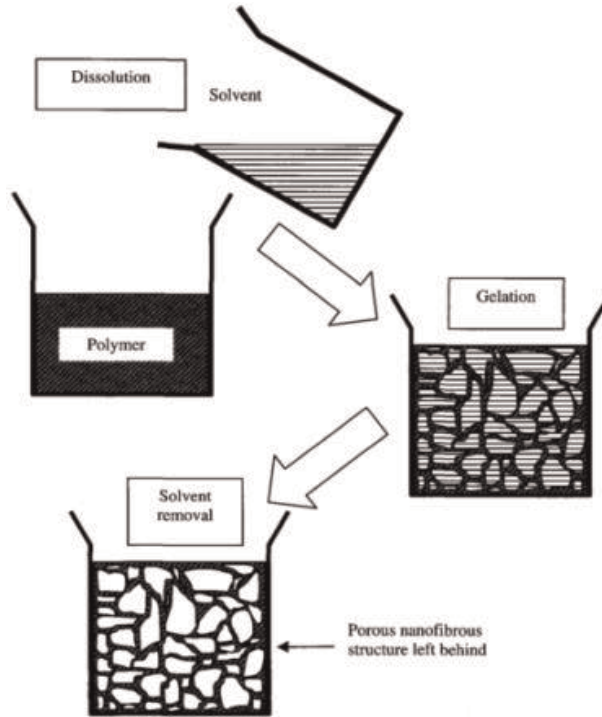
Figure 5.
Phase separation [21].
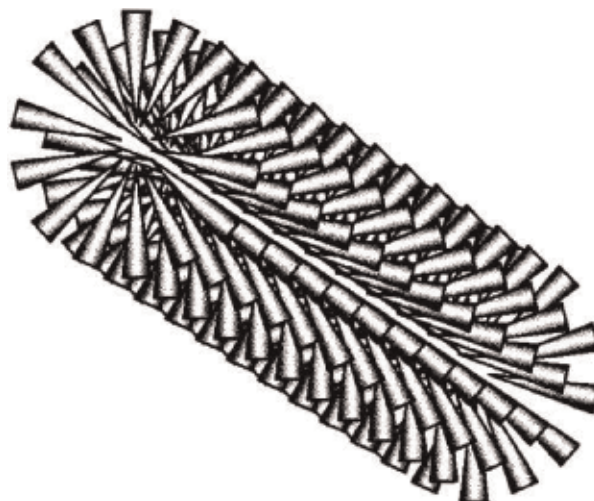
Figure 6.
Self-assembly [22].

1.1.5 Electrospinning

Instruments used for electrospinning are given below:

1. High-voltage DC power supply

2. Syringe pump

3. Spinneret (a small diameter needle connected to the syringe)

4. Metal collector

The polymer is dissolved in a solvent before electrospinning, and when it is completely dissolved, it forms polymer solution. The polymer fluid is then introduced into the syringe tube for electrospinning. The positive terminal of the DC power supply is connected to the hollow needle [23], and the negative terminal is connected to the metal collector. With the increase of intensity of the electric field, the repulsive electrostatic force overcomes the surface tension, and the charged jet of the fluid is ejected from the tip of the Taylor cone. The discharged polymer jet undergoes an instability and elongation process, which allows the polymer in the jet to become very long and reduces the diameter of the extruded polymer fiber. The solvent that is used to dissolve the polymer evaporates, and the polymer in the jet is dried. The solvent evaporation depends on the distance between the tip and collector, the solution vapor pressure, and the inside chamber temperature. Stable environmental conditions are therefore important in getting good quality nanofibers. The maximum applied voltage for a needle electrospinning setup is normally less than 30 kV and is also highly humidity dependent [24]. **Figure 7** illustrates the schematic diagram of the complete electrospinning setup.

Needleless electrospinning presented as an option electrospinning innovation that deliver nanofibers on a substantial scale. Needleless electrospinning is included as electrospinning of nanofibers straightforwardly from an open fluid surface. Many planes are shaped at the same time from the needleless fiber generator (spinneret) without the impact of capillary effect that is regularly connected with needle electrospinning. Since the fly start in needleless electrospinning is a self-composed process which happens on a free fluid surface, the spinning process is hard to control. In needleless electrospinning process, many shapes of spinneret
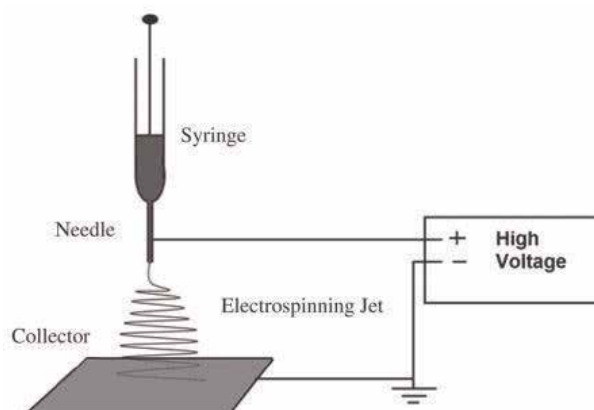
Figure 7.
Needle electrospinning.
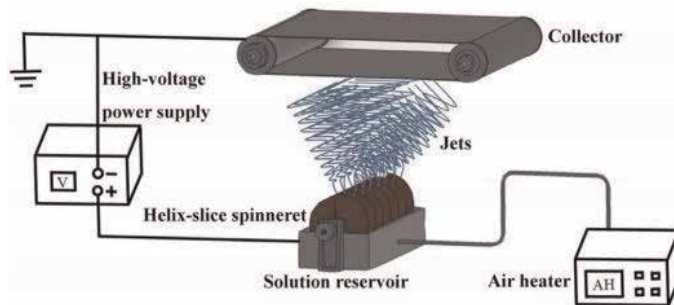
Figure 8.
Needleless electrospinning [33].

have been invented that have different levels of production. **Figure 8** illustrates a schematic diagram of the complete needleless electrospinning setup.

One of the problems also created with needle electrospinning method is low production rate that is typically less than 0.3 g/h [25]. With needleless electrospinning method, production of nanofibers is 250 times [26] more than needle electrospinning. Production depends upon the shape of spinneret used in needleless electrospinning. With different shapes of spinnerets, production rates of 2.5–100 g/h can be achieved.

Different needleless setups, like conical wire coil electrospinning spinneret [25], edge-plate electrospinning setup [27], splashing electrospinning setup [28], rotary cone [29], roller electrospinning process [30], cylinder [31], disk [32], and spiral coil electrospinning processes [33], were made for large-scale production of nanofibers. In all these needleless setups, the spinneret shape is different. Due to this variation in spinneret shape, nanofiber production rate and fiber morphology is different.

1.2 Production of nanofibers

Based on the jet formation and the way of using the needles, electrospinning methods can be classified as:
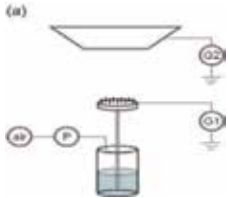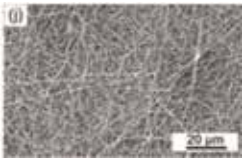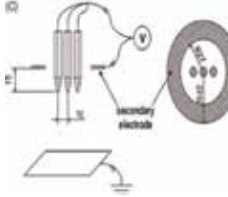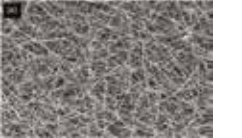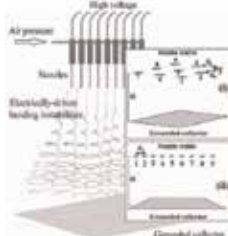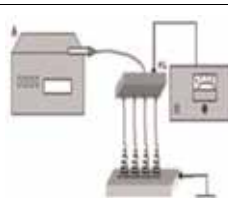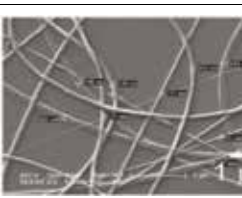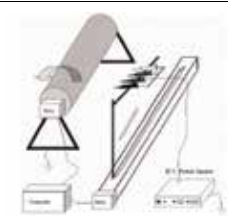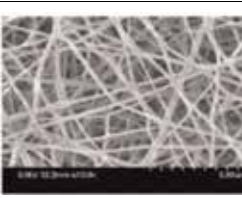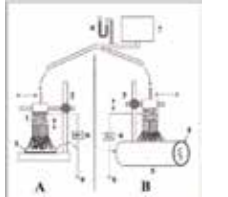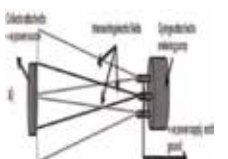
- Multi-jet electrospinning methods

- Multi-needle electrospinning methods

- Needleless electrospinning methods

1.2.1 Multi-jet electrospinning methods

In this electrospinning method, multi-jets were used for nanofiber formation. Production of nanofiber increased as compared to needle spinning. Due to multi-jets, uniform web of nanofiber is not formed; this is due to repletion effect between jets. Some multi-jet electrospinning methods are given in **Table 1**.

1.2.2 Multi-needle electrospinning methods

In multi-needle electrospinning method, a number of needles are used as spinnerets that contain one or different types of polymer solutions. High voltage is

Year	Author	Setup	Morphology	Fiber bundling/ polymer
A. 2010	Varesano et al.			Ethylene oxide polymer solution was used for nanofiber. Feeding of solution to each nozzle is done at flow rate of about 0.45 g/h
B. 2009	Varesano et al.			Polyethylene oxide solution was made in water with ratio 93:7. Flow rate of polymer solution form nozzle tip is 1 ml/h
C. 2005	Theron et al.			Polyethylene oxide was used to prepare solution for working fluid in this needless setup. The production rate was in the range of 22.5 ml/(cm^2 min) to 22.5 ml/(cm^2 min) per 1 cm^2 of the spinneret plate
D. 2007	Yasmin et al.			Polyvinylpyrrolidone and polypyrrole polymers are used in this experiment. Production of 8-spinneret device is 0.1 g/h
E. 2004	Ding et al.			PVA and cellulose acetate (CA) polymers are used with concentration 10%. Throughput (mg/min jet) PVA solution is 1.9, while CA solution is 2.3
F. 2005	Tomaszewski et al.			PVA was used in this experiment; its concentration was 15 wt%. With elliptic head production is 11 +/− 3 g per min; with concentric head dry nanofiber production is 12+/− 3 g
G. 2010	Kumar et al.			12 wt% of polyethylene oxide was used in this experiment. With 3 jets, production is 0.3 ml/min; with 7 jets, it is 0.45 ml/min

A. In this multi-jet electrospinning setup, a pilot plan was used that consist of spinning head. On this spinning head, nine plastic nozzles are deposited in two rows; each nozzle's internal diameter was 0.43 mm. These nozzles are 2 cm away from each other. The polymer solution was provided to the nozzles at spinning head at 0.2 bar; flow rate of solution was about 0.45 g/h. Nanofibers were collected on the nonwoven substrate. Nanofibers were collected that form nine spots on collector, uniform web not formed [34].

B. High-voltage power supply is attached in multi-jet setup; solution is filled in the tube that ejects downward by gravity flow at the rate of 1 ml/h from plastic tip that have orifice diameter of 750 mm. Tests demonstrated that the disparity angles between polymer jets can be lessened by utilizing an auxiliary electrode. Jets used in this setup are 2–16 that have different arrangements [1].

C. This work portrays the consequences of the test examination and modeling of multi-jet amid the electrospinning of polymer solution. The outcomes exhibit how the outside electric fields and shared electric collaboration of various charged jets impact their way and advancement among electrospinning. In this multi-jet electrospinning setup, nine syringes were arranged, and polymer solution was placed identical in all syringes. When electric field is applied to syringes, nanofibers were produced that collected on metal collector. It is observed that nanofibers are collected at nine spots that show repletion effect in multi-jet electrospinning process [35].

D. This setup was the same as conventional needle electrospinning, only microfluidic device was used instead of syringes. The polymer solution was constantly fed through the microfluidic gadget utilizing a syringe pump. High voltage 10–15 kV was applied with spinning distance of 10 cm. It was shown that the morphology and measurement of the nanofibers can be altered by modifying the polymer focus, surface strain, salt, quality of the potential, and nourish rate [36].

E. In this multi-jet electrospinning setup, polymers (PVA and cellulose acetate (CA)) were physically blended with each other. This setup contained four syringes placed on the setup which moved along the track. Distance between the tips of syringes was 3 cm and rotating collector was used. The speed of the rotatable tubular layer and the mobile stand can be controlled by PC. The PVA and CA arrangements were set in various syringes as indicated by the necessity. The consistent nanofiber mats were gathered on the surface of foil and dried at 80°C in vacuum for 24 h [37].

F. The electrospinning testing done with three sorts of electrospinning heads, series, elliptic, and concentric, demonstrated that the last two enabled the procedure to continue on the premise of minimal multi-jet frameworks utilizing at least 10 turning channels. The concentric electrospinning head, which turned out best as to both the effectiveness and the nature of the procedure, can deliver 1 mg of dry PVA nanofibers from one turning channel amid 1 min [38].

G. The attention was on investigating the fiber repulsion in multi-jet electrospinning. The utilization of multi-jet was hazardous because of fiber repulsion. In this multi-jet setup, a novel spinneret was used to make nanofiber, and increment in the yield has been illustrated. A plastic channel plan with numerous pores exhibited decreased fiber repulsion. This novel plastic channel setup yielded strands with more steady and smaller diameter fibers than with multi-needle electrospinning [39].
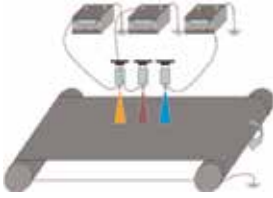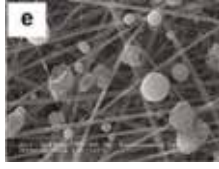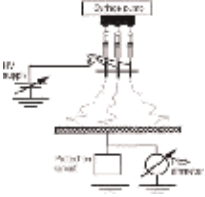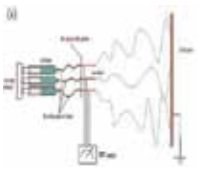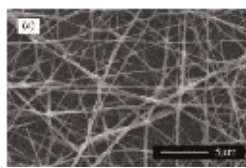
Table 1.
Multi-jet electrospinning methods.

applied to the tip of the needle and nanofibers are deposited on collector. The main advantage of multi-needle electrospinning is we can mix different polymers at our required ratio (**Table 2**).

1.2.3 Classification of electrospinning methods

It may be defined as the method in which fiber jets are produced or generated from the free surface of liquid. It can also be defined as the technique of producing the fibers from open liquid surface. Based on the fiber generating method, the motion of spinneret, and collection direction of fibers, the needleless electrospinning techniques can be classified as:

Year	Author	Setup	Morphology	Fiber bundling/polymer
A. 2014	Wang et al.			Polystyrene, polyvinylidene fluoride, and polyacrylonitrile solutions are used in this setup with concentrations of 4, 21, and 12% by weight, respectively
B. 2011	Angammana et al.			Aldrich polyethylene oxide was employed for preparation of solution; concentration of solution was 5% by weight. The solution was forced through syringe pump at the rate of 0.1 ml/min
C. 2012	Sheng Xie et al.			Polyoxyethylene solution concentration 7 wt % was used for experiments. All experiments were carried out at 22 kV voltage, 22 cm collecting distance, and 0.3 ml/h solution flow rate per needle

A. In this multi-needle electrospinning setup, three syringes were used that contain different polymers. Conveyor belt was used as collector. During electrospinning three types of fibers were mixed together very easily. During electrospinning repletion, polymer jets were observed that could be reduced by increasing distance between needle jets [40].
B. Three needles were used in this setup that are mounted vertically. Polymer solution was pumped through syringes at rate of 0.1 ml/min. The point of this paper is to research the electric field bending in various needles by utilizing limited component investigation and to decide its consequences for the electrospinning procedure. It can be presumed that as the quantity of needles in the course of action expands, the electric field at the tip of each needle diminishes essentially because of the impact of the encompassing needles in the needle arrangement [41].
C. In this multi-needle electrospinning setup, three needles were used, which are arranged in triangle. An auxiliary plate anode has been utilized to be associated with a three-needle framework to get a more uniform electric field. This electrospinning investigations and electric field reenactment exhibit that the multi-needle spinneret with an auxiliary plate can deliver better and more uniform nanofibers [42].

Table 2.
Multi-needle electrospinning methods.

1.2.3.1 Free surface spinning method
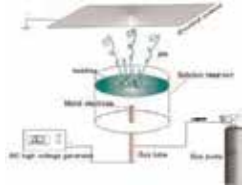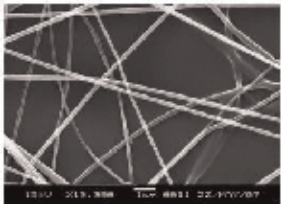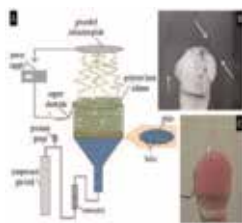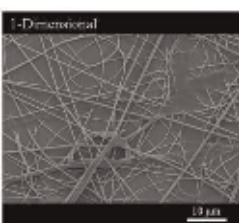
1.2.3.1.1 Bubble spinning methods

In bubble spinning method, air is supplied from porous surface that is placed at the bottom of polymer solution. Bubble is made at the surface of polymer solution, and

jet is formed at the charged surface of the bubble. Very fine nanofibers are deposited on collector that is placed at the top of the polymer container (**Table 3**).

1.2.3.1.2 Free solution spinning methods

In this electrospinning setup, two layers were used: the lower layer was ferromagnetic and the upper layer was polymer solution (**Table 4**). When electrospinning

Year	Author	Setup	Morphology	Fiber bundling/ polymer
A. 2008	Ji-Huan et al.			Polyacrylonitrile (PAN) was dissolved in N,N-dimethylformamide (DMF) solvent, and the weight concentration was 12 wt%. Bubble electrospinning leads to different little rises on surface with little surface tension; minimum diameter achieved with this setup was 50 nm
B. 2014	Higham			Polyvinyl alcohol (PVA) was used as polymer. Production rate was 300 times more than syringe electrospinning

A. The polymer arrangement was filled; the supply and the stature of fluid surface were higher than that of electrode and tube. By turning on gradually the pneumatic weight control valve, we could discover a few air pockets created at the pinnacle of tube. The delivered air pockets will be broken down into smaller ones on the arrangement surface. At the point when surface strain of the little air pockets lessens to the basic esteem which can be overcome by the connected electric field, nano-planes discharge from the peak of the air pockets. Nanofibers that are produced from this method have very fine diameter of 50 nm [43].
B. This is a new method to produce nanofiber with a single bubble electrospinning process which is a concept based on keeping the bubble from bursting during electrospinning. Compress gas was supplied to porous surface. This porous surface was placed below the polymer solution. When gas was supplied to this surface, bubbles were produced that formed charged polymer jets [44].

Table 3.
Bubble electrospinning methods.
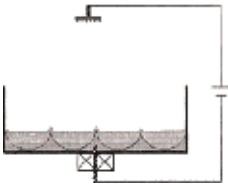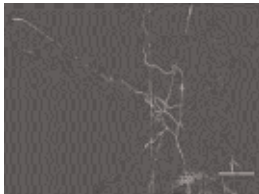
Year	Author	Setup	Morphology	Fiber bundling/polymer
A. 2004	Yarin et al.			Polyethylene oxide in water-ethanol mixture was used in this setup. Production is 12 times more than traditional needle electrospinning

Table 4.
Free solution electrospinning methods.
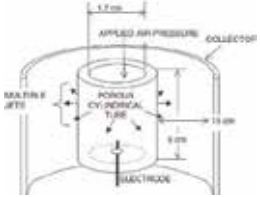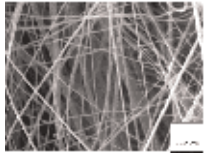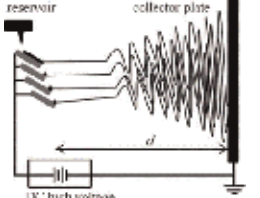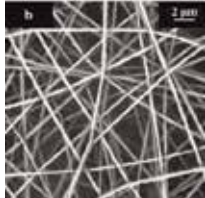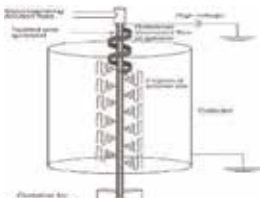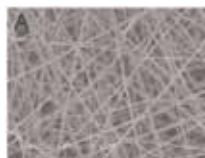
process was started, a customary electric field was utilized to the gadget; steady vertical spikes of attractive suspension were formed. When high voltage was applied, electrified jets undertake strong stretch by the electric field, solvent evaporates, and solidified nanofibers deposit on the upper counter electrode [45].

1.2.3.2 Spinneret spinning methods

1.2.3.2.1 Stationary spinnerets

In this needleless electrospinning method, stationary spinneret is used for nanofiber generation. High voltage is applied to spinneret, and there is special mechanism to feed polymer solution on spinneret. Polymer jets are formed on the edges of stationary spinneret that produce nanofibers. Stationary spinnerets are further classified into three categories depending upon the spinneret position:

Horizontal stationary spinnerets.
Downward stationary spinnerets.
Upward stationary spinnerets.

Year	Author	Setup	Morphology	Fiber bundling/ polymer
A. 2006	Dosunmu et al.			Polyvinylpyrrolidone and nylon 6 were used in ceramic porous tube for this setup. Nanofibers were made at the rate of more than 5 g/h
B. 2010	Thoppey et al.			Polyethylene oxide in water at 6 wt% was used in this experiment. Fabrication rate is 0.11–0.27 g/h
C. 2014	Holopainen et al.			Polyvinylpyrrolidone, hydroxyapatite and bioglass were used as polymers. Production was 5.23 and 1.40 g h^{-1}, respectively

A. In this setup solid porous polyethylene tube was used as a spinneret that fixed vertically inside tube polymer solution was filled that ejected from outside pores by applying pressurized air that formed drops on the outer surface of tube wall. This porous tube was surrounded by circular wire mesh collector. When high voltage was applied, charged drops form nanofibers. When length of the tube increased, production of nanofibers increased by 4.2 g/min per meter length of tube [2].
B. The edge of a flat plate has been utilized as a spinneret onto which polymer solution was set as beads or experiences a gravity-helped stream. When high voltage was applied, nanofibers were ejected from the edge of plates. Collector was placed vertically at a working distance [27].
C. In this electrospinning setup, twisted wire was used that was placed vertically connected with high-voltage power supply. Cylindrical collector was used to collect nanofiber placed around the wire. Polymer solution was flowing downward on the twisted wire. Multi-jets were formed at the wire that produced nanofibers [46].
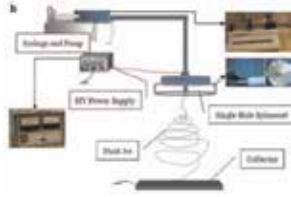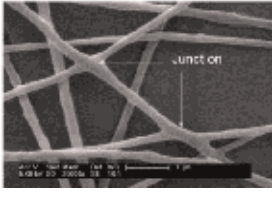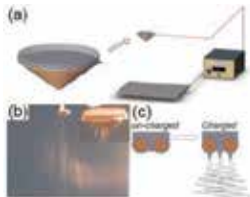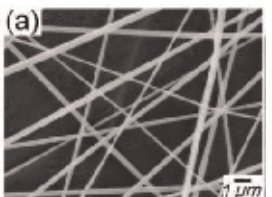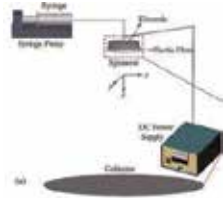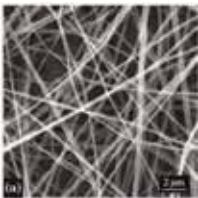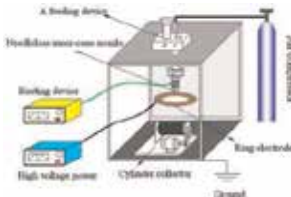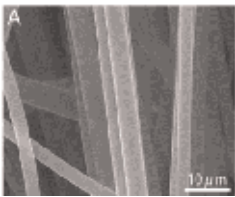
Table 5.
Horizontal stationary spinneret methods.

1.2.3.2.1.1 Horizontal stationary spinnerets

In horizontal stationary spinnerets, polymer jets are formed in horizontal direction. Nanofibers are collected on vertical mounted plates. Some of these are given in **Table 5**.

Year	Author	Setup	Morphology	Fiber bundling/ polymer
A. 2009	Zhou et al.			Polyethylene oxide was used as polymer with water as a solvent. With four holes, production is 1.68 g/h with flow rate 28 ml/h
B. 2009	Wang Xin et al.			PVA solution was used, and production of dry nanofibers was found to be 0.86 and 2.75 g/h at 45 and 70 kV, respectively
C. 2013	Zheng et al.			Polyethylene oxide solution with water is used in this setup. Flow rate was 9.5 ml/h
D. 2014	Li et al.			Polypropylene was used that melted before electrospinning

A. In this electrospinning setup, a flat spinneret was connected to the positive point of high-voltage power supply. Polymer solution was pumped by syringe to the hollow cylindrical metallic cavity. There was a hole in the flat end surface where the solution was ejected and formed nanofibers. Nanofibers were collected on the sheet placed below [47].

B. In this novel electrospinning setup, a conical wire coil was used as spinneret. PVA solution was filled in this conical wire coil; when high voltage was applied to this cone, jets were produced from the surface of wire coil. Nanofibers were collected on the metal plate placed below the conical wire coil [25].

C. Multi-hole spinneret was used that contained electrode and thick plastic plate. This plastic plate has 19 holes which produce more uniform electric filed during electrospinning process. The polymer solution was placed between the plastic plate and electrode. Polymer was pumped by syringe. It was found that electric field lines play leading role in jet repulsion during nanofiber production [48].

D. Variable high-voltage power supply was used that is supplied to needleless inner-cone nozzle. Heating device was used to melt polypropylene, and a cylinder collector was used to collect nanofibers [49].

Table 6.
Downward stationary spinnerets methods.

1.2.3.2.1.2 Downward stationary spinnerets

In downward stationary spinnerets, nanofibers are made in downward direction. Polymer solution is placed in shower-like spinnerets, polymer jets are stretched downward due to high voltage, and nanofibers are collected on the plate that was placed in the bottom. Some of these types of spinnerets are described in **Table 6**.

1.2.3.2.1.3 Upward stationary spinnerets methods

In this needleless electrospinning setup, a novel spinneret was used that have a stepped pyramid shape (**Table 7**). When electric field was applied to the system, then nanofibers were generated from the edges of stepped pyramid-shaped spinneret. These nanofibers were collected on the collector that was negatively charged, placed at the top of the spinneret. Nanofiber production increased by increasing applied voltage and keeping working distance and concentration of polymer solution constant [50].

1.2.3.2.2 Rotating spinnerets

In this needleless electrospinning method, the spinneret is rotated in polymer solution that licks polymer solution into its surface. When high voltage is applied to the spinneret, polymer jets are formed on the surface of spinneret, and nanofibers are formed that are deposited on the collector. Rotating spinnerets are further classified into three categories that are given below:

Horizontal rotating spinnerets
Downward rotating spinnerets
Upward rotating spinnerets

1.2.3.2.2.1 Horizontal rotating spinnerets

In this setup a metal roller was used as spinneret that was connected with high-voltage power supply (**Table 8**). Polymer solution was splashed onto metal roller through a hole of the solution provider that was placed above the metal roller spinneret. Nanofibers were collected on a metal collector that was placed horizontally [28].
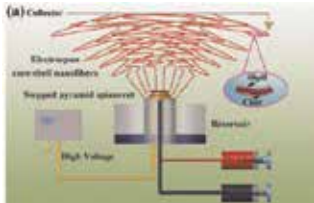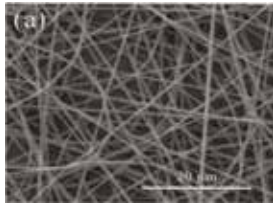
Year	Author	Setup	Morphology	Fiber bundling/ polymer
A. 2014	Jiang et al.			Polyvinyl alcohol is used as polymer; with concentration 8–10%, production of nanofiber is 2.46–5.84 g/h

Table 7.
Upward stationary spinnerets methods.

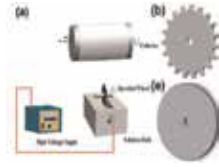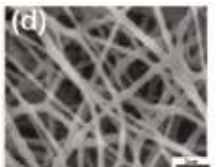| Year	Author	Setup	Morphology	Fiber bundling/ polymer
A. 2010	Tang et al.			Polyoxyethylene was used with water solvent. Productivity of nanofibers were 24–45 times more than single needle electrospinning

Table 8.
Horizontal rotating spinnerets.

1.2.3.2.2.2 Downward rotating spinnerets

In this electrospinning setup, polymer solution was continuously fed to the rotating cone by a tube (**Table 9**). This cone was connected with positively charged applied voltage. When high voltage was applied to cone, nanofibers were generated from the edges of the cone. These nanofibers were collected on a negatively charged collector placed in a downward direction [29].
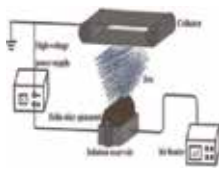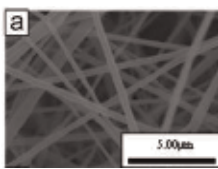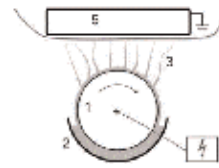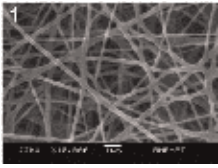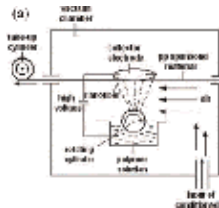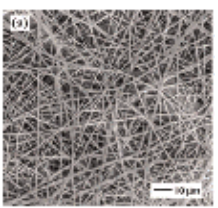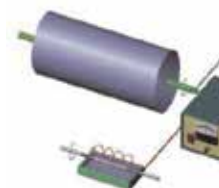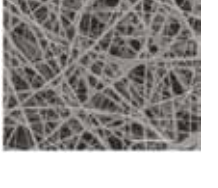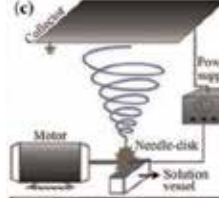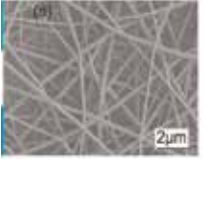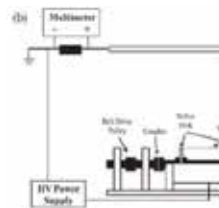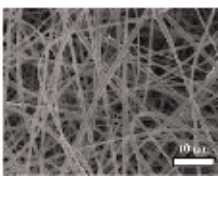
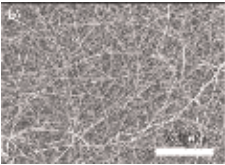### 1.2.3.2.2.3 Upward rotating spinnerets

This kind of spinnerets is used for more production and uniform nanofiber web formation. Polymer solution is placed in tub and spinneret is rotated in solution. Polymer solution layer is formed on the surface of spinneret. When high voltage is applied to spinneret, then polymer jets are formed that produce nanofiber. These nanofibers are moved in an upward direction and deposited on the collector (**Table 10**).

Year	Author	Setup	Morphology	Fiber bundling/polymer
A. 2010	Lu et al.			Polyvinylpyrrolidone is used as polymer. Production of this setup is 10 g/min

Table 9.
Downward rotating spinnerets.

Year	Author	Setup	Morphology	Fiber bundling/ polymer
A. 2012	Chen et al.			Polystyrene with 10 wt % is used in this setup. Production is 6.85 g/h

Year	Author	Setup	Morphology	Fiber bundling/polymer
B. 2014	Lu et al.			Gelatin powder was used in this setup; solvent is water. Production is this setup was 100 g/h
C. 2009	Kostakova et al.			Polyvinyl alcohol 10 wt % with water solution plus glyoxal 2.5 wt% and phosphoric acid 2.5 wt% of PVA were used. Production capacity of this setup was 2 g/min/m
D. 2010	Cengiz et al.			Polyvinyl alcohol polymer solution is used in this setup; productivity is not mentioned
E. 2012	Xin et al.			Polyurethane is used in this nanofiber production setup. Production of nanofibers is 2.94–9.42 g/h
F. 2016	Liu et al.			Polyvinylidenefluoride-co-hexa-fluoropropylene polymer is used in this setup. Production of nanofibers is 13.5 g/h
G. 2017	Ali et al			Polyvinyl alcohol polymer solution was used; maximum production was 5.24 g/h
H. 2012	Forward Keith et al.			Polyvinylpyrrolidone (PVP) was used as polymer with M_w = 55 kDa and 1.3 MDe. Production was not mentioned

Year	Author	Setup	Morphology	Fiber bundling/ polymer
I. 2017	Seongjun Moon et al.			Poly methyl methacrylate, polyacrylonitrile, polyvinyl alcohol, and lactic-co-glycolic acid were used as polymers; production was 3.2 g/h

A. In this upward rotating spinneret design, rotating disk was used to produce nanofibers. Sharp edges of disk produce high intensity of electric field that causes more productivity and fine nanofibers. In this study ultrafine polystyrene fibers were produced that contain parallel line surface structure, by using highly volatile solvent [32].

B. In this needleless electrospinning setup design for massive production of nanofibers, helix slice spinneret was used that rotates in Teflon solution bath which contains polymer solution. Air heater was used to maintained temperature of polymer solution. When helix slice rotates in polymer solution, edges of spinneret was coated with polymer; when there is high-voltage direct current supply, then polymer jets were formed at the edges of the helix slice that produced nanofibers [33].

C. This needleless electrospinning setup contains positively charged metal roller that rotates in solution bath. This metal roller is licked with solution when electric field exceeded surface tension of the polymer solution; then nanofibers jets were formed, and nanofibers were collected on nonwoven substrate that was placed below the collector electrode that was grounded [51].

D. Roller spinning device was used to produce nanofibers; it contained metal cylindrical roller that rotates in solution bath. High voltage was supplied to the solution; when a thin layer of polymer solution was made on the roller, nanofiber was produced from the edges of the cylinder. Collector electrode was grounded [52].

E. This electrospinning setup was designed to make fine nanofibers and high productivity. Conical wire coil was used as spinneret. This conical wire coil was licked with polymer solution; when electric field was applied. Nanofibers were produced that were collected on the rotating drum [53].

F. In this work, new spinneret was designed, and needle disk was used as spinneret. In this article, comparison between disk and needle disk was done. It was observed that electric intensity of needle disk is 5.33 times more than disk electrode. Productivity of nanofibers is 183 times more than traditional needle electrospinning. In the spinning process, when needle disk was rotated in polymer solution, needle was coated with polymeric solution. High voltage was applied to the system, nanofiber jets were formed at the tip of needles that produced competitive quality of nanofibers by enhancing throughput [54].

G. In this work, new spinneret was designed for massive production of nanofiber. The effect of the spinneret shape on large-scale production of nanofibers was described here. Comparison of disk and sprocket wheel in terms of electric field intensity, fiber production, and fiber morphology was done. Setup consists of rotating spinneret in solution bath. When high-voltage DC power was supplied to the solution, nanofiber jets were formed at the teeth of sprocket wheel that produce nanofibers; these nanofibers were collected on rotating cylinder [55].

H. In this needleless electrospinning setup, a thin wire was used as nanofiber generator. DC voltage was applied to the wire that was placed in solution bath. Wire spinneret was swept with polymer solution, a thin layer was formed on the surface of the wire that produced nanofiber jets, which was collected on the metal collector [56]. In this electrospinning setup, there is no mention of the effect of wire size on production and fiber morphology.

I. In this needleless electrospinning setup rotating, helically probed cylinder was used for nanofiber production. This system gives an easy and flexible method for setting up an electrospun nanofiber web. In this method breadths are placed that have a distance of between 0.1 and 1 mm; DC voltage is supplied that produce a Taylor cone. These changes influence the electrospinning to process a clump-based ceaseless framework and, in this way, abstain from suffering from repetitive streamlining technique. In this syringe less framework, comes about indistinguishable to those of customary electrospinning can be acknowledged generally effectively. Moreover, a few specialized leaps forward are proposed to overcome difficulties introduced by the traditional electrospinning strategy [57]. In this setup there is no optimization of needle distances and effect of needle size on production.

Table 10.
Upward rotating spinnerets.

Author details

Muhammad Waqas Munir* and Usman Ali
College of Textile Engineering, Bahauddin Zakariya University, Multan, Pakistan

*Address all correspondence to: mwaqasmunir786@yahoo.com

IntechOpen

References

[1] Varesano A, Carletto RA, Mazzuchetti G. Experimental investigations on the multi-jet electrospinning process. Journal of Materials Processing Technology. 2009; **209**(11):5178-5185

[2] Dosunmu O et al. Electrospinning of polymer nanofibres from multiple jets on a porous tubular surface. Nanotechnology. 2006;**17**(4):1123

[3] Gopal R et al. Electrospun nanofibrous filtration membrane. Journal of Membrane Science. 2006; **281**(1):581-586

[4] Jia H et al. Enzyme-carrying polymeric nanofibers prepared via electrospinning for use as unique biocatalysts. Biotechnology Progress. 2002;**18**(5):1027-1032

[5] Kedem S et al. Composite polymer nanofibers with carbon nanotubes and titanium dioxide particles. Langmuir. 2005;**21**(12):5600-5604

[6] Abidian MR, Kim DH, Martin DC. Conducting-polymer nanotubes for controlled drug release. Advanced Materials. 2006;**18**(4):405-409

[7] Wang X et al. Electrospun nanofibrous membranes for highly sensitive optical sensors. Nano Letters. 2002;**2**(11):1273-1275

[8] Thavasi V, Singh G, Ramakrishna S. Electrospun nanofibers in energy and environmental applications. Energy & Environmental Science. 2008;**1**(2):205-221

[9] Ma Z, Kotaki M, Ramakrishna S. Electrospun cellulose nanofiber as affinity membrane. Journal of Membrane Science. 2005;**265**(1):115-123

[10] Fang J et al. Applications of electrospun nanofibers. Chinese Science Bulletin. 2008;**53**(15):2265

[11] Saeed K et al. Preparation of amidoxime-modified polyacrylonitrile (PAN-oxime) nanofibers and their applications to metal ions adsorption. Journal of Membrane Science. 2008; **322**(2):400-405

[12] Lu X, Wang C, Wei Y. One-dimensional composite nanomaterials: Synthesis by electrospinning and their applications. Small. 2009;**5**(21): 2349-2370

[13] Khil MS et al. Electrospun nanofibrous polyurethane membrane as wound dressing. Journal of Biomedical Materials Research Part B: Applied Biomaterials. 2003;**67**(2):675-679

[14] Bergshoef MM, Vancso GJ. Transparent nanocomposites with ultrathin, electrospun nylon-4, 6 fiber reinforcement. Advanced Materials. 1999;**11**(16):1362-1365

[15] Gibson P, Schreuder-Gibson H. Production and characterization of nanoporous polymer membranes produced by an electrospraying process. In: Symposium on Porous, Cellular, and Microcellular Materials. Orlando, Florida: International Mechanical Engineering Congress and Exposition, Materials Division; 2000

[16] Gibson P, Schreuder-Gibson H, Rivin D. Transport properties of porous membranes based on electrospun nanofibers. Colloids and Surfaces A: Physicochemical and Engineering Aspects. 2001;**187**:469-481

[17] Choi SW et al. An electrospun poly (vinylidene fluoride) nanofibrous membrane and its battery applications. Advanced Materials. 2003;**15**(23): 2027-2032

[18] Huang Z-M et al. A review on polymer nanofibers by electrospinning and their applications in

nanocomposites. Composites Science and Technology. 2003;**63**(15):2223-2253

[19] Sarbatly R, Krishnaiah D, Kamin Z. A review of polymer nanofibres by electrospinning and their application in oil-water separation for cleaning up marine oil spills. Marine Pollution Bulletin. 2016;**106**(1):8-16

[20] Martin CR. Template synthesis of electronically conductive polymer nanostructures. Accounts of Chemical Research. 1995;**28**(2):61-68

[21] Vasita R, Katti DS. Nanofibers and their applications in tissue engineering. International Journal of Nanomedicine. 2006;**1**(1):15

[22] Malkar NB et al. Characterization of peptide-amphiphiles possessing cellular activation sequences. Biomacromolecules. 2003;**4**(3):518-528

[23] Li D, Xia Y. Electrospinning of nanofibers: Reinventing the wheel? Advanced Materials. 2004;**16**(14): 1151-1170

[24] Medeiros ES et al. Effect of relative humidity on the morphology of electrospun polymer fibers. Canadian Journal of Chemistry. 2008;**86**(6): 590-599

[25] Wang X et al. Needleless electrospinning of nanofibers with a conical wire coil. Polymer Engineering & Science. 2009;**49**(8):1582-1586

[26] Dosunmu OO et al. Polymer nanofibers from multiple jets produced on a porous surface by electrospinning. Nanotechnology. 2006;**17**(4):1123-1127

[27] Thoppey NM et al. Unconfined fluid electrospun into high quality nanofibers from a plate edge. Polymer. 2010;**51**(21): 4928-4936

[28] Tang S, Zeng Y, Wang X. Splashing needleless electrospinning of

nanofibers. Polymer Engineering & Science. 2010;**50**(11):2252-2257

[29] Lu B et al. Superhigh-throughput needleless electrospinning using a rotary cone as spinneret. Small. 2010;**6**(15): 1612-1616

[30] Huang X et al. Needleless electrospinning of multiple nanofibers. In: 2007 7th IEEE International Conference on Nanotechnology—IEEE-Nano 2007, Proceedings; Hong Kong. 2007

[31] Wu D et al. High throughput tip-less electrospinning via a circular cylindrical electrode. Journal of Nanoscience and Nanotechnology. 2010;**10**(7):4221-4226

[32] Huang C et al. Needleless electrospinning of polystyrene fibers with an oriented surface line texture. Journal of Nanomaterials. 2012;**2012**:1-7

[33] Lu W et al. Gelatin nanofibers prepared by spiral-electrospinning and cross-linked by vapor and liquid-phase glutaraldehyde. Materials Letters. 2014; **140**:1-4

[34] Varesano A et al. Multi-jet nozzle electrospinning on textile substrates: Observations on process and nanofibre mat deposition. Polymer International. 2010;**59**(12):1606-1615

[35] Theron SA et al. Multiple jets in electrospinning: Experiment and modeling. Polymer. 2005;**46**(9): 2889-2899

[36] Srivastava Y, Marquez M, Thorsen T. Multijet electrospinning of conducting nanofibers from microfluidic manifolds. Journal of Applied Polymer Science. 2007;**106**(5): 3171-3178

[37] Ding B et al. Fabrication of blend biodegradable nanofibrous nonwoven mats via multi-jet electrospinning. Polymer. 2004;**45**(6):1895-1902

[38] Tomaszewski W, Szadkowski M. Investigation of electrospinning with the use of a multi-jet electrospinning head. Fibres & Textiles in Eastern Europe. 2005;**13**(4):22

[39] Kumar A et al. Controlling fiber repulsion in multijet electrospinning for higher throughput. Macromolecular Materials and Engineering. 2010;**295**(8): 701-708

[40] Wang S, Yang Y, Zhang Y, Fei X, Zhou C, Zhang Y, et al. Fabrication of large-scale superhydrophobic composite films with enhanced tensile properties by multinozzle conveyor belt electrospinning. Journal of Applied Polymer Science. Jan 5 2014;**131**(1)

[41] Angammana CJ, Jayaram SH. The effects of electric field on the multijet electrospinning process and fiber morphology. IEEE Transactions on Industry Applications. 2011;**47**(2): 1028-1035

[42] Xie S, Zeng Y, et al. Industrial and Engineering Chemistry Research. 2012; **51**(14):5336-5345

[43] He J-H et al. BioMimic fabrication of electrospun nanofibers with high-throughput. Chaos, Solitons & Fractals. 2008;**37**(3):643-651

[44] Higham AK et al. Foam Electrospinning: A Multiple Jet, Needle-less Process for Nanofiber Production. AIChE. Vol. 602014. pp. 1355-1364

[45] Yarin AL, Zussman E. Upward needleless electrospinning of multiple nanofibers. Polymer. 2004;**45**(9): 2977-2980

[46] Holopainen J et al. Needleless electrospinning with twisted wire spinneret. Nanotechnology. 2014;**26**(2): 025301

[47] Zhou F-L, Gong R-H, Porat I. Polymeric nanofibers via flat spinneret electrospinning. Polymer Engineering & Science. 2009;**49**(12):2475-2481

[48] Zheng Y, Zeng Y. Electric field analysis of spinneret design for multihole electrospinning system. Journal of Materials Science. 2013; **49**(5):1964-1972

[49] Li X, Yang W, Li H, Wang Y, Bubakir MM, Ding Y, et al. Water filtration properties of novel composite membranes combining solution electrospinning and needleless melt electrospinning methods. Journal of Applied Polymer Science. 2015;**132**(10)

[50] Jiang G, Zhang S, Qin X. Effect of processing parameters on free surface electrospinning from a stepped pyramid stage. Journal of Industrial Textiles. 2016;**45**(4):483-494

[51] Kostakova E, Meszaros L, Gregr J. Composite nanofibers produced by modified needleless electrospinning. Materials Letters. 2009;**63**(28):2419-2422

[52] Cengiz F, Dao TA, Jirsak O. Influence of solution properties on the roller electrospinning of poly(vinyl alcohol). Polymer Engineering & Science. 2010;**50**(5):936-943

[53] Wang X et al. Needleless electrospinning of uniform nanofibers using spiral coil spinnerets. Journal of Nanomaterials. 2012;**2012**:1-9

[54] Liu Z, Ang KKJ, He J. Needle-disk electrospinning inspired by natural point discharge. Journal of Materials Science. 2017;**52**(4):1823-1830

[55] Ali U et al. Needleless electrospinning using sprocket wheel disk spinneret. Journal of Materials Science. 2017;**52**(12):7567-7577

[56] Forward KM, Rutledge GC. Free surface electrospinning from a wire electrode. Chemical Engineering Journal. 2012;**183**:492-503

[57] Moon S, Gil M, Lee KJ. Syringeless electrospinning toward versatile fabrication of nanofiber web. Scientific Reports. 2017;**7**:41424

Computational Analysis of Nanostructures for Li-Ion Batteries

Jameela Fatheema and Syed Rizwan

Abstract

Due to the energy crisis, the focus on the study of new materials has increased vastly. For the increasing demand of renewable energy, there are different ways suggested to attain that, which include the rechargeable batteries and the need to achieve them at smaller costs and for longtime use. Lithium ion batteries have gained a lot of attention for that specific reason. Along with the experiments, the easier way to understand and increase the efficiency of these materials for LIBs is to study them through simulations and theoretically. Density functional theory (DFT)-based study gives us an insight into the internal workings of the compounds used in lithium ion batteries (LIBs). In this chapter, an analysis of different structures is presented for use in LIBs, which mainly includes carbon nanostructures or nanotubes as well as 2D material graphene. The various ways in which the carbon-based structure is enhanced include doping into the structure, heterostructure of graphene with other 2D materials, and adsorption of atoms like Si onto the surface. The adsorption of Li on these various structures and the varying binding energies and capacity with the changing structure along with the understanding at atomic and nanoscale are mentioned.

Keywords: density functional theory, lithium ion battery, nanostructures, graphene, nanocarbons, adsorption, doping, computational

1. Introduction

We live in a world where most of the daily tasks in our life are dependent on energy like transport and communication over large distances. To satisfy the need for energy we have various sources, some of which are wind energy, solar energy, fossil fuel, nuclear energy, and so much more. For all of these, storage of energy in a device is an important part for which we have several kinds depending on the usage and need. Examples include capacitors, supercapacitors, batteries, fuel cells, flywheel, etc. A battery consists of one or more electrochemical cells and is connected externally to provide power to different appliances such as smartphones, electric car, laptop, etc. the electrochemical cell provides with electrical energy from a chemical reaction [1]. Now, batteries have two main types depending on the fact of rechargeable and non-rechargeable as illustrated in **Figure 1**. Primary batteries are nonrechargeable and provide electricity as soon as the connection is made with an electrical device's electrodes. Primary cell can only be used one time, and once they are discharged, they cannot be charged again and are discarded. Some of the examples of primary batteries are Daniel cell, dry cell, zinc air battery, mercury battery, etc. The usage of primary cell includes a wide range of devices like remote controls,

pacemakers, toys, and clocks [1], whereas secondary battery is rechargeable and needs to be charged first for providence of energy. Secondary batteries can be used for longer time than primary cells, due to their recharging capability as they can go from 100 to 1000 cycles of charge and discharge. There are numerous examples of secondary batteries, which are magnesium ion battery, nickel zinc battery, sodium ion battery, lithium ion battery, etc. [2]. Lithium ion battery has a higher amount of importance in the industry for a number of reasons. The light weight of Li element, that is, density = 0.53 g/cm^3 and the highest electropositive nature in the periodic table has helped in the arranging of battery with high energy density. Still, there are many issues to be addressed for improving the performance [3, 4].

1.1 Lithium-ion battery (LIB)

Lithium-ion battery (LIB) is a type of rechargeable battery in which Li ion moves during discharge from the negative electrode (cathode) to the positive electrode (anode) and then during charging Li ions move back from the anode to the cathode. There are four important components: anode, cathode, electrolyte, and separator [3, 4, 7]. Separator has the main role of keeping the electrodes apart, and, to allow the transport of only the charge carriers which in this case are lithium ions [8, 9]. Electrolyte has an important role in the transport as well and is usually made of lithium salts. Whereas, cathodes are made of lithium compounds like lithium cobaltates and lithium phosphates, and anode materials are usually made of 2D materials and their respective compounds. **Figure 2** shows a schematic representation of LIBs. When a source is supplied for charging of LIB, Li ions travel from the cathode through the electrolyte and separator to the anode and are intercalated into the 2D material. After fully charged, the source can be removed and the discharging starts in which the Li ions are desorbed from the anode and are transported back to the cathode [10]. The 2D materials that are preferred are graphene and carbon-based compounds because of their high conductivity and Li storage capability, not only on defect-free sites but defective as well [9, 11].

1.2 Simulations for LIBS

For a long time, the development and creation of new materials have been due to the experimental procedures, which were based entirely upon the intuition and judgment of the experimental researchers, depending upon the facilities as well as
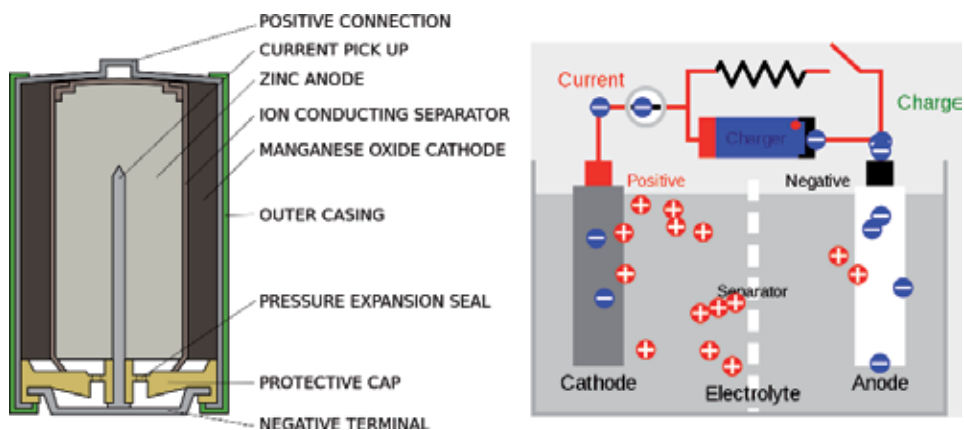

Figure 1.
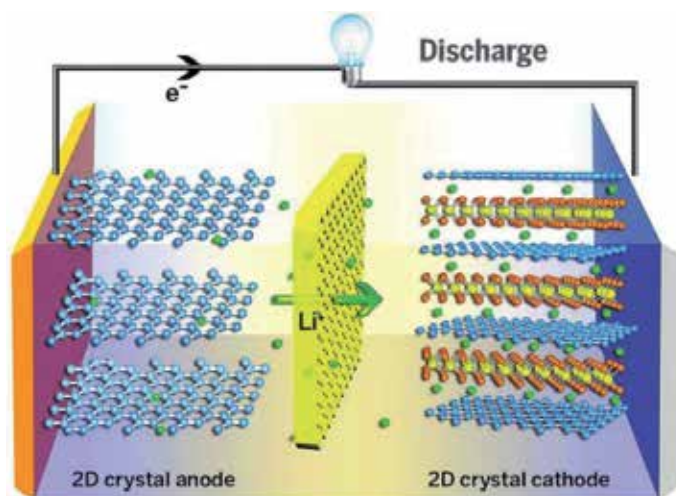*Illustration of (a) alkaline battery as an example of primary battery [5] and (b) general secondary battery [6].*

Figure 2.
A schematic reperesentation of lithium ion battery [10].

the availability of compounds and materials needed for conduction of an experiment. With the passing of time, we have developed computational techniques and codes for investigation of different aspects of a material and how to improve those materials. While the experimental methods are a complete hit in a dark room and waiting for the results to turn out for the best, we can simulate different structures, materials and compounds and alter them to our requirements and desire and then work on how to perform an experiment to get those results. Another way to think is that, when an experiment goes a specific way and we are unable to comprehend the reason, the theoretical calculations and modeling can help us understand on nano and atomic level about the hows and whys. Regarding the lithium ion batteries, there has been a lot of work done to improve its working by studying different materials to be used as a cathode along with studies for improvement of the anode and electrolyte. In this chapter, a brief review of studies made theoretically on nanocarbons for lithium-ion batteries is discussed.

2. Analysis of nanostructures

For the analysis of nanostructures, first, a brief general idea of the computational methods is necessary. There are several computational codes and different theoretical backgrounds that are used for these studies. The two main theories are potential-based methods and density functional theory. Here, we will focus on the DFT-based studies and the understanding of the electronic structure. Density functional theory (DFT) is a quantum mechanical approach to the study of the properties of matter on a microscopic basis that is most prevalent and effective [12]. The fundamental principle of DFT is that the total energy of the system is an exclusive functional of the electron density as given by Kohn-Sham equations [13]. The exchange-correlation potential that is introduced into a system helps to calculate the values accurately for which there are several formalisms, like local spin density approximation (LSDA) and generalized gradient approximation (GGA) [14, 15]. Moreover, including the Hubbard potential increases the accuracy of the system as it accounts for the columbic repulsions of the system [16].

The most important part is the simulation of a structure that will complement the experimental procedures. Then, we proceed to see the movement of electrons in these structures and analyze some of the important characteristics, like voltage

profile, formation energy, density of states, and diffusion of lithium ion. Here, our focus is on carbon-based compounds, which are mainly used as anodes in LIBs, more specifically graphene structures. Following this the doping, adsorption, heterostructures, cluster systems, composites, and other such possibilities used for enhancement of anode materials are conversed.

2.1 Doping mechanisms

One of the important ways to improve the performance of a material is the doping process. Graphene and carbon nanostructures have been doped through various procedures with different elements and studied for use in LIBs. For instance, Yang et al. have done a study on doping of germanium in graphene sheets, resulting in germagraphene and proceeded with observing the adsorption of lithium on different sites. The amount of Li adsorption is shown to be enhanced by doping germanium [17].

Ullah et al. have reported a large capacity anode material for LIBs by doping Be onto the graphene structure and studying the adsorption properties using the SIESTA code [18]. They have simulated single vacancy beryllium doped and double vacancy Be doped graphene structures and then proceeded to study the adsorption of different amounts of Li atoms on top side of the surface as well as bottom side of the surface (**Figure 3**). The doping of Beryllium makes it an electron-deficient system and the adsorption energy goes to −2.53 eV/Li atom and the rise in the capacity up to 2303.295 mAh/g for the Li_8BeC_7 structure. The reason for the huge capacitance is that in mono vacancy structure and divacancy structure the Li atoms get attached easily as the doping of Beryllium reduces the electrons and for divacancy the Li adsorption amount is more than mono vacancy.

Proceeding with Be doping, Ullah et al. have done the dual doping of graphene by modeling boron and beryllium, N and Be, and O and Be co-doped structures [19]. Doping of N and O increases the n-type characteristic while doping of B is for p-type characteristic. As Li is adsorbed onto the structures, it is indicated that the BeB doped structure shows good adsorption as the adsorption is ~3.1 times increased. The specification is that B addition increases the p-type nature of the
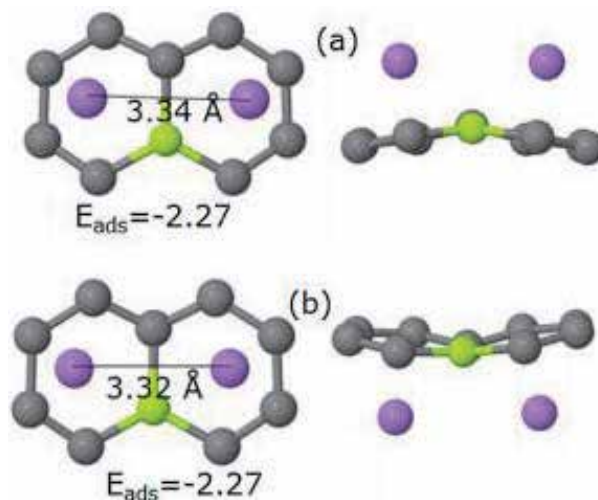

Figure 3.
Li adsorption on Be-doped graphene (top view on left and side view on right): (a) 2 Li atoms with up orientation and (b) 2 Li atoms with down orientation [18].

compound that already contains Be and C and hence the Li ion is adsorbed to the dual doped graphene sheet.

A different morphology-based structure was studied recently, in which graphene nanoribbons doped by B and undoped structures were simulated. The adsorption of Li on both the structures was observed which indicated that the capacity increases from 52 to 783 mAh/g when doped with B. The significance of this study is the fact that boron doping in graphene nanoribbons is more effective than the doping into pristine graphene structures [20].

The adsorption of lithium on undoped graphene and N or B doped graphene was studied indicating that the energy of adsorption is highest for Boron-doped graphene and lowest for Nitrogen-doped graphene [21]. The study was performed using the nudged elastic band method and the concentration for doping of both N and B was 12.5 at%, respectively, as shown in **Figure 4**. The conclusion was that N-doped graphene has better diffusion and desorption qualities than that of pristine graphene and boron doped graphene.

The doping of pyridinic and graphitic nitrogen in a double vacancy graphene structure, that is, 5-8-5 graphene vacancy is studied and the different structures are illustrated in **Figure 5** [22]. The potential surfaces, adsorption of 1 Li, adsorption of more than one lithium, and the diffusion of Li across the structure are investigated. Kong et al. have suggested that 4 pyridinic N doped graphene has good adsorption characteristic for Li as well as the diffusion, and hence it will be useful to synthesize for use as anode in LIBs.

Another point of importance is the amount of nitrogen doping that will be sufficient and what kind of doping will be useful, that is, the sites that are occupied by nitrogen. Yang has studied the nitrogen doping extensively along with the presence of defects and the adsorption of lithium on different structure shown in **Figure 6** [23]. The structures include pristine graphene, single N doping, two nitrogen doped at different sites, single nitrogen with single vacancy, and pyridinic structure with single and double vacancy and pyrrolic structure with single and double vacancy. On all these structures the electrical, magnetic, and adsorption properties are studied. The adsorption energy is more for the pristine graphene and single N doped structure while the energy is in negative for all the structures containing vacancies. Furthermore, the magnetic moment is shown to decrease with the adsorption of Li atom by the formation of a bond between free electrons with the electron in Li. Insert figure of structure.

Moreover, Watanabe et al. studied the upper limit for the nitrogen in carbon materials both theoretically and experimentally [24]. In the experimental study, they have concluded that with any increase in the carbonization temperature, the limit for nitrogen content in N doped carbon structures is decreasing. Moreover, the upper limits of N were found to be 14.32 and 21.66 wt% at 1000 and 900,
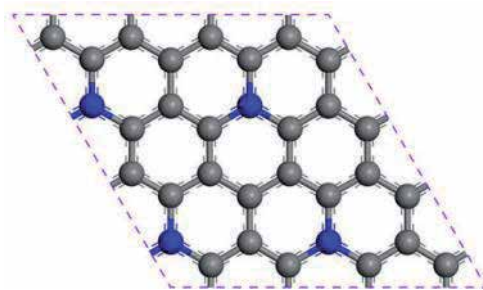

Figure 4.
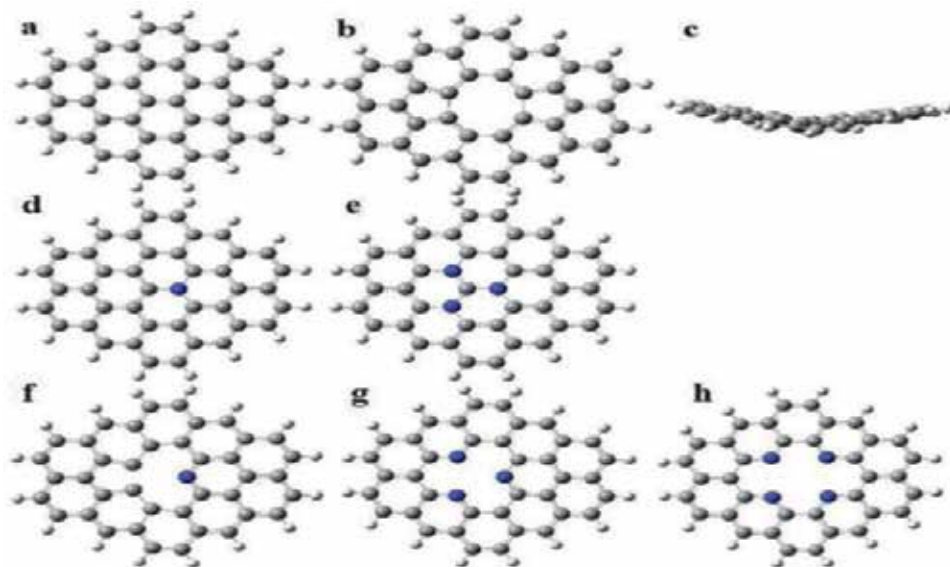*Doped graphene structure (gray color atoms = C and blue color atoms = B or N) [21].*

Figure 5.
(a) Pure graphene, (b) top view of 5-8-5 divacancy graphene, (c) side view of 5-8-5 divacancy graphene, (d) single graphitic N doped graphene, (e) 3 graphitic N doped graphene, (f) 1 pyridinic N doped graphene, (g) 3 pyridinic N doped graphene, and (h) 4 pyridinic N doped graphene [22].
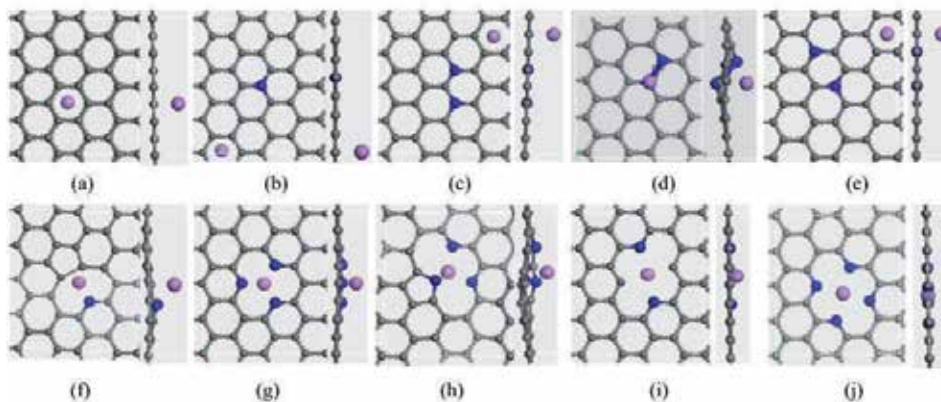

Figure 6.
Top and side view of Li adsorbed structures: (a) pristine graphene, (b) single N doped graphene, (c–e) double N doped graphene with diffent sites, (f) single N doped structure with single vacancy, (g–i) three nitrogen doped and single vacancy graphene, (j) double N doped divacancy graphene, and (j) 4 N doped and single vacancy structure [23].

respectively (**Figure 7**). Then they proceeded with studying the energetically favored structures at 1000 by doping N into C structure. The results they found were in close agreement with their experiment indicating that the existence of doped N in these structures is graphitic.

Agrawal et al. studied nanocarbon balls and microcarbon balls with and without nitrogen doping, both experimentally and theoretically [25]. Nitrogen doped porous carbon balls had been synthesized in the micro and nano range using the hydrothermal synthesis. According to their work, the nitrogen doped compounds had more electrical conductivity then undoped compounds. Their experimental results showed a similar situation as the charging capacity of N doped structures is more than the undoped micro and nano carbon balls. More recently, N and S co-doped graphene
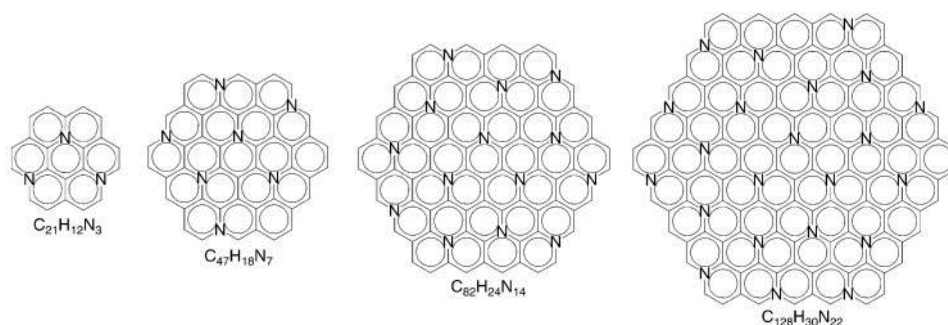
Figure 7.
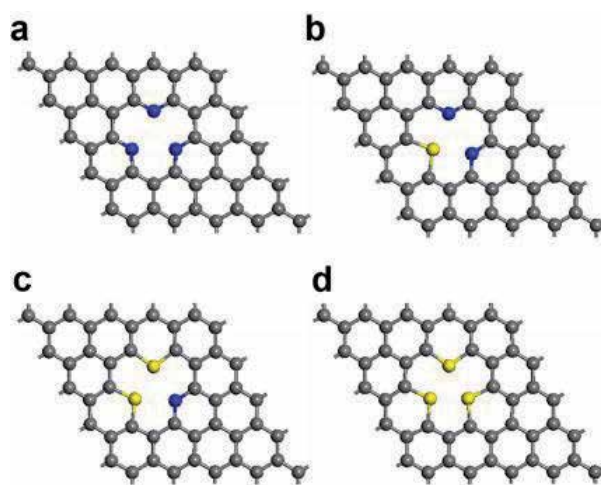*Graphene structure with varying N/C ratio [24].*

Figure 8.
Single vacancy graphene structures with (a) 3 N, (b) 2 N and 1 S, (c) 2 S and 1 N, and (d) 3 S doping [26].

structures were studied theoretically using VASP code [26]. 3N doped graphene, 2N and 1S doped graphene, 1 N and 2 S doped graphene, and 3 S doped graphene structure were simulated with single vacancy site near the doped atoms as shown in **Figure 8**. It was concluded that the bandgap goes from 0.4473 to 0.255 eV for 3N doped structure and 3S doped structure and that the N on the sited has a negative nature compared to s-doped structure which has a positive structure. With the increasing amount of S atoms, the charge on s decreases and we can tune the properties of graphene from this co-doping for electronic devices like Li-ion batteries.

The theoretical study of Yun et al. on doping of sulfur in graphene nanosheets is a good example of connecting the experiment with calculations and simulations to understand the possibility of sites that are being occupied by a dopant [27]. They have simulated three structures for doping of sulfur in graphene nanosheets as demonstrated in **Figure 9**. **Figure 9a** is the adsorption of sulfur on the graphene nanosheet, (**b**) is the substitution of sulfur in the graphene nanosheet, that is, replacing a carbon, and (c) is the placement of S_2 in a divacancy defect graphene nanosheet. The binding energies for adsorbed sulphur, substitutional sulfur, and S_2 divacancy sulfur are 0.85, 7.25, and 4.89 eV, respectively, whereas the bulk sulfur cohesive energy is 2.45 eV. They suggest that substitutional sulfur-doped structure is most likely possibility and that the doping of sulfur contributes to the increase of conductivity in sulfur-doped graphene nanosheet.
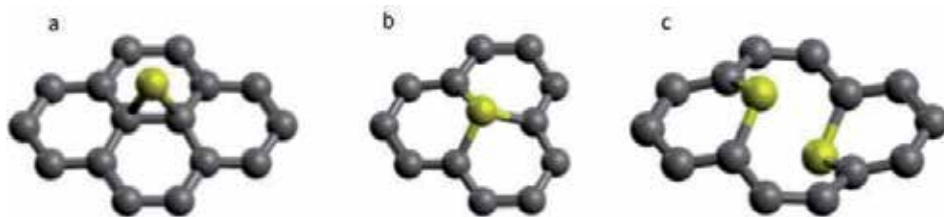
Figure 9.
Structure of (a) adsorbed S on graphene, (b) substitution of S in graphene, and (c) dimer S_2 on divacancy graphene.

2.2 Adsorption and diffusion

Besides the other properties of graphene and carbon nanostructure, it is important for LIBs that the extraction and reinsertion of lithium ion happen smoothly and the resultant is a long-lasting battery. The ionic mobility is an important characteristic; as the material capacitance and other properties improve, for the use of a material as an anode, it is necessary to see the mechanism that is happening in the structure. Adsorption plays an important role along with the doping of the structure.

Zheng et al. provide insight, which shows that in interaction between positive Li ion and graphene, Li ion favors the center of ring position [28]. Their study is based on VASP code and GGA functional. Vacancy-induced structure is also discussed, showing that the vacancy defects decrease the diffusion of positive lithium ion on the surface of the structure. Furthermore, the mechanism of lithiation in pristine graphene and defective graphene was studied by Vivek et al. [29]. They had concluded that the adsorption of Li onto the pristine graphene surface is highly unlikely whereas as the presence of the divacancy and Stone-Wales defects increases the chances of lithiation. As the defects are created, the potential around the defective zone increases which in turn increases the capability of adsorption of Li onto the surface as an adatom. The highest capacity (1675 mAh/g) is seen for the 25% divacancy defect, whereas the highest possibility for Stone-Wales defect at 100% ~1100 mAh/g where the defective structures are shown in **Figure 10**. A further insight is provided by Zhou et al. who claim that the divacancy defect is more attractive to the Li than the SW defect [30].

The effect of defects generated in graphene on Li adsorption has been studied in detail with different structure simulations [11, 31]. The formation of lithium clusters on the single vacancy and divacancy defective site was studied by Chen et al. [32]. They have shown the high amount of lithium storage in these defective sites.
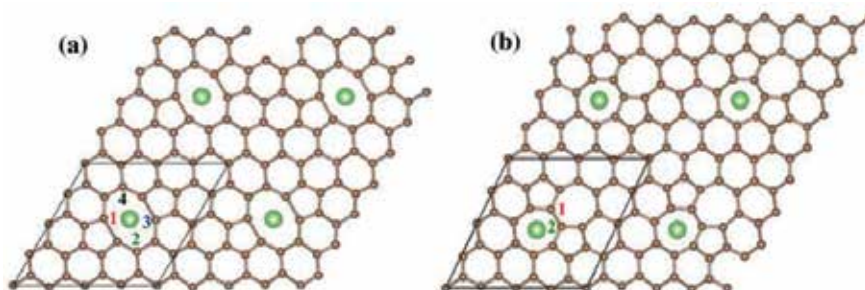

Figure 10.
(a) Divacancy defect graohene structure and (b) Stone-Wales defect graphene structure [29].

Mukherjee et al. studied the defective graphene experimentally and theoretically by synthesizing the porous graphene network and simulating it in different divacancy defect percentages [33]. They found their studies to be in agreement and that the Li adsorption had increased around the divacancy defect sites as well as the increasing divacancy defect percentage resulting in increasing lithium storage capacity [33].

The formation of lithium clusters on the (0 0 1) terminated surface suggested that the binding energy is less than that of Li on Li metal [34]. Fan et al. also studied the adsorption of single Li on to the pristine graphene structure and the different possibilities when more than one Li was adsorbed onto the surface that results into a cluster formation. The Li_4 is the most stable configuration; as the atoms were placed farther apart, the energy also increases, which is unfavorable. **Figure 11** shows the four possible configurations in which **Figure 8a** is the visualization of the stable state.

Modification of graphene to form zigzag edges is explored, which shows that the zigzag edges offer sites for the adsorption of Li and increases the adsorption as compared to pristine graphene or graphite [35, 36]. Furthermore, termination group adsorption onto edge modified graphene and graphite structure was simulated and then the diffusion of Li across these structures had been studied [37]. The termination groups included –O, –H and –OH. **Figure 9** shows the charge distribution on the edge modified graphene structure along with the presence of the termination groups on the edge-modified structure. The edge-modification increases the diffusion of lithium across the structure as compared to the pristine graphene. In
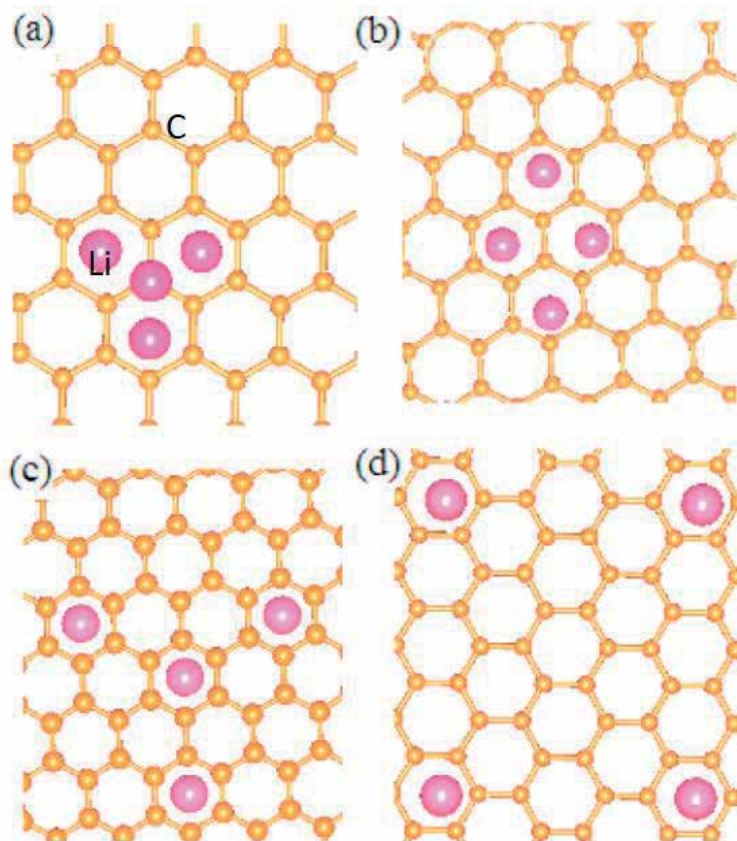

Figure 11.
Structure of Li adsorbed on graphene (a) Li_4 adsorption, (b) single Li at short distance, (c) single Li at slightly more distance, and (d) single Li at the corners of the structure [34].

the terminated structures, the –OH and –H termination decreases the diffusion as compared to the oxygen terminated structure, and from **Figure 12** we can see that oxygen has the highest charge contribution.

Recently, Si clusters have gained the attention of both experimental and theoretical researchers for different applications. The capability of Si for high Li adsorption when combined with the stability of the graphene or carbon-based materials increases the overall performance of silicon graphene composites [38, 39]. Hu et al. studied the adsorption of Li on a defective graphene surface with silicon cluster already adsorbed [40]. They had simulated various N-doped structures including graphitic graphene, pyridinic graphene, and pyrrolic graphene. After that they proceeded with the different possible configurations of Si adsorptions as shown in **Figure 13**. Then, Si_6 adsorbed structure were observed with Li adsorption, where Li forms bond with Si as along with C. Their study gives a detailed insight about the adsorption of structures where the N-doped defective sites have an important role. Si clusters move towards the defective site, where the volume expansion was decreased because of the defects and makes the adsorption of Li easier.

Liou et al. studied the different configurations for adsorption of lithium into a silicon graphene composite and concluded that in graphene silicon composite, intercalation of lithium happening in the interlayer of these two is more stable than the outside [41]. Furthermore, they proceeded with increasing the concentration of graphene layers and silicon percentage and observed that the structures are more stable with the increased concentration of Si [42]. This provides a good insight into the use of Si-incorporated graphitic structures to be used as anodes in LIBs.

2D planar carbon known as popgraphene which is composed of a network of 5-8-5 C rings was shown to be a low energy structure by the bottom-up design [43]. It was reported as an excellent material based on its high adsorption capacity, low diffusion barriers, and its metallic structure because of the attachment of CNTs. **Figure 14** shows the adsorption of 12 Li atoms on the popgraphene structure.
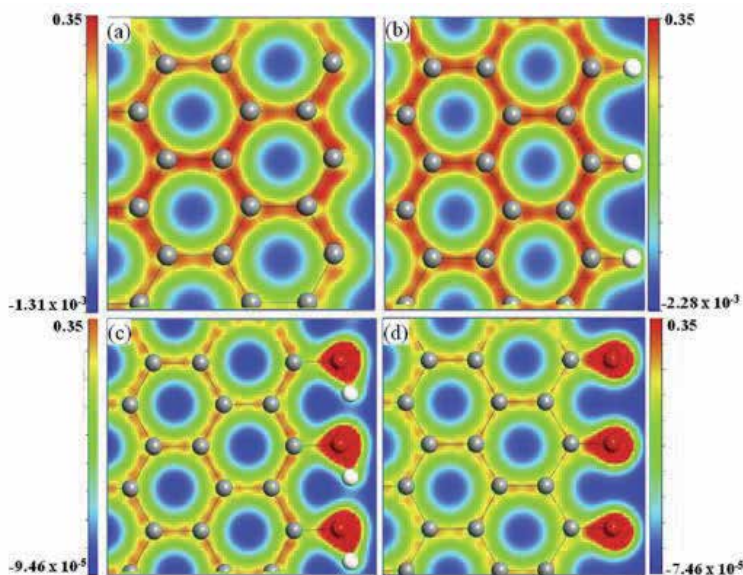

Figure 12.
Charge distribution in edge modified structure: (a) graphene, (b) −H terminations, (c) -OH terminations, and (d) −O terminations [37].
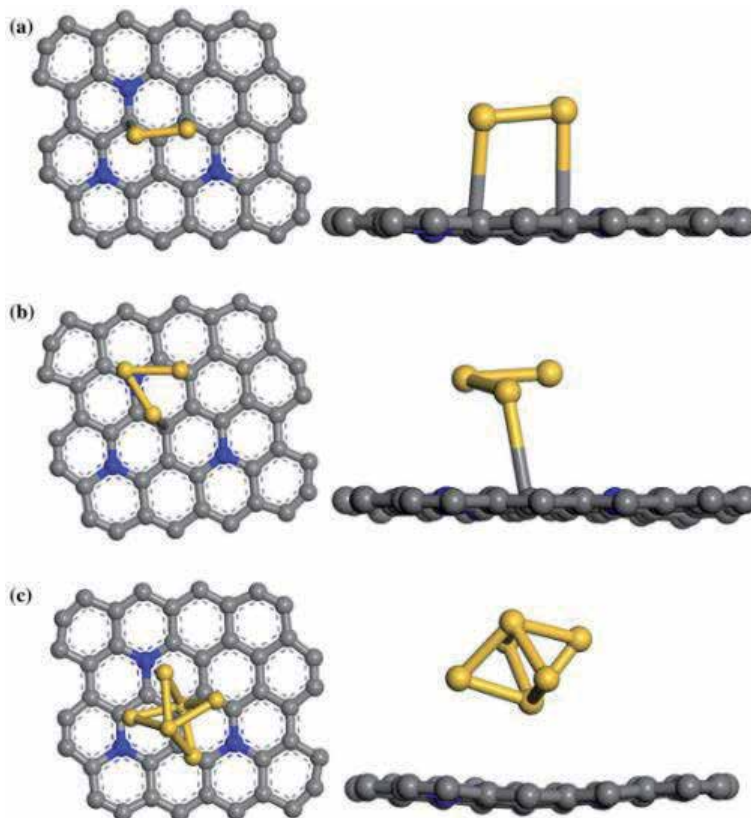
Figure 13.
(a) Si_2 cluster adorption on graphitic graphene, (b) Si_3 cluster adsorption on graphitic graphene, and (c) Si_6 cluster adorption on graphitic graphene [40].

2.3 Heterostructures of 2D compounds with graphene

The formation of heterostructures between carbon-based 2D material graphene and other 2D materials has also been studied for anode applications specifically in the LIB industry. 2D molybdenum oxide MoO_2 and graphene heterostructure were studied using the VASP code with GGA [44]. It shows a high theoretical capacity ~1400 mAh/g and high energy density for lithiation and fast charge and discharge rate. Rao et al. studied in detail the monolayer of C_2N and the bilayer heterostructure of C_2N/graphene [45]. Their results show that the diffusion coefficient for the heterostructure was better than the monolayer after the diffusion of lithium, whereas the capacity of monolayer was 220% the bilayered heterostructure.

The heterostructure of phosphorene and graphene was studied by Wang et al. and showed that the Li intercalation into the phosphorene/graphene heterostructure is better than the pristine phosphorene and pristine graphene [46]. However, there is a small band gap, which indicates the semimetal nature of the phosphorene/graphene heterostructure. Blue phosphorene and graphene heterostructure also shows a similar behavior and high theoretical capacity for lithium intercalation [47]. A bilayer hybrid structure of molybdenum sulfide 2D material with graphene was studied by experimentation as well as simulation [48]. Their purpose was to present a hybrid of these two compounds for lithium storage and concluded that their experimentation is in agreement with the simulation.
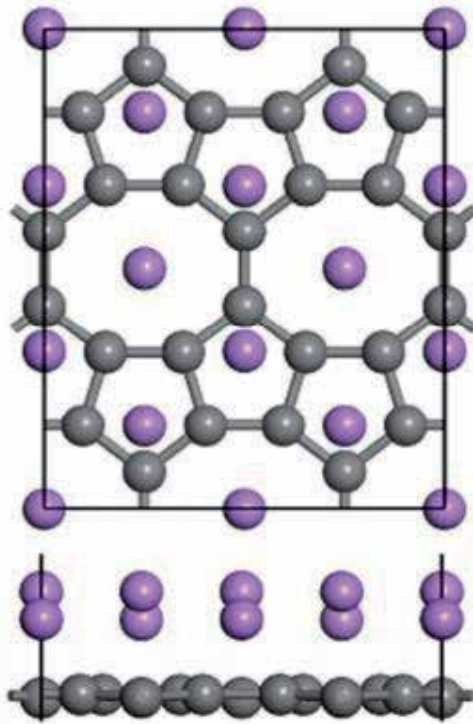
Figure 14.
Top and side view of pop graphene sheet with Li adsorption (purple = Li atom and gray = C atom) [43].

A new two-dimensional family of transition metal compounds called MXene and graphene heterostructure were simulated for lithium battery applications [49]. The study includes the intercalation of lithium into many different compounds of MXene as well as MXene and graphene heterostructure in the presence of the functional groups which are −O and −OH terminations attached to MXene as shown in **Figure 15**. They have established that the stability of the compound is maintained as the lattice parameter and interlayer separation remain almost the same after the intercalation of Li.

2.4 Carbon-based structures for cathode

Mainly for cathode in LIBs, the compounds used are lithium-based salts, phosphates, etc. Wang et al. have done an extensive study based on simulations as well as experimentations and have proposed structures containing $LiFePO_4$ (LFP) and carbon nanotubes (CNTs) [50]. Their DFT calculations provide a profound understanding of the electrochemical processes. For the DFT study, the structure of CNTs is attached at the (010) interface of LFP and the valence electron cloud charge for the structure is shown in **Figure 16**. Pure LFP structure has less density of states compared to the structure with CNTs, showing that the electrochemical activity of LFP was enhanced by the attachment of CNTs.

Jiang et al. studied the composite of vanadium oxide with vertically aligned CNT by the synthesis and characterization and then for the mechanism at atomic level the structures were simulated as well [51]. They have simulated CNT, pure vanadium oxide, and then the combination of these two with possible Li adsorption sites as shown in **Figure 17**. They have concluded that the vanadium oxide inclusion
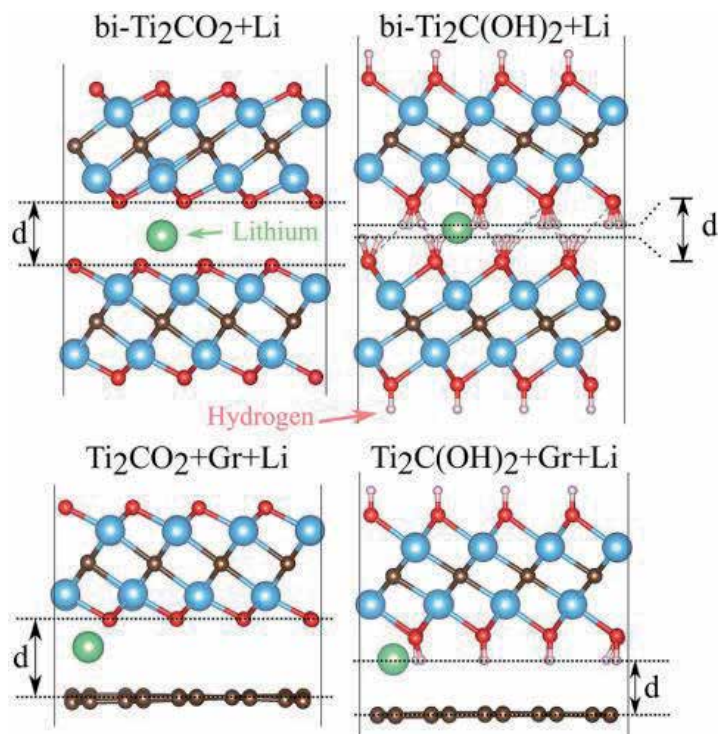
Figure 15.
(a) and (b) Bi-layer MXene Ti_2CT_x with intercalated lithium adsorbed (c) and (d) MXene Ti_2CT_x and graphene with intercalated lithium [49].
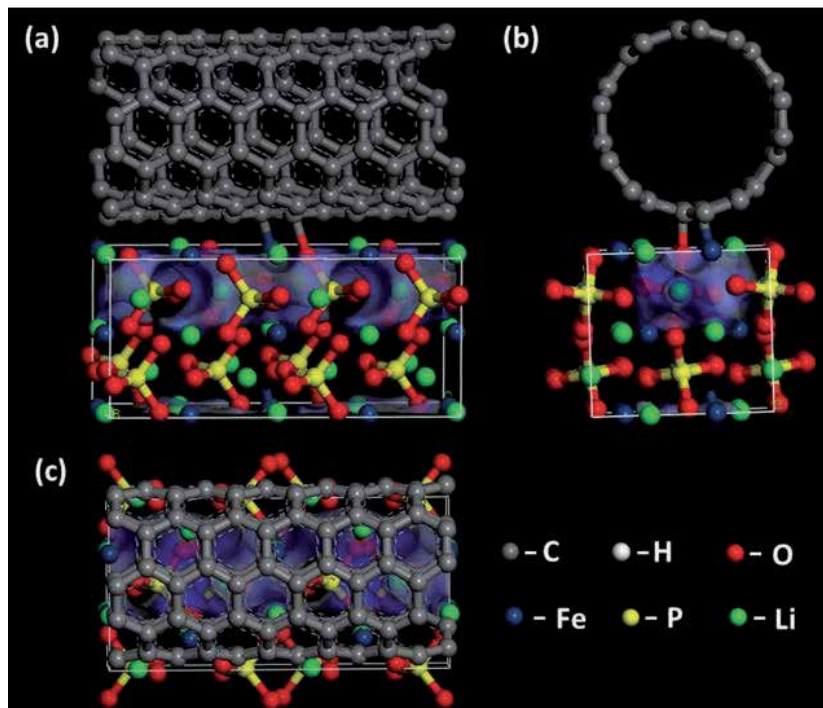

Figure 16.
(a) Front-view, (b) side-view, and (c) top-view, for compound interface of LFP and CNTs showing the valence electron cloud distribution [50].
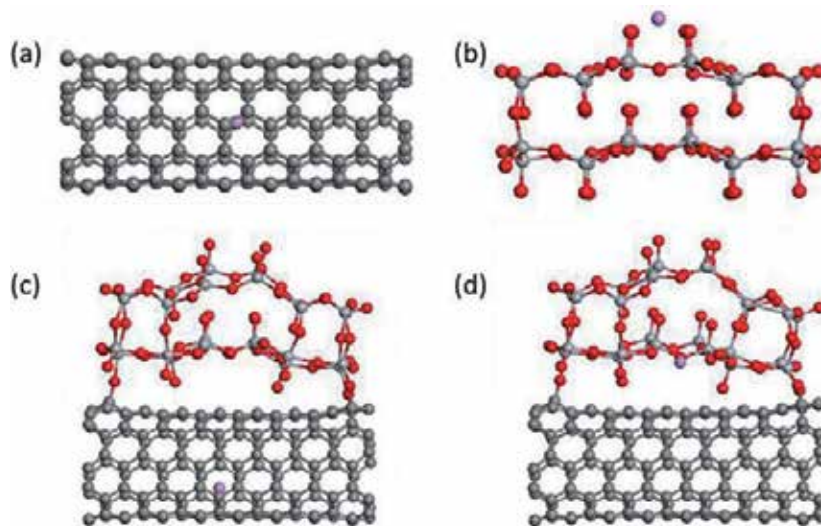
Figure 17.
Li adsorption on (a) CNT, (b) vanadium oxide, (c) and (d) composite of vanadium oxide on vertically aligned CNT [51].

onto the vertically aligned CNT decreases the path for diffusion of Li and aids the adsorption of Li.

Cui et al. presented the composite of orthorhombic MoO_3 and graphene as a cathode in LIBs with higher conductivity and adsorption of lithium. They studied the structure in bulk form as well as the monolayer structure. They have established that the Li charge and discharge rate have increased in the composite structure along with the capacity of lithium [52].

3. Conclusion

In conclusion, we can say that the carbon nanostructures are of great importance for use in the LIBs especially as anodes. Nitrogen doping and the various ways in which that is achieved showed very good results. The doping of C-based structures with beryllium, boron, and the co-doping of nitrogen and sulfur gave a different view on the possibilities. The adsorption mechanism of lithium was discussed which gave us a theoretical viewpoint of the procedures that goes on inside the LIBs. Also, the effect of defective sites in graphene structures as well as doped graphene structures on Li adsorption shows that these enhance the lithiation and de-lithiation of Li ion. The heterostructures of graphene with other 2D materials show the many possibilities for experimentation to improve the anode materials.

Acknowledgements

Conflict of interest

There are no conflicts of interest.

List of acronyms/abbreviations

LIB	lithium ion battery
DFT	density functional theory
GGA	generalized gradient approximation
LSDA	local spin density approximation
SIESTA	Spanish Initiative for Electronic Simulations with Thousands of Atoms
VASP	Vienna ab initio simulation package
SW	Stone-Wales
CNT	carbon nanotube

Author details

Jameela Fatheema and Syed Rizwan*
Physics Characterization and Simulations Lab (PCSL), School of Natural Sciences,
National University of Sciences and Technology (NUST), Islamabad, Pakistan

*Address all correspondence to: syedrizwanh83@gmail.com

IntechOpen

References

[1] Crompton TPJ. Battery Reference Book. Elsevier; 2000

[2] Linden D, Reddy TB, editors. Handbook of Batteries. 3rd ed. New York: McGraw-Hill; 2002

[3] Nitta N, Wu F, Lee JT, Yushin G. Li-ion battery materials: Present and future. Materials Today. 2015;**18**:252-264. DOI: 10.1016/j.mattod.2014.10.040

[4] Tarascon J-M, Armand M. Issues and challenges facing rechargeable lithium batteries. In: Materials for Sustainable Energy: A Collection of Peer-Reviewed Research and Review Articles from Nature Publishing Group. World Scientific; 2011. pp. 171-179

[5] Wikipedia. Alkaline-battery-English. Alkaline battery. Wikipedia [Internet]. 5/20/2019. Available from: https://en.wikipedia.org/w/index.php?oldid=898014065 [Accessed 2019-05-22]

[6] Wikipedia. Secondary Cell Diagram. Rechargeable battery. Wikipedia [Internet]. 5/16/2019. Available from: https://en.wikipedia.org/w/index.php?oldid=896056453 [Accessed 2019-05-22]

[7] Landi BJ, Ganter MJ, Cress CD, DiLeo RA, Raffaelle RP. Carbon nanotubes for lithium ion batteries. Energy & Environmental Science. 2009;**2**:638. DOI: 10.1039/b904116h

[8] Ji L, Meduri P, Agubra V, Xiao X, Alcoutlabi M. Graphene-based nanocomposites for energy storage. Advanced Energy Materials. 2016;**6**:1502159. DOI: 10.1002/aenm.201502159

[9] Ji L, Lin Z, Alcoutlabi M, Zhang X. Recent developments in nanostructured anode materials for rechargeable lithium-ion batteries.

Energy & Environmental Science. 2011;**4**:2682-2699

[10] Bonaccorso F, Colombo L, Yu G, Stoller M, Tozzini V, Ferrari AC, et al. Graphene, related two-dimensional crystals, and hybrid systems for energy conversion and storage. Science. 2015;**347**:1246501

[11] Okamoto Y. Density functional theory calculations of lithium adsorption and insertion to defect-free and defective graphene. The Journal of Physical Chemistry C. 2016;**120**:14009-14014. DOI: 10.1021/acs.jpcc.6b05458

[12] Fiolhais C, Nogueira F, Marques MAL. A Primer in Density Functional Theory. Springer Science & Business Media; 2003

[13] Burke K, Wagner LO. DFT in a nutshell. International Journal of Quantum Chemistry. 2013;**113**:96-101

[14] Perdew JP, Burke K, Ernzerhof M. Generalized gradient approximation made simple. Physical Review Letters. 1996;**77**:3865

[15] Oliver GL, Perdew JP. Spin-density gradient expansion for the kinetic energy. Physical Review A. 1979;**20**:397

[16] von Barth U, Hedin L. A local exchange-correlation potential for the spin polarized case. I. Journal of Physics C: Solid State Physics. 1972;**5**:1629

[17] Hu J, Ouyang C, Yang SA, Yang HY. Germagraphene as a promising anode material for lithium-ion batteries predicted from first-principles calculations. Nanoscale Horizons. 2019;**4**:457-463. DOI: 10.1039/C8NH00333E

[18] Ullah S, Denis PA, Sato F. Beryllium doped graphene as an efficient anode material for lithium-ion batteries

with significantly huge capacity: A DFT study. Applied Materials Today. 2017;**9**:333-340. DOI: 10.1016/j. apmt.2017.08.013

[19] Ullah S, Denis PA, Sato F. First-principles study of dual-doped graphene: Towards promising anode materials for Li/Na-ion batteries. New Journal of Chemistry. 2018;**42**:10842-10851. DOI: 10.1039/C8NJ01098F

[20] Liu H, Dong H, Ji Y, Wang L, Hou T, Li Y. The adsorption, diffusion and capacity of lithium on novel boron-doped graphene nanoribbon: A density functional theory study. Applied Surface Science. 2019;**466**:737-745. DOI: 10.1016/j.apsusc.2018.10.107

[21] Wu DH, Li YF, Zhou Z. First-principles studies on doped graphene as anode materials in lithium-ion batteries. Theoretical Chemistry Accounts. 2011;**130**:209-213. DOI: 10.1007/ s00214-011-0961-5

[22] Kong X-K, Chen Q-W. Improved performance of graphene doped with pyridinic N for Li-ion battery: A density functional theory model. Physical Chemistry Chemical Physics. 2013;**15**:12982-12987. DOI: 10.1039/ c3cp51987b

[23] Yu Y-X. Can all nitrogen-doped defects improve the performance of graphene anode materials for lithium-ion batteries? Physical Chemistry Chemical Physics. 2013;**15**:16819-16827. DOI: 10.1039/c3cp51689j

[24] Zhang S, Tsuzuki S, Ueno K, Dokko K, Watanabe M. Upper limit of nitrogen content in carbon materials. Angewandte Chemie (International ed. in English). 2015;**54**:1302-1306. DOI: 10.1002/anie.201410234

[25] Agrawal A, Biswas K, Srivastava SK, Ghosh S. Effect of N-doping on hard carbon nano-balls as anode for Li-ion battery: Improved hydrothermal

synthesis and volume expansion study. Journal of Solid State Electrochemistry. 2018;**22**:3443-3455. DOI: 10.1007/ s10008-018-4044-6

[26] Lee JH, Kwon SH, Kwon S, Cho M, Kim KH, Han TH, et al. Tunable electronic properties of nitrogen and sulfur doped graphene: Density functional theory approach. Nanomaterials (Basel, Switzerland). DOI: 10.3390/nano9020268

[27] Yun YS, Le V-D, Kim H, Chang S-J, Baek SJ, Park S, et al. Effects of sulfur doping on graphene-based nanosheets for use as anode materials in lithium-ion batteries. Journal of Power Sources. 2014;**262**:79-85. DOI: 10.1016/j. jpowsour.2014.03.084

[28] Zheng J, Ren Z, Guo P, Fang L, Fan J. Diffusion of Li+ ion on graphene: A DFT study. Applied Surface Science. 2011;**258**:1651-1655. DOI: 10.1016/j. apsusc.2011.09.007

[29] Datta D, Li J, Koratkar N, Shenoy VB. Enhanced lithiation in defective graphene. Carbon. 2014;**80**:305-310. DOI: 10.1016/j. carbon.2014.08.068

[30] Zhou L-J, Hou ZF, Wu L-M. First-principles study of lithium adsorption and diffusion on graphene with point defects. The Journal of Physical Chemistry C. 2012;**116**:21780-21787. DOI: 10.1021/jp304861d

[31] Yu Y-Z, Guo J-G, Zhou L-J. Theoretical investigation on the adsorption and diffusion of lithium-ion on and between graphene layers with size and defect effects. Adsorption Science & Technology. 2016;**34**:212-226. DOI: 10.1177/0263617415623429

[32] Huo L, Su F, Yi Z, Cui G, Zhang C, Dong N, et al. First-principles studies of Li nucleation on double-layered defective graphene. ChemElectroChem.

2019;**6**:810-817. DOI: 10.1002/celc.201801187

[33] Mukherjee R, Thomas AV, Datta D, Singh E, Li J, Eksik O, et al. Defect-induced plating of lithium metal within porous graphene networks. Nature Communications. 2014;**5**:3710. DOI: 10.1038/ncomms4710

[34] Fan X, Zheng WT, Kuo J-L, Singh DJ. Adsorption of single Li and the formation of small Li clusters on graphene for the anode of lithium-ion batteries. ACS Applied Materials & Interfaces. 2013;**5**:7793-7797. DOI: 10.1021/am401548c

[35] Jiao J, Xiao R, Tian M, Wang Z, Chen L. First-principles calculations on lithium and sodium adsorption on graphene edges. Electrochimica Acta. 2018;**282**:205-212. DOI: 10.1016/j.electacta.2018.05.200

[36] Uthaisar C, Barone V. Edge effects on the characteristics of Li diffusion in graphene. Nano Letters. 2010;**10**:2838-2842. DOI: 10.1021/nl100865a

[37] Leggesse EG, Chen C-L, Jiang J-C. Lithium diffusion in graphene and graphite: Effect of edge morphology. Carbon. 2016;**103**:209-216. DOI: 10.1016/j.carbon.2016.03.016

[38] Wang G, Xu B, Shi J, Lei X, Ouyang C. Confined Li ion migration in the silicon-graphene complex system: An ab initio investigation. Applied Surface Science. 2018;**436**:505-510. DOI: 10.1016/j.apsusc.2017.11.237

[39] Wang H, Wu M, Lei X, Tian Z, Xu B, Huang K, et al. Siligraphene as a promising anode material for lithium-ion batteries predicted from first-principles calculations. Nano Energy. 2018;**49**:67-76. DOI: 10.1016/j.nanoen.2018.04.038

[40] Hu R, Zhou J. A DFT study of Li adsorption on surface of Si clusters

anchored N-doped defective graphene composite. Applied Surface Science. 2018;**457**:789-796. DOI: 10.1016/j.apsusc.2018.07.004

[41] Zhou F, Liao N, Zhang M, Xue W. Lithiation behavior of graphene-silicon composite as high performance anode for lithium-ion battery: A first principles study. Applied Surface Science. 2019;**463**:610-615. DOI: 10.1016/j.apsusc.2018.08.258

[42] Zhou F, Liao N, Zhou H, Xue W. Atomic investigation on reversible and irreversible lithium storage in silicon incorporated with multi-layered graphene. Materials Letters. 2019;**244**:108-110. DOI: 10.1016/j.matlet.2019.02.068

[43] Wang S, Yang B, Chen H, Ruckenstein E. Popgraphene: A new 2D planar carbon allotrope composed of 5-8-5 carbon rings for high-performance lithium-ion battery anodes from bottom-up programming. Journal of Materials Chemistry A. 2018;**6**:6815-6821. DOI: 10.1039/C8TA00438B

[44] Ma J, Fu J, Niu M, Quhe R. MoO2 and graphene heterostructure as promising flexible anodes for lithium-ion batteries. Carbon. 2019;**147**:357-363. DOI: 10.1016/j.carbon.2019.03.006

[45] Ding Y, Xiao B, Li J, Deng Q, Xu Y, Wang H, et al. Improved transport properties and novel Li diffusion dynamics in van der Waals C 2 N/graphene heterostructure as anode materials for lithium-ion batteries: A first-principles investigation. The Journal of Physical Chemistry C. 2019;**123**:3353-3367. DOI: 10.1021/acs.jpcc.8b11044

[46] Guo G-C, Wang D, Wei X-L, Zhang Q, Liu H, Lau W-M, et al. First-principles study of phosphorene and graphene heterostructure as anode materials for rechargeable Li batteries. The Journal of Physical Chemistry

Letters. 2015;**6**:5002-5008. DOI:
10.1021/acs.jpclett.5b02513

[47] Li Y, Wu W, Ma F. Blue phosphorene/
graphene heterostructure as a promising
anode for lithium-ion batteries: A
first-principles study with vibrational
analysis techniques. Journal of Materials
Chemistry A. 2019;**7**:611-620. DOI:
10.1039/C8TA09423C

[48] Jing Y, Ortiz-Quiles EO,
Cabrera CR, Chen Z, Zhou Z. Layer-
by-layer hybrids of MoS2 and reduced
graphene oxide for lithium ion batteries.
Electrochimica Acta. 2014;**147**:392-400.
DOI: 10.1016/j.electacta.2014.09.132

[49] Aierken Y, Sevik C, Gülseren O,
Peeters FM, Çakır D. MXenes/graphene
heterostructures for Li battery
applications: A first principles
study. Journal of Materials
Chemistry A. 2018;**6**:2337-2345. DOI:
10.1039/C7TA09001C

[50] Wang B, Liu T, Liu A, Liu G,
Wang L, Gao T, et al. A hierarchical
porous C@$LiFePO_4$/carbon nanotubes
microsphere composite for high-rate
lithium-ion batteries: Combined
experimental and theoretical
study. Advanced Energy Materials.
2016;**6**:1600426. DOI: 10.1002/
aenm.201600426

[51] Jiang H, Wei Z, Cai X, Lai L, Ma J,
Huang W. A cathode for Li-ion batteries
made of vanadium oxide on vertically
aligned carbon nanotube arrays/
graphene foam. Chemical Engineering
Journal. 2019;**359**:1668-1676. DOI:
10.1016/j.cej.2018.10.223

[52] Cui Y, Zhao Y, Chen H, Wei K, Ni S,
Cui Y, et al. First-principles study of
MoO_3/graphene composite as cathode
material for high-performance lithium-
ion batteries. Applied Surface Science.
2018;**433**:1083-1093. DOI: 10.1016/j.
apsusc.2017.10.147

Edited by Morteza Sasani Ghamsari
and Soumen Dhara

The book, Nanorods and Nanocomposites aims to provide the reader with an overview of the recent advances made on the synthesis of nanorods and nanocomposites and their emerging applications for a better lifestyle. The nanorods are a surprising gift to materials science from the research field of nanoscale materials. Nanorods promise to serve as a building block of the next-generation electronic and optoelectronic devices. Nanocomposite materials are multiphase solid materials that have one organic or inorganic nanoarchitectured compound with various nanostructures, such as nanoparticles, nanowires, nanorods, and nano-films, etc., or with multiphase solid materials (metals, oxides, polymers, and carbon). Due to the progressive physical, chemical, electrical, thermal, optical, electrochemical, and catalytic properties of nanocomposites, they exhibit multi-functional characteristics in a variety of engineering applications such as piezoelectrics, thermoresistors, sensors, energy-related technologies, water purification catalysts, electro-photonics, and so on. Despite the wide variety of applications due to their unique nanostructures, the fabrication of nanocomposites and the realization of their applications in different fields remains a challenging task. The focus of this book is to provide a platform for presentation of the latest knowledge and recent progress in synthesis, functionalization, and applications of nanocomposite materials. It is expected that this book presents the most attractive and versatile technological developments in the field of nanorods and nanocomposite materials and their applications that will provide a better understanding of the currently ongoing research in related fields.

IntechOpen